VOLUME 80 SEPTEMBER 9, 1976 NUMBER 19

JPCHAx

THE JOURNAL OF PHYSICAL CHEMISTRY

PUBLISHED BIWEEKLY BY THE AMERICAN CHEMICAL SOCIETY

THE JOURNAL OF

PHYSICAL CHEMISTRY

Published by the
AMERICAN CHEMICAL SOCIETY
BOOKS AND JOURNALS DIVISION
D. H. Michael Bowen, Director

Editorial Department: Charles R. Bertsch, Head; Marianne C. Brogan, Associate Head; Celia B. McFarland, Joseph E. Yurvati, Assistant Editors
Graphics and Production Department: Bacil Guiley, Head
Research and Development Department: Seldon W. Terrant, Head

Advertising Office: Centcom, Ltd., 50 W. State St., Westport, Conn. 06880.

Published biweekly by the American Chemical Society at 20th and Northampton Sts., Easton, Pennsylvania 18042. Second class postage paid at Washington, D.C. and at additional mailing offices.

Editorial Information

Instructions for authors are printed in the first issue of each volume. Please conform to these instructions when submitting manuscripts.

Manuscripts for publication should be submitted to *The Journal of Physical Chemistry,* Department of Chemistry, University of Minnesota, Minneapolis, Minn. 55455. Correspondence regarding **accepted papers and proofs** should be directed to the Editorial Department at the ACS Easton address.

Page charges of $60.00 per page are assessed for papers published in this journal. Ability to pay does not affect acceptance or scheduling of papers.

Bulk reprints or photocopies of individual articles are available. For information write to Business Operations, Books and Journals Division at the ACS Washington address.

Requests for **permission to reprint** should be directed to Permissions, Books and Journals Division at the ACS Washington address. The American Chemical Society and its Editors assume no responsibility for the statements and opinions advanced by contributors.

Subscription and Business Information

1976 Subscription rates—including surface postage

	U.S.	PUAS	Canada, Foreign
Member	$24.00	$29.75	$30.25
Nonmember	96.00	101.75	102.25
Supplementary material	15.00	19.00	20.00

Air mail and air freight rates are available from Membership & Subscription Services, at the ACS Columbus address.

New and renewal subscriptions should be sent with payment to the Office of the Controller at the ACS Washington address. **Changes of address** must include both old and new addresses with ZIP code and a recent mailing label. Send all address changes to the ACS Columbus address. Please allow six weeks for change to become effective. **Claims** for missing numbers will not be allowed if loss was due to failure of notice of change of address to be received in the time specified; if claim is dated (a) North America—more than 90 days beyond issue date, (b) all other foreign—more than 1 year beyond issue date; or if the reason given is "missing from files". Hard copy claims are handled at the ACS Columbus address.

Microfiche subscriptions are available at the same rates but are mailed first class to U.S. subscribers, air mail to the rest of the world. Direct all inquiries to Business Operations, Books and Journals Division, at the ACS Washington address or call (202) 872-4444. **Single issues** in hard copy and/or microfiche are available from Special Issues Sales at the ACS Washington address. Current year $4.75. Back issue rates available from Special Issues Sales. **Back volumes** are available in hard copy and/or microform. Write to Special Issues Sales at the ACS Washington address for further information. **Microfilm** editions of ACS periodical publications are available from volume 1 to the present. For further information, contact Special Issues Sales at the ACS Washington address. **Supplementary material** must be ordered directly from Business Operations, Books and Journals Division, at the ACS Washington address.

Microfiche	U.S.	PUAS, Canada	Other Foreign
Photocopy	$2.50	$3.00	$3.50
1–7 pages	4.00	5.50	7.00
8–20 pages	5.00	6.50	8.00

Orders over 20 pages are available only on microfiche, 4 × 6 in., 24X, negative, silver halide. Orders must state photocopy or microfiche if both are available. Full bibliographic citation including names of all authors and prepayment are required. Prices are subject to change.

American Chemical Society
1155 16th Street, N.W.
Washington, D.C. 20036
(202) 872-4600

Member & Subscription Services
American Chemical Society
P.O. Box 3337
Columbus, Ohio 43210
(614) 421-7230

Editorial Department
American Chemical Society
20th and Northampton Sts.
Easton, Pennsylvania 18042
(215) 258-9111

Notice to Authors last printed in the issue of January 1, 1976

THE JOURNAL OF
PHYSICAL CHEMISTRY

Volume 80, Number 19 September 9, 1976

JPCHAx 80(19) 2049-2142 (1976)

ISSN 0022-3654

■ Supplementary material for this paper is available separately (consult the masthead page for ordering information); it will also appear following the paper in the microfilm edition of this journal.

* In papers with more than one author, the asterisk indicates the name of the author to whom inquiries about the paper should be addressed.

AUTHOR INDEX

THE JOURNAL OF
PHYSICAL CHEMISTRY

VOLUME 80, NUMBER 19 SEPTEMBER 9, 1976

Estimated Future Atmospheric Concentrations of CCl_3F (Fluorocarbon-11) for Various Hypothetical Tropospheric Removal Rates[1]

F. S. Rowland* and Mario J. Molina

Department of Chemistry, University of California, Irvine, California 92717 *(Received March 10, 1976)*

Publication costs assisted by the U.S. Energy Research and Development Administration

The variation in CCl_3F tropospheric concentrations vs. time has been calculated with different assumptions for the rates of its removal by hypothetical tropospheric removal processes. A comparison has been made of the actual total atmospheric release from anthropogenic sources to that date. The observed CCl_3F exceeds by about 20% the amount calculated to be present with stratospheric photolysis as the only removal process. Consequently, an increase of 10–20% in the estimated manufacture of CCl_3F through 1975 is needed to obtain agreement with the observed concentrations on the assumption that tropospheric removal processes are negligible. If the estimates of manufacture are stretched to the upper limit and of observed atmospheric concentration to the lower limit (total change of 30%), agreement could be reached on the assumption of about equal losses to stratospheric and tropospheric sinks. Faster tropospheric removal rates for CCl_3F are incompatible with the observed atmospheric concentrations.

Introduction

The recognition that the amount of CCl_3F (fluorocarbon-11) in the earth's atmosphere was in approximate agreement with the accumulated anthropogenic production to that date[2] was an important factor in stimulating a search for the terrestrial sinks for such chlorofluorocarbon molecules.[3] (We use the term sink for both the geophysical location and the physicochemical process by which a molecule is either decomposed or else removed from the atmosphere.) However, many sinks which are effective in removing other compounds from the troposphere (e.g., rainfall, chemical reaction, photolysis by visible or near-ultraviolet light) do not affect CCl_3F molecules, with the consequence that its tropospheric residence time is long enough to permit major fractions of these molecules to penetrate into the mid-stratosphere. At altitudes above about 20 km, ultraviolet photolysis is possible for $\lambda \leq 230$ nm, and CCl_3F is decomposed with the release of Cl atoms, as in[3]

$$CCl_3F + h\nu \rightarrow Cl + CCl_2F \quad (1)$$

The subsequent depletion of stratospheric ozone through the ClO_x chain reaction of

$$Cl + O_3 \rightarrow ClO + O_2 \quad (2)$$

and

$$ClO + O \rightarrow Cl + O_2 \quad (3)$$

poses a potentially very serious long term problem with continued use of CCl_3F and other volatile saturated, perhalo chloro compounds at the world-wide rates characteristic of the early 1970's.[3-7]

Quantitative evaluation of the magnitude of such ozone depletion reactions has been carried out by several different research groups, with the general conclusion that the present world-wide average level of ozone has been depleted by about 1% from past atmospheric releases of CCl_3F and CCl_2F_2, with long-term depletions of the order of 10% to be expected at steady state for current rates of use.[3,5,6] Since ozone depletion of this magnitude is potentially sufficiently hazardous that further atmospheric release of these molecules may need to be drastically curtailed, a search for possible ameliorating processes is very important. If an appreciable fraction of the CCl_3F molecules were destroyed in the troposphere, by an as yet unidentified process, then both the fraction of decompositions leading to stratospheric release of Cl atoms and the resultant ozone depletion would be correspondingly lessened.

The search for such tropospheric sinks can be carried out by two general methods. First, specific mechanisms can be identified (e.g., dissolution in the ocean; trapping in Antarctic snow; reaction with ions; etc.) and assessed in quantitative fashion. To date, such specific sinks have all proven, when evaluated, to be quantitatively of minor importance. However,

the possibilities either that an undiscovered major tropospheric sink might exist, or that an accumulation of many minor sinks might add up to a major effect makes a more general evaluation of tropospheric sinks for CCl_3F of considerable importance.

Such a general search can be carried out by continual evaluation of the comparison between the amount of CCl_3F already released to the atmosphere and the amount of CCl_3F currently to be found there. Such a comparison depends rather sensitively upon the precision of knowledge both of atmospheric release figures and of present atmospheric concentrations. The comparison is even more sensitive since a large fraction of the CCl_3F molecules has been released within the past decade and has therefore been exposed to the various possible removal processes for only a relatively short time. Our estimate in October, 1974, was that the observed amount of CCl_3F in the atmosphere was consistent with any overall atmospheric residence time longer than 20 years.[3b]

Estimates of World Production

The data for U.S. production and sales of various chlorofluorocarbon molecules are reported each year by the U.S. Tariff Commission, and the data for CCl_3F and CCl_2F_2 have been individually listed beginning with the 1958 report. McCarthy has estimated U.S. production of CCl_3F before 1958, and production in the rest of the world for the entire period, although he has indicated that the accuracy of the latter is not as great as for U.S. production figures.[8] He has given ±20% as the accuracy of his overall estimates. These data have been widely quoted and have served as the basis for all quantitative calculations published to date, and our present calculations are also based on these data. As shown in Figure 1, the production through 1973 can be accurately represented by an exponential growth curve in two segments with coefficients of 0.266 to the end of 1962 and 0.135 from the beginning of 1963 to the end of 1973. The production data for 1974 and 1975 are estimated separately in our calculations. Our comparison is made for September 1, 1975 because of the availability of good quality data on northern hemisphere tropospheric concentrations during September, 1975.[9]

The total amount of CCl_3F manufactured to the end of 1973 has been given as 2267 ktons (metric).[8] We have assumed the production of an additional 313 ktons during 1974 (McCarthy's estimate for 1973) plus 200 ktons during the first eight months of 1975, for a total of 2780 ktons of CCl_3F produced to September 1, 1975. We have further assumed that natural sources of CCl_3F are negligible.

Corrections for CCl_3F Not Yet Released to the Atmosphere

The total integrated atmospheric release of CCl_3F is always less than the integrated production because of delays between manufacture and release, and through usage in technological applications *not* involving atmospheric release. Several estimates are now available for the percentage use of CCl_3F in various applications, and these can be used for estimates of the fractional release of CCl_3F to the atmosphere.

The chief uses of CCl_3F are in propellant mixtures for aerosol sprays, in refrigeration, and in the manufacture of foamed plastics, although a variety of lesser uses have also been identified. The aerosol propellant gases are released to the atmosphere soon after manufacture, while the refrigerant gases have a greater delay time before release. However, the longest delay time is probably involved in the "blowing" of closed-cell polyurethane foams. In these foams the CCl_3F molecules are retained within the cells of plastic, and atmospheric release will occur only with the destruction of the structure of the plastic. One estimate suggests that most such foam will be buried in sanitary land-fills (and not incinerated), while some more recent practices involve shredding with the destruction of the plastic structure. In the long run, the eventual atmospheric release of CCl_3F from closed-cell foams will be dependent upon the prevalence of these various disposal processes. At the present time, however, it seems apparent that most of the CCl_3F originally incorporated into closed-cell foams has not yet been released to the atmosphere.

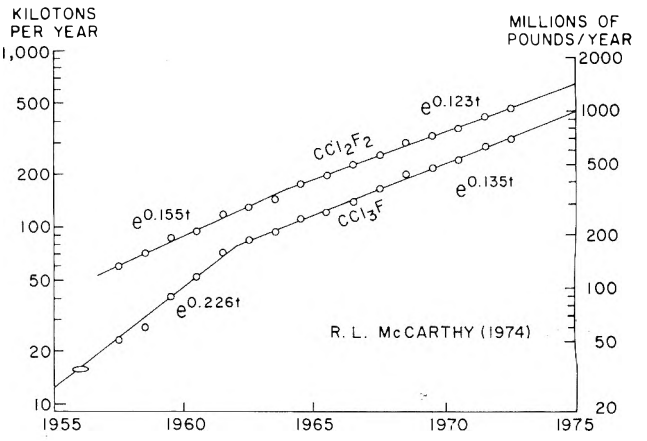

Figure 1. Production of CCl_3F and CCl_2F_2 vs. calendar year, as estimated by McCarthy.

About half of the plastic foamed with CCl_3F is classified as "open-cell", and release of the foaming agent to the atmosphere occurs at the time of manufacture without further delay.

Correction Factors for Delay in Atmospheric Release

The most important nonatmospheric reservoir for CCl_3F already manufactured is that still retained in closed-cell polyurethane foams. Estimates of the fraction of CCl_3F used for blowing both open and closed cell foams in the United States have been given, as shown in Table I.[10-12] Such estimates are not always entirely consistent with one another, but a reasonable estimate of the percentage use of CCl_3F in the foaming of plastic is 19 ± 2% in the U.S. in the early 1970's. Since the distribution between open-cell and closed-cell plastics has been stated to be approximately equal,[13] a satisfactory approximation can be made that 9% of the 1972–1973 production of CCl_3F in the U.S. is still trapped in the cells of closed-cell plastics and has not been released to the atmosphere. Noting that 40% of all CCl_3F manufactured to date has been made since January, 1972, and lacking year by year estimates, we have assumed that the same factor can be applied to the total U.S. production. In addition, since the estimate has also been made that the percentage use in the foaming of plastics is approximately the same for the rest of the world as it is in the U.S.,[14] we have calculated that 9% of the integrated world production of CCl_3F has not been released to the atmosphere because of enclosure in closed-cell foamed plastic. This correction amounts to 250 ktons for the 2780 ktons manufactured to September 1, 1975.

Several separate estimates have been made of the percentage use of CCl_3F as a refrigerant in the U.S., with 7 and 3% given in Table I. A separate estimate of 3% has also been given by Howard and Hanchett.[15] We have averaged these roughly, and have made an estimate that the typical large

TABLE I: Technological Use of CCl_3F in the United States in 1972 and 1973

	Millions of pounds				Percentage use			
	Aerosol propellants	Foaming agents	Refrigerant	Solvent	Aerosol propellants	Foaming agents	Refrigerant	Solvent
1972[a]	215	50	19	5	74	17	7	2
1973[a]	267	75	10	5	75	21	3	1

[a] Reference 10. Estimates of the IMOS committee based on personal communication with DuPont Co. (see ref 5, p 88). [b] Reference 11. Estimates of the IMOS committee based on personal communication with A. D. Little and Co. (see ref 5, p 88).

commercial refrigeration unit (the primary refrigerant use for CCl_3F) requires 25% refill per year, or an average of a 4-year delay before release. Since about 1200 ktons of CCl_3F have been manufactured in the past 4 years, a 4% use in refrigeration would indicate about 50 ktons stored in refrigeration units.

The final correction that must be made is for the time lag between manufacture and atmospheric release of CCl_3F used as an aerosol propellant. This delay includes inventory time following manufacture, shelf time before sale, and then release spread over a period of time. We estimate about 6 months as the average time from manufacture to release, with the result that about 120 ktons ($313 \times 0.76 \times 0.5$) already manufactured and designated for aerosol usage has not yet been released to the atmosphere.

Our estimate of the atmospheric release to September 1, 1975, of the 2780 ktons of CCl_3F manufactured to that date is reduced downward by 250 + 50 + 120 ktons, for a total of 2360 ktons. Since the usage pattern was not changing too rapidly, at least into early 1975, we have also assumed that 85% atmospheric release (2360/2780) is a reasonable estimate at any time all through the early 1970's (1 kton of CCl_3F contains 4.38×10^{30} molecules).

Current Tropospheric Concentrations

Many research groups are now measuring the concentrations of CCl_3F and CCl_2F_2 in ambient air in a variety of locations. While measurements in the mid-stratosphere are essential for the verification of stratospheric photochemistry,[16-19] the variability with altitude and location and the relatively small number of samples make these data of only secondary importance in the assessment of the current atmospheric burden of CCl_3F. The infrared detection of CCl_2F_2, and with lesser accuracy, of CCl_3F, have shown by comparison of 1975 data with a retroactive examination of 1968 data an increase of more than a factor of 2 in the concentration of these molecules in the stratosphere over that period.[18] However, the primary data for estimates of the current atmospheric burden of CCl_3F are the much more numerous measurements of background tropospheric concentrations.[9,20-24] Several sets of such data have been published which show the steady buildup of CCl_3F with time in the troposphere. However, most of these experiments have been carried out with only rough (typically, ±30%) absolute calibration of detector accuracy, and with no interlaboratory calibration. Our estimates of current tropospheric concentrations are chiefly based on the measurements of Rasmussen, who gave the background mixing ratio of CCl_3F in rural locations of eastern Washington state in September, 1975, as 123 ± 2 ppt (10^{-12} by volume) with a stated absolute accuracy of ±10%.[9] This value is in reasonable agreement with other data reported in late 1975.

No permanent measuring stations have yet been established in the southern hemisphere, so that data of comparable quality do not exist for the southern half of the atmosphere. However, four sets of data are available from which the concentration ratios of the southern/northern hemispheres can be estimated. Rasmussen has simultaneously measured CCl_3F in oceanic air off Peru and Ecuador vs. that found in Pullman, Washington, and has found 20% less CCl_3F in the southern hemisphere.[25] Lovelock has reported a comparison of concentrations of CCl_3F in Adrigole, Ireland, and Capetown, South Africa, and has found a south/north ratio of 0.77.[21] (Approximately half of the area of the southern hemisphere lies north of the latitude of Capetown.) Comparative measurements have also been made in Antarctica, both at surface level and with aircraft sampling, with regular calibration against a standard sample of rural eastern Washington air. The ground level measurement of CCl_3F showed 0.72 times as much in Antarctica as in the northern hemisphere standard. However, the aircraft measurement was regularly about 10% higher or about 0.8 of the northern hemisphere value.[26] In view of the reported absorption of CCl_3F into snow and the observed negative concentration gradient, the aircraft value is probably more representative of southern hemisphere tropospheric air. All three direct comparisons of north/south ratios for CCl_3F are consistent with a ratio of 1.0/0.8.

Finally, measurements in both hemispheres of the concentrations of radioactive ^{85}Kr have also shown a south/north ratio of 0.8.[27] The inert gas ^{85}Kr is formed in nuclear fission, and since the atmospheric nuclear test ban of the early 1960's its initial release to the atmosphere occurs primarily during processing of spent fuel elements from reactors used for electric power production. These processing plants, as with the technological uses of CCl_3F, are almost entirely in the much more heavily industrialized northern hemisphere. Since the total amount of uranium being fissioned is rapidly increasing, and the 10-year half-life of ^{85}Kr prevents its long term accumulation, the north/south pattern of ^{85}Kr must also represent an interhemispheric distribution of an inert gas most of which has been released in the northern hemisphere during the past decade. With all four estimates in close agreement, we have assumed a south/north tropospheric concentration ratio of 0.8, and hence a world-wide average tropospheric concentration equal to 0.9 times the northern hemisphere background, i.e., from the Rasmussen data, a value of 111 ppt, ±10% in September, 1975.

These average surface level concentrations should also be applicable all the way to the tropopause, and indeed Krey's measurements (not intercalibrated) showed concentrations at the 100 ppt level as high as 15 km in tropical regions in April, 1975.[19] The concentration of CCl_3F falls off immediately ately as soon as the measurements cross the troposphere into the stratosphere, and reach a level about half of the sea-level

concentration at about 20 km altitude in mid-latitudes.[16-19] With the 90% of the atmosphere below 15 km all at approximately the sea-level concentration of CCl_3F, and another 5% of the atmosphere between 15 and 20 km, we conclude that the average CCl_3F concentration over the *entire* atmosphere is about 0.95 times the surface background concentration, or 105 ppt ±10% in September, 1975. The estimated atmospheric burden of CCl_3F in September, 1975, is then 105 ppt × 1.1 × 10^{44} molecules in the atmosphere ÷ 4.38 × 10^{30} molecules CCl_3F/kton, or 2640 ktons (±10%). Inasmuch as this measured atmospheric burden is 12% larger than the calculated atmospheric release to that time, some discrepancy obviously exists in one or both of the estimates.

Effects of Tropospheric and Stratospheric Sinks on Fraction of CCl_3F Surviving in the Atmosphere

The rapid mixing of gases to all altitudes within the troposphere ensures quick accessibility of newly released CCl_3F to any removal processes operating within the troposphere. The very low concentration of the chlorofluorocarbon molecules makes it extremely unlikely that any possible tropospheric removal processes could be even partially saturated, and all tropospheric sinks can therefore be represented by an average rate constant for removal applicable to the entire tropospheric concentration of CCl_3F. If removal were predominantly by tropospheric processes then the actual rate of removal is directly proportional at all times to the existing tropospheric burden. Such exponential removal would be applicable to all tropospheric sinks involving contact with atmospheric gases (e.g., lightning strokes; reaction with trace ingredients; condensation on cold surfaces; etc.)

Such a direct exponential removal is, however, not applicable to a removal process acting in the stratosphere until a steady-state condition is attained. Until that time, the actual stratospheric concentrations available for such removal processes lag behind the tropospheric concentration because of the time scale of years applicable to upward mixing in the stratosphere.[3] Similarly, a deep-ocean sink would also have a diffusion barrier and a time lag during the slow downward mixing, and would not be fully effective until steady state is reached.

The stratospheric measurements of CCl_3F concentration vs. altitude have clearly indicated the existence of a major photochemical sink in mid-stratosphere,[16-19] consistent with the average photochemical lifetimes calculated earlier (e.g., about 1 month at 30 km altitude).[3] Any other potential sinks operating anywhere other than the troposphere must have comparably rapid rates of removal or else be negligible in terms of quantitative removal of CCl_3F simply because such a small fraction of CCl_3F is currently found outside of the troposphere. For this reason, all of our calculations described below about the possible influence of sinks other than stratospheric photolysis have been carried out for hypothetical tropospheric sinks with removal rates directly proportional to the existing tropospheric concentration of CCl_3F. These hypothetical removal rates have been arbitrarily applied to all of the atmosphere below 10 km, i.e., to about 75% of the atmospheric CCl_3F.

Calculations of Survival Fractions for CCl_3F

Very precise modeling of the atmospheric release of CCl_3F would involve distribution of the production among the various technological uses, evaluation of the time delays and patterns for each use, and summation of all of these release patterns into a combined atmospheric release function. We have, however, assumed that a simpler approximation is satisfactory within the probable accuracy of any resulting comparisons in the foreseeable future. Our calculations have all been carried out as though there were immediate release without any time lag for all CCl_3F as soon as it has been manufactured. Then, for specific comparisons with observational data we have estimated the amounts not yet released to the atmosphere, as done above for comparisons in September, 1975.

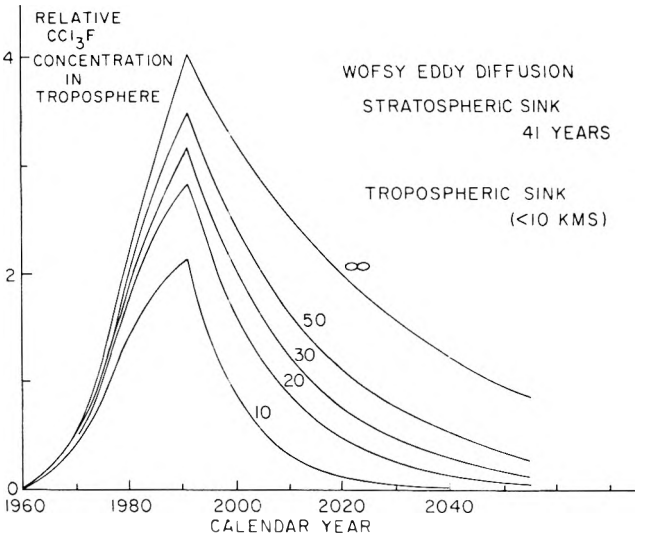

Figure 2. Relative concentration of CCl_3F in the troposphere with various hypothetical tropospheric sinks, using eddy diffusion coefficient from ref 28. Atmospheric release assumed constant from 1976 to 1990, terminating at end of 1990. Tropospheric removal rates expressed as reciprocals: $k = 0.02$ year^{-1} for CCl_3F below 10 km is marked as 50 (years).

Earlier we calculated the expected tropospheric and stratospheric concentrations vs. time using a one-dimensional eddy diffusion model, and the manufacturing pattern for CCl_3F illustrated in Figure 1. In those calculations, we separately evaluated the expected patterns for a series of eddy diffusion coefficients developed by others for treatment of NO_x-stratospheric chemistry.[3] We have now repeated some of these calculations with the inclusion of an additional removal term operating on all of the molecules present below 10 km. The primary goal of these calculations has been to evaluate how the survival time for CCl_3F in the atmosphere, its fractional removal in the stratosphere, and the variation of tropospheric CCl_3F concentration vs. time are affected by the inclusion of such tropospheric removal terms.

These calculations have been carried out with the actual exponential growth pattern for the use of CCl_3F shown in Figure 1 to the end of 1975, and then extended at a constant yearly production rate for various lengths of time. The increase in tropospheric concentration of CCl_3F with time is shown in Figure 2 for an assumed continuation at constant yearly production for 15 additional years followed by an abrupt termination of further atmospheric release at the end of 1990. In this one-dimensional calculation we have utilized the eddy diffusion coefficient vs. altitude developed by Wofsy et al.[28] A similar calculation was also performed with the Hunten eddy diffusion coefficient,[29] as shown in Figure 3. We have also used other eddy diffusion coefficients,[3] but these models are typical of the spread in stratospheric mixing rate assumptions in the current literature.

We have listed in Table II the relative tropospheric concentrations indicated for December, 1975. for all of the hy-

TABLE II: Calculated Concentrations of CCl_3F for Stratospheric Plus Various Assumed Tropospheric Sinks

	Tropospheric removal rate $1/k$, years	Hunten[a]		Wofsy[b]	
		Rel trop. concn	Atmos. burden,[c] Mtons	Rel trop. concn	Atmos. burden,[c] Mtons
Inert tracer with no removal processes	∞	(1.00)	2.36	(1.00)	2.36
Stratospheric photolysis only	∞	0.95	2.24	0.90	2.12
Stratospheric photolysis plus tropospheric removal, k year^{-1} for all CCl_3F below 10 km	50	0.88	2.08	0.84	1.98
	30	0.83	1.97	0.80	1.88
	20	0.79	1.86	0.75	1.77
	10	0.66	1.56	0.64	1.52

[a] Calculations for December, 1975, using eddy diffusion coefficient of Hunten (ref 29). [b] Calculations for December, 1975, using eddy diffusion coefficient of Wofsy (ref 28). [c] Atmospheric burden in megatons, assuming total atmospheric release of 2.36 Mtons of CCl_3F by September, 1975 (see text).

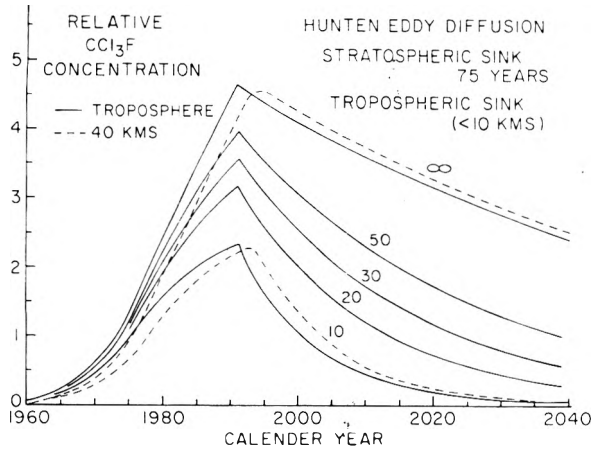

Figure 3. Relative concentration of CCl_3F in the troposphere with various hypothetical tropospheric sinks, using eddy diffusion coefficient from ref 29. Atmospheric release assumed constant from 1976 to 1990, terminating at end of 1990. Tropospheric removal rates expressed as reciprocals: k = 0.02 year^{-1} for CCl_3F below 10 km is marked as 50 (years). CIX concentrations at 40 km indicated by dashed lines.

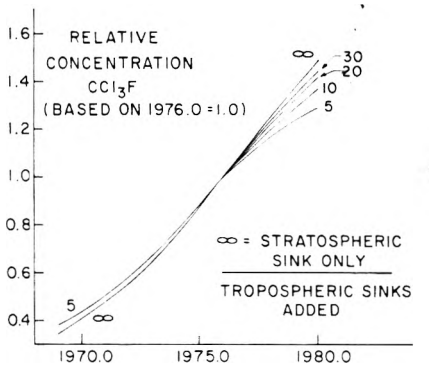

Figure 4. Relative concentration of CCl_3F normalized to concentration at end of 1975 as 1.0, with various hypothetical tropospheric sinks using eddy diffusion coefficient from ref 29. Atmospheric release assumed constant from 1976 to 1980.

pothetical tropospheric sinks with both of these eddy diffusion assumptions. The relative fractions remaining with each tropospheric assumption differ very little at any time from 1970 to 1975. With stratospheric photolysis as the only sink, about 5 (Hunten) to 10% (Wofsy) of the CCl_3F is estimated to have been decomposed by the end of 1975. The inclusion of a hypothetical tropospheric sink with k = 0.02 year^{-1} ("50-year tropospheric sink") would have increased the total CCl_3F removed to 12 (Hunten) or 16% (Wofsy), while faster hypothetical tropospheric removal rates would naturally have resulted in still larger removal percentages. The fraction of CCl_3F surviving for each assumed tropospheric removal rate has been converted into an estimated total atmospheric burden of CCl_3F in September, 1975, using the production input data of McCarthy corrected for 15% nonrelease to the atmosphere, as described in an earlier section. These estimates of hypothetical atmospheric burdens are also given in Table II.

The data on the expected patterns of growth for CCl_3F from Figure 3 have been normalized to the December, 1975, concentration as 1.0, for each hypothetical tropospheric removal rate. As shown in Figure 4 the rate of increase in CCl_3F concentration over the next few years is practically independent of the presence or absence of tropospheric sinks with lifetimes of 20 years or longer.

It is highly unlikely that we will be experimentally able to distinguish in 1980 whether the CCl_3F concentration has increased over the concentration of December, 1975, by 50 (no tropospheric sink) or 40 (20-year tropospheric sink), or even 35% (10-year tropospheric sink). Similarly, examination of *ratios* of tropospheric (or stratospheric) concentrations in the past offers even less chance for obtaining information about the possible existence of tropospheric sinks, as illustrated also in Figure 4. We conclude that it will not be possible to obtain concentration measurements now or in the future that are accurate enough to indicate within the next 10 years the presence or absence of tropospheric sinks by the *rate* of increase of tropospheric or stratospheric concentrations.[30] The quantitative evaluation of the cumulative importance of all tropospheric sinks will thus depend upon measurements of absolute concentrations, and not of rates of increase in CCl_3F concentration in any part of the atmosphere. A corollary to this conclusion is that the amount of CCl_3F to be found in the atmosphere in the year 2000, and the ozone depletion to be caused by it, are not very dependent on whether slow tropospheric removal processes exist or not. Instead both are dependent primarily upon how much CCl_3F has already been released to the atmosphere, and how much additional CCl_3F is released during the next 25 years. Only tropospheric removal processes corresponding to 10–20-year tropospheric sinks could appreciably reduce the CCl_3F concentration by the year 2000, and tropospheric sinks of this size are inconsistent with actual atmospheric concentrations, as described below.

The CCl_3F concentration data of Figures 2 and 3 can be

TABLE III: Calculated Atmospheric Residence Times for Stratospheric and Assumed Tropospheric Sinks

Tropospheric sink, k_{10}^{-1}, years	Eddy diffusion from Hunten: Lifetime k_t^{-1}, years	k_t ×10^{-2} year^{-1}	k_{st} ×10^{-2} year^{-1}	k_{tr} ×10^{-2} year^{-1}	F	Wofsy: Lifetime, k_t^{-1}, years	k_t × 10^{-2} year^{-1}	k_{st} × 10^{-2} year^{-1}	k_{tr} × 10^{-2} year^{-1}	F
∞	75.1	1.3	1.3		1.00	41.3	2.4	2.4		1.00
50	35.1	2.8	1.3	1.5	0.47	25.6	3.9	2.4	1.5	0.62
30	26.0	3.8	1.3	2.5	0.35	20.5	4.9	2.4	2.5	0.49
20	19.6	5.1	1.3	3.8	0.26	16.3	6.1	2.4	3.7	0.40
10	11.3	8.9	1.3	7.5	0.15	10.2	9.8	2.4	7.4	0.25

[a] The symbols signify the following: k_{10} is the first-order rate constant for decomposition of all CCl_3F molecules in the atmosphere at altitudes less than 10 km. The other three (k_t, k_{st}, k_{tr}) are equivalent first-order rate constants for decomposition of CCl_3F applied to the total atmospheric burden of CCl_3F. The rate constant k_{st} applies to removal by stratospheric photolysis alone; k_{tr} to removal by tropospheric processes alone; and k_t to the total of k_{st} and k_{tr}. For example, a tropospheric sink of 0.02 year^{-1} for the CCl_3F below 10 km (about 75% of the total) is the equivalent of a rate of 0.015 year^{-1} for the total burden. The ratio F is defined as k_{st}/k_t.

analyzed into the fractions of removal by stratospheric and tropospheric processes, respectively, as summarized in Table III. The average atmospheric residence time for the stratospheric sink alone is longer (75 years) with the Hunten eddy diffusion coefficient than for the Wofsy model (41 years), because of the slower stratospheric mixing postulated by Hunten, and the fraction removed by particular hypothetical tropospheric processes is therefore always larger for the Hunten model. If a tropospheric sink were also operative for CCl_3F, then estimates of ozone depletion from its decomposition would be reduced by the fraction of stratospheric reaction, F, as indicated in Table III. However, such lowered depletion estimates are not applied uniformly with time, as in Figures 2 and 3. The data of Table III show that the presence of a "30-year tropospheric sink" would reduce the fraction of decomposition estimated for the stratosphere by the Wofsy model to only 49% of the original estimate. However, the presence of a 30-year sink lowers the peak concentration of Figure 2 only to about 80% of the "no tropospheric sink" estimate, and the tropospheric CCl_3F concentration for the "30-year sink" does not decline to 49% of the "no tropospheric sink" value until about the year 2010, 20 years after termination of atmospheric release.

Other stratospheric eddy diffusion coefficients even faster than that given by Wofsy have sometimes been proposed. If shorter *stratospheric* lifetimes are proposed, then the fractional influence of *tropospheric* processes becomes much less. For example, if an overall atmospheric lifetime of 26 years were measured for CCl_3F, then the fraction of CCl_3F molecules decomposing in the stratosphere would be 0.35 for the Hunten coefficient, about 0.62 for the Wofsy coefficient, and 1.00 for a model giving a 26-year stratospheric lifetime.

The increase in stratospheric concentrations of the decomposition products (ClX) at 40 km shows an additional time lag behind that of CCl_3F at 40 km, and well behind that of tropospheric CCl_3F, as illustrated in Figure 5. The concentration of ClX represents the sum of Cl, ClO, and of HCl formed when Cl reacts with CH_4, H_2, or HO_2, and the distribution of chlorine among these three species is not strongly dependent on the total amount of chlorine present. The actual removal of O_3 by ClO_x catalysis then closely parallels the ClX concentrations, and the 40-km level represents roughly the altitude of maximum ClO_x effect on ozone removal. (Below 30 km the ClO + O reaction is not competitive with ClO + NO and the ClO_x catalysis of O + O_3 becomes less important.) Therefore, the ClX concentrations of Figure 5 can also be read

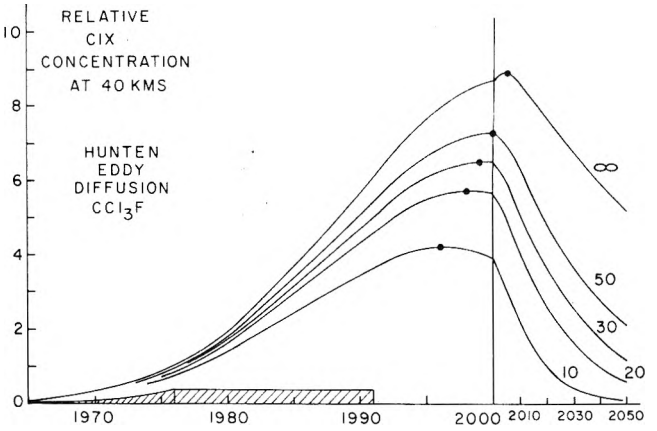

Figure 5. Relative concentration of ClX decomposition products from CCl_3F at 40-km altitude with various hypothetical tropospheric sinks, using eddy diffusion coefficient from ref 29. Atmospheric release as shown by cross-hatched area. Maxima in calculated concentrations are indicated by closed circles.

approximately as relative ozone depletion from the decomposition of CCl_3F.

One important conclusion that can be drawn from Figure 5 is that the presence or absence of a "50-year tropospheric sink" makes only a small difference for the concentrations of stratospheric ClX during the next half-century. Although the data of Table III indicate that with a 50-year sink, the value of F with the Hunten model is less than half (0.47), this reduction in stratospheric decomposition by a factor of 2 for hypothetical tropospheric sinks is accounted for *not* by large reductions in the maximum effect or the effect over the next few decades but primarily by a shortening of the number of decades over which appreciable stratospheric decomposition of CCl_3F occurs.

The prospective depletion of ozone by the chlorofluoromethanes is only about 1/3 attributable to CCl_3F, with CCl_2F_2 the more important molecule both because it is more widely used and because it rises to higher altitudes before undergoing stratospheric photolysis.[3] Since CCl_2F_2 is less reactive than CCl_3F toward most chemical processes, it is likely that any undiscovered tropospheric removal process would be less effective for CCl_2F_2 than for CCl_3F. Consequently, it is unlikely that any particular tropospheric removal process will be more important (relative to stratospheric removal rates) for CCl_2F_2 than for CCl_3F.

Comparison of Estimated Atmospheric Release and Observed Atmospheric Burdens in September, 1975

As calculated above, the estimated atmospheric release to September, 1975, is 2360 ktons, based chiefly on U.S. Tariff Commission reports for U.S. production and McCarthy's estimates of production for the rest of the world. The observations of stratospheric profiles for CCl_3F clearly indicate the operation of the photochemical sink there, and the total atmospheric release must be reduced by the amount already destroyed by this route. Our calculations with different eddy diffusion coefficients indicate that 5–10% of the amount released has already been destroyed, leaving 2120–2250 ktons of CCl_3F as the September, 1975, atmospheric burden. This calculated atmospheric burden is 17–25% less than the amount observed to be there.

If there were natural sources of CCl_3F in addition to the known anthropogenic contributions, then the total atmospheric burden would be the sum of the two. Indeed, one report of the presence of CCl_3F in volcanic gases appeared several years ago.[31] However, this report appeared prior to the general realization of the ubiquitous nature of the anthropogenic CCl_3F contribution world-wide, as well as to the severe CCl_3F contamination problems found in laboratory and/or urban surroundings. Direct sampling of active fumaroles of Mt. Kilauea during volcanic activity did not indicate any incremental amount of CCl_3F vs. that found in the background atmosphere away from the volcano.[22] (By way of comparison, the CCl_3F concentration in urban Los Angeles is never at background levels because the daily anthropogenic emission is always sufficient to increase the measured CCl_3F to several times the current world-wide background.)

The observed relative concentrations of chlorofluorocarbon molecules parallel closely the industrial production rates (for example, $CClF_3$, fluorocarbon-13, has not yet been reported) suggesting very low natural levels. Furthermore, tropospheric measurements have shown a steady increase in CCl_3F level since the first measurements in 1970–1971, and stratospheric infrared measurements have shown that the concentrations of both CCl_3F and CCl_2F_2 have increased by more than a factor of 2 since 1968.[18] Since these patterns parallel the industrial growth patterns, any natural concentrations must be small compared to the 1968 concentrations, and negligible compared to the current levels of anthropogenic CCl_3F.

From all of these calculations, then, we are led to the conclusion that the amount of anthropogenic CCl_3F in the atmosphere (2640 ± 270 ktons) exceeds by about 20% the estimated atmospheric burden (2120–2250 ktons) with only a stratospheric sink. This discrepancy indicates that the published estimates of CCl_3F production are too low, and must be increased by at least 10–20%, in order to be consistent with the actual atmospheric burden. Approximately a 20% increase is required for agreement if Rasmussen's estimate of 123 ppt for September, 1975, is correct for the northern hemisphere concentration of CCl_3F. Alternatively, a 10% increase in the estimates of release together with the quoted lower limit of the tropospheric measurement (−10%) would also give agreement.

Current evaluation of the cumulative magnitude of possible tropospheric sinks then rests on the possibility of stretching the estimated upper error limit of production (and release) upward and of the error limit of the actual atmospheric concentrations downward. If the combined errors were 30%, then consistency could still be obtained with a 50-year tropospheric sink, while a combined error at about 45% would be required for a 20-year tropospheric sink. The current data, of course, indicate that an upward adjustment of 10–20% in atmospheric release is required just to account for the observed concentrations of CCl_3F. By stretching the error limits, the possible existence of tropospheric removal processes summing to a 50-year tropospheric sink cannot be eliminated although there is no indication of its presence in the data. However, the error limits are not sufficiently elastic to permit much larger tropospheric losses. As indicated in Figure 5, the presence of an undiscovered 50-year tropospheric sink would mean an overestimate of the CCl_3F contribution to ozone depletion by a factor of about 1.13 when atmospheric release is terminated, increasing to a factor of 2 about 45 years later. Thus, the possible existence of as yet unidentified sinks cumulatively summing to a 50-year tropospheric sink is more important for the concentrations of CCl_3F a half-century or so from now than it is for the effects to be anticipated during the next several decades.

NOTE ADDED IN PROOF: The Manufacturing Chemists Association has released its estimate of the total amount of CCl_3F manufactured to the end of 1975 by the 20 leading producers.[32] This estimate can also be compared with the current assessment of the amount of CCl_3F actually in the atmosphere. The MCA estimate for these 20 companies is 3273 ktons to December 31, 1975, with 308 ktons for the entire year of 1975. The total to September 1, 1975, would then be about 103 ktons less than the end-of-year figure, or 3170 ktons.

The same MCA report indicates that more CCl_3F has been used in refrigeration (203 ktons, 6%) and in closed-cell foams (447 ktons, 14%) than we have estimated in our paper. After correcting the closed-cell foam use to September 1, 1975 (431 ktons), we estimate 10% loss in the foaming process (43 ktons) and still assume a 4-year delay in refrigeration uses (77 ktons). The 6-months delay in aerosol usage accounts for another 120 ktons. This basic estimate of the expected atmospheric burden on September 1, 1975, is then $3170 - (431 - 43) - 77 - 120 = 2585$ ktons.

Two additional small corrections to this atmospheric CCl_3F estimate then need to be added: (a) the loss from rigid foams after formulation, (b) production by the eastern block countries, not included in the above totals. The release from rigid foams has been estimated by A. D. Little, Inc., to be 20% at the end of 10 years, including the immediate release during the foaming process.[12] The 20% total in 10 years can be reached with an arbitrary calculation of 1% loss per year, for an additional 24 ktons released by September 1, 1975. The MCA figures, on the other hand, assume total release of all CCl_3F from all rigid foams in 20 years. With this assumption the MCA estimate is 153 ktons already released from rigid foams by the end of 1975, as compared to 67 (= 43 + 24) for a model patterned after the A. D. Little estimate.

Information about the production of CCl_3F and CCl_2F_2 in eastern-block countries is quite difficult to obtain, as are data on the split between CCl_3F and CCl_2F_2 in the production. Until 1970 production was quite low, and the MCA cumulative estimate through 1970 is about 25 ktons for CCl_3F. Production has increased since, and MCA now estimates a 1975 production rate 16% as large as the western rate (48.1 ktons vs. 7.3 ktons in 1970), and a cumulative eastern-block production of 157 ktons. For our September 1, 1975, estimate the MCA data correspond to 140 ktons cumulative. Other estimates show a less rapid growth and numbers from 70 to 140 ktons cumulative production to September 1, 1975 are consistent with our present knowledge. The situation is further complicated by uncertainty in the end use of CCl_3F. There is relatively little use of aerosol propellant in the eastern-block countries, while

the 48 kton of CCl_3F/39 kton of CCl_2F_2 production ratio reported by MCA in 1975 is not comparable to western U.S. patterns dominated by aerosol propellant use. The fractional use for foam-blowing is probably much higher in the eastern countries, but the split between open-cell and closed-cell foams is also uncertain. We have estimated a cumulative release by eastern-block countries of 70 ktons of CCl_3F to September 1, 1975.

Our current estimate of total release of CCl_3F by September 1, 1975 is then about 2585 + 24 + 70 or 2680 ktons. This is an increase of 14% over the McCarthy estimate, consistent with the statement in our paper that the release figures needed to be raised by 10–20% over that calculated from McCarthy's data. When this new release figure is then reduced by 5 (Hunten) or 10% (Wofsy) for stratospheric photolysis, the resulting estimates of residual atmospheric burden are then 2550 (Hunten) and 2410 (Wofsy) vs. the 2640 ktons calculated actually to be there on the basis of the 123 ppt northern hemisphere measurement of Rasmussen.[9,26] If the September, 1975 northern hemisphere value were about 110 ppt instead of 123 ppt, then the calculated amount of CCl_3F in the atmosphere would be 2360 ktons, in excellent agreement with the Wofsy eddy diffusion estimate for stratospheric photolysis alone, and leaving a deficit of 190 ktons of CCl_3F with the Hunten eddy diffusion. Put differently, a measurement of 110 ppt in September, 1975 (or 2360 ktons) would represent about 88% of the 2680 ktons of CCl_3F released to the atmosphere by that time. This would correspond to a total atmospheric residence time of about 38 years (Table III), or negligible tropospheric removal with the Wofsy model and about a 50–80 year tropospheric sink with the Hunten model for stratospheric removal.

References and Notes

(1) This research was supported by ERDA Contract No. AT(04-3)-34, P.A. 126. This paper has been revised from a memorandum written on Oct 23, 1975, for the National Academy of Sciences Panel on Atmospheric Chemistry.

(2) J. E. Lovelock, R. J. Maggs, and R. J. Wade, *Nature (London)*, **241**, 194 (1973).

(3) (a) M. J. Molina and F. S. Rowland, *ibid.*, **249**, 810 (1974); (b) F. S. Rowland and M. J. Molina, *Rev. Geophys. Space Phys.*, **13**, 1 (1975).

(4) "Fluorocarbons-Impact on Health and Environment", Hearings before the Subcommittee on Public Health and Environment of the Committee on Interstate and Foreign Commerce, U.S. House of Representatives, Dec 11, 12, 1974. Serial No. 93-110, U.S. Government Printing Office, Washington, D.C.

(5) "Fluorocarbons and the Environment", Report of Federal Task Force on Inadvertent Modification of the Stratosphere (IMOS), June, 1975. GPO Stock No. 038-000-00226-1, U.S. Government Printing Office, Washington, D.C.

(6) "Stratospheric Ozone Depletion", Hearings before the Subcommittee on the Upper Atmosphere of the Committee on Aeronautical and Space Sciences, U.S. Senate, Sept 8–23, 1975, U.S. Government Printing Office, Washington, D.C.

(7) "Environmental Impact of Stratospheric Flight", Climatic Impact Committee, H. G. Booker, Chairman, National Academy of Sciences, Washington, D.C., 1975.

(8) R. L. McCarthy, presented at the 169th National Meeting of the American Chemical Society, Philadelphia, Pa., April 6–11, 1975.

(9) R. Rasmussen, estimates given at EPA meeting in Research Triangle, N.C., Oct 14, 1975.

(10) Estimates of the IMOS Committee based on personal communications with DuPont Co., Table VI-10, p 88, ref 5.

(11) Estimates of the IMOS Committee based on personal communications with the A.D. Little Co., Table VI-12, p 88, ref 5.

(12) "Preliminary Economic Impact Assessment of Possible Regulatory Action to Control Atmospheric Emissions of Selected Halocarbons", K. H. Lloyd, Project Officer, Arthur D. Little, Inc., Cambridge, Mass., Sept, 1975. ADL No. 76072-80.

(13) An estimate of 41.9 million pounds released to the atmosphere within 10 years (most of it immediately) and 38.3 million pounds *not* released has been given for U.S. production of rigid plus flexible polyurethane foam in 1973. Almost all of the foaming agent was CCl_3F. See Table IV-9, IV-79, of ref 12.

(14) Reference 12, II-11.

(15) P. H. Howard and A. Hanchett, *Science*, **189**, 217 (1975).

(16) A. L. Schmeltekopf et al., *Geophys. Res. Lett.*, **2**, 393 (1975).

(17) L. E. Heidt, R. Lueb, W. Pollock, and D. H. Ehhalt, *Geophys. Res. Lett.*, **2**, 445 (1975).

(18) D. G. Murcray, F. S. Bonomo, J. N. Brooks, A. Goldman, F. H. Murcray, and W. J. Williams, *Geophys. Res. Lett.*, **2**, 109 (1975); W. J. Williams, J. J. Kosters, A. Goldman, and D. G. Murcray, Paper presented at American Geophysical Union Meeting, San Francisco, Calif., Dec, 1975.

(19) P. W. Krey, R. Lagomarsino, M. Schonberg, and J. C. Frey, in H.A.S.L-298, U.S. Energy Research and Development Administration, 1976, p I-83; P. W. Krey and R. J. Lagomarsino, H.A.S.L.-294, ERDA, 1975, pp 97–123.

(20) J. E. Lovelock, *Nature (London)*, **252**, 292 (1974).

(21) J. E. Lovelock, *Nature (London)*, **256**, 193 (1975).

(22) P. E. Wilkniss, J. W. Swinnerton, R. A. Lamontagne, and D. J. Bressan, *Science*, **187**, 832 (1975).

(23) N. E. Hester, E. R. Stephens, and O. C. Taylor, *Environ. Sci. Technol.*, **9**, 875 (1975).

(24) P. H. Hanst, L. L. Spiller, D. M. Watts, J. W. Spence, and M. F. Miller, *Air Pollut. Assoc.*, **25**, 1220 (1975).

(25) R. Rasmussen, private communication.

(26) R. A. Rasmussen, K. J. Allwine, and W. H. Foller, *Antarctic J.*, 232 (1975).

(27) K. Telegadas and G. J. Ferber, *Science*, **190**, 882 (1975).

(28) S. C. Wofsy, M. B. McElroy, and N. D. Sze, *Science*, **187**, 535 (1975).

(29) D. Hunten in "The Natural Stratosphere of 1974", C.I.A.P. Monograph 1, DOT-TST-75-51, U.S. Department of Transportation, Sept, 1975, p 2-131.

(30) N. D. Sze and M. F. Wu, unpublished manuscript.

(31) R. E. Stoiber, D. C. Leggett, T. F. Jenkins, R. P. Murrmann, and W. I. Ross, *Geol. Soc. Am. Bull.*, **82**, 2299 (1971).

(32) The MCA estimates were obtained from an Appendix prepared by Farbwerke Hoechst to an unpublished report by Battelle of Frankfurt, May, 1976: "Studie uber die Auswirkung Von Fluorchlorkohlenstoffverbindungen auf die Ozonschicht der Stratosphare und die Moglichen Folgen".

Effect of Molecular Oxygen on the Gas Phase Kinetics of the Ozonolysis of Olefins[1]

S. M. Japar, C. H. Wu, and H. Niki*

Research Staff, Ford Motor Company, Dearborn, Michigan 48121 *(Received April 5, 1976)*

Publication costs assisted by the Ford Motor Company

The kinetics of the gas phase reaction of ozone with ethylene, propylene, and *trans*-2-butene have been investigated as a function of a number of experimental variables, including molecular oxygen concentration, at atmospheric pressure. Under all conditions there is secondary consumption of propylene in the ozone–propylene reaction, while in ozone excess with no O_2 present, secondary consumption of ozone becomes important. In large olefin excesses, the ozone decay is exponential and is dependent on the O_2 content of the system below 50 ppm. In the absence of O_2, a lower limit for the ozone decay rate constant is obtained in large propylene excesses, which is equal to the value obtained in air, 1.3×10^{-17} cm^3 molecule^{-1} s^{-1}. The available data indicate that the bimolecular rate constants for ozone–olefin reactions can be directly determined from ozone decay in air in a large olefin excess.

Introduction

The reaction of ozone with olefins has been recognized as playing an important role in the formation of photochemical smog.[2,3] Numerous measurements of the rate constants for these gas phase reactions, at low reactant concentrations in diluent air at 1 atm pressure, are in general agreement.[4–10] Earlier attempts in this laboratory[9] to measure the effect of O_2 on the kinetics and reaction stoichiometries of the ozonolysis of propylene and *trans*-2-butene showed no detectable change with O_2 concentrations as low as 20 ppm (1 ppm = 0.76 mTorr = 2.5×10^{13} molecules cm^{-3} at 300 K and 1 atm) in N_2 at 1 atm. This observation is in apparent disagreement with earlier studies of relative ozone–olefin reactivities carried out by Cvetanović and co-workers[11] at total pressures near 100 Torr; with investigations of the ozonolysis of electron-rich chloroethylenes[12] in the Torr pressure range; and with a series of recent studies[13–16] at total pressures below 10 Torr. In the former case, relative rates for all olefins were slightly smaller in N_2 than in O_2, while in the latter two cases removal of O_2 resulted in up to a 100% increase in the measured rate constants for the reaction.

With the objective of validating the existing technique for determining bimolecular rate constants for the highly complex ozone–olefin reactions, the present paper examines the effect of O_2 on the kinetics of the reactions of ozone with ethylene, propylene, and *trans*-2-butene, with O_2 as low as 1 ppm in helium at atmospheric pressure. In addition, the kinetics and stoichiometry of the ozone–propylene reaction have been measured as a function of reactant concentration, and a generalized unified model is presented which explains most of the available data.

Experimental Section

The apparatus and techniques employed in the present study have been described in detail previously.[9,10] Ozonolyses were carried out in a 45-l. Pyrex bell jar reactor. Ozone samples were prepared by flowing ozonized oxygen into a silica gel trap at 195 K and pumping off the oxygen. Research grade olefins (Phillips) were vacuum distilled prior to use. Diluent air (UPC, Air Products and Chemicals, dew point −125 °F) and O_2 were used as received.

Numerous efforts were made to minimize the O_2 impurity in the reaction mixtures. Helium (Matheson Gas Co., the stated $[O_2]$ = 0.045 ppm) was used as diluent. The stated O_2 concentration was substantially below the estimated overall oxygen background in the reactor, as described below. The reactor was evacuable below 1 mTorr with a mechanical pump and a liquid nitrogen trap, and the leak rate was less than 1 mTorr min^{-1} upon isolation from the pumping system. As filling times were less than 2 min, the air impurity never reached 3 mTorr. This corresponds to a maximum residual oxygen level of 0.8 ppm in the reactor. In addition, to avoid air leakage into the reactor during gas handling, the sample lines were pressurized slightly above 1 atm with helium at all times. Another possible source of impurity oxygen was the ozone sample, which contained a maximum of 5% oxygen. Since the maximum ozone concentration was 7 ppm, the possible contribution of the oxygen concentration was, at most, 0.35 ppm. Therefore, the overall oxygen impurity in the reactor, with helium as the diluent, was estimated to be 0.5–1.0 ppm.

Reactant mixtures of ozone and olefin in the ppm concentration range were prepared by standard pressure–volume expansion techniques using calibrated sample volumes. The total pressure in the reactor was 760 Torr at 26 °C.

During the course of the reaction analysis, the ozone was monitored continuously with an NO/O_3 chemiluminescence detector.[17] Olefins were analyzed gas chromatographically using a flame ionization detector and a stainless steel column (⅛ in. × 12 ft) packed with DC 200 on Chromosorb W.[9]

Results

Data Analysis. The kinetics of the reaction of ozone with olefins were investigated under a wide range of reactant mixing ratios, and bimolecular rates for these reactions were determined under two different conditions. For the case of ozone decay in a large olefin excess, i.e., [olefin]/$[O_3]$ = 10–100, the data were analyzed using the pseudo-first-order expression

$$\mathrm{d} \ln [O_3]/\mathrm{d}t = -n_{O_3} k [\text{olefin}]_0 \qquad \text{(I)}$$

where $[\text{olefin}]_0$ is the initial olefin concentration, k is the bimolecular rate constant, and n_{O_3} is the stoichiometry, defined as the number of ozone molecules consumed for each primary reaction between ozone and olefin. Although the value of n_{O_3} cannot be absolutely measured under these conditions, it can be determined whether its value remains constant.

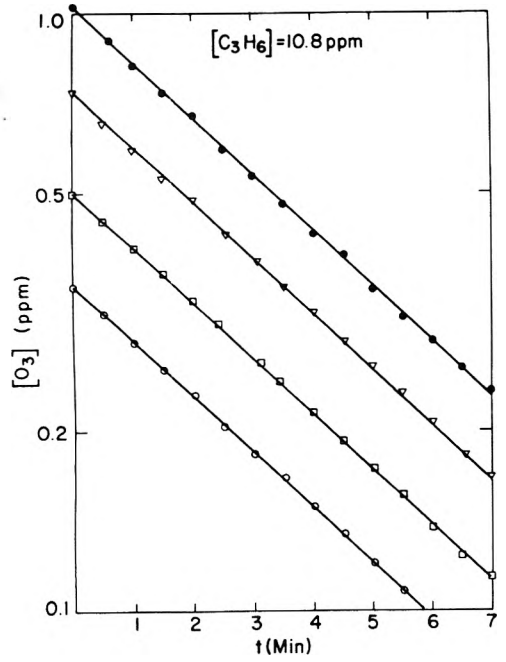

Figure 1. The decay of ozone as a function of ozone concentration in the presence of 10.8 ppm of propylene and 760 Torr of air.

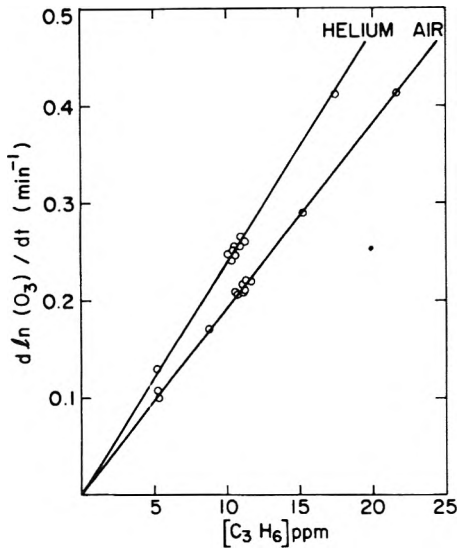

Figure 2. First-order decay rate of ozone as a function of excess propylene at 299 °C and 760 Torr total pressure.

In experiments where the reactant concentrations were more nearly equimolar, both the olefin and ozone concentrations change as a function of time, and the following integrated second-order equations were used for analysis:

$$\ln \frac{[O_3]_{t_2}}{[O_3]_{t_1}} = -n_{O_3} k \int_{t_1}^{t_2} [\text{olefin}]\, dt \qquad \text{(II)}$$

$$\ln \frac{[\text{olefin}]_{t_2}}{[\text{olefin}]_{t_1}} = -n_{\text{olefin}} k \int_{t_1}^{t_2} [O_3]\, dt \qquad \text{(III)}$$

where $[O_3]_{t_1}$, $[O_3]_{t_2}$, $[\text{olefin}]_{t_1}$, and $[\text{olefin}]_{t_2}$ refer to the appropriate concentration at times t_1 and t_2, k is the bimolecular rate constant, and n_{O_3} and n_{olefin} correspond to the number of ozone and hydrocarbon molecules consumed for each primary reaction step.

TABLE I: Decay Rate Constants for Ozone in Excess Olefin (760 Torr of Air)

$[HC]_0$, ppm	$[O_3]_0$, ppm	d ln O_3/dt, min^{-1}	nk, 10^{-17} cm^3 molecule^{-1} s^{-1}
		Ethylene (Air)	
35.6	1.60	0.102	0.19
70.6	1.40	0.204	0.19
105	1.25	0.301	0.19
109	1.20	0.301	0.18
			Av (0.19 ± 0.01)
		Ethylene (Helium)	
55	1.50	0.221	0.27
105	4.0	0.436	0.28
105	6.0	0.361	0.23
107	1.5	0.422	0.27
160	1.8	0.563	0.24
			Av (0.26 ± 0.02)
		Propylene (Air)	
5.40	0.35	0.112	1.36
8.75	0.50	0.179	1.37
10.7	0.75	0.210	1.34
10.8	0.50	0.201	1.25
10.8	0.95	0.210	1.30
10.8	1.05	0.211	1.31
10.8	1.50	0.212	1.32
11.2	0.80	0.225	1.35
11.4	0.80	0.229	1.35
21.6	0.70	0.414	1.28
			Av (1.32 ± 0.03)
		Propylene (Helium)	
5.30	0.35	0.129	1.64
5.30	0.35	0.130	1.65
10.2	1.00	0.254	1.67
10.8	0.066	0.255	1.52
10.8	0.80	0.274	1.70
10.8	1.00	0.306	1.90
11.0	0.15	0.261	1.59
17.5	0.80	0.411	1.57
100	10.0	2.46	1.65
102	8.2	2.66	1.75
			Av (1.67 ± 0.10)
		trans-2-Butene (Air)	
1.03	0.098	0.350	23.1
1.34	0.13	0.530	26.5
1.72	0.16	0.660	25.7
2.01	0.098	0.820	25.3
2.06	0.26	0.796	25.9
2.06	0.20	0.750	24.4
3.44	0.20	1.45	28.2
			Av (25.6 ± 1.5)
		trans-2-Butene (Helium)	
2.02	0.20	0.821	27.3
2.06	0.15	0.884	28.7
2.06	0.20	0.890	28.9
			Av (28.3 ± 0.7)

Effect of O_2 on Ozone Decay in Olefin-Rich Systems. The effect of O_2 on the ozone decay was first examined under olefin-rich conditions, i.e., $[\text{olefin}]/[O_3] = 10$–$100$, using both air and helium as diluents. Some of the results, for propylene in air, are presented in Figure 1. The ozone decay is always exponential, and over at least a 10-fold range is independent of its own concentration. Both of these observations indicate that the stoichiometry n is independent of reaction time.

TABLE II: Reaction of Equimolar Concentrations of Ozone and Propylene

t, min[a]	$[C_3H_6]$, ppm	$[O_3]$, ppm	$n_{O_3}k$	$n_{C_3H_6}k$	$\Delta[C_3H_6]/\Delta[O_3]$
			10^{-17} cm^3 molecule^{-1} s^{-1}		
		$[C_3H_6]_0$ = 2.58 ppm, $[O_3]_0$ = 2.43 ppm, 760 Torr of Air			
0	2.58	2.43	1.5	1.7	1.3
2.8	2.22	2.12	1.3	1.6	1.2
6.0	1.88	1.86	1.4	1.8	1.1
10.0	1.57	1.60	1.4	1.7	1.2
14.0	1.35	1.43	1.2	1.6	1.3
19.4	1.12	1.24	1.2	1.6	1.1
		$[C_3H_6]_0$ = 2.76 ppm, $[O_3]_0$ = 2.37 ppm, 760 Torr of Helium			
0	2.76	2.37	2.2	2.0	0.8
1.9	2.45	2.01	2.1	1.9	0.9
3.8	2.20	1.76	2.0	1.9	1.1
7.0	1.91	1.45	1.8	1.8	0.8
11.2	1.68	1.18	1.6	1.7	0.9
15.8	1.46	0.97	1.6	1.7	1.0

[a] Zero time is taken as 1 min after initiation of mixing.

Pseudo-first-order rate constants were measured as a function of propylene concentration in air and helium (Figure 2). Over the propylene concentration range from 5 to 25 ppm, the values increase linearly in both air and helium. However, the slope of the line is larger in helium by about 30%. This suggests that there is a corresponding change in the value of n_{O_3}. For the other olefins investigated, ethylene, and *cis*- and *trans*-2-butene, the ozone decay is qualitatively similar to that in Figures 1 and 2.

For the olefins studied the observed second-order rate constants, $n_{O_3}k$, determined with eq I are presented in Table I, where the stated error limits are one standard deviation. The rate constants are larger in He than in air. The differences range from 11% for the fastest reaction studied, i.e., *trans*-2-butene, to 35% for the slowest reaction studied, i.e., ethylene. The values obtained in air are in good agreement with previous determinations in this laboratory.[10]

To examine the effect of O_2 further, the second-order rate constants, $n_{O_3}k$, for the propylene–ozone system were measured as a function of added O_2, ranging from 600 ppm down to <1 ppm. These results are summarized in Figure 3. At O_2 concentrations as low as 50 ppm the value of $n_{O_3}k$ is the same as that obtained in air, 1.3×10^{17} cm^3 molecule^{-1} s^{-1} (all future rate constants will be in these units). However, as the O_2 content is decreased further $n_{O_3}k$ increases to a limiting value of 1.7×10^{-17}. For all O_2 concentrations, the O_3 decay showed good exponential behavior. Therefore, the ozone stoichiometry, n_{O_3}, increases as the O_2 content of the system is lowered to the vicinity of 1 ppm.

Effects of O_2 and Reactant Concentrations on the Kinetics of the Ozone–Propylene System under Nearly Equimolar Conditions. Most of the data reported in this section were obtained under conditions where both propylene and ozone concentrations changed with time, and the integrated forms of the rate equation, eq II and III, were used for analysis.

The propylene–ozone system was chosen for the detailed study of the effects of O_2 and reactant concentration on the kinetics because of its compatibility with the analytical techniques, i.e., for C_3H_6 and O_3 at 1–5 ppm, the total reaction time is about 30 min, which allows sufficient time to sample the hydrocarbon concentration at least ten times. The much faster *trans*-2-butene reaction would have required a considerable decrease in initial reactant concentrations, with a concurrent increase in experimental uncertainties, while the use of ethylene would have required much higher concentrations for measurable decay to occur.

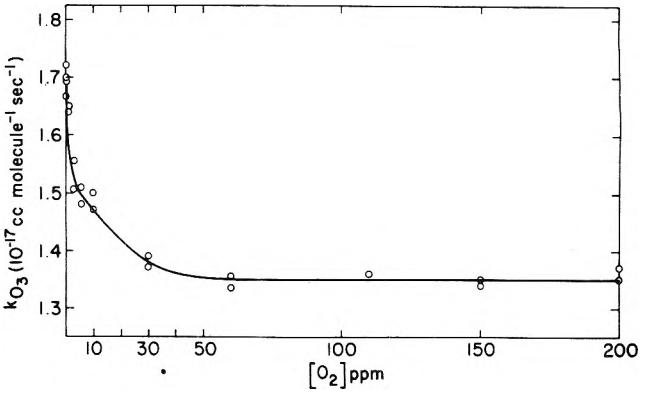

Figure 3. The effect of O_2 on the measured bimolecular rate constant for the ozone–propylene reaction at 299 °C and 760 Torr total pressure of helium.

Kinetic data for the O_3–C_3H_6 reaction in air and helium are presented in Table II. For initial reactant concentrations of 2.5 ppm, both reactants decreased by ~50% after 16 min in air or helium. In air, the second-order rate constants for the decay of ozone and propylene, $n_{O_3}k$ and $n_{C_3H_6}k$, 1.3×10^{-17} and 1.7×10^{-17}, respectively, were invariant with reaction time within the 10% experimental error. The stoichiometry ratio, $\Delta[C_3H_6]/\Delta[O_3]$ (hereafter $\Delta(C_3H_6/O_3)$), equaled 1.3 ± 0.1. In helium the kinetic behavior of the reactants was different. The value of $n_{O_3}k$ decreased by about 30% with increasing reaction time, whereas, for this particular run, the value of $n_{C_3H_6}k$ remained constant at a value of $(1.9 \pm 0.2) \times 10^{-17}$. Thus, in helium the reaction stoichiometry n (= $n_{C_3H_6}/n_{O_3}$) varies slightly with time, with the change presumably occurring in the consumption of ozone.

Some representative air data, obtained under a wide range of conditions, are presented in Table III. The data cover a 20-fold change in reactant ratio. Under all conditions $n_{O_3}k$, $n_{C_3H_6}k$, and the stoichiometry ratio $\Delta(C_3H_6/O_3)$ do not vary with time and the average values are reported in Table III. The value of $n_{C_3H_6}k$ does not change for any of the conditions investigated and its average value is 1.6×10^{-17}. Similar results

TABLE III: Kinetics and Stoichiometry of the Ozone–Propylene Reaction in 760 Torr of Air

$[C_3H_6]_0$, ppm	$[O_3]_0$, ppm	$\Delta[C_3H_6]/\Delta[O_3]$	$n_{O_3}k$	$n_{C_3H_6}k$
			10^{-17} cm^3 molecule^{-1} s^{-1}	
2.06	8.27	0.9	1.7	1.6
2.06	8.40	0.9	1.6	1.5
2.06	4.00	1.0	1.8	1.6
3.10	3.60	1.1	1.4	1.6
3.00	3.00	1.2	1.4	1.6
3.10	2.35	1.3	1.3	1.7
2.70	2.06	1.2	1.3	1.7
5.00	2.06	1.2	1.3	1.7
5.20	1.42	1.4	1.5	1.7
5.80	1.14	1.4	1.2	1.5

TABLE IV: Kinetics and Stoichiometry of the Ozone–Propylene Reaction in 760 Torr of Helium

$[C_3H_6]$, ppm	$[O_3]$, ppm	$\Delta[C_3H_6]/\Delta[O_3]$	$n_{O_3}k$[a]	$n_{C_3H_6}k$
			10^{-17} cm^3 molecule^{-1} s^{-1}	
0.664	5.78	0.3 ± 0.1	7.8	1.7
1.12	4.67	0.4 ± 0.1	5.3	2.1
1.69	2.37	0.6 ± 0.1	4.0	2.4
2.76	2.37	0.9 ± 0.1	2.6	1.8
10.4	0.438	1.0 ± 0.2	1.8	1.8

[a] The ozone decay rate constants are time dependent. See text.

were obtained for both the stoichiometry ratio and $n_{O_3}k$ in propylene-rich as well as slightly ozone-rich systems. The average values are 1.3 for the stoichiometry ratio and 1.3×10^{-17} for $n_{O_3}k$. Therefore, n_{O_3} and $n_{C_3H_6}$ are invariant over the range of conditions, and their ratio, $n_{C_3H_6}/n_{O_3}$, is 1.3. In ozone-rich systems the value of $n_{O_3}k$ increases to 1.7×10^{-17} and the measured stoichiometry decreases to about 1.0. The insensitivity of $n_{C_3H_6}k$ to reaction conditions shows that the propylene stoichiometry does not change in air. However, n_{O_3} increases when the system changes from propylene-rich to ozone-rich. This is in agreement with previous data obtained in this laboratory although in that case sufficient data were not available to delineate the trend.

Data obtained in helium for $[C_3H_6]_0/[O_3]_0 = 0.1$–20 are presented in Table IV. The average value for $n_{C_3H_6}k$ is $(2.0 \pm 0.4) \times 10^{-17}$. The measured stoichiometry ratios decrease from 1.0 in propylene-rich systems to about 0.3 under ozone-rich conditions, and although the experimental uncertainties are high in the ozone-rich systems, the measured stoichiometries increase with reaction time. The values for $n_{O_3}k$ in ozone-rich systems decrease with reaction time by as much as 35%. The values of $n_{O_3}k$ in Table IV are taken from the initial stages of the reaction, and the values of $n_{O_3}k$ and $\Delta(C_3H_6/O_3)$ thus show that the value of n_{O_3} increases rapidly with the increase of $[O_3]$.

The change of $n_{O_3}k$ over the course of the reaction is illustrated in Figure 4, as a function of reactant ratio, $[C_3H_6]/[O_3]$. The circles connected by lines represent single runs, and in all cases the value of $n_{O_3}k$ decreased with reaction time. The squares represent data from Table I, where a large propylene excess was used. Over the range of conditions surveyed $n_{O_3}k$ decreased from a value near 7.8×10^{-17} under ozone-rich conditions to a limiting value near 1.4×10^{-17} in a large propylene excess. This variation of a factor of 5.5 is a direct measure of the change of the ozone stoichiometry, n_{O_3}, as a function of experimental condition.

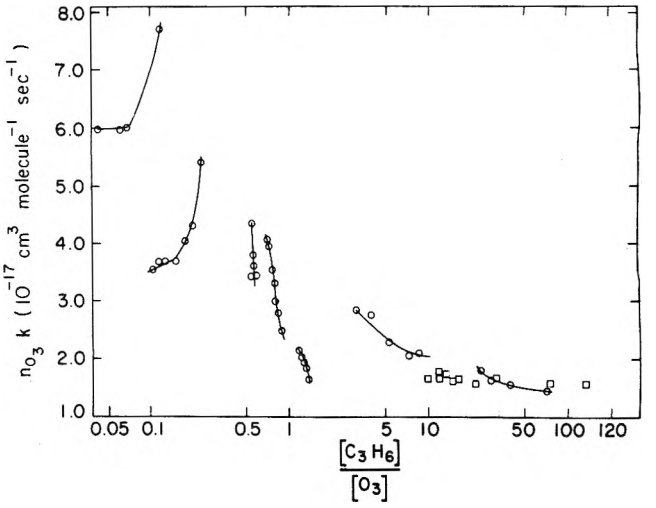

Figure 4. The bimolecular ozone decay rate constant as a function of reactant ratio at 299 °C and 760 Torr total pressure of helium. The squares represent data from Table I. The circles connected by lines represent individual runs, some of which are detailed in Table IV.

Discussion

The data presented in the preceding section demonstrate that the reaction of ozone with olefins, as a function of O_2 concentration, involves varying degrees of secondary consumption of both ozone and propylene by reaction intermediates. The results can be explained in terms of a minimum of two intermediates, only one of whose secondary reactions are quenchable by molecular oxygen. The intermediates are formed either in the primary reaction between ozone and propylene or through a series of experimentally indistinguishable primary and secondary reactions. A simplified mechanism to account for the major features of the observed propylene data is postulated below.

$$O_3 + C_3H_6 \rightarrow \alpha_1 R_1 + \alpha_2 R_2 + P_1(1 - \alpha_1 - \alpha_2) \quad (1)$$
$$k_1 = 1.3 \times 10^{-17} \qquad \alpha_1 = \alpha_2 = 0.3$$

$$R_1 + R_1 \rightarrow P_2 \qquad k_2 = 3 \times 10^{-12} \quad (2)$$

$$R_1 + O_3 \rightarrow P_3 \qquad k_3 = 1 \times 10^{-14} \quad (3)$$

$$R_1 + C_3H_6 \rightarrow P_4 \qquad k_4 = 1 \times 10^{-13} \quad (4)$$

$$R_2 + O_2 \rightarrow P_5 \qquad k_5 = 1 \times 10^{-14} \quad (5)$$

$$R_2 + O_3 \rightarrow P_6 \qquad k_6 = 2 \times 10^{-12} \quad (6)$$

$$R_2 + C_3H_6 \rightarrow P_7 \qquad k_7 \leq 3 \times 10^{-16} \quad (7)$$

R_1 and R_2 are the intermediate species and the various P_i's are the products (stable or metastable) of the reactions of these intermediates with propylene and ozone.

The rate constants were obtained by fitting the data in step-by-step fashion through numerical integration of differential equations representing the pertinent chemical reaction,[3,18] as illustrated in the detailed discussion below.

Effect of O_2 on the Kinetics of Ozone Decay. The present results in air, i.e., exponential ozone decay that is a linear function of olefin concentration (Figures 1 and 2), and the calculated values of the second-order rate constants, $n_{O_3}k$

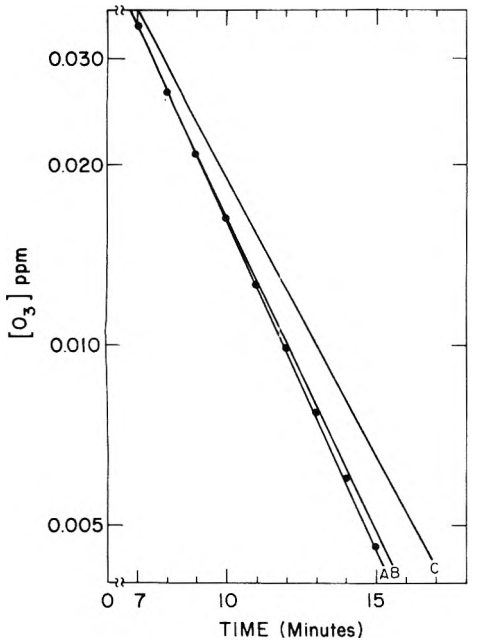

Figure 5. Numerical modeling of ozone decay data to obtain a value for the rate constant k_6: $[O_3]_0 = 2.0 \times 10^{-1}$ ppm, $[C_3H_6]_0 = 10$ ppm; $[O_2] = 1.0$ ppm. The points are the experimental data and the lines are the computer fits to the data for specific values of k_6: line A, $k_6 \geq 2 \times 10^{-12}$ cm^3 molecule^{-1} s^{-1}; line B, $k_6 = 1 \times 10^{-12}$; line C, $k_6 = 1 \times 10^{-13}$.

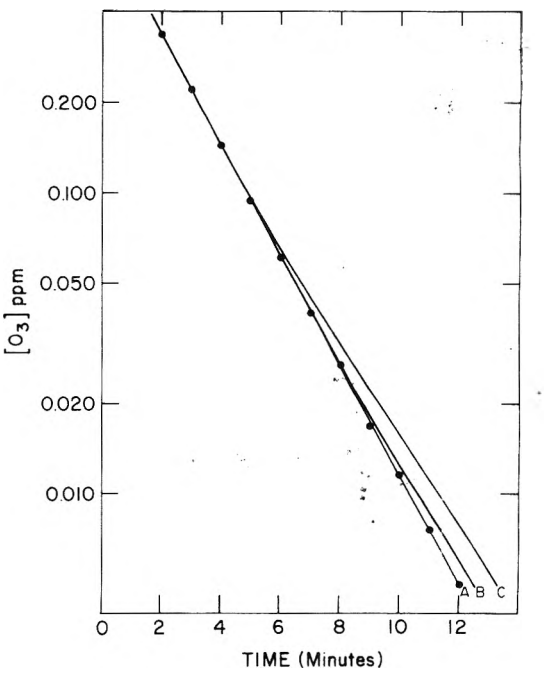

Figure 6. Numerical modeling of ozone decay data to obtain a value for the rate constant k_5: $[O_3]_0 = 8.0 \times 10^{-1}$ ppm, $[C_3H_6]_0 = 17$ ppm, $[O_2] = 1.0$ ppm. The points are the experimental data and the lines are the computer fits to the data for specific values of k_5: line A, $k_5 \leq 1 \times 10^{-14}$ cm^3 molecule^{-1} s^{-1}; line B, $k_5 = 3 \times 10^{-14}$; line C, $k_5 = 1.5 \times 10^{-13}$.

(Table I), are in excellent agreement with previous results from this laboratory[9,10] and other literature data obtained under similar conditions.[8]

The observed effect of $[O_2]$ (Table I and Figures 2 and 3) has not previously been investigated for these reactions at low reactant concentrations and at atmospheric pressure. In the cases of the three olefins for which an O_2 effect has been observed, the removal of O_2 leads to an increase in the measured second-order rate constant, and the magnitude of the increase is a sensitive function of $[O_2]$ below 50 ppm. These results suggest an increase in n_{O_3} at low $[O_2]$. These results can be explained by reactions 1 and 5–7, where O_2 acts as a scavenger of the ozone destroying intermediate, reaction 5.

Values for k_5 and k_6 can be obtained from the data in Figure 2, where $n_{O_3}^{air}k = 1.3 \times 10^{-17}$ and $n_{O_3}^{He}k = 1.7 \times 10^{-17}$ on the assumption that the value of $n_{O_2}^{air} = 1$. Reaction 6 is required to explain the increased rate of exponential O_3 decay in the absence of O_2. To satisfy this condition k_6 must have, as a lower limit, a value of 2×10^{-12} (Figure 5). For the value of $n_{O_3}^{He}k$ to increase only 30% over the value in air, the efficiency of R_2 production by reaction 1 must also be limited to 30%, i.e., $\alpha_2 = 0.30$. The value of k_5 can be determined directly from the effect of O_2 on the system (Figures 2 and 3). The upper limit for $[O_2]$ present in the He system is 1 ppm. For this concentration of O_2 $n_{O_3}k = 1.7 \times 10^{-17}$, and an upper limit for $k_5 = 10^{-14}$ can be derived (Figure 6). A similar evaluation of k_5 from the data in Figure 3 gives a consistent value of k_5 within a factor of 3. The present data do not provide any indication concerning an oxygen quenchable consumption of propylene by secondary intermediates, reaction 7. However, it is possible to obtain an upper limit for k_7 of 3×10^{-16}.

Reactions 1 and 5–7 and their derived rate constants adequately explain all the exponential ozone decay data. There is no need to include the possibility of ozone regeneration[2b] through a sequence of reactions involving

$$C_3H_6 + O_3 \rightarrow RO_2 + \cdots \quad (1')$$

$$RO_2 + O_2 \rightarrow O_3 + RO \quad (8)$$

In fact, if reaction 8 were important, the ozone decay rate constant, $n_{O_3}k$ in Figure 3, should have decreased as the $[O_2]$ in the system was raised above 50 ppm.

Effect of Reactant Concentration on the Ozonolysis Kinetics. The data obtained in the absence of O_2 as well as under ozone-rich conditions in air (Tables III and IV) are consistent with secondary consumption of both ozone and propylene.

Under these conditions the kinetic behavior of both reactants can be readily explained in terms of the generalized mechanism encompassing reactions 1–7. The decrease of $n_{O_3}k$ with increasing reactant ratio ($[C_3H_6]/[O_3]$ in Figure 4) can be explained by competition in the removal of R_1 by ozone and propylene, i.e., reactions 3 and 4. This is further substantiated by the fact that $\Delta(C_3H_6/O_3)$ (Table III) decreases with increasing $[O_3]$. The values for k_3 and k_4 which best fit all the data are shown with the mechanism. Reaction 2 is included as a regulator of the R_1 intermediate and prevents its too rapid growth in the mathematical iteration of the mechanism. The value of k_2 was chosen to be consistent with the assumed rate constants for reactions involving alkoxy radicals.[16,19] As the choices of k_3 and k_4 are dependent on the selected value for k_2, the ratio $k_4/k_3 \simeq 10^1$ is more significant than the absolute values for these rate constants. The value of α_1 (reaction 1) = 0.3 was required to give maximum values of $n_{O_3}k$ and $n_{C_3H_6}k$ of 1.7×10^{-17}.

For helium, the effect of reactant concentration on the reactant decay kinetics (Table IV and Figure 4) is of such complexity as to render any discussion of it in terms of a simplified mechanism of little value. However, it is possible to draw some important conclusions about the initial ozone–olefin reactions from these data.

With the earlier assumption that $n_{O_3} = 1$ in air in large olefin excess, the stoichiometry data can be summarized as in Table V, where the first and third columns are carried over

TABLE V: Summary of Reaction Stoichiometries in the Absence of Air and Olefin Excess

$n_{O_3}k(\times 10^{-17})$	n_{O_3}	$\frac{\Delta[C_3H_6]}{\Delta[O_3]} = \frac{n_{C_3H_6}}{n_{O_3}}$	$n_{C_3H_6}$
7.8	6.0	0.3	1.8
5.3	4.1	0.4	1.7
4.0	3.1	0.6	1.9
2.1	1.6	0.9	1.5
1.8	1.4	1.0	1.4
Air 1.3	1.0[a]	1.3	1.3

[a] With this assumption the bimolecular rate constant for $O_3 + C_3H_6$ is 1.3×10^{-17}. This is used to calculate the values of n_{O_3} in column 2.

from Table IV. It is apparent from the values of n_{O_3} and $n_{C_3H_6}$ that as the amount of ozone in the system is increased, the reaction of ozone with propylene becomes increasing complex and takes on the character of a short chain with n_{O_3} as high as 6 molecules consumed for each primary reaction.

The variation of $n_{O_3}k$ as a function of a 2000-fold change in reactant ratio in helium is plotted in Figure 4. Although the behavior is complex, there is a clear trend toward a limiting value of $n_{O_3}k = 1.4 \times 10^{-17}$ as the reactant ratio increases. This is an indication that the excess ozone consumption is being limited by propylene, presumably through a competing reaction such as reaction 7, and that if the reactant ratio is increased further, the lower limit of $n_{O_3}k$, i.e., $n_{O_3} = 1$, will be reached.

Such an experiment is not feasible with the current apparatus although this has been done in some low pressure flow tube experiments carried out in this laboratory[20] where reactant ratios as high as 10^5 were used ($[O_3]_0 = 4.0 \times 10^{-3}$ ppm, $[C_3H_6]_0 = 4.0 \times 10^2$ ppm). The same limiting value for $n_{O_3}k$ was obtained, while the effect of O_2 was eliminated. The latter observation demonstrates that any reactions involving intermediate species occur only with propylene, while the former indicates that the bimolecular rate constant, k, is 1.3×10^{-17}, the value of $n_{O_3}k$ obtained in air in propylene excess. Therefore, $n_{O_3} = 1.0$ as previously assumed.

It should be mentioned that the time dependence of $n_{O_3}k$ in helium, as demonstrated in Figure 4, can be explained if the decrease of n_{O_3} with time is accompanied by an increase in the value of the reaction stoichiometry. The latter is probably the case, although the magnitude of the effect, ~20%, is comparable to the uncertainties associated with the measurement of reaction stoichiometries in ozone excess in helium (see Results section).

It is very tempting at this point to speculate on the nature of R_1 and R_2 and the various other products formed in reactions 1–7. This has been the subject of a number of recent investigations, both theoretical[21] and experimental,[15,16] and a large number of intermediate radical species and stable products have been observed at low pressure. A detailed discussion of the ozonolysis of ethylene at reactant pressures in the 0.1 Torr pressure range has recently been published,[16] and although the results are qualitatively similar to those reported here, detailed speculation concerning the mechanism of propylene ozonolysis would be premature in the present case until detailed product analyses accompany the kinetic investigations, or are obtained separately under otherwise identical experimental conditions.

Conclusion

The kinetics of the ozone–olefin system have been investigated as a function of a number of experimental variables at atmospheric pressure. In large olefin excess, the ozone decay is exponential and is dependent on the oxygen content of the system below 50 ppm. Under all conditions there is secondary consumption of propylene in the ozone–propylene reaction, while in ozone-excess with no O_2 present, secondary consumption of ozone becomes very important. Investigation of the ozone kinetics as a function of reactant ratio in helium shows that a limiting value for the ozone decay rate constant is obtained in large propylene excesses. The available data indicate that this value, which equals the value of the rate constant obtained in air in propylene excess, i.e., 1.3×10^{-17} cm^3 $molecule^{-1}$ s^{-1}, is the bimolecular rate constant for the gas-phase ozone–propylene reaction. Therefore, bimolecular rate constants for ozone–olefin reactions can be directly determined from ozone decay in air in a large olefin excess.

References and Notes

(1) Presented in part at the 168th National Meeting of the American Chemical Society, Atlantic City, N.J., Sept 9–14, 1974.
(2) (a) P. A. Leighton, "Photochemistry of Air Pollution", Academic Press, New York, N.Y., 1961; (b) A. P. Altshuller and J. J. Bufalini, *Photochem. Photobiol.*, **4**, 97 (1965).
(3) H. Niki, E. E. Daby, and B. Weinstock, *Adv. Chem. Ser.*, **No. 113**, 16 (1972).
(4) P. L. Hanst, E. R. Stephens, W. E. Scott, and R. C. Doerr, "Atmospheric Ozone-Olefin Reactions", The Franklin Institute, Philadelphia, Pa., 1958.
(5) B. E. Saltzman and N. Gilbert, *Ind. Eng. Chem.*, **51**, 1415 (1959).
(6) E. A. Schuck, G. J. Doyle, and N. Endow, Report No. 31, Air Pollution Foundation, San Marino, Calif., 1960.
(7) J. J. Bufalini and A. P. Altshuller, *Can. J. Chem.*, **45**, 2243 (1965).
(8) R. A. Cox and S. A. Penkett, *J. Chem. Soc., Faraday Trans. 1*, **68**, 1735 (1972).
(9) D. H. Stedman, C. H. Wu, and H. Niki, *J. Phys. Chem.*, **77**, 2511 (1973).
(10) S. M. Japar, C. H. Wu, and H. Niki, *J. Phys. Chem.*, **78**, 2318 (1974).
(11) Y. K. Wei and R. J. Cvetanovic, *Can. J. Chem.*, **43**, 913 (1963); T. Vrbaski and R. J. Cvtanovic, *ibid.*, **38**, 1053, 1063 (1960).
(12) L. A. Hull, I. C. Hisatsune, and J. Heicklen, *Can. J. Chem.*, **51**, 1504 (1973); C. W. Blume, I. C. Histasune, and J. Heicklen, *Int. J. Chem. Kinet.*, **VIII**, 235 (1976).
(13) J. T. Herron and R. E. Huie, *J. Phys. Chem.*, **78**, 2085 (1974).
(14) K. H. Becker, U. Schurath, and H. Seitz, *Int. J. Chem. Kinet.*, **VI**, 725 (1974).
(15) B. J. Finlayson, J. N. Pitts, Jr., and R. Atkinson, *J. Am. Chem. Soc.*, **96**, 5356 (1974).
(16) F. S. Toby, S. Toby, and H. E. O'Neal, *Int. J. Chem. Kinet.*, **VIII**, 25 (1976).
(17) D. H. Stedman, E. E. Daby, F. Stuhl, and H. Niki, *J. Air Pollut. Contr. Assoc.*, **22**, 260 (1972).
(18) T. E. Sharp and E. E. Daby, "A Time-Sharing Computer Program for Chemical Reaction Mechanisms", Ford Motor Co., Scientific Research Staff Report, Aug 19, 1971.
(19) G. R. McMillan and J. G. Calvert, *Oxid. Combust. Rev.*, **I**, 83 (1965); J. Heicklen, *Int. Oxid. Symp.*, **I**, 343 (1967); J. A. Howard, K. Adamic, and K. U. Ingold, *Can. J. Chem.*, **46**, 2655 (1968), **47**, 3793, 3709, 3803 (1969).
(20) Unpublished results.
(21) H. E. O'Neal and C. Blumenstein, *Int. J. Chem. Kinet.*, **V**, 397 (1973).

Isotope Effects in Hot Atom Abstraction Reactions of H* and D* with CH_3CD_3

G. D. Beverly and R. M. Martin*

Department of Chemistry, University of California, Santa Barbara, California 93106 *(Received April 12, 1976)*

Hot H and D (H* and D*) reactions with ethane were studied in Br_2 scavenged systems using HBr and DBr as photodissociation hot atom sources. Quantum yields for the abstraction reactions of H* + C_2D_6 and H* + CH_3CD_3 were determined at an initial hot atom energy E_i = 1.6 eV, and found to be in good agreement with previous yields determined by the integral reaction probability method. Abstraction isotope effects for H* and D* + CH_3CD_3 were determined over the range E_i = 1.1–2.9 eV, in 94% ethane systems. With H* + CH_3CD_3 the H_2/HD product ratio increased from 2.4 ± 0.1 at 1.1 eV to 2.8 ± 0.1 at 2.9 eV, whereas with D* + CH_3CD_3 the HD/D_2 product ratio was approximately constant with change in E_i, 2.0 ± 0.1 at 1.6 eV and 1.9 ± 0.1 at 2.0 and 2.9 eV. In mixtures with a large mole fraction of Br_2 to scavenge low energy atoms the isotope effects at E_i = 2.9 eV increased to 3.1 ± 0.1 for H* + CH_3CD_3 and 2.8 ± 0.4 for D* + CH_3CD_3. These results, taken together with a previous determination of the abstraction isotope effect in the T* + CH_4–CD_4 system at 2.9 eV, give a consistent trend favoring H over D abstraction, with the H/D isotope effect increasing with decreasing hot atom mass. It is concluded that both the H/D preference and the hot atom mass effect can be understood in terms of inertial considerations and that a zero point energy effect may also contribute to the H/D preference.

Introduction

The study of high energy H*, D*, and T* atom reactions in thermal substrates has provided a large amount of information on the high energy reactivity of these atoms above threshold. High energy hydrogen atoms can be generated in thermal substrates using nuclear recoil and photodissociation methods. The most extensive work has been with T* generated in the $^3He(n,p)^3T^*$ nuclear reaction, producing T* atoms with 1.9×10^5 eV of recoil kinetic energy.[1,2] The recoil T* atoms are moderated down to about 10^3 eV below which they begin to form chemical bonds via abstraction and displacement reactions. A substantial fraction are thermalized without reaction, showing that recoil T* atoms sample the entire reactive energy range down to the reaction threshold energy E_0.

In the photochemical studies hydrogen halides have been photodissociated via repulsive excited states. Use of monochromatic radiation produces hydrogen atoms with known initial kinetic energy E_i. By varying the choice of hydrogen halide and photodissociation wavelength hydrogen atoms can be produced over a range of E_i and their reactions studied within energy bands E_0 to E_i. In this way H*, D*, and T* reactions have been studied over the E_i region 0.6–3.6 eV.

Both the nuclear recoil and photodissociation thermal substrate methods have been conveniently referred to as "hot atom chemistry". The term "superthermal atom chemistry" would be more appropriate to indicate the presence of a superthermal collisional energy distribution rather than a Boltzmann thermal energy distribution. Atoms generated with high kinetic energy in thermal substrates attain a superthermal energy distribution determined by the reactive and moderating collisions occurring in the substrate medium.[3–5] It has therefore not been possible to study reactions within a narrow band of collision energies using hot atom thermal substrate techniques. In spite of this limitation, the variety of broad-band integrated data available has provided sufficient information to permit the testing of phenomenological models of high energy reaction mechanisms.

A number of features of hot atom reactions have also been studied by quasiclassical trajectory calculations. With theoretical reaction cross section and moderating functions the Porter integral reaction probability equation[3] can be used to calculate reaction yields as a function of E_i. In the most elaborate such theoretical study to date Raff[6] has obtained good to excellent agreement with most of the experimental data for the T* + (CH_4,CD_4) systems.

Chou and Rowland[7] studied T* + (CH_4,CD_4) mixtures and found an H/D abstraction isotope effect of 1.7 ± 0.3 at E_i = 2.8 eV. Hong and Mains[8] studied the H/D abstraction isotope effect for H* with a maximum E_i of 1.8 eV. Isotope effects of 5–8 favoring H abstraction over D were found. The authors noted that such large values are closer to those expected for thermal hydrogen atoms than for H* atoms well above the E_0 of about 0.5 eV.[5] In an integral reaction probability study of H* and D* abstraction yields with C_2–C_6 hydrocarbons in this laboratory[9] an abstraction "composite isotope effect" for (D* + RH)/(H* + RD) of 2.2 ± 0.3 was found for the C_2–C_4 hydrocarbons over the E_i range 1.1–2.9 eV. Whereas the other isotope effects were determined in a single substrate medium, the study of ref 9 employed different media (e.g., D* + C_2H_6 vs. H* + C_2D_6). It was concluded that the composite isotope effect was nevertheless mainly due to reactive rather than moderating effects. The theoretical results of Raff[6] support earlier evidence[1,9] for the generalization that in hot hydrogen atom–hydrocarbon systems moderator effects on *relative* hot atom yields are small compared to reactive effects.

The purpose of the present study was to determine the H/D abstraction isotope effect for H* and D* reacting with CH_3CD_3 over the E_i range of 1.1–2.9 eV. HBr and DBr were used as the photodissociation hot atom sources. In order to determine the abstraction isotope effects from the H_2/HD and HD/D_2 product ratios it was necessary to eliminate or otherwise take account of the H_2 and D_2 resulting from H + HBr and D + DBr reactions. This was accomplished by carrying out the reactions in mixtures having Br_2/HBr or Br_2/DBr ratios of about 5. Under these conditions Br_2 acts as the principal H or D atom scavenger, reducing the H_2 and D_2 products from reaction with the source to small, correctable levels.

Experimental Section

A. *Photolysis and Analysis Methods.* The equipment and procedures used in this series of experiments have been described previously.[9] Hot H and D atoms were produced with known initial energies by photolyses of HBr and DBr at various wavelengths. Quartz photolysis cells of 2.40-cm i.d. diameter by 10.0 cm length fitted with Suprasil quartz windows and Pyrex stopcocks greased with Kel-F 90 were used for all photolyses. Low-pressure metal vapor lamps were used to obtain lines in the desired spectral range as follows: Hanovia Hg lamp with Suprasil quartz window (185 nm), Phillips Zn lamp (214 nm), Phillips Cd lamp (229 nm), and the Hanovia Hg or General Electric U tube Hg germicidal lamp (254 nm). Details on minor line emissions from these lamps are given in ref 9. The filters used to remove minor line emissions were Vycor with the 254-nm source, an interference filter with the 229-nm source, and hexafluoroacetonimine (HFAI) with the 185-nm source.[10] The 214-nm source was used without a filter. It was found that 1 atm of HFAI in a 1-cm filter cell became opaque within 5 h when exposed to a low pressure mercury lamp providing 1×10^{14} quanta/s at 185 nm and 2.6×10^{15} quanta/s at 254 nm. However 65 Torr of HFAI in a 10-cm cell was stable during experiments totaling 50 h of irradiation time, and thereafter 10-cm filter cells were used.

The initial hot atom laboratory translational energies in electron volts may be calculated, assuming ground state Br formation,[11] from the relationship

$$E_i = \frac{m_{Br}}{m_{ABr}}\left[\frac{1239}{\lambda} + \bar{E}_{rot}(ABr) - D_0°(ABr)\right] \quad (1)$$

where m is the atomic or molecular mass, A is H or D, λ is the photolysis wavelength, $D_0°$ is the dissociation energy from the ground state, and $\bar{E}_{rot}$ is the average rotational energy. All the photolyses were carried out at room temperature (23 ± 1 °C) where the average vibrational ABr energy and A translational energy associated with ABr motion are negligible. Taking $D_0°$ values of 3.75 eV for HBr and 3.80 eV for DBr,[12] the initial A atom energies in eV for 254, 229, 214 and 185 nm are respectively 1.14, 1.67, 2.04 and 2.94 for H atoms and 1.08, 1.60, 1.97 and 2.86 for D atoms.

For isotope effect product analysis, (H_2,HD) and (HD,D_2) standard mixtures were made up and used to calibrate the mass spectrometer. The mixtures were prepared to within 1% H_2/HD or HD/D_2 ratio accuracy. Different standards gave the same sensitivity ratio on the mass spectrometer within experimental error (±1%).

For quantum yield determinations an HBr actinometer was run before and after each sample photolysis, and the average of the two experimental intensities used to calculate the quantum yield. Actinometers were run with a minimum HBr pressure of 10 Torr in 10-cm cells. Percent HBr decompositions were ≤0.6% giving intensities approximately 1% low due to Br_2 scavenging. Agreement between actinometer intensities was usually excellent, within 3%. Quantitative analysis of the H_2 actinometer product and H_2 and HD products in the hot atom–hydrocarbon quantum yield determinations was accomplished using internal standard techniques. Ne was used as the internal standard, and to avoid spurious contributions to the ^{20}Ne peak, the ^{22}Ne peak was used for analysis. Ne/H_2 and Ne/H_2/HD standard mixtures were used to calibrate the mass spectrometer for relative sensitivities before and after each product analysis. A known amount of Ne was added to the H_2 or H_2/HD products and the resulting mixture analyzed to give the absolute amounts of H_2 and HD. No sensitivity ratio variations in the mass spectrometer were detected during an analysis sequence within the experimental precision of ±1%.

B. *Reagents.* DBr, C_2D_6, and CH_3CD_3 were purchased from Merck Sharpe and Dohme. No uv absorption was detected in the degassed CH_3CD_3 down to 175 nm, but when the reagent was combined with prepurified Br_2 a strong absorption peaking around 201 nm was noted. The absorbance was identified as ethylene dibromide formed by the addition of Br_2 to ethylene. Assuming complete addition of Br_2, the CH_3CD_3 was estimated to contain 0.6% ethylene. To eliminate this impurity, the CH_3CD_3 was treated with Br_2 and then distilled twice in vacuo from −112 to −196 °C. The distillate was treated with NaOH pellets to remove possible HBr and DBr produced by the reaction ethylene + Br_2 → ethylene bromide + hydrogen bromide, and then distilled again under the same conditions. Following this procedure, no uv absorption was detected in the CH_3CD_3 with or without added Br_2.

Isotopic purity analysis by infrared spectroscopy gave 2.8 atom % H in the C_2D_6. The C_2D_6 was also found to contain 0.1% ethylene by the method described above, and this impurity was not removed.

Isotopic purity checks were performed on the DBr by photolyzing it in the pure state under identical conditions with each mixture photolysis. Effective isotopic purities as determined by the H_2/HD/D_2 ratio in the photolysis products were in the 96–97% range.

Research grade C_2H_6 from Phillips was degassed and used without further purification. No uv absorption was detected under experimental conditions.

Difficulty was encountered in obtaining bromine without impurity absorption bands in the ultraviolet. Research grade Br_2 was degassed and distilled in vacuo from 0 °C through a trap at −23 to −196 °C, the first half of the Br_2 in the −196 °C trap being retained. This procedure was repeated three times until no further improvement in the uv absorption could be attained. Two weak absorption bands in the 190–195-nm range were still observed, and judged to be impurity absorptions. Optronic grade Br_2 was then obtained from Alfa Inorganics in a sealed ampoule. This was vacuum distilled from −23 °C through a trap at −23 to −196 °C twice, each time retaining the fraction in the second −23 °C trap. The resulting Br_2 did not have the impurity bands, and gave a strong absorption beginning about 180 nm, attributed to Br_2. Molar extinction coefficients were 5 cm^{-1} M^{-1} at 214 nm and 2.3 cm^{-1} M^{-1} at 185 nm.

H_2, HD, and D_2 were used to make standards for product analysis on the mass spectrometer. High purity H_2 and research grade D_2 were obtained from Matheson. The H_2 was purified by diffusion through a palladium thimble. The only detectable impurity in mass analysis was 0.3% air. The D_2 was found to contain 0.16% air. HD from Merck Sharp and Dohme was found to contain 0.5% air, 0.8% D_2, and 1.0% H_2.

C. *Reaction Systems.* The object of the present experiments was to effectively eliminate hot and thermal atom reactions with the photolytic source (HBr or DBr), so that the observed H_2/HD or HD/D_2 ratios could be directly related to the hot atom abstraction rates with CH_3CD_3. This was accomplished by running the reactions with bromine in excess of hydrogen bromide: typical Br_2/hydrogen bromide ratios were 5. The important reactions are listed below for H atoms. The reaction scheme is equally valid for D reactions with the appropriate notation changes

$$HBr + h\nu \rightarrow H^* + Br \quad (2)$$

$$H^* + RD \rightarrow HD + R \quad (3^*)$$

$$H^* + RH \rightarrow H_2 + R \quad (4^*)$$

$$H^* + HBr \rightarrow H_2 + Br \quad (5^*)$$

$$H^* + Br_2 \rightarrow HBr + Br \quad (6^*)$$

$$H^* + M \rightarrow H + M \quad (7^*)$$

$$R + Br_2 \rightarrow RBr + Br \quad (8)$$

$$Br + Br + M \rightarrow Br_2 + M \quad (9)$$

$$H + HBr \rightarrow H_2 + Br \quad (5)$$

$$H + Br_2 \rightarrow HBr + Br_2 \quad (6)$$

Hot atoms are considered to be those with translational energies above the threshold for reactions 3 and 4. Atoms which are moderated below this energy (without asterisks) are assumed to be "quasithermal", with energy distributions which are higher than Maxwellian, but insufficient for reaction with the hydrocarbon. The percent decomposition of the hydrogen bromide was not a critical factor in these experiments, in contrast to earlier ones,[9] since Br_2 was added as the scavenger. Hydrogen bromide percent decompositions were <1%. Photolysis of the ethyl bromide products under the conditions employed would not be important at percent decompositions an order of magnitude higher than those used. All the experiments were carried out at room temperature.

In order to establish the scavenging efficiency of the Br_2, the photolysis cell was filled with 1000 Torr of CH_3CD_3 and 10 Torr of HBr, and photolyzed at 229 nm. This produced a small average Br_2 concentration in the photolysis products. After the H_2 and HD products had been removed additional Br_2 was added to the cell and the photolysis repeated. The H_2/HD product ratio was determined in this way as a function of the Br_2/HBr ratio. The results are shown in Figure 1. For Br_2/HBr > 3, the H_2/HD ratio was constant within experimental error, indicating that under these conditions H_2 production by reaction with HBr was small compared to that from hot reaction with the CH_3CD_3.

Experiments were run to determine the quantum yields for H_2 and HD in systems where pressures in Torr of HBr/Br_2/ethane were 10/30/1000 or 10/50/1000. Measurable amounts of H_2 and HD were found to be produced without the HBr, due to reactions resulting from Br_2 light absorption. To correct for Br_2-induced H_2 and HD, the Br_2/ethane system was first photolyzed without the HBr and the products measured. HBr was then added and the photolysis and analysis repeated. The uv absorbance of the cell, the cell with Br_2, and the cell with Br_2 and HBr was measured before and after each photolysis at the photolysis wavelength on a Cary 10 spectrophotometer, and the resultant absorbances of the contents, A_{Br_2} and A_{HBr}, used to correct for Br_2-induced H_2 and HD. HBr actinometers were run before and after each photolysis of the ethane system to determine the light intensity absorbed by the HBr and Br_2 in the hot atom experiment. The product yield and actinometer data taken together provided quantum yields for hot atom H_2 and HD production. Since the major interest in this work was to obtain competitive isotope abstraction ratios for hot H and D atoms, most of the data was taken without actinometry and the calculation of quantum yields. Otherwise the procedure was as described above.

Results

A. *Quantum Yields.* Experiments were performed with Br_2/HBr $\gtrsim$ 5 in order to minimize the H_2 formation from reaction with HBr.[13] The uncorrected experimental quantum yield data are given in Table I. All quantum yields in Tables I and II are expressed in percent for convenience; 100% corresponds to an absolute quantum yield of unity. Correction to the primary data must be made for both the effect of induced H_2 and HD yields by Br_2 and for the small amount of H_2 produced by HBr scavenging of H atoms.

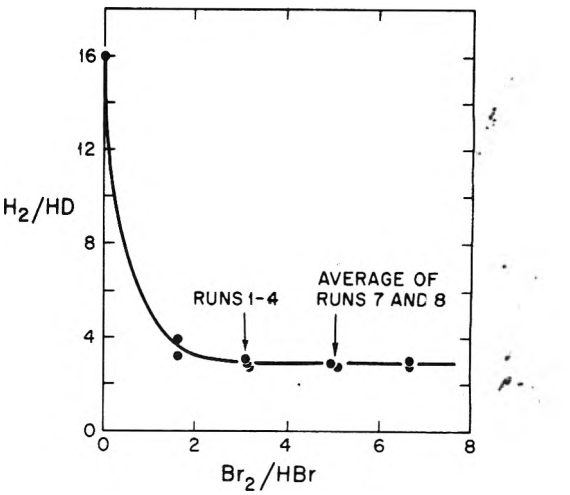

Figure 1. Scavenging efficiency of Br_2 vs. HBr for 1.6 eV H* + CH_3CD_3.

To make the corrections for the Br_2-induced yields, we first write for the total experimental rate R and total absorbed light intensity I

$$R = R_{HBr} + R_{Br_2}$$
$$I = I_{HBr} + I_{Br_2} \quad (10)$$

where R is the rate of formation of either H_2 or HD, R_{HBr} is the rate due to HBr, R_{Br_2} is the rate due to Br_2, I_{HBr} the light intensity absorbed by HBr, and I_{Br_2} the light intensity absorbed by Br_2. The experimental quantum yields are given by

$$\varphi_{expt} = \frac{R}{I} = \frac{R_{HBr} + R_{Br_2}}{I_{HBr} + I_{Br_2}} \quad (11)$$

R_{Br_2} is calculated from $R_{Br_2} = \varphi_{Br_2} I_{Br_2}$, where φ_{Br_2} is the product quantum yield measured in photolysis of the Br_2/ethane system. I_{Br_2} in the HBr/Br_2/ethane system is calculated from the expression

$$I_{Br_2} = \left(\frac{A_{Br_2}}{A_{HBr} + A_{Br_2}}\right) I_0(1 - T) \quad (12)$$

where $A = \epsilon cl$ is the Beer's law absorbance, I_0 is the light intensity entering the reaction cell as determined by actinometer experiments, and T is the transmittance of the cell contents. The quantum yield corrected for the effect of Br_2-induced yield is then given by

$$\varphi' = \frac{R_{HBr}}{I_{HBr}} = \frac{\varphi_{expt} I - R_{Br_2}}{I_{HBr}} \quad (13)$$

The φ' values for the data of Table I are given in Table II.

The correction for H atom scavenging by HBr is approached by considering the H_2 yield in the C_2D_6 system (Table II). We define the first-order value of the istope effect as $[\varphi'_{H_2}/\varphi'_{HD}]_{CH_3CD_3}$. To make the HBr scavenging correction let $H_2(e)$ be the hydrogen from hot atom reaction with the ethane, and $H_2(s)$ be the hydrogen from reaction with the hot atom source, HBr. The ratio of H/D abstraction from the perdeuterated

TABLE I: Uncorrected H_2 and HD Quantum Yields for H* + Ethane at E_i = 1.6 eV

Run	Ethane	HBr/Br_2/ethane, Torr	φ_{H_2}, %	φ_{HD}, %	$\varphi_{H_2}/\varphi_{HD}$	Comments
6	CH_3CD_3	0/33.8/1372	0.93	0.31	3.0	
7	CH_3CD_3	11.3/58.1/1017	9.03 ± 0.50	3.32 ± 0.30	2.73 ± 0.10	*a*
8	CH_3CD_3	11.5/58.5/995	8.67 ± 0.60	3.18 ± 0.20	2.73 ± 0.02	*a*
9	C_2D_6	11.7/56.1/1018	1.88 ± 0.08	6.25 ± 0.37	0.30 ± 0.01	*a*
10	C_2D_6	0/56.6/1027	0.63	0.69	0.91	

[a] Averages of duplicate runs. Errors in quantum yields give the range of results. Errors in $\varphi_{H_2}/\varphi_{HD}$ ratios give the range of quantum yield experimental ratios.

TABLE II: Corrected H_2 and HD Quantum Yields for H* + Ethane at E_i = 1.6 eV

Run	Ethane	φ'_{H_2},[a] %	φ'_{HD},[a] %	$\varphi'_{H_2}/\varphi'_{HD}$	$\varphi'_{H_2}(e)$,[b] %	$\varphi'_{H_2}(e)/\varphi'_{HD}$
7	CH_3CD_3	17.0	6.27	2.71	15.2	2.42
8	CH_3CD_3	16.2	5.97	2.71	14.3	2.39
9	C_2D_6	3.04	11.4	0.23	0.79	0.07

[a] Data of Table I, corrected for Br_2 light absorption and Br_2-induced yields of HD and H_2. [b] Hot atom H_2 yield with ethane after correction for H_2 from reaction with HBr.

ethane can be calculated using the first-order value and the isotopic purity. In the present case the perdeuterated ethane contained 2.8 atom % H, giving

$$\left[\frac{\varphi'_{H_2}(e)}{\varphi'_{HD}}\right]_{C_2D_6} = \frac{2.8}{97.2}\left[\frac{\varphi'_{H_2}}{\varphi'_{HD}}\right]_{CH_3CD_3} \quad (14)$$

With a first-order value of 2.71 (Table II), $[\varphi'_{H_2}(e)/\varphi'_{HD}]$ = 0.078 and $\varphi'_{H_2}(e) = 0.078\varphi'_{HD}$ = 0.89%, where φ'_{HD} = 11.4% in the C_2D_6. The total hot atom quantum yield for reaction with the perdeuterated ethane is given by $\varphi'_{HD} + \varphi'_{H_2}(e)$ = 12.3%. The remainder reacts with HBr and Br_2, $\varphi_{H_2}(s) + \varphi_{Br_2}$ = 87.7%. The quantum yield for reaction with HBr is $\varphi_{H_2}(s) = \varphi'_{H_2} - \varphi_{H_2}(e)$ = 3.04–0.89 = 2.15%, giving φ_{Br_2} = 85.6%. The ratio $\varphi_{Br_2}/\varphi_{H_2}(s)$ is given by

$$\frac{\varphi_{Br_2}}{\varphi_{H_2}(s)} = \frac{k_6^*(Br_2)}{k_5^*(HBr)} \quad (15)$$

In the C_2D_6 system (run 9) k_6^*/k_5^* is found to be 8.3. Since there is no significant difference in the per bond D abstraction yield in C_2D_6 and CH_3CD_3 it was assumed that the hot atom energy density distribution in the C_2D_6 and CH_3CD_3 systems was nearly the same, giving the same k_6^*/k_5^* ratio for the two systems. Using this ratio and the experimental quantum yields, $\varphi_{H_2}(s)$ in the CH_3CD_3 system can be calculated, giving the corrected hot atom quantum yield $\varphi'_{H_2}(e)$, and the second-order corrected hot atom abstraction isotope effect $\varphi'_{H_2}(e)/\varphi'_{HD}$. Iteration changed only $\varphi'_{H_2}(e)$ for the C_2D_6 system, run 9. The final results are given in Table II.

B. *Yield Ratios for H* + CH_3CD_3.* Following the quantum yield work on the H* + CH_3CD_3 and H* + C_2D_6 systems at 1.6 eV initial energy, actionometry was discontinued and only yield ratios were determined. For each run, the rate of formation of H_2 and HD was measured with and without the presence of HBr. Correction for the Br_2-induced yields was made using the equation

$$R_{HBr} = R - R_{Br_2} = R - R'_{Br_2}\left(\frac{f_{Br_2}}{f'_{Br_2}}\right) \quad (16)$$

where R'_{Br_2} is the Br_2-induced rate in the Br_2/ethane mixture, f'_{Br_2} the fraction of light absorbed by Br_2 in this mixture, and f_{Br_2} the fraction of light absorbed by Br_2 in the HBr/Br_2/ethane mixture.

Equation 16 assumes a constant light intensity over the 1–3 h time required for the two rate determinations with and without HBr. Experience with the light sources showed that their intensity was constant to within a few percent variation over a period of 3 h under the conditions used.

For the correction for H_2 due to reaction with HBr, the first-order isotope effect and $[H_2'(e)/HD']_{C_2D_6}$ were first calculated as described above. The ratio of $H_2(s)$ to HD is given by[14]

$$\left[\frac{H_2(s)}{HD}\right]_{C_2D_6} = \left[\frac{H_2}{HD} - \frac{H_2'(e)}{HD'}\right]_{C_2D_6} = \frac{k_5^*(HBr)}{k_3^*(C_2D_6)} \quad (17)$$

where k_3^* here refers to the hot atom rate coefficient for abstraction from C_2D_6. Assuming that the rate coefficient for abstraction of D from CH_3CD_3 is half of that for C_2D_6, we have

$$\left[\frac{H_2(s)}{HD}\right]_{CH_3CD_3} = \frac{2k_5^*(HBr)}{k_3^*(CH_3CD_3)} \quad (18)$$

The second-order corrected isotope effect is then

$$\left[\frac{H_2(e)}{HD}\right]_{CH_3CD_3} = \left[\frac{H_2}{HD} - \frac{H_2(s)}{HD}\right]_{CH_3CD_3} \quad (19)$$

The third-order corrected value is obtained by iteration, and no change was found with further iteration. The results are given in Table III as $(H_2/HD)''$.

At 1.1 eV, where no experiments were run with C_2D_6, the value of $[H_2(s)/HD]_{CH_3CD_3}$ was calculated by estimating k_5^*/k_3^* at 1.1 eV from the values found at the higher energies: 15.7 at 2.0 eV and 14.8 at 2.9 eV. The observed increase in k_5^*/k_3^* with decreasing energy is expected, due to the decreasing k_3^* with decreasing energy. A value of 18 for k_5^*/k_3^* in C_2D_6 at 1.1 eV was assumed, giving $(H_2/HD)''$ = 2.40 in CH_3CD_3.

C. *Yield Ratios for D* + CH_3CD_3.* Corrections to the experimental yields for Br-induced HD and D_2 were made in the same way as for the H* + CH_3CD_3 experiments. Corrections for D_2 due to scavenging of D atoms by DBr were made analogously to the H + HBr experiments, except that corrections for isotope purity were unnecessary with the C_2H_6. No experiments were run with C_2H_6 at 1.6 eV, and k_5^*/k_3^* (for the isotopically reversed case) was therefore estimated from the values of 3.2 at 2.0 eV and 3.1 at 2.9 eV. Again, this trend is as expected, and k_5^*/k_3^* in C_2H_6 was assumed to be 3.3 at 1.6 eV, giving $(HD/D_2)''$ = 1.97 in CH_3CD_3. These results are given in Table IV.

TABLE III: Integral Yield Ratios for H* + Ethane [a]

E_i, eV	Ethane	$(H_2/HD)'$ [b]	$(H_2/HD)''$ [c]
1.1	CH_3CD_3	2.80 ± 0.10 [d]	2.40 [g]
2.0	CH_3CD_3	2.91 ± 0.05 [e]	2.62
2.9	CH_3CD_3	3.09 ± 0.11 [f]	2.80
2.0	C_2D_6	0.23 ± 0.01 [d]	
2.9	C_2D_6	0.23	

[a] The composition of all systems was approximately HBr/Br_2/ethane = 10 Torr/50 Torr/1000 Torr. For each experiment the yields were measured with and without HBr to provide the data needed to correct for Br_2-induced yields. [b] Average yield ratio after correction for Br_2-induced yields. Error ranges indicate the range of the experimental data. [c] Yield ratio after correction for both Br_2-induced yields and H_2 due to scavenging by HBr. [d] Average of two experiments. [e] Average of four experiments. [f] Average of three experiments. [g] Based on k_5^*/k_3^* value of 18 in C_2D_6. See text.

TABLE IV: Integral Yield Ratios for D* + Ethane [a]

E_i, eV	Ethane	$(HD/D_2)'$ [b]	$(HD/D_2)''$ [c]
1.6	CH_3CD_3	1.75 ± 0.02 [d]	1.97 [f]
2.0	CH_3CD_3	1.71 ± 0.13 [e]	1.92
2.9	CH_3CD_3	1.69 ± 0.09 [e]	1.88
2.0	C_2H_6	34.0 ± 1.0 [d]	
2.9	C_2H_6	34.0 ± 4.0 [d]	

[a] The composition of all systems was approximately HBr/Br_2/ethane = 10 Torr/50 Torr/1000 Torr. For each experiment the yields were measured with and without HBr to provide the data needed to correct for Br_2-induced yields. [b] Average yield ratio after correction for Br_2-induced yields. Error ranges indicate the range of the experimental data. [c] Yield ratio after correction for both Br_2-induced yields and D_2 due to scavenging by DBr. [d] Average of two experiments. [e] Average of three experiments. [f] Based on k_5^*/k_3^* value of 3.3 in C_2H_6. See text.

The "effective" isotopic purity of the DBr was determined by photolyzing a sample of DBr with each photolysis run, using identical procedures as for mixture preparation. The ratio $r = D_2/HD$ was determined for the DBr photolysis products, and the effective isotopic purity f calculated according to the equation

$$f = \frac{2r}{2r + 1} \tag{20}$$

This is a probability equation, and does not take into account isotope effects in the hot atom rate coefficients, which are unknown. The DBr isotopic purity determined via eq 20 ranged from a low of 95.4% to a high of 97.8% during the course of the experiments. The amount of HD(s) produced is expected to be negligible with this isotopic purity in view of the small amount of D_2(s) produced, as indicated by the $(HD/D_2)'$ ratios in C_2H_6 (Table IV).

D. *Yield Ratios with High Br_2 Mole Fraction.* The yield ratios of Tables I–IV are for hot atom reactions in systems with HBr/Br_2/ethane compositions of approximately 1%/5%/94%. Most of the hot atoms will be moderated by collisions with ethane in these systems, and the average energy of hot atom abstraction of H or D from the ethane is expected to be considerably below the initial energy E_i. Several experiments were carried out with HBr/Br_2/ethane compositions of approximately 1.5%/43%/55.5% in order to shift the average ethane abstraction energy toward the upper limiting value E_i. The results are given in Table V. Corrections for Br_2-induced yields were made as described previously by carrying out a photolysis with and without the HBr for each experiment. In the 94% ethane systems the k_5^*/k_3^* ratios were quite insensitive to E_i over the 2.0–2.9-eV region, as previously discussed. The ratios should therefore be nearly the same in the 55% ethane systems, and the previous 2.9-eV values were used to make the hydrogen bromide scavenging correction. For the H* + CH_3CD_3 system the equation is

$$\left(\frac{H_2}{HD}\right)' = \frac{k_4^*(CH_3CD_3) + k_5^*(HBr)}{k_3^*(CH_3CD_3)} = \left(\frac{H_2}{HD}\right)'' + \frac{k_5^*(HBr)}{k_3^*(CH_3CD_3)} \tag{21}$$

The $(H_2/HD)''$ and $(HD/D_2)''$ ratios are given in Table V, and are significantly larger than found in the 94% ethane systems at the same E_i (Tables III and IV).

Discussion

A. *Quantum Yields.* From Table II the per bond quantum yields at 1.6 eV of 1.9% in C_2D_6 and 2.0% (average of runs 7 and 8) in CH_3CD_3 agree within experimental error, and indicate no secondary isotope effect greater than 5%. The ϕ'_{HD} values may be compared with integral reaction probabilities determined previously. Compton, Beverly, and Martin[9] obtained an IRP of 9.5% for H* + C_2D_6 at 1.6 eV, in good agreement with the present work. For H* atoms with an average E_i of 1.4 eV,[15] Hong and Mains[8] found IRP's of 9.6% with C_2D_6 and 5.2% with CH_3CD_3 to give HD, again in good agreement with this work.[16]

B. *Abstraction Isotope Effects.* The corrected average hot atom abstraction isotope effects from Tables II–V are summarized in Table VI with the double primes omitted to simplify the notation for discussion. The H_2/HD ratio rises slowly but significantly with increasing E_i, and this trend is confirmed by the increased ratio in the high-Br_2 system where reactive collisions with CH_3CD_3 are shifted to higher energies. In contrast, HD/D_2 does not appear to depend on E_i over the 1.6–2.9-eV region in the 94% CH_3CD_3 systems, but does show a significant increase in the high-Br_2 systems. The isotope

TABLE V: Integral Yield Ratios with High Br_2 Mole Fractions at E_i = 2.9 eV

Isotopic bromide (ABr)	ABr/Br_2/CH_3CD_3, Torr	$(H_2/HD)_{expt}$ [a]	$(H_2/HD)'$ [b]	$(H_2/HD)''$ [c]	$(HD/D_2)_{expt}$ [a]	$(HD/D_2)'$ [b]	$(HD/D_2)''$ [c]
HBr	5.4/158/206	3.77	3.81	3.03			
HBr	5.4/164/205	3.86	3.88	3.10			
DBr	5.5/157/217				2.15	2.15	3.25
DBr	5.4/156/224				1.78	1.77	2.40
DBr	5.3/154/225				1.94	1.92	2.67

[a] Experimental yield ratios. [b] Yield ratio after correction for Br_2-induced yields. [c] Yield ratio after correction for both Br_2-induced yields and HBr or DBr scavenging.

TABLE VI: Hot Atom Abstraction Isotope Effects for H* and D* + CH_3CD_3 [a]

E_i, eV	H_2/HD	HD/D_2
1.1	2.4 ± 0.1	
1.6	2.4 ± 0.1	2.0 ± 0.1
2.0	2.6 ± 0.1	1.9 ± 0.1
2.9	2.8 ± 0.1	1.9 ± 0.1
2.9[b]	3.1 ± 0.1	2.8 ± 0.4

[a] Average $(H_2/HD)''$ and $(HD/D_2)''$ values from Tables II–V. Error ranges indicate the range of the experimental data. [b] Yields in high-Br_2 systems, Table V.

effect favoring H over D abstraction is larger for H* than D* for all systems at all E.

The TH/TD abstraction isotope effect of 1.7 ± 0.3 found by Chou and Rowland[7] in T* + CH_4/CD_4 mixtures at E_i = 2.8 eV is consistent with the trend of the present work, i.e., the isotope effect decreases with increasing hot atom mass. However, the present results are not in agreement with those of Hong and Mains[8] (HM) who obtained an H_2/HD value of 4.8 ± 0.8 at an average E_i of 1.4 eV, twice the value found in this work at 1.1 and 1.6 eV. HM used an IRP technique to determine the abstraction isotope effect, in contrast to our corrected yield method. An I_2/HI ratio of 2.3 was used to suppress H_2 formation by reaction with HI, and the HI/CH_3CD_3 ratio varied over the range 0.1–0.5. The H_2/HD vs. HI/CH_3CD_3 IRP plot gave a straight line which extrapolated to H_2/HD = 4.8 at HI/CH_3CD_3 = 0. HM attributed the large isotope effects observed using this method to thermal or near thermal reactions, and concluded that I_2 must be a much better moderator for hot atoms than ethane. This seems unlikely from consideration of the atomic masses, and from the work of Fass and co-workers who have shown that CO_2 is a much poorer moderator than He[17a] and also find that thermalization by HBr and Br_2 is undetectable relative to reactive collisions of hot hydrogen atoms.[17b] HI and I_2 would be expected to behave similarly. A more likely cause of the discrepancy lies in the validity of the IRP method when using a mixed scavenger such as I_2/HI. The hot and thermal H atom rate coefficient ratios for this mixture are $k^*_{I_2}/k^*_{HI}$ = 4[18] and k_{I_2}/k_{HI} = 12,[19] although there is some question whether determinations of the latter quantity have been made in completely thermalized systems.[17b] HM assumed that the *thermal* ratio applied to their systems. This would result in a maximum error of 4% in the assumption which they made that all thermalized atoms reacted with I_2. However it is clear that H* atoms not reacting with CH_3CD_3 are only partially moderated in systems with the composition range used, and that over the HI/CH_3CD_3 range 0.1–0.5 the $k^*_{I_2}/k^*_{HI}$ "epithermal" rate coefficient ratio will change. This is illustrated by measurements of HM on a system with composition I_2/HI/C_2D_6 = 2.3/1.0/5.0. When He moderator was added to this system up to a He/HI ratio of 26 the HD yield decreased by a factor of 2 while the HD/H_2 ratio remained constant, indicating that the H_2 yield also decreased by a factor of 2. Therefore the $k^*_{I_2}/k^*_{HI}$ epithermal ratio increased by a factor of 2 with addition of the moderator. The absence of thermalization is also seen in the present work for 1.6-eV H atoms in 94% C_2D_6. A $k^*_{Br_2}/k^*_{HBr}$ ratio of 8.3 was found in this system, compared to rate coefficient ratios of $k^*_{Br_2}/k^*_{HBr}$ = 5–6[17,20] in unmoderated mixtures and k_{Br_2}/k_{HBr} = 23[17a] for thermal atoms at 25 °C.

Over the composition range used by HM in the IRP studies most of the H_2 produced is by reaction with HI. It is probable that if the intercept were approached more closely experimentally an increasing slope would be observed due to the increase in k_{I_2}/k_{HI} in the limit of complete thermalization, giving a lower intercept and resulting isotope effect, H_2/HD.[21]

C. *Abstraction Isotope Effects in High-Br_2 Systems.* Trajectory calculations have been reported by White[22] on the systems H* + Br_2, D* + Br_2, H* + HBr, and D* + DBr. Within the relative energy region 0.5–3.0 eV the cross sections were found to be approximately equal for the H* + HBr and D* + DBr reactions, but larger for D* + Br_2 than for H* + Br_2 due mainly to inertial effects. The H* + HBr and D* + DBr abstraction cross sections were 0.5–1.0 Å^2 over the relative energy range 0.5–3.0 eV, showing a weak energy dependence within this range peaking in the center. The H* + Br_2 and D* + Br_2 cross sections decreased strongly and monotonically with increasing energy from thermal energies up to 3 eV. Over the 0.5–2.0-eV range the H* + Br_2 cross section decreased from 10 to 1 Å^2 while the D* + Br_2 cross section decreased from 13 to 2 Å^2. Calculations using approximate collisional distributions showed that the cross section functions gave correct qualitative predictions of the $k^*_{Br_2}/k^*_{HBr}$ and $k^*_{Br_2}/k^*_{DBr}$ ratios. The White trajectory results are thus in good agreement with the experimental hot atom data on these four reactions, and predict that Br_2 will change from a good hot atom scavenger in the threshold region to a poor hot atom scavenger at 3 eV.

Gann, Ollison, and Dubrin[5] studied the cross sections for H* + n-C_4D_{10} primary and secondary abstraction using a hot atom IRP method, and obtained cross section functions with maxima (σ_0) in the 1.0–1.5-eV region of σ_0(sec) = 0.35 ± 0.15 Å^2 and σ_0(pri) = 0.26 ± 0.14 Å^2. Previous hot atom studies[23] had also indicated that the D* + C_2H_6 and H* + C_2D_6 average hot atom abstraction cross sections at E_i = 2.9 eV are small compared to momentum transfer cross sections, ≲1 Å^2. Slopes of the IRP plots giving $(k_5^* + k_7^*)/k_3^*$, where k_5^* and k_7^* are for the hydrogen or deuterium bromide and k_3^* (or k_4^*) for the hydrocarbon, are consistent with this, being 10.0–10.5 for H* + C_2D_6 and 3.87–2.15 for D* + C_2H_6 over the 1.1–2.9-eV range.[9] The sum of the evidence then shows that, for the HBr/Br_2/ethane composition of 1.5%/43%/55.5% in the high-Br_2 experiments, Br_2 should begin to compete effectively for hot atoms above 2 eV, and will increasingly be the dominant hot atom reactant below 2 eV. Also the abstraction cross sections with the ethanes are expected to drop off sharply below 1 eV. The net effect of the Br_2 addition will be to shift the hot atom energy distribution at E_i = 2.9 eV toward higher energies from that in 94% ethane, and to shift the average abstraction energy with the ethane up accordingly.

The greater increase of HD/D_2 compared to H_2/HD in high Br_2 is somewhat surprising in view of the lack of E_i dependence of HD/D_2 in 94% CH_3CD_3. This result may be due to the shapes of the abstraction cross section functions in the high energy region, but it could also involve a high energy moderation effect. A more explicit description cannot be derived from the present data.

D. *Inertial and Bond Energy Effects.* Polanyi and coworkers[24] have explored inertial effects in three-body model trajectory calculations on hot T atom abstraction reactions. At 2 eV they found that the effect of increasing the mass of the attacked atom was qualitatively the same as the effect of decreasing the mass of the attacking atom, both tending to decrease the abstraction cross section. Both changes result in fewer abstraction captures, because for many trajectories the attacked atom is not able to move rapidly enough to form a

new bond with the attacking atom as it rebounds away. Data on hot atom abstraction from isotopic hydrocarbons are all consistent with expected inertial effects: (a) abstraction of H is favored over D by both H* and D*, (b) H_2/HD is larger than HD/D_2, and (c) T* + CH_4/CD_4 has a smaller isotope effect[7] than D* + CH_3CD_3. However another factor to be considered in interpreting these results is that RH bonds are weaker than RD bonds due to vibrational zero-point energy. Extensive recoil T* studies by Rowland and co-workers[2] have demonstrated the existence of the "bond energy effect", i.e., a correlation between H or D abstraction yields and the strength of the C–H or C–D bonds. The bond energy effect has also been found in H* and D* abstraction reactions with hydrocarbons in the E_i = 1–3-eV region.[5,9,25] There has been strong evidence that the bond energy effect is due to a lowering of the potential energy barrier with decreasing bond strength, which results in enhanced cross sections not only in the barrier region, but also extending to energies far above the barrier height.[25,26] This conclusion has been confirmed by classical trajectory calculations.[27] In the case of isotopic reactions the potential energy surfaces are identical, and the difference in bond energies is a zero-point energy effect. If the zero-point energies of the different isotopic reaction transition states do not affect the reaction cross sections, the bond energy effect predicts an enhanced reactivity for the reactant with the largest zero-point energy. On the other hand, if the reaction cross sections depend on the zero-point energies of the transition state this will tend to cancel the effect of reactant zero-point energy, reducing the bond energy effect. Based on the vibrational frequencies of C_2H_6 and C_2D_6[28] the C–H bond is expected to be about 0.10 eV weaker than the C–D bond. This is about the same as the difference in primary and secondary bond strengths in n-C_4D_{10}, and the yield ratios in the two cases are also the same within experimental error, i.e., at E_i = 2.0 eV H_2/HD is 2.6 ± 0.1 for CH_3CD_3 (Table VI) and the per bond secondary/primary yield ratio is 2.5 ± 0.3 for H* + n-C_4D_{10}.[25] This agreement is suggestive of a bond energy effect in C–H vs. C–D abstraction. However the theoretical basis for such an effect in the case of isotopic abstraction is unclear, and will probably be difficult to establish. At present the best interpretation of the data is in terms of inertial effects, which account for both the preferred abstraction of H over D, and the increase in the H/D isotope effect with decreasing mass for the hot atoms T*, D*, and H*.

Dedication. Dedicated to Professor John E. Willard on the occasion of his 70th year.

Acknowledgment. Support from the National Science Foundation (Grant No. GP-8579) is gratefully acknowledged.

References and Notes

(1) R. Wolfgang, *Prog. React. Kinet.*, **3,** 97 (1965).
(2) F. S. Rowland, *Chem. Kinet.*, **9,** 109 (1972).
(3) R. N. Porter, *J. Chem. Phys.*, **45,** 2284 (1966).
(4) C. Rebick and J. Dubrin, *J. Chem. Phys.*, **53,** 2079 (1970).
(5) R. G. Gann, W. M. Ollison, and J. Dubrin, *J. Chem. Phys.*, **54,** 2304 (1971).
(6) L. M. Raff, *J. Chem. Phys.*, **60,** 2220 (1974).
(7) C. C. Chou and F. S. Rowland, *J. Phys. Chem.*, **75,** 1283 (1971).
(8) K. Hong and G. J. Mains, *J. Phys. Chem.*, **76,** 3337 (1972).
(9) L. E. Compton, G. D. Beverly, and R. M. Martin, *J. Phys. Chem.*, **78,** 559 (1974).
(10) S. Toby and G. O. Pritchard, *J. Phys. Chem.*, **75,** 1326 (1971).
(11) R. S. Mulliken, *J. Chem. Phys.*, **8,** 382 (1940). Mulliken estimated theoretically that less than 2% of the ultraviolet continuum transitions of HBr are to the $^3\Pi_{0^+}$ state, which dissociates to give $Br^*(4^2P_{1/2})$ with 0.435 eV of electronic energy.
(12) B. de B. Darwent, *Natl. Stand. Ref. Data Ser., Natl. Bur. Stand.*, **No. 3** (1970).
(13) The initial quantum yield experiments were run at a Br_2/HBr ratio of 3. The agreement between the quantum yields was poor, the range being ±50% of the average value. In contrast, the H_2/HD ratio was highly consistent with a range of only ±3.5%. A dark run gave very small hydrogen yields corresponding to apparent quantum yields of only 0.1% of those in the photolyses, thus eliminating thermal reactions as the causative factor in the quantum yield variations. The variability in quantum yields continued when C_2D_6 was substituted for CH_3CD_3. The various actinometers were in close agreement indicating stability in the optical and analytical systems. Subsequent experiments with Br_2/HBr = 5 gave excellent agreement between quantum yields. The initial variability in the yields was probably associated with problems in the absolute yield analysis rather than spurious kinetic processes at the lower Br_2/HBr ratio.
(14) Where only ratios of rates are of interest, as in eq 17–19 and 21 and Tables III–V, the R's for rates have been dropped to simplify the notation. For example, in eq 16 R_{HBr} refers to the rate of formation of H_2 *or* HD due to reaction of hot atoms from HBr. In eq 17 the products are specified and $[R_{H_2(s)}/R_{HD}]_{C_2D_6}$ can be simplified to $[H_2(s)/HD]_{C_2D_6}$. Also the quantum yield notation is dropped where only product ratios were determined, so that $[\varphi'_{H_2}(e)/\varphi'_{HD}]_{C_2D_6}$ of eq 14 becomes $[H_2'(e)/HD']_{C_2D_6}$.
(15) Hong and Mains used the photodissociation of HI at 254 nm as the hot atom source. HI photodissociation produces both $I(^2P_{3/2})$ ground state and $I^*(^2P_{1/2})$ first excited state with 0.94 eV, the latter reducing the H* energy by this amount. R. D. Clear, S. J. Riley, and K. R. Wilson, *J. Chem. Phys.*, **63,** 1340 (1975), found 36 ± 5% $I^*(^2P_{1/2})$ production at 266 nm, and predicted that the percent I* increases with decreasing wavelength reaching a maximum of about 50% at about 250 nm and decreasing at lower wavelengths. Assuming 50% I* production at 254 nm, the average H* energy will be 1.4 eV.
(16) The authors regret that the comparison of IRP's from ref 8 and 9 was inadvertently omitted from ref 9.
(17) (a) R. A. Fass, *J. Phys. Chem.*, **74,** 984 (1970); (b) R. A. Fass, J. W. Hoover, and L. M. Simpson, *ibid.*, **76,** 2801 (1972).
(18) (a) R. R. Williams and R. A. Ogg, Jr., *J. Chem. Phys.*, **13,** 586 (1945); (b) H. A. Schwartz, R. R. Williams, Jr., and W. H. Hamill, *J. Am. Chem. Soc.*, **74,** 6007 (1952).
(19) (a) J. L. Holmes and P. Rogers, *Trans. Faraday Soc.*, **64,** 2348 (1968); (b) R. Penzhorn and B. de B. Darwent, *J. Phys. Chem.*, **72,** 1639 (1968).
(20) J. M. White and H. Y. Su, *J. Chem. Phys.*, **57,** 2344 (1972).
(21) Another way to approach the error due to the mixed scavenger effect is to consider the quantum yields. In the present work at 1.6 eV (Table II), about 20% of the H atoms react with 94% CH_3CD_3, leaving 80% to react with the scavengers. Using the unmoderated $k^*_{I_2}/k^*_{HI}$ ratio of 4 and I_2/HI ratio of 2.3, about 10% of these would react HI, giving a $\varphi_{HI} \simeq 8\%$, and a H_2/HD ratio of about 3.7. With the photolysis of HI at 254 nm giving 50% 0.9-eV H* atoms and 50% 1.8-eV H* atoms, the yields with CH_3CD_3 will be lower, and the H_2/HD ratio correspondingly higher. Use of the unmoderated $k^*_{I_2}/k^*_{HI}$ ratio exaggerates the effect, but note that the $k^*_{Br_2}/k^*_{HBr}$ ratio found in the present work in 94% CH_3CD_3 is closer to the unmoderated value than to the thermal value.
(22) J. M. White, *J. Chem. Phys.*, **58,** 4482 (1973).
(23) R. M. Martin and J. E. Willard, *J. Chem. Phys.*, **40,** 3007 (1964).
(24) P. J. Kuntz, E. M. Nemeth, J. C. Polanyi, and W. H. Wong, *J. Chem. Phys.*, **52,** 4654 (1970).
(25) R. G. Gann, W. M. Ollison, and J. Dubrin, *J. Am. Chem. Soc.*, **92,** 450 (1970).
(26) E. Tachikawa and F. S. Rowland, *J. Am. Chem. Soc.*, **90,** 4767 (1968).
(27) S. Chapman, T. Valencich, and D. L. Bunker, *J. Chem. Phys.*, **60,** 329 (1974).
(28) T. Shimanouchi, *Natl. Stand. Ref. Data Ser., Natl. Bur. Stand.*, **No. 6,** (1967).

Direct Measurement of Intramolecular Proton Transfer in the Excited State of 2,4-Bis(dimethylamino)-6-(2-hydroxy-5-methylphenyl)-*s*-triazine with Picosecond Pulses

H. Shizuka,* K. Matsui,

Department of Chemistry, Gunma University, Kiryu Gunma 376, Japan

Y. Hirata, and I. Tanaka

Department of Chemistry, Tokyo Institute of Technology, Meguro-ku, Tokyo, Japan *(Received March 5, 1976)*

Publication costs assisted by Gunma University

Intramolecular proton transfer in the excited state of 2,4-bis(dimethylamino)-6-(2-hydroxy-5-methylphenyl)-*s*-triazine (TH) has been measured by means of picosecond spectroscopy. The lifetime of the excited singlet of TH (enol form) τ_{S_1} and the rate constant k_{PT} for the proton transfer in the S_1 state in cyclohexane at 298 K were 6.3×10^{-11} s and 1.1×10^{10} s^{-1}, respectively.

Introduction

Proton transfer in the excited state is one of the elementary processes in photochemistry. However, no rate constants for intra- and intermolecular proton transfers have, until recently, been reported. El-Bayoumi, Avouris, and Ware[1] have measured the rate constant for intermolecular proton transfer in the excited state of the 7-azaindole (7AI) hydrogen bonded dimer with nanosecond time resolution. Since double proton transfer in the excited dimer of 7AI is too fast to be followed at room temperature, the study was performed at 77 K. A deuterated sample of 7AI was used to further slow down the intermolecular proton transfer, whose rate constant is 1.9×10^8 s^{-1} at 77 K. They suggest that the proton transfer at 77 K occurs via quantum mechanical tunneling.

In a previous paper,[2] we showed that a rapid deactivation process competing with intramolecular proton transfer exists in the excited TH at higher temperatures (>230 K). This fact prompted us to measure the rate constant k_{PT} for intramolecular proton transfer in the S_1 state of TH at room temperature. This paper reports the absolute value of k_{PT} in cyclohexane at 298 K determined by picosecond spectroscopy. What makes the intramolecular proton transfer fast in the S_1 state is also discussed.

Experimental Section

The picosecond optical measurements were performed using a mode-locked ruby laser system. A train of about 20 pulses, separated by the laser cavity round trip time, i.e., 10 ns, was produced at the output of the oscillator. The pulse width was measured by the two photon fluorescence method,[3] using a methanol solution of rhodamine 6G and the pulse width was determined to be 15 ps. A single optical pulse was taken from the pulse train and the pulse passed through an amplifier ruby rod 160 mm in length, which enhanced the intensity by about 50-fold. The pulse (694.3 nm) was split into two beams. One was frequency doubled to obtain the wavelength of 347.2 nm using a phase matched ADP crystal 20 mm in length. The fundamental light was removed with a band pass filter (Tohshiba UVD 1A), and the second harmonic pulse of about 0.5 mJ excited the sample. The other was focused into a cell containing CCl_4 in which the picosecond continuum was generated. After removal of the incident ruby laser by a glass filter, the continuum was used as a probing light. Time-resolved induced emission spectra were measured with optical delay lines and analyzed by the photographic method.[4]

The preparation and purification of materials were described previously.[2,5] A thin cell 3 mm in length was used and a cyclohexane solution of TH (4×10^{-4} M) was degassed by the freeze–pump–thaw method.

Results and Discussion

Figure 1 shows the transient absorption spectrum (a) and the induced emission spectrum (b) of the cyclohexane solution of TH (4×10^{-4} M) at 298 K, taken 200 ps after excitation. Measurements of the buildup of the induced emission were carried out at 520 nm. Figure 2 shows the values of $\Delta OD(t)/\Delta OD(\infty)$ as a function of delay time t, where the intensity of induced emission is presented in optical density units. The value of $\Delta OD(\infty)$ was determined by averaging data over the range 120 ps $\leq t \leq$ 500 ps for each shot and $\Delta OD(t)$ is the intensity of the induced emission at t ps after excitation. The induced emission spectrum (Figure 1b) was very similar to that of spontaneous emission from the proton-transferred excited TH(S_1'), indicating that the induced emission occurs from the S_1' state. The buildup time of the transient absorption band (λ_{max} 433 nm) was about 120 ps. The buildup curve of the absorption band could not be measured accurately because of its low intensity. Judging from the buildup time of the transient absorption band, it was assigned to the electronic transition $S_n' \leftarrow S_1'$ (see Figure 3).

Under these measurement conditions, only amplification occurred; there was no laser oscillation or superradiance.

Thus, the experimental results can be accounted for by the scheme shown in Figure 3. We assume that the S_1' state has a significantly greater transition probability to S_0' at 520 nm than that of $S_n \leftarrow S_1$. The intensity of induced emission $|\Delta OD(t)|$ at t ps after excitation can be expressed by

$$|\Delta OD(t)| \propto B[S_1']_t \qquad (1)$$

where B is the Einstein transition probability for absorption ($S_1' \leftarrow S_0'$), and $[S_1']_t$ denotes the concentration of the S_1' state of TH at t ps after excitation. The value of $|\Delta OD(t)|$ is proportional to that of $[S_1']_t$. The production of S_1' is related to

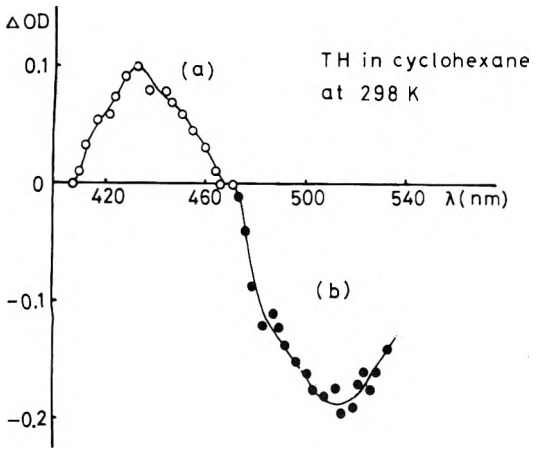

Figure 1. The transient absorption spectrum (a) and the induced emission spectrum (b) of a cyclohexane solution of TH (4×10^{-4} M) at 298 K taken 200 ps after excitation.

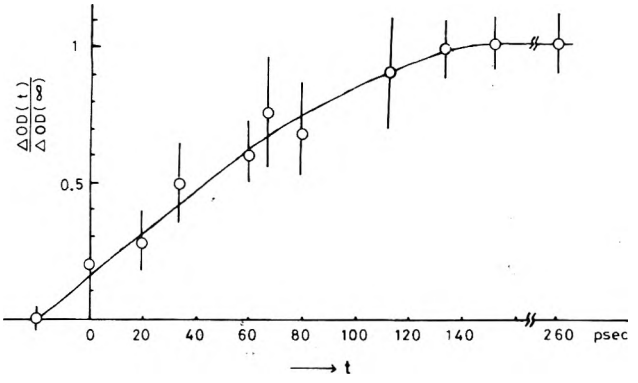

Figure 2. The S_1' state formation, $\Delta OD(t)/\Delta OD(\infty)$ vs. delay time t in cyclohexane at 298 K.

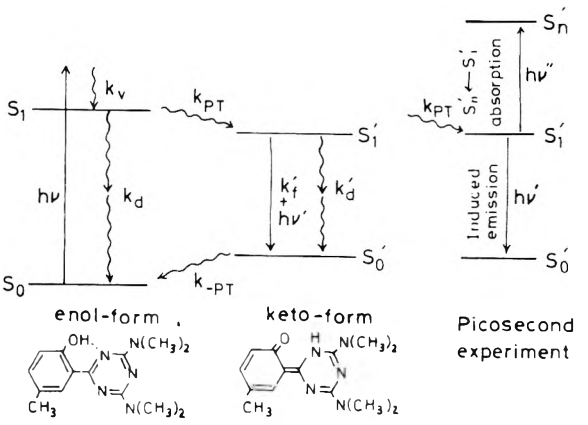

Figure 3. A schematic energy state diagram for the intramolecular proton transfer in excited TH.

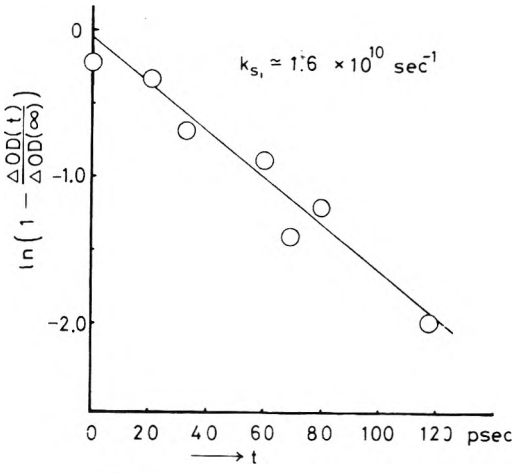

Figure 4. A plot of $\ln\{1 - \Delta OD(t)/\Delta OD(\infty)\}$ vs. t.

the decay of the S_1 state (the excited enol form of TH, see Figure 3), and the following can be also obtained:

$$[S_1]_t \propto 1 - \frac{\Delta OD(t)}{\Delta OD(\infty)} \tag{2}$$

If we further assume an exponential decay of S_1 whose decay constant is k_{S_1}, eq 3 is derived from eq 2:

$$\ln\left\{1 - \frac{\Delta OD(t)}{\Delta OD(\infty)}\right\} = -k_{S_1}t + \text{constant} \tag{3}$$

The plot of $\ln\{1 - \Delta OD(t)/\Delta OD(\infty)\}$ vs. the delay time t is shown in Figure 4. The value of k_{S_1} can be obtained from the slope of the linear plot.

$$k_{S_1} \simeq 1.6 \times 10^{10}\ s^{-1} \tag{4}$$

From Figure 3, k_{S_1} is given by

$$k_{S_1} = k_{PT} + k_d \tag{5}$$

where k_{PT} and k_d are the rate constants for the intramolecular proton transfer and the deactivation process in the S_1 state, respectively. The ratio of k_d/k_{PT} is equal to 0.45.[2] Thus, the values of k_{PT} and k_d in cyclohexane at 298 K can be determined:

$$\begin{aligned} k_{PT} &\simeq 1.1 \times 10^{10}\ s^{-1} \\ k_d &\simeq 0.5 \times 10^{10}\ s^{-1} \end{aligned} \tag{6}$$

The lifetime of S_1 is then derived from eq 4.

$$\tau_{S_1} = k_{S_1}^{-1} = 6.3 \times 10^{-11}\ s \tag{7}$$

The value of τ_{S_1} becomes very small due to the radiationless transition via the photochemical channel (the intramolecular proton transfer process). A similar situation to this has been shown in the excited 9,10-dimethylenebianthracene.[8] However, the lifetime of S_1 is long enough to relax an excess vibrational energy of S_1 to a Boltzmann distribution, since the vibrational relaxation times in condensed media are the order of 10^{-12} s.[6,7] It has been experimentally shown that the intramolecular proton transfer in excited TH originates from the vibrationally relaxed S_1 state.[2]

The following data are also known:[2] (1) the enthalpy change ΔH^* between S_1 (enol form) and S_1' (keto form) in TH is large enough to prevent the reverse proton transfer $S_1 \leftarrow S_1'$, and (2) the values of Φ_f', τ_f' and $\tau_f'k_f'$ in degassed nonpolar solvents at 298 K are 0.38, 5 ns, and 0.55, respectively, where Φ_f' is the spontaneous fluorescence quantum yield from S_1', τ_f' is the observed lifetime of S_1', and k_f' is the natural radiative rate constant from S_1' to S_0'.

The value of k_{PT} in the S_1 state of TH at 298 K is about a factor of 100 greater than that of the excited 7AI hydrogen bonded dimer at 77 K. This difference may be attributed to the facts that the proton transfer in the former occurs via a potential barrier between S_1 and S_1' and in the latter case occurs via a quantum mechanical tunneling.[1] The reasons the k_{PT} in the excited TH at 298 K is very fast can be explained as follows:

(1) The intramolecular hydrogen bond between proper atoms is formed in the ground state S_0.[9] This favors proton transfer in the excited state.

(2) The migration of the π electron from the oxygen atom to the benzene ring takes place in the S_1 state, resulting in an increase in acidity on the oxygen atom (the π-formal charge is +0.2668).[2]

(3) The electron pair at the proper nitrogen atom in the triazine nucleus is localized as a proton acceptor.[10]

(4) Furthermore, the basicity of the nitrogen atom is increased in the S_1 state (the π-formal charge is −0.4084).[2]

In conclusion, the absolute value of intramolecular proton transfer in excited TH in cyclohexane at 298 K was determined to be 1.1×10^{10} s^{-1} by picosecond spectroscopy.

Acknowledgment. H.S. is grateful to the Ministry of Education of Japan for a Scientific Research Grant-in-Aid.

References and Notes

(1) M. A. El-Bayoumi, P. Avouris, and W. R. Ware, *J. Chem. Phys.*, **62**, 2499 (1975).
(2) H. Shizuka, K. Matsui, T. Okamura, and I. Tanaka, *J. Phys. Chem.*, **79**, 2731 (1975), and references cited therein.
(3) J. A. Giordmaine, P. M. Rentzepis, S. L. Shapiro, and K. W. Wecht, *Appl. Phys. Lett.*, **11**, 216 (1967).
(4) E.g., D. Magde and W. Windsor, *Chem. Phys. Lett.*, **27**, 31 (1974).
(5) H. Shizuka, T. Kanai, T. Morita, Y. Ohto, and K. Matsui, *Tetrahedron*, **27**, 4021 (1971); Y. Ohto, H. Shizuka, S. Sekiguchi, and K. Matsui, *Bull. Chem. Soc. Jpn.*, **47**, 1209 (1974).
(6) A. Laubereau, D. von der Linde, and W. Kaiser, *Phys. Rev. Lett.*, **28**, 1162 (1972).
(7) J. E. Griffiths, M. Clerc, and P. M. Rentzepis, *J. Chem. Phys.*, **60**, 3824 (1974).
(8) H. Shizuka, Y. Ishii, M. Hoshino, and T. Morita, *J. Phys. Chem.*, **80**, 30 (1976).
(9) Y. Ohto, Y. Hashida, S. Sekiguchi, and K. Matsui, *Bull. Chem. Soc. Jpn.*, **47**, 1301 (1974).
(10) A similar explanation has recently been made for the proton transfer in the ground state by Kresge: A. J. Kresge, *Acc. Chem. Res.*, **8**, 354 (1975), and many references cited therein.

Reaction Intermediates Produced in 2-Methyltetrahydrothiophene and Its Solutions in 2-Methyltetrahydrofuran by γ Radiolysis and Photolysis at 77 K[1,2a]

G. Charles Dismukes and John E. Willard*

Department of Chemistry, University of Wisconsin, Madison, Wisconsin 53706 *(Received April 21, 1976)*

Publication costs assisted by the U.S. Energy Research and Development Administration

The optical and ESR spectra of the trapped intermediates produced by γ irradiation of the cyclic thioether 2-methyltetrahydrothiophene (MTHT) in the glassy state at 77 K have been investigated for the purpose of comparing the radiation chemistry of MTHT with that of the much studied oxygen analogue 2-methyltetrahydrofuran (MTHF). The MTHT, in contrast to MTHF, does not physically trap electrons. The electrons react with the MTHT producing a product or products, with a broad absorption at 460 nm, assigned to paramagnetic anions such as $CH_3CH_2CH_2CH_2\dot{C}HS^-$ or $CH_3CH_2CH_2\dot{C}(CH_3)S^-$. A band centered at 625 nm, which is reduced by positive charge scavengers, is attributed to the cation radical of MTHT. Both the ESR and optical spectra show selective bleaching effects with near-ultraviolet and visible light. The products of γ radiolysis of solutions of 10% of MTHT in MTHF glass reveal both the electron scavenging ability of MTHT and positive charge stabilization by MTHF. Photolysis of MTHT glass at 254 nm produces thiyl radicals. Photoionization of tetramethyl-*p*-phenylenediamine (TMPD) in MTHT glass is accompanied by formation of MTHT radicals.

Introduction

2-Methyltetrahydrofuran (MTHF, I) glass at 77 K and below has been extensively used as a matrix for the study of trapped electrons (e_t^-) produced by γ radiolysis and by photoionization of solutes.[3] Unlike the broad nonstructured optical absorption bands of e_t^- in glassy hydrocarbons, the e_t^- absorption in MTHF at 77 K shows peaks (at 1180 and 1375 nm) and a shoulder (at 1000 nm). This implies trapping sites of different favored energies which depend on the orientation

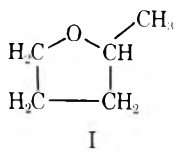

I

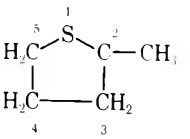

II

of MTHF molecules, or, possibly, the existence of bound excited states of the traps. The present work was initiated to determine whether 2-methyltetrahydrothiophene (MTHT, II), which has a sulfur atom in place of the oxygen of the MTHF ring, would trap electrons in the glassy state and, if so, whether their spectrum would yield further information on the nature of trapping sites. The results, presented here, show that MTHT glass does not trap electrons, but give information on its radiation chemistry and the relation of this chemistry to that of MTHF,[3] solutions of MTHT in MTHF, and adamantane solutions of MTHT and MTHF.[4]

Experimental Section

Reagents. 2-Methyltetrahydrothiophene (MTHT) was synthesized[5] from 1,4-dibromopentane and sodium sulfide, purified by fractional distillation, and stored over activated

type 3A molecular sieve in a glass bulb with Teflon stopcock. It was degassed to $<10^{-5}$ Torr while still fluid, at 200 K. The absorption spectra from 210 to 400 nm and from 15 to 30 μ and the mass spectrum were identical with those previously reported.[6] Both gas chromatography, using a column of Carbowax 1540 on Chromosorb P with thermal conductivity detection, and thin-layer chromatography on silica gel with hexane as the solvent showed only one component present. The proton NMR spectrum was consistent with that expected for MTHT by comparison with the spectra of MTHF and tetrahydrothiophene (THT).

2-Methyltetrahydrofuran (Aldrich Chemical Co.) contained water, 2-methylfuran, 2-methyldihydrofurans, and 1% of hydroquinone antioxidant. Purification methods described in the literature[7] did not remove the 0.1% olefinic ether impurities. We have used two methods to reduce all of the contaminents noted above to below the detectability limits of the optical and gc analyses. (1) The commercial MTHF was passed through a column of alumina which had been activated at 425 °C, and was then subjected to preparative gas chromatography, using a column of Ucon-50 on Chromosorb P. (2) Larger quantities were prepared by a sequence of refluxing for 3 days under bubbling nitrogen to remove the more volatile impurities, passage through a column of freshly activated alumina with collection in a nitrogen atmosphere, and fractional distillation through a column of stainless steel helices. Figure 1 shows the effects of treatments of this type on the ultraviolet absorption spectrum of the MTHF. The purified MTHF was stored over NaK alloy in glass bulbs with Teflon stopcocks after degassing to $<10^{-5}$ Torr at 200 K. Aldrich tetrahydrothiophene (THT) was fractionally distilled through stainless steel helices. The fraction boiling at 118 °C was used after degassing at 200 K to 10^{-5} Torr. Chemically purified and recrystallized *N,N,N′,N′*-tetramethyl-*p*-phenylenediamine was sublimed under vacuum before use.

Sample Preparation and Irradiation. The purified MTHT, MTHF, and THT were prepared for optical and ESR studies by vacuum distillation from the storage flasks to Suprasil cells, followed by degassing at 200 K to $<10^{-5}$ Torr and sealing at 77 K. The optical cells were 1 cm × 1 cm or 1 cm × ~0.1 cm in cross section, and the ESR tubes 2 or 3 mm i.d. γ-Irradiations were made with a ^{60}Co source, with the sample under liquid nitrogen. Dose rates ranged from $\sim 3 \times 10^{18}$ to 6×10^{18} eV g^{-1}.

Light Sources. A 1000-W tungsten projector lamp with two Corning 7-56 filters gave ~30 mW cm^{-2} of bleaching light at wavelengths >900 nm, and with 1-75 and 0-51 Corning filters plus 1 cm of water gave ~30 mW cm^{-2} in the 360–900-nm range. An Osram 200-W superpressure mercury lamp, filtered by a 1.4-cm thickness of Corning 7-54 glass and a solution of 0.2 M $NiSO_4$ and 0.005 M $CuSO_4$ gave ~20 mW cm^{-2} of light between 270 and 360 nm. A Vycor spiral low-pressure mercury lamp gave ~80 mW cm^{-2} in the center of the spiral of which 72% was at 254 nm and none below 200 nm. The light intensities at the sample positions were measured with a thermopile power meter.

Optical and ESR Absorption Measurements. A Cary Model 14R spectrophotometer was used to measure optical absorption spectra, with the samples under liquid nitrogen. The samples could be rotated through 90° for exposure to bleaching light through a hole in the side of the analysis chamber, and then rotated back 90° for analysis.

ESR measurements were made in the X-band with a Varian E-15 or 4502 spectrometer using 100-kHz field modulation, and a V-4531 type cavity with a slotted window allowing 50% transmission of light onto the sample or with an open piece of p-band wave guide projecting from the front of the cavity to allow 100% light transmission. Microwave powers were measured with a Hewlett-Packard 431-C power meter. The samples were at 77 K under liquid nitrogen in a Suprasil ESR dewar, or at ≥83 K in a Varian variable temperature controller. A copper–constantan thermocouple internally referenced to a digital thermocouple meter was used for temperature measurements. ESR g value measurements were made relative to the silica radical signal produced in the γ-irradiated sample tubes, using $g = 2.0009$ for the prominent high-field peak.[8]

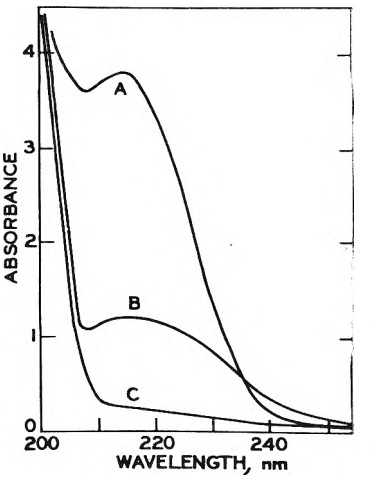

Figure 1. Spectrum of MTHF following different purification steps. (A) Commercial MTHF after removal of water and stabilizer by passage through freshly activated alumina. (B) Commercial MTHF refluxed for 3 days while bubbling N_2 through the liquid, and passed through alumina. (C) Sample B after fractional distillation through an 18-in. column of stainless steel helices.

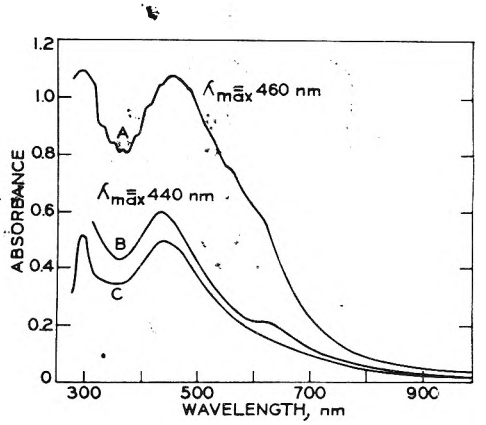

Figure 2. Optical spectrum of γ-irradiated MTHT glass at 77 K: (A) immediately following dose of 1.6×10^{19} eV g^{-1}; (B) following partial bleaching of sample A with ~30 mW cm^{-2} of 365–900-nm light from filtered tungsten source; (C) after additional bleaching. Cell path ~0.1 cm.

Results

Optical Absorption of γ-Irradiated MTHT Glass. γ-Radiolysis of MTHT glass at 77 K produces absorption bands with maxima at 300 and 460 nm (Figure 2) with no absorption between 1100 and 2200 nm. Poorly resolved small peaks are superimposed on the dominant spectrum every 1400 cm^{-1} between 325 and 625 nm. Warming of the sample to room temperature and recooling to 77 K removes all of the absorption. Bleaching with 360–900-nm light reduces the ab-

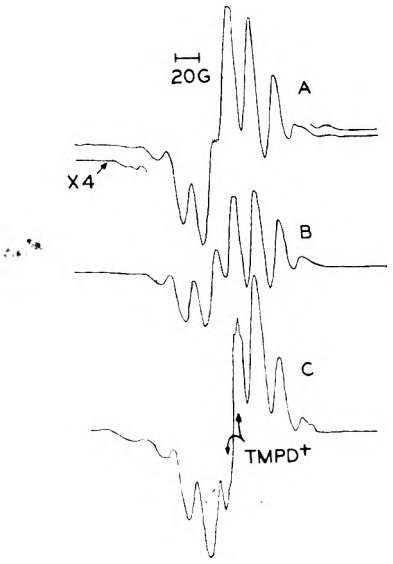

Figure 3. ESR spectrum of irradiated MTHT glass at 77 K: (A) immediately after γ irradiation; (B) after 7.5 min bleaching of sample A with ~30 mW cm^{-2} of 360–900-nm light which caused a 40% decrease in the integrated ESR absorption. Dose, 3.3×10^{19} eV g^{-1}; microwave power, 0.5 mW; modulation amplitude, 2 G; gain, 320; recorder, 0.6 V. (C) After photoionization of 5×10^{-4} M TMPD in MTHT glass at 77 K. 40 min at ~20 mW cm^{-2} with quartz-jacketed AH4 medium-pressure Hg lamp; microwave power, 0.2 mW; modulation amplitude, 2 G; gain, 500; recorder, 120 mV.

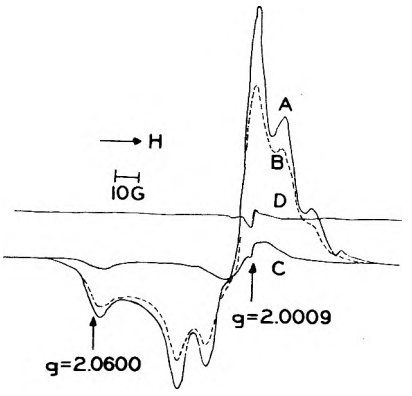

Figure 4. (A) ESR spectrum of MTHT glass at 77 K following 254-nm photolysis for 28 min with spiral Vycor low-pressure Hg lamp. (B, C, D) Successive scans as the sample warmed up following emptying of liquid nitrogen from the ESR dewar. Microwave power, 0.5 mW; modulation amplitude, 2 G; gain, 1×10^3 except (D) which is 2.5×10^3; recorder, 1 V. The g markers indicate the positions of the ESR signal induced in Suprasil ($g = 2.0009$), and the signal of the $CH_3S\cdot$ radical ($g = 2.0598$). The baseline in scan D is shifted upward.

sorption from both bands and reveals a weaker band peaking at 625 nm. The 460-nm band shifts considerably to the blue during this treatment.

ESR Spectrum of γ-Irradiated MTHT Glass. The initial ESR spectrum from MTHT glass γ irradiated at 77 K has at least nine hyperfine lines separated by 18–19 G (Figure 3A), with further poorly resolved structure on the wings. There is no evidence for the narrow singlet signal of trapped electrons even at powers as low as 0.001 mW and high sensitivity. The spectrum bleaches with light between 360 and 900 nm to 60% of its initial intensity, accompanied by loss of some of the structure and a change in relative peak heights (Figure 3B). The remaining seven-line spectrum continues to diminish on further bleaching, but with little additional change in structure, indicating the presence of a single radical after this bleaching treatment.

ESR Spectrum of Photolyzed MTHT Glass. The ESR spectrum of MTHT glass resulting from photolysis at 77 K with the Vycor low-pressure Hg lamp (predominately 254 nm), shown in Figure 4, is completely different from the spectrum caused by γ irradiation. The absorption near $g = 2.055$ is characteristic of thiyl radicals ($g = 2.0598$ for $CH_3S\cdot$)[9a] and the absorption centered at $g = 2.002$ is probably the carbon radical which also forms during ring rupture.

Optical Absorption of γ-Irradiated 9.5% MTHT in MTHF at 77 K. MTHT and MTHF are miscible in all proportions. γ-Irradiation of a glass containing 9.5 mol % MTHT in MTHF at 77 K produces the absorption shown in Figure 5, and on an expanded scale in Figure 6A. In addition to the peak at 460 nm produced in pure MTHT, and one at 320 nm shifted from 300 nm in pure MTHT, there is a broad structured peak centered at ~1200 nm and extending from <600 to ~2100 nm. The latter is characteristic of trapped electrons (e_t^-) in MTHF glass,[3] and indicates that electrons in the MTHT–MTHF mixture are trapped in environments not appreciably different from those in pure MTHF. The width of this peak is the same

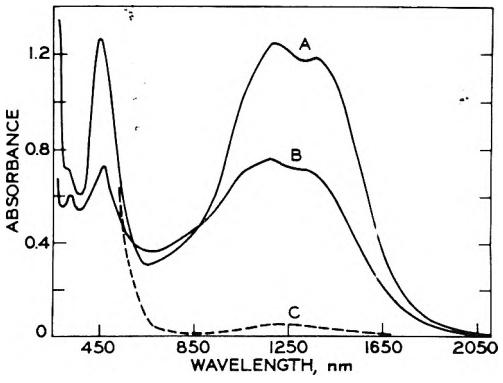

Figure 5. Optical spectrum at 77 K of γ-irradiated MTHF glass containing 9.5 mol % MTHT: (A) after dose of 9.1×10^{19} eV g^{-1}; (B) after dose of 2.9×10^{19} eV g^{-1}; (C) Sample A after exhaustive bleaching with light of >900 nm. Light path 0.16 cm. The spectrum of ir bands of the unirradiated glass has been subtracted in each case.

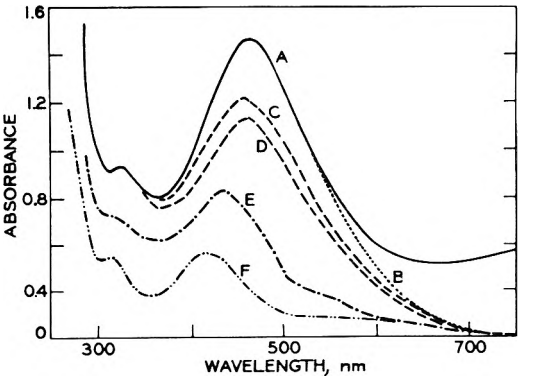

Figure 6. Optical spectrum at 77 K of γ-irradiated MTHF glass containing 9.5 mol % MTHT. Dose, 9.1×10^{19} eV g^{-1}. (A) Initial. (B) Following bleaching with filtered tungsten light of >900 nm (~30 mW cm^{-2}). (C and D) Following successive additional bleachings with 360–900-nm light (~30 mW cm^{-2}). (E) After additional bleaching with 270–360-nm light (~20 mW cm^{-2}). (F) After additional bleaching with unfiltered tungsten light (~200 mW cm^{-2}). Light path 0.16 cm.

as observed for e_t^- in pure MTHF. The absorption which increases steeply with decreasing wavelengths below 310 nm appears to be assignable to the tertiary α radical of MTHF on the basis of studies[10] in pure MTHF.

The ratio of the intensity of the 320-nm peak relative to the 460-nm peak is much lower for the solution of MTHT in MTHF than the ratio of the 300-nm peak to the 460-nm peak in pure MTHT (Figures 2 and 5). The 320- and 460-nm peaks thus appear to be due to different trapped species.

The absorbance at the 460-nm peak is 0.5 times as great as that of the same peak in MTHT at an equal γ dose (after subtracting the small absorption by e_t^- at this wavelength, which is known from independent measurements of the e_t^- spectrum in MTHF). Per molecule of MTHT, the yield of the 460-nm species is therefore 5 times greater in the mixture, indicating that during radiolysis energy absorbed by MTHF or charge separation produced within the MTHF is transferred to MTHT. In parallel with this increase in the intensity of the 460-nm peak per molecule of MTHT, the yield of e_t^- per molecule of MTHF in the 90% MTHF mixture is reduced by a factor of 5 relative to that in pure MTHF, as indicated by the absorbance at 1180 nm for equal doses and cell paths. The ratio of the effects was the same for both γ doses of Figure 5, i.e., the 460-nm and e_t^- bands grow in parallel with increasing γ dose.

An approximate extinction coefficient of 4×10^3 M^{-1} cm^{-1} at the maximum of the 460-nm band can be estimated if it is assumed that the lowering of the e_t^- concentration in the MTHT–MTHF mixture relative to the yield in pure MTHF is accompanied by an equivalent production of the 460-nm species in excess of the yield per MTHT molecule found in pure MTHT. This was determined using the data of Figure 5B, taking 1.7×10^4 cm^{-1} as the extinction coefficient of e_t^- in MTHF.[10] The concentration of e_t^- in the sample was 3×10^{-4} M whereas it would have been 1.5×10^{-3} M for the same dose to the MTHF in the sample (G = 2.6) if it was unaffected by the MTHT. From the estimated extinction coefficient of the 460-nm species (which is a lower limit) it may be estimated that the G value for the species in pure MTHT (Figure 2) is 4 (an upper limit).

Photobleaching of γ-Irradiated 9.5% MTHT in MTHF at 77 K. Figures 5 and 6B show that exhaustive bleaching of the e_t^- band in 9.5% MTHT–MTHF mixtures with light of wavelengths longer than 900 nm removes all e_t^-, but has no effect on the absorption below 550 nm. The spectra of Figures 5 and 6B for samples bleached at >900 nm show considerably lower absorption on the red tail of the 460-nm band than the spectra of γ-irradiated samples of pure MTHT, which are unaffected by light of such wavelengths. This difference in absorption has been determined by subtraction after normalization at 460 nm. Normalization at this wavelength appears reliable since infrared bleaching does not alter the absorbance in the glass below ~550 nm (Figure 6B). The result, plotted in Figure 7, indicates that there is a species with an absorption peaking at 625 nm which is present in the pure MTHT sample but not in the mixture after bleaching the e_t^-. This peak matches the position of the shoulder (Figure 2) revealed upon partial bleaching of the 460-nm band in pure γ-irradiated MTHT by visible light.

Figure 6 indicates that light of 360–900 nm bleaches the 460-nm band in the MTHT–MTHF mixture without affecting the 320-nm band. Light of 270–360 nm bleached both the 320- and 460-nm bands. Exposure to a tungsten lamp giving ~200 W cm^{-2} on the sample caused further bleaching, probably as a result of warming the matrix. A 42-nm blue shift in the original 460-nm peak resulted from these successive bleaching treatments.

Spectra Induced by Photolysis of TMPD in MTHT. Photolysis of a 5×10^{-4} M solution of TMPD in MTHT with the 270–370-nm light produced a large $TMPD^+$ optical absorption signal, but no other absorption between 350 and 1200 nm (Figure 8C). This spectrum is identical with the $TMPD^+$ spectrum in a variety of other organic glasses.[11] The ESR spectrum produced by a similar illumination (Figure 3C) consists of a narrow $TMPD^+$ signal superimposed on a broader signal of a radical resembling that produced from MTHT by γ radiolysis.

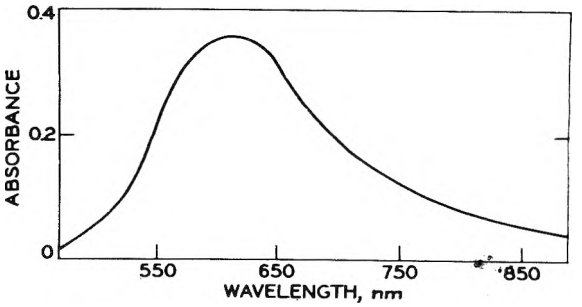

Figure 7. Difference in absorption of γ-irradiated MTHT and 9.5% MTHT–MTHF at 77 K (Figure 2 minus Figure 6B normalized at 460 nm) after exhaustive ir bleaching of e_t^- in the MTHT–MTHF sample at >900 nm. Light path ~0.1 cm.

Optical Absorption of γ-Irradiated TMPD–MTHT. γ-Radiolysis of a solution of 5×10^{-4} M TMPD in MTHT at 77 K to a dose of 9.1×10^{19} eV g^{-1} produced the optical absorption shown in Figure 8A, which changed to that of 8B on partial bleaching with filtered tungsten light of wavelength >422 nm. In addition to the $TMPD^+$ band the 460-nm band found in MTHT and in 9.5% MTHT–MTHF is present in high yield. However, the absorbance at 700 nm and above and near 360 nm is considerably lower relative to the 460-nm peak in the TMPD-containing sample than in pure MTHT (Figures 2A and 8A when normalized at 460 nm following subtraction of the $TMPD^+$ absorption reveal these marked differences). Measurements below 360 nm could not be made due to the interfering absorbance by TMPD. The decreased absorbance at 700 and 360 nm relative to 460 nm indicates that the species produced by γ radiolysis of pure MTHT, which have absorption maxima at 625 and 300 nm, are substantially absent in γ-radiolyzed solutions of MTHT containing a low concentration of TMPD.

Discussion

Absence of Physical Trapping of Electrons in MTHT. The initial goal of this work was to determine whether electrons produced by γ radiolysis of MTHT glass become physically trapped. That they do not is shown by the absence of both the narrow ESR singlet and the near-infrared absorption band which are characteristic of e_t^- in other organic glasses.

Assignment of the 460-nm Band. The absorption band peaking at 460 nm in γ-irradiated pure MTHT glass (Figure 2) must be a composite of absorptions by several species. The appearance of a pronounced shoulder at 625 nm and the substantial blue shift (both as a result of bleaching with visible light) indicate the complexity of the band.

The poorly resolved small peaks between 325 and 625 nm on curve A of Figure 2 appear to be due to vibrational structure from the predominant 460-nm species. Since the electronic transition presumably involves the sulfur atom, it is plausible that carbon–sulfur vibrational or bending modes account for the substructure. The uniform 1400-cm^{-1} separation is close to the vibrational frequency of a carbon–sulfur double bond (the C=S vibration in propanethione is 1269

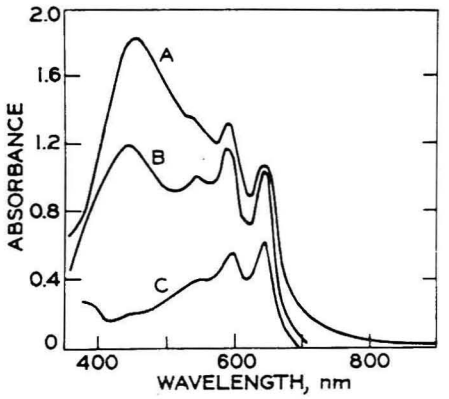

Figure 8. Optical spectra induced by γ irradiation and by photoionization in MTHT glass containing 5×10^{-4} M TMPD at 77 K. (A) After γ dose of 9.1×10^{19} V g^{-1}. (B) After partial bleaching of sample A with wavelengths >420 nm from tungsten lamp. (C) $TMPD^+$ spectrum produced by 1 min exposure of fresh sample to 270–370-nm light (~20 mW cm^{-2}). The light paths of all samples were 0.1 cm. The observed absorbances of (C) have been multiplied by 2 for convenient plotting.

cm^{-1}).[12] The unusually long progression of the bands in Figure 2 implies a substantially different geometry for the excited state than the ground state.

The lower yield of e_t^- in the MTHT–MTHF mixture than in pure MTHF implies that the MTHT reacts with electrons in competition with their trapping in MTHF, while the higher yield of the 460-nm species per molecule of MTHT in the mixture than in pure MTHT strongly suggests that this electron scavenging reaction produces the 460-nm species. If this conclusion is correct, the MTHT must capture the electrons before they are thermalized, i.e., at energies of several tenths of an electron volt or higher. This follows from the observation that neither low energy electrons produced by photoionization of TMPD in MTHT or by photobleaching of e_t^- in MTHT–MTHF mixtures produce the 460-nm species. It is known that mercaptans and disulfides undergo dissociative capture in the gas phase with thresholds >0.35 eV.[13] They form three types of products, of which the analogues that could be formed by electron capture by MTHT are:

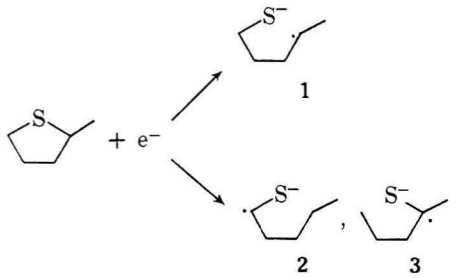

The paramagnetic anions of type **2** or **3** would be expected to have properties consistent with those of the species which accounts for the major absorption at 460 nm. No electronic absorption data were found in the literature for radicals of type **2** or **3**, or for the isoelectronic radical RR'ĊCl (R = CH_3, H) which probably has a similar spectrum. A less suitable analogue is the molecule $(CH_3)_2C{=}S$ for which λ_{max} is at 499 nm.[14] The low oscillator strengths for n → π^* transitions in thioketones yield extinction coefficients in the range of 10 to 100 M^{-1} cm^{-1},[14] appreciably below the estimated value of 4×10^3 M^{-1} cm^{-1} for the 460-nm band. However, radical **2** or **3** may be expected to have a higher value than the thioketones because of greater $\pi \rightarrow \pi^*$ character than for the nonbonding electrons in thioketones. This is a result of the π overlap between sulfur and the trigonal carbon, which produces a bond of partial double bond character as affected by the electron delocalization from sulfur to carbon. The existence of the double bonded nature of radical **2** or **3** is supported by the evidence for a double bond C to S species implied from the resolved vibrational structure on the 460-nm band.

$MTHT^-$, the molecular anion radical, appears less probable than a ring-opened radical anion (**2** or **3**) as the species responsible for the 460-nm absorption. If MTHT could form stable $MTHT^-$ by electron attachment in the glass, the process might be expected to have a low energy barrier, allowing it to occur with mobile electrons produced by the photoionization of TMPD and by photodetrapping of e_t^- from the γ-irradiated MTHT–MTHF matrix. Also, the ring opened structure seems most consistent with the structure and λ_{max} of the 460-nm band, on comparison with the vibrational structure and λ_{max} of thioketones.

The experiment in which MTHT containing 5×10^{-4} M TMPD was γ irradiated shows that the presence of this hole scavenger has little influence on the yield of the 460-nm species yield, although it appreciably reduces the absorption at 700 nm (vide infra). The indication is that the 460-nm band is not derived from a cationic precursor.

The optical absorption maxima of the radical cation of alkyl disulfides occur at longer wavelengths than the maxima for the corresponding radical anions.[15] For *n*-amyl disulfide these wavelengths are 780 and 420 nm, respectively. It is interesting to note that the 460-nm band attributed above to an anion radical in MTHT falls in a similar relation to the 625-nm band, which is attributed below to the MTHT cation radical.

Assignment of the 625-nm Band. Three lines of evidence imply the existence of an unresolved band on the red side of the 460-nm peak, due to another trapped species produced by radiolysis. Each is consistent with assignment of this band to the MTHT cation radical. These observations are: (1) During photobleaching the λ_{max} at 460 nm shifts toward the blue and an absorption with λ_{max} at 625 nm is revealed; (2) The absorbance induced at 625 nm per unit energy absorbed during γ irradiation of a 10% MTHT–MTHF mixture (Figure 6) is much less than that induced by irradiation of pure MTHT (Figure 2), in contrast to the yield of the 460-nm species, which is greater in the mixture. Subtraction of curve B of Figure 6 from curve A of Figure 2, after normalization at the 460-nm peak yields the difference spectrum, which is plotted in Figure 7 and reveals a spectrum peaking at 625 nm for a species present in γ-irradiated MTHT; (3) The yield of a species absorbing at 700 nm is much less in MTHT containing TMPD than in pure MTHT. This is shown by subtracting the spectrum of Figure 8A from that of Figure 2A after first subtracting the overlapping $TMPD^+$ spectrum and normalizing at 460 nm (to correct for the four-fold higher dose of the sample of Figure 8A).

Since it is known that glassy MTHF stabilizes positive charge against migration to solutes,[3,15,16] and that TMPD scavenges positive charge in several organic glasses (because of its relatively low ionization potential), the reductions in the yield of the 625-nm species by MTHF and TMPD, noted above, imply that the 625-nm species is positively charged. $MTHT^+$, the radical cation of MTHT, is formed by the action of the ionizing radiation on MTHT and it is plausible that this is responsible for the 625-nm absorption. ESR evidence indicates that the dimer cation of MTHT does not form in γ-irradiated MTHT at 77 K, although the dimer cation of THT

has been observed in oxidizing solutions under conditions quite different than present here.[17]

Assignment of the 300-nm Peak. The absorption peak at 300 nm in γ-irradiated MTHT glass (Figure 2A), and the peak at 325 nm in γ-irradiated 9.5% MTHT–MTHF (Figures 5 and 6) may be presumed to represent the same species. In MTHT the peak is approximately equal in absorbance at λ_{max} to the 460-nm peak. In 9.5% MTHT–MTHF the peak is much smaller relative to the 460-nm peak. γ-Irradiation of MTHT containing 5×10^{-4} M TMPD induces an absorption in which the tail of the 460-nm peak at 360 nm (and presumably at 300 nm, although this is obscured by the TMPD absorbance) is much lower relative to the 460-nm absorbance (Figure 8A) than for MTHT irradiated in the absence of TMPD.

The fact that both TMPD and MTHF are positive hole scavengers and that both reduce the 300–325-nm peak suggests that the species responsible for the peak may be a cation or be formed from a cation. It is thought that in MTHF glass $MTHF^+$ cations convert to tertiary α-MTHF radicals by proton transfer.[10] If some $MTHT^+$ cations in MTHT undergo proton transfer rather than being stabilized to give the 625-nm absorption (see above) it may be that the 300-nm peak is the spectrum of MTHT radicals. The 300-nm λ_{max} relative to λ_{max} of the tertiary α-MTHF radical of 250 nm[10] is a plausible shift for the spectrum of the thioether relative to the ether.

Spectra of any radiation induced species in MTHT which absorb below the 300-nm band are obscured by the absorption of unirradiated MTHT,[2] which starts at ~290 nm and rises to 3 absorbance units per 0.1 cm path at 270 nm. Pure MTHF shows little absorption above 220 nm (Figure 1).

ESR Spectra of γ-Irradiated and Photolyzed MTHT. The seven line ESR spectrum which remains after 40% bleaching of the initial ESR spectrum of γ-irradiated MTHT glass (Figure 3B) is similar to that of the tertiary α-MTHF[4,10] radical formed by γ irradiation of MTHF glass. Using coupling constants of $a(CH_3) = 20$ G, $a(CH_2) = 17$ G, and $a(CH_2') = 34$ G for the tertiary α-MTHT radical (inferred from the observed low temperature coupling constants of the secondary α-MTHT radical[4]), a theoretical spectrum in agreement with that in Figure 3B is obtained when line broadening is included.

Of the radicals which might be produced from MTHT, the most plausible to account for the 160 G total width of the spectrum of Figure 3A is $CH_3\dot{C}HCH_2CH_2CH_2S^-$, produced as in eq 1. This radical should have an overall width of 162 G based on reported coupling constants for alkyl radical centers at low temperatures.[18,19] The spectral change from Figure 3A to 3B on exposure of the sample to 360–900-nm light seems to indicate the preferential removal of the species responsible for the 160 G width from the radical mixture in addition to other changes which may or may not be due to bleaching of other radicals. Additional exposure further decreases the intensity of the spectrum of Figure 3B without changing the relative peak heights.

The production of radicals during photoionization of TMPD in MTHT glass (Figure 3C) indicates transfer of energy from the TMPD to the matrix either without ionization or involving the energy of neutralization or attack by methyl radicals ejected from TMPD by the energy of neutralization.

The thiyl radicals formed by photolysis of MTHT glass (Figure 4) indicate rupture of a C–S bond of MTHT in contrast to the loss of H from the tertiary position which seems to occur in γ radiolysis, but in accord with the C–S bond cleavage which is the dominant process in organic sulfides at 254 nm in the gas phase[20] and in solid matrices at 77 K.[21]

References and Notes

(1) This work has been supported in part by the U.S. Energy Research and Development Administration under Contract No. AT(1101)-1715 and by the W. F. Vilas Trust of the University of Wisconsin.
(2) Additional details of this work are given in the Ph.D. Thesis of G. C. Dismukes, University of Wisconsin—Madison, 1975.
(3) For examples and references see J. E. Willard, *J. Phys. Chem.*, **79**, 2966 (1975).
(4) G. C. Dismukes and J. E. Willard, *J. Phys. Chem.*, **80**, 1435 (1976).
(5) J. K. Lawson, W. K. Easley, and W. S. Wagner, *Org. Syn.*, **36**, 89 (1963).
(6) American Petroleum Institute, Research Project 44.
(7) (a) J. R. Miller, *J. Chem. Phys.*, **56**, 5173 (1972); (b) T. Huang, I. Eisele, D. P. Lin, and L. Kevan, *ibid.*, **56**, 4702 (1972); (c) K. F. Baverstock and P. J. Dyne, *Can. J. Chem.*, **48**, 2182 (1970); (d) D. R. Smith and J. J. Pieroni, *ibid.*, **46**, 2723 (1967); (e) T. Sawai and W. H. Hamill, *J. Phys. Chem.*, **73**, 3452 (1969).
(8) J. G. Castle, D. W. Feldman, P. G. Klemens, and R. A. Weeks, *Phys. Rev.*, **130**, 577 (1963).
(9) T. Gillbro, *Chem. Phys. Lett.*, **4**, 476 (1974).
(10) F. S. Dainton and G. A. Salmon, *J. Chem. Soc. A*, 285, 318 (1965).
(11) For examples and references see A. C. Albrecht, *Acc. Chem. Res.* **3**, 238 (1970).
(12) C. Andrieu, M. Denauynick, and Y. Mullien, *C. R. Acad. Sci., Paris, Ser. A*, **B265**, 127 (1967).
(13) J. Wendenburg, Second Tihany Symposium on Radiation Chemistry Hungarian Academy of Sciences, Budapest, 1967, p 225.
(14) J. Fabian, H. Viola, and R. Mayer, *Tetrahedron*, **23**, 4323 (1967).
(15) (a) T. Shida, *J. Phys. Chem.*, **74**, 305 (1970); (b) *ibid.*, **72**, 2597 (1968).
(16) For examples and references see: W. H. Hamill in "Radical Ions," E. T. Kaiser and L. Kevan, Ed., Interscience, New York, N.Y., 1967, pp 321–416; and J. E. Willard in "Fundamental Processes in Radiation Chemistry," P. Ausloos, Ed., Interscience, New York, N.Y., 1968, pp 599–649.
(17) B. C. Gilbert, D. K. C. Hodgeman, and R. O. C. Norman, *J. Chem. Soc., Perkin Trans. 2*, 1748 (1973).
(18) R. W. Fessenden and R. H. Schuler, *J. Chem. Phys.*, **39**, 2147 (1963).
(19) P. J. Krusic, P. Meakin, and J. P. Jesson, *J. Phys. Chem.*, **75**, 3438 (1971).
(20) J. G. Calvert and J. N. Pitts, "Photochemistry," Wiley, New York, N.Y., 1966.
(21) (a) P. S. H. Bolman, I. SaFarik, D. A. Stiles, W. J. R. Tyerman, and O. P. Strausz, *Can. J. Chem.*, **48**, 3872 (1970); (b) F. Truby, *J. Cnem. Phys.*, **42**, 3846 (1965).

Empirical Free-Ion Polarizabilities of the Alkali Metal, Alkaline Earth Metal, and Halide Ions

Howard Coker

Department of Chemistry, University of South Dakota, Vermillion, South Dakota 57069 *(Received October 7, 1975; Revised Manuscript Received June 25, 1976)*

Empirical values for the free-ion polarizabilities of alkali metal, alkaline earth metal, and halide ions have been obtained from static crystal polarizabilities. The crystalline environment significantly reduces the polarizabilities of the anions, but the refractive index data do not support a significant perturbation of the cation polarizabilities. The result for the cations contradicts earlier conclusions, but is in agreement with recent experimental and theoretical work. The empirical polarizabilities obtained were: $K^+ = 0.85 \pm 0.02$; Rb^+, 1.41 ± 0.02; Cs^+, 2.42 ± 0.03; Ba^{2+}, 1.73 ± 0.05; F^-, 1.38 ± 0.1; Cl^-, 3.94 ± 0.2; Br^-, 5.22 ± 0.2; I^-, 7.81 ± 0.3 Å^3.

Introduction

The polarizabilities of free or gaseous ions are not susceptible to direct experimental determination. For their determination recourse must be made to purely theoretical calculation or to some type of empirical or semiempirical procedure. Reported here is an empirical correlation of crystal polarizabilities that is believed to give reliable estimates of free-ion polarizabilities.

The set of polarizabilities obtained by Pauling[2] and the set obtained by Fajans and his co-workers[3-5] are the best known estimates of free-ion polarizabilities. Both sets are dependent upon the polarizabilities of ions in aqueous solution. Pauling empirically corrected an approximate theoretical treatment of the quadratic Stark effect by requiring the screening constants to be those that reproduce the polarizabilities of the noble gases. In order to estimate the variation of the screening constants with atomic number, he assumed the free-ion polarizabilities of the bromide and iodide ions to be equal to the solution polarizabilities of Heydweiller.[6]

Fajans' polarizabilities were obtained from the molar refractions of salts at infinite dilution. The solution polarizabilities of the salts were partitioned into polarizabilities for the individual ions on the basis of a solution polarizability, α_d, of 0.080 Å^3 for the sodium ion. One may expect that a given change in nuclear charge will cause a greater relative change in polarizability the smaller the magnitude of the nuclear charge. This expectation implies a number of inequalities which Fajans identified and used to justify his choice for the solution polarizability of the sodium ion.

Fajans identified the solution polarizabilities of the three heavier alkali metal ions and the three heavier halide ions with the free-ion polarizabilities. Systematic variation of polarizabilities was then used to define the free-ion polarizabilities of the sodium and fluoride ions and those of the alkaline earth and chalcogenide ions. The differences between the solution and free-ion polarizabilities for the ions of greater charge density were rationalized in terms of a principle that has also been used to rationalize the nonadditive trends in the polarizabilities of crystals: Polarizability is diminished in the field of positive charge and increased in the field of negative charge.

This principle implies that the polarizabilities of cations be enhanced in crystals and that those of the anions be decreased. The more diffuse anions should suffer decreases in polarizability greater than the increases experienced by the cations. Thus, crystal polarizabilities are expected to be less than the sum of the free-ion polarizabilities of the constituent ions.

Tessman, Kahn, and Shockley[7] obtained a set of ion polarizabilities from the condition of a least-squares fit to the crystal polarizabilities of the alkali halides. In accord with Fajans' principle, the anion polarizabilities were smaller and the cation polarizabilities were larger than the corresponding free-ion polarizabilities. Systematic nonadditive trends indicated the need for a model that would allow the polarizabilities of the individual ions to differ in different crystals.

Fajans' principle is electrostatic in origin. A quantification of this principle has been presented by Ruffa.[8] He calculated crystal polarizabilities from Pauling's free-ion polarizabilities and found reasonable agreement between the calculated and experimental crystal polarizabilities. When the polarizabilities for each ion were averaged, excellent agreement was found with the polarizabilities of Tessman, Kahn, and Shockley.[7]

Petrashen', Abarenekov, and Krostofel'[9] have presented a model which allows for the modification of the Hartree–Fock distribution by the Madelung potential. The expected dilation of the cation and contraction of the anion were demonstrated. The corresponding perturbations of the polarizabilities have been investigated by Ledovskaya.[10] Qualitatively similar results have been obtained by Paschalis and Weis[11] using the model of an ion embedded in a hollow sphere, a sphere which carries an electric charge of the same magnitude but opposite in sign to that of the ion considered.

Wilson and Curtis[12] have treated the variation of anion polarizability in the alkali halides using the model of a compressible conducting sphere. They assume that the relative decrease of the polarizability experienced by the anion is proportional to the compressive force acting upon the anion. This force was approximated by the Coulomb force. Applying their model to the alkali halides having the sodium chloride structure, they found free anion polarizabilities that were essentially equal to the cube of the anion radii. The refractive index data did not seem to require significant enhancement of the cation polarizabilities.

Pirenne and Kartheuser[13] have obtained a set of free ion polarizabilities that is based on the presumption that crystal polarizabilities are enhanced by a dipole–dipole interaction. Some theoretical support for this position, which contradicts Fajans' principle, is given by Heinrichs.[14]

The principal empirical support for the application of Fajans' principle to ions in crystals has been the results of x-ray

diffraction studies. Schoknecht's[15] study of sodium chloride, for example, shows a dilation of the outer electron distribution of the sodium ion and a contraction of the outer electron distribution of the chloride ion. However, the more recent study of Linkoaho[16] shows the electron distributions to be almost identical with the Hartree–Fock distributions. Similarly, the study of lithium fluoride by Krug, Witte, and Wölfel[17] has been revised by the study of Merisalo and Inkinen.[18] The lithium ion is shown to be compressed as well as the fluoride ion. Maslen[19] does not believe the data on fluorite to be of sufficient accuracy to demonstrate either radial or angular distortion of the calcium or fluoride ions. However, the data do *contradict* the electrostatic distortion model of Petrashen', Abarenkov, and Kristofel'.[9] The ions in lithium,[20] potassium,[21] and rubidium[22] chlorides are very similar to the Hartree–Fock ions. There is some indication of a slight compression of the rubidium ion. Both the potassium and bromide ions are compressed relative to the free ions in potassium bromide.[23]

The present conclusions are based more on improved methods for analyzing the experimental data than upon improvements in the available x-ray diffraction data.[24] The errors in the experimental structure factors are somewhat less than 1%[25,26] and the limits on the information obtainable from them have been carefully assessed by Kurki-Suonio.[27] It seems unlikely that these conclusions will need to be revised materially.

Aikala and Mansikka[28] have recently investigated the radial distortion of Hartree–Fock distributions attending the formation of lithium fluoride and sodium fluoride crystals. The study showed a slight dilation, about 0.3%, of the lithium ion. The fluoride ion was found to experience a contraction of about 2% in both cases. No radial distortion of the sodium ion was found. The present evidence, both theoretical and experimental, demonstrates that the electrostatic dilation of cations was overestimated in earlier theoretical work or that this effect is countered by the effect of compressive forces.

Since both compressive forces and the Madelung potential act to contract anions, the evidence of the diffraction studies for little or no radial compression of the chloride ion is surprising. Particularly is this so in view of the evidence for compression of the fluoride and bromide ions. Perhaps the Hartree–Fock distribution for the chloride ion does not adequately represent the true electron distribution of the free chloride ion. Thorhallsson, Fisk, and Fraga[29] have questioned the accuracy of the outer electron distribution for anions given by extant Hartree–Fock calculations. In their investigation of the representation of Hartree–Fock form factors with Gaussian functions, Kurki-Suonio, Meisalo, and Peltola[30] found excellent fit for a number of common atoms and ions, but found that the fit was poor for the chloride and sulfide ions. The reason for the apparent lack of compression of the chloride ion is an unresolved problem. A true failure in systematic behavior seems most unlikely.

It may be that neither the theoretical nor the experimental results are significantly in error, and that the answer lies in the electron distributions lying outside the spheres defined by the ionic radii. In lithium fluoride[18] a charge of −0.5e lies outside these spheres. In sodium[16] and potassium[21] chloride the charges external to the ionic spheres are approximately −0.7e and −1.0e, respectively. To within experimental error, no charge lies outside the ionic spheres in potassium bromide.[23]

Compression of the charge of the chloride ion external to its ionic sphere can be presumed without contradiction of the diffraction results since the electronic charge distribution is not well defined by the diffraction data outside the ionic spheres. This possibility would allow for significant compression of all halide ions as seems necessary to account for the nonadditivity of crystal polarizabilities.

In this study, the model of Wilson and Curtis[12] has been thoroughly reinvestigated. It has been extended to include the alkali halides having the simple cubic structure and to include 13 of the alkaline earth chalcogenides having the sodium chloride structure. Several empirical forms in addition to the WC form have also been investigated. The effect of the crystal on the polarizability of a cation has been investigated through the introduction of a scaling factor into an expression obtained by Ruffa.[8]

Determination of the polarizabilities of the free ions from the crystal polarizabilities presumes that the ions retain their identity in the crystal phase and that the perturbations can be described in some manner. The crystal polarizability is taken to be the sum of the two perturbed polarizabilities. The unperturbed polarizabilities and the parameters describing the perturbation are determined by the condition of a least-squares fit to the equation:

$$\alpha_c = \alpha_+ + \alpha_- \tag{1}$$

The solution is not defined unless the polarizability of one ion is fixed a priori. The accepted practice has been to take the crystal polarizability of the smallest cation to be the free ion polarizability as calculated from first principles. The absolute error introduced in this fashion is minimal. The determination of individual ion polarizabilities is a non-linear least-squares problem. Solutions were obtained using a program constructed in Fortran IV.

Polarizabilities Assuming Constant Cation Polarizabilities

The results that will be considered first are those for the alkali halides assuming that the cations retain their free-ion polarizabilities. The static crystal polarizabilities used are those accepted by Wilson and Curtis[12] after a careful review of the extant data. The polarizability of the lithium ion was set equal to 0.0285 Å^3, the ab initio value obtained by Weinhold.[31] Correlations proved to be such that it was necessary to fix the sodium ion polarizability a priori as well in order to obtain well-defined polarizabilities for the remaining alkali cations. The most reliable technique which has been applied to 10 and 18 electron systems is the coupled Hartree–Fock (CHF) technique. The results are consistently about 10% low.[32] When polarizabilities are determined for an isoelectronic sequence using the same method of calculation, scaling the polarizabilities of the entire sequence, using the ratio of the observed to the calculated polarizability of the noble gas, should give improved estimates for the polarizabilities of the ionic species. The polarizability of the sodium ion obtained by Lahiri and Mukherji,[33] 0.140 Å^3, was scaled in this fashion to obtain the value used in this investigation, 0.158 Å^3. Additional evidence for the use of this simple scaling procedure is presented later in the paper.

The Wilson–Curtis function is

$$\alpha_- = \alpha_-^0 \exp(-C/r_0^2) \tag{2}$$

The crystal and free anion polarizabilities are denoted α_- and α_-^0, C is a parameter to be varied, and r_0 is the least cation–anion distance. The four cesium halide polarizabilities were omitted in the initial investigation since three of the salts have the simple cubic structure and only a value for $\alpha(Cs^+)$ would

have been provided by the molar polarizability of CsF. When the value of C was set equal to zero, that is, when the anion polarizabilities were presumed constant, σ, the standard deviation of the calculated from the observed crystal polarizabilities, was 0.12 Å^3. When C was allowed to vary, σ was reduced by a factor of 3 to 0.034 Å^3. When each of the four anions was allowed to assume its own value for C, σ was further reduced to 0.011 Å^3. Inclusion of the polarizabilities of the cesium halides increased the standard deviation to 0.027 Å^3, but this was again reduced to 0.011 Å^3 when a structure parameter, s, was introduced. The structure parameter is defined by $C(\mathrm{CsCl}) = sC(\mathrm{NaCl})$. Twelve parameters, the polarizabilities of the potassium, rubidium, and cesium ions, the polarizabilities and C's of the four halide ions, and the structure parameter, fit the 20 experimental data to within the uncertainty of much of the data.

The crystal polarizabilities range over a factor of 10. A more appropriate weighting of the crystal polarizabilities is the weighting for which the relative deviations from eq 1 are minimized. With this weighting, and with the 12 variable parameters mentioned above, the standard relative deviation was 0.24%. The differences between the parameters as determined by the different weighting procedures were quite small. The parameters obtained by minimizing the relative deviations are listed in Table I.

The relatively large number of parameters requires that some caution be maintained in the interpretation of the parameters α_+ and α_-^0 as free-ion polarizabilities. Alternate empirical forms might fit the data as well and yield "free-ion" polarizabilities that are significantly different. In order to obtain a more certain estimate of the free-ion polarizabilities, several other empirical forms were investigated.

One criticism of the WC form is its neglect of the van der Waals' forces. In some cases, these are even larger than the Coulomb forces. Rather than neglect the van der Waals' forces, one may assume that they are balanced, along with the Coulomb forces, against the Pauli repulsive forces, and presume the relative decrease of the ion polarizabilities from the free-ion values to be proportional to the repulsive force. This presumption leads to

$$\alpha_- = \alpha_-^0 \exp(-CF_-) \tag{3}$$

in which C is a proportionality constant and

$$F_- = MbC_{+-}\rho^{-1} \exp((r_+ + r_- - r_0)/\rho) + M'abC_{--}\rho^{-1} \exp((2r_- - ar_0)/\rho) \tag{4}$$

The quantities C_{+-} and C_{--} are the Pauling factors, M is the number of the nearest neighbors, M' is the number of next-nearest neighbors, b is a constant, r_+ and r_- are cation and anion radii, r_0 is the nearest-neighbor distance, a is a geometrical factor depending upon the crystal structure, and ρ is the hardness parameter. Values for these parameters were taken from the study by Cubicciotti[34] rather than from the more recent work by Tosi and Fumi,[35] since the latter did not include the simple cubic cesium halides in their investigation. It is important to use radii and hardness parameters determined from compressibility data.

The results for this second empirical form are shown in Table I. In this case, there was no significant improvement obtained when the number of parameters varied was increased from 9 to 12 by allowing the proportionality constants C to differ for the four different anions. The values for the three cation polarizabilities are a few percent higher than those obtained using the WC form, but the anion polarizabilities obtained are significantly lower. The results are dependent upon the van der Waals' constants since the latter were used to define the radii and hardness parameters. Cubicciotti, as well as Tosi and Fumi, were forced to use van der Waals' constants which are astute estimates based upon very limited data.[36]

An improved set of van der Waals' constants might significantly lower the standard deviation. The fit is still quite good with $\sigma = 0.48\%$. The standard deviation using the WC form and a common value of C for the anions is approximately 50% larger. The form suggested by Pirenne and Kartheuser[13]

$$\alpha_c = \alpha_+ + \alpha_- + \lambda\alpha_+\alpha_- \tag{5}$$

fits eq 1 with σ equal to 1.1%. Using the same number of variable parameters, their standard deviation is twice as large as that obtained using eq 3.

Two additional empirical forms have been investigated:

$$\alpha_- = \alpha_-^0(1 + Cr_0^{-n})^{-1} \tag{6}$$

and

$$\alpha_- = \alpha_-^0(1 - e^{-x}(1 + x + \cdots x^{n-1}/(n-1)!)) \tag{7}$$

with $x = Cr_0$. Both functions vary as r_0^n for small values of r_0 and approach α_-^0 for large values of r_0, the first as an inverse power of r_0 and the second exponentially. The results for both eq 6 and 7 are shown in Table I for $n = 2$, 3, and 4. In each case the standard deviation is essentially the same as that for the WC form, so that fit alone cannot be used to determine the function most likely to give the true values of the free-ion polarizabilities. The model of a conducting, compressible, spherical shell predicts a dependence of the polarizability on r_0^3. Electrons confined to a spherical box would exhibit a dependence on r_0^4. Hence, the results for $n = 3$ and 4 should give the more reliable polarizabilities. Fortunately, the four sets of polarizabilities given by eq 6 and 7 are quite similar. Listed in Table II as the best empirical estimate of each free ion polarizability is the average of the results for these four cases. The anion polarizabilities obtained from eq 3 agree well with these estimates, and so lend additional support.

The general trend obtained on increasing the value of n in eq 6 and 7 is a decrease of the anion polarizabilities. The cation polarizabilities are *nearly independent* of the model for anion polarizability. The two sets of results obtained for $n = 2$ give anion polarizabilities that are significantly higher than the values chosen as the best values, polarizabilities similar to those obtained using the WC form.

Boswarva[37] has used the static polarizabilities of 13 of the alkaline earth chalcogenides having the sodium chloride structure to define polarizabilities for the alkaline earth and chalcogenide ions. He assumed Pauling's value for the polarizability of the magnesium ion and assumed both cation and anion polarizabilities to be independent of the counterion. Using his data, his results have been reproduced. The polarizabilities obtained for the calcium, strontium, and barium ions are approximately double the polarizabilities of Pauling, and the standard deviation was found to be 0.14 Å^3. The large enhancement of the cation polarizabilities is not required by the data, however. When the four cation polarizabilities were presumed to be those of Pauling and a single value of C was used in the WC form, an essentially identical fit was obtained, $\sigma = 0.15$ Å^3, even though five rather than seven variables were used to fit the data.

Correlations again required that the polarizabilities of two of the cations be fixed. The polarizabilities of the magnesium and calcium ions were taken to be 0.0784 and 0.522 Å^3, respectively. These polarizabilities are the CHF polarizabilities

TABLE I: Polarizability Parameters for the Alkali Halides

Eq no.	n	Structure parameter	Free-ion polarizabilities, Å^3							C^a				σ, %
			K^+	Rb^+	Cs^+	F^-	Cl^-	Br^-	I^-	F	Cl^-	Br^-	I^-	
2		1.123	0.85	1.40	2.40	1.59	4.48	5.90	8.88	2.37	2.91	2.92	3.81	0.24
3		0.927	0.91	1.50	2.50	1.33	3.84	5.17	7.46		0.0334			0.48
6	2	1.118	0.83	1.37	2.36	1.96	5.00	6.43	9.75	4.90	4.85	4.60	5.98	0.24
6	3	1.189	0.85	1.41	2.41	1.45	4.11	5.44	8.16	5.16	7.22	7.50	10.61	0.23
6	4	1.260	0.87	1.43	2.45	1.28	3.78	5.06	7.54	7.32	13.57	15.17	23.46	0.22
7	2	0.947	0.82	1.36	2.35	1.84	4.53	5.80	8.79	0.807	0.843	0.869	0.763	0.24
7	3	0.966	0.84	1.39	2.39	1.47	4.03	5.30	7.95	1.55	1.44	1.44	1.28	0.23
7	4	0.945	0.85	1.41	2.41	1.34	3.82	5.07	7.58	2.24	2.00	1.97	1.76	0.23

[a] The values for C correspond to r_0 in angstroms.

TABLE II: Free-Ion Polarizabilities of the Alkali and Halide Ions (Å^3)

	Li^+	Na^+	K^+	Rb^+	Cs^+	F^-	Cl^-	Br^-	I^-
Empirical	(0.0285)[a,b]	(0.158)[a]	0.85 ± 0.02	1.41 ± 0.02	2.42 ± 0.03	1.38 ± 0.1	3.94 ± 0.2	5.22 ± 0.2	7.81 ± 0.3
Coupled Hartree-Fock[c]	0.0281	0.140	0.789			1.40	3.76		
Scaled CHF		0.158	0.867			1.58	4.13		
Thomas-Fermi[d]		0.55	1.03	1.76	2.27				
Scaled TF		0.179	0.845	1.39	2.43				
Quadratic Stark effect[e]	0.029	0.181	0.840	1.42	2.44	1.05	3.69	4.81	7.16
Solution based[f]	0.03	0.188	0.887	1.48	2.54	0.95	3.46	4.82	7.22

[a] Assumed values. [b] Reference 31. [c] Reference 33. [d] Reference 39. [e] Reference 2. [f] Reference 5.

scaled by the ratio of the experimental to the CHF polarizability of the corresponding noble gas. The crystal polarizabilities were fit using the WC form and using eq 6 and 7 with $n = 3, 4$. Relative deviations were minimized with a common value of C for the four anions. There was not much decrease in σ when the values of C were allowed to vary separately for each of the anions, and the C's did not vary monotonely with atomic number. As may be seen from Table III, consistent results were obtained for the strontium and barium ions. The polarizabilities for these ions listed in Table IV are the average of the values obtained using eq 6 and 7.

The anions are metastable in the free state. Thus, the expressions for anion polarizability can only be expected to treat the variation of the polarizability of an anion as it is stabilized within a crystal. The "free-ion" polarizabilities are not to be taken seriously as such, and do not agree well with each other.

Variation of Cation Polarizabilities

The above results are not greatly sensitive to the values assumed for the lithium and magnesium ions since each makes only a small contribution to the crystal polarizabilities. The values chosen for the sodium and calcium ions, on the other hand, do affect the results materially. If, as has been commonly held, cation polarizabilities are enhanced in the crystal, larger values should be used for these ions. More appropriately, a theory such as Ruffa's should be used which specifically allows for this enhancement in terms of the Madelung potential of the individual crystals.

The polarizability of the sodium ion obtained from photoelectric data by Michael[38] is 0.301 Å^3. When this value is assumed, the result is to produce a fluoride ion polarizability that is essentially constant in each of the alkali fluorides. Since the nonadditivity of the crystal polarizabilities does require some variation in individual ion polarizabilities, a variation that must arise primarily from the softer anions, Michael's value would appear to be an upper limit for the polarizability of the sodium ion in the alkali halides. A value of 0.311 Å^3 is obtained when each alkali and halide ion is assumed to have a polarizability independent of its counterion. Variation of the sodium ion polarizability in steps of 0.05 Å^3 from 0.10 to 0.30 Å^3 was investigated using both eq 6 and 7 with $n = 3, 4$. The results were similar in each of the four cases. The higher values for the sodium ion polarizability lead to correspondingly higher values for the heavier cations and lower values for each of the anions. The results for eq 7 with $n = 3$ are shown in Table V. When the sodium ion polarizability was released, it assumed a value of 0.273 Å^3 and σ became 0.20 Å^3. This is to be compared to the standard deviation of 0.23 Å^3 obtained when the sodium ion polarizability was fixed at 0.158 Å^3. When the WC form was used, a polarizability and standard deviation of 0.265 Å^3 and 0.24% were obtained.

However, this is not a reliable indication of enhanced cation polarizability. Using a common value of C in eq 6 with $n = 3$, the standard deviation of 1.0% was reduced to 0.48% when the polarizability of the sodium ion was released from 0.158 Å^3 and allowed to vary. However, the unreasonably low sodium ion polarizability of 0.056 Å^3 was obtained. An unreasonably low value was also obtained for the polarizability of the calcium ion when that polarizability was released in the fitting of the polarizabilities of the alkaline earth chalcogenides.

The variation of cation polarizability predicted by Ruffa is that given by

$$\alpha_+^0/\alpha_+ = (1 - (2\pi Aed/r_0h)(m\alpha_+^0/N)^{1/2})^2 \qquad (8)$$

in which A is the Madelung constant, e is the electronic charge, d is a scaling parameter introduced by this author, h is Plank's constant, m is the mass of the electron, and N is the number of electrons in the ion. Ruffa's result was obtained by assuming that cationic ground state levels are raised by the

TABLE III: Polarizability Parameters for the Alkaline Earth Chalcogenides

Eq no.	n	"Free-ion" polarizabilities, Å^3						C	σ, %
		Sr^{2+}	Ba^{2+}	O^{2-}	S^{2-}	Se^{2-}	Te^{2-}		
2		0.82	1.79	6.5	10.8	12.4	14.6	5.98	1.8
6	3	0.83	1.71	7.2	11.9	13.4	15.5	30.0	2.0
6	4	0.82	1.80	4.9	8.2	9.4	11.1	37.4	2.0
7	3	0.86	1.69	11.4	19.0	21.1	23.9	0.636	2.3
7	4	0.83	1.69	7.5	12.4	13.9	15.9	1.156	2.0

TABLE IV: Polarizabilities of the Alkaline Earth Cations (Å^3)

	Mg^{2+}	Ca^{2+}	Sr^{2+}	Ba^{2+}
Empirical	(0.0784)[a,b]	(0.522)[a,b]	0.84 ± 0.02	1.73 ± 0.05
Coupled Hartree–Fock[b]	0.0697	0.475		
Thomas–Fermi[c]	0.27	0.56	1.11	1.70
Scaled TF	0.088	0.46	0.87	1.82
Quadratic Stark effect[d]	0.094	0.47	0.65	1.56
Solution based[e]	0.010	0.55	1.01	1.85

[a] Assumed, scaled CHF values. [b] Reference 33. [c] Reference 39. [d] Reference 2. [e] Reference 5.

TABLE V: Variation of Polarizabilities with the Sodium Ion Polarizability[a]

Free-ion polarizabilities, Å^3								
Na^+	K^+	Rb^+	Cs^+	F^-	Cl^-	Br^-	I^-	σ, %
0.10	0.70	1.21	2.17	2.17	4.65	5.89	8.62	0.24
0.15	0.82	1.36	2.36	1.54	4.11	5.37	8.03	0.23
0.20	0.93	1.50	2.52	1.19	3.71	4.97	7.57	0.22
0.25	1.03	1.62	2.66	0.99	3.42	4.67	7.20	0.21
0.30	1.10	1.70	2.74	0.88	3.24	4.49	6.96	0.26
0.273[b]	1.07	1.67	2.71	0.92	3.31	4.56	7.06	0.20

[a] Equation 7, n = 3. [b] Sodium ion polarizability for minimum σ.

Madelung energy while the excited state levels are left approximately unchanged. To the extent that the perturbation of the cations is electrostatic in origin, the ground state energy levels of a cation in a crystal are raised by an amount equal to the Madelung energy. The wave functions for the excited state levels are more delocalized. Thus their energy levels are raised to a lesser extent by the electrostatic potential of the crystal. In addition, short-range and exchange potentials become more significant for the excited state levels, and both act to diminish the effect of the Madelung potential. The scaling parameter d, which has been introduced for empirical evaluation, is reduced from unity by localization of the excited state wave functions.

In order to provide room for an alternate fitting of the experimental data, a single value of C was used for the anions. Any of the suggested forms for the description of anion polarizability should serve adequately for investigation of the enhancement of cation polarizability. The lithium ion polarizability may be assumed constant because of its very small contribution to the crystal polarizabilities.

The results for eq 6 with n = 3 were as follows: With the value of d set equal to zero for the lithium ion and equal to 0.5 for the remaining four cations, a standard deviation of 1.28% was obtained. When d was released, but required to remain the same for the four cations, it converged to zero with σ = 1.00%. The parameters obtained were identical with those obtained when cation polarizabilities were assumed constant. Convergence was slow, and, when the d's were released to vary separately, the program was terminated before all of the d's became negligibly small. In another run, which excluded the cesium salts to avoid the complication of differing crystal structures, the WC form was used and convergence was continued until the calculated enhancements of polarizability for the sodium, potassium, and rubidium ions had each become negligible.

Ruffa's equation should have described adequately any Coulombic enhancement of the cation polarizabilities. Thus, the failure to find evidence for significant enhancement is evidence against such enhancement in the alkali halides. The enhancement obtained by assuming constant anion polarizabilities is apparently an artifact of an overly simple model.

Discussion

If the polarizability of the sodium ion in the sodium halides is, in fact, not significantly perturbed from the free-ion polarizability, then the free-ion polarizabilities of the three heavier alkali cations should be well approximated by the empirical polarizabilities obtained in this study. Scaling of the CHF polarizability of the potassium ion yields a value of 0.867 Å^3 which is in excellent agreement with the empirical value of 0.85 ± 0.02 Å^3. CHF polarizabilities for the rubidium and cesium ions were not found, so recourse was made to the Thomas–Fermi polarizabilities of Vinogradov, Pustovalov, and Shevelko.[39] As may be seen from Table II, their value for the sodium ion differs from the scaled CHF polarizability by a factor of 3. Scaling reduces the disagreement to 13%. Scaling of their polarizability for the potassium ion gives 0.845 Å^3 which differs by only 2.5% from the scaled CHF polarizability. This convergence shows that significant improvement of the

TABLE VI: Fajans' Ratios

	$Q'(-/0)$	$Q'(0/+)$	Q''	$Q'''(-/0)$	$Q'''(0/+)$
Ne	3.50	2.50	1.40		
Ar	2.41	1.93	1.25	1.45	1.29
Kr	2.10	1.76	1.19	1.15	1.10
Xe	1.93	1.67	1.15	1.09	1.05

TABLE VII: Relative Decreases (%) in Anion Polarizability on Crystal Formation

	F^-	Cl^-	Br^-	I^-
Li^+	36	27	23	25
Na^+	26	21	18	21
K^+	17	16	14	16
Rb^+	15	14	12	14
Cs^+	13	12	10	12

theoretical alkali metal ion polarizabilities is obtained by the scaling procedure. Since the accuracy of the statistical model increases with atomic number, the scaled TF polarizabilities for the rubidium and cesium ions should be quite accurate. As may be seen from Table II, *the empirical and scaled theoretical polarizabilities agree to within the uncertainties cited for the empirical polarizabilities.*

Similar data are presented for the alkaline earth cations in Table IV. The scaled TF polarizabilities are about 4% higher than the empirical values, a difference which is probably not significant. The experimental noble gas polarizabilities used to scale the theoretical polarizabilities of the ionic species are those listed in the extensive tabulation of Teachout and Pack.[40]

Fajans' inequalities provide an additional test to which the empirical polarizabilities must be subjected. The inequalities relate the polarizability ratios Q' and quotients of these ratios, Q'' and Q'''. $Q'(-,0)$, for example, denotes the ratio of the polarizability of a halide ion to that of the corresponding noble gas. $Q''(-,0,+)$ denotes the ratio $Q'(-,0)/Q'(0,+)$ in which the polarizabilities are those of isoelectronic ions. $Q'''(-,0)$ denotes the ratio of $Q'(-,0)$ for one period to that for the next period. These ratios for the halide ions, the noble gases, and the alkali metal ions are given in Table VI. Fajans' inequalities require a monotone decrease in each of the three types of ratios with atomic number. Smoothly systematic behavior is observed. The empirical polarizabilities that have been obtained prove to be an internally consistent set.

Fajans' inequalities are not quite obeyed when the table is extended to include the alkaline earth cations. Smoothly systematic behavior is restored when the strontium ion polarizability is increased by 11% to 0.93 Å^3, and the cesium and barium ion polarizabilities are taken to be 2.45 and 1.70 Å^3, respectively. The latter two polarizabilities are at the limits of the uncertainty of their empirical definition.

Another test for consistency is provided by the relative decreases of anion polarizability on crystal formation and these are shown in Table VII. The general periodic trend reflects a lessening perturbation as the electrostatic forces decrease. Reduction of the polarizability of the iodide ion by 4% leads to a monotone periodic trend.

The decreases listed in Table VII are those for formation of crystals having NaCl structure. The molar polarizabilities for the three unstable fccub cesium halides were estimated to be 5.91 ± 0.02, 7.09 ± 0.02, and 9.28 ± 0.03 Å^3. The polarizability of simple cubic CsF was estimated to be 3.61 ± 0.01 Å^3. These were obtained by first calculating the change for a phase transition at constant nearest-neighbor distance by including or excluding the structure parameter as required. There is a 2% increase in anion polarizability attending the shift to the NaCl structure. However, there is a compensating decrease in polarizability arising from the decrease in the nearest-neighbor distance associated with the transition. The nearest-neighbor distances for the unstable phases were estimated to be 3.111, 3.464, 3.614, and 3.855 Å from the variations of r_0 predicted by Pauling.[41] The exponents for the inverse power law needed for the calculation were taken from the tabulation by Dekker.[42] The polarizability changes obtained were added to yield a net polarizability change on transition to the NaCl structure of 0.01 ± 0.01, 0.03 ± 0.02, 0.04 ± 0.02, and 0.11 ± 0.03 or, to within the uncertainty of the changes, 1% of the anion polarizability.

The empirical polarizabilities are compared to those of Pauling and Fajans in Tables II and IV. The greatest differences are those for the 10-electron systems. Both give fluoride ion polarizabilities that are much lower and sodium ion polarizabilities that are significantly higher than the scaled CHF polarizability. Fajans[43] has recently defended his polarizability of 0.95 Å^3 for the fluoride ion. It is shown in the following paper that the solution polarizabilities, upon which his free-ion polarizabilities are based, actually require a polarizability for the fluoride ion greater than 1.4 Å^3.

Pauling's theory of the quadratic Stark effect[2] also supports a larger polarizability for the fluoride ion if the scaled CHF polarizability is used for the sodium ion. It is first to be noted that when Pauling's eq 24 is simplified to $\alpha = A(Z - S)^{-4}$, the polarizability of a halide ion may be related to the polarizabilities of the isoelectronic noble gas and alkali metal ion by

$$\alpha_- = \alpha_0(2 - (\alpha_0/\alpha_+)^{1/4})^{-4} \quad (9)$$

This equation reproduces Pauling's polarizabilities for the three heavier halide ions from his noble gas and alkali metal ion polarizabilities to 1% or better. Using the empirical alkali metal ion polarizabilities and their uncertainties and the noble gas polarizabilities recommended by Teachout and Pack,[40] the polarizabilities of the chloride, bromide, and iodide ions were calculated to be, respectively 6–12, 6–10, and 5–8% lower than the empirical polarizabilities. When the scaled CHF polarizability is used for the sodium ion, the polarizability calculated for the fluoride ion is 1.30 Å^3, 6% less than the empirical polarizability. The halide ion polarizabilities predicted by the theory of the quadratic Stark effect are all lower than the empirical polarizabilities by a similar relative amount.

There are two CHF polarizabilities in the literature for the fluoride ion, Cohen's[32] 1.56 Å^3 and Lahiri and Mukherji's[33] 1.40 Å^3. Litt[44] has recently obtained a polarizability of 1.28 Å^3 using a technique that approximates the CHF calculation. This supports the lower CHF polarizability which is in excellent agreement with the empirical polarizability.

The scaling of the CHF and TF polarizabilities for the cations was empirically justified, so the scaling correction cannot be extended to the halide ions without further justification. Lahiri and Mukherji's $\alpha_0(F^-)$ is in agreement with the empirical value without scaling. Their polarizability for the chloride ion is 5% lower than the empirical polarizability whereas the scaled CHF polarizability is 5% higher than the empirical polarizability. No CHF or TF polarizabilities were found for the bromide and iodide ions, so it was not possible to make a systematic comparison between the empirical and theoretical anion polarizabilities.

The evidence of the recent x-ray diffraction studies and the theoretical work of Aikala and Mansikka[28] adequately demonstrate that alkali metal cations are not greatly perturbed in the alkali halides. This overturn of the historically held position placed the conclusions of most earlier studies of crystal polarizabilities in a contradictory position. Plausible empirical forms that allow for the nonadditivity of individual ion polarizabilities have been found to provide results in agreement with the recent evidence. The agreement between the empirical and scaled theoretical cation polarizabilities indicates that the alkali metal cation polarizabilities have been defined to within a few percent of their true values. The polarizabilities of the alkaline earth metal ions and those of the halide ions are less well defined. They are defined more precisely in the following paper on solution polarizabilities.

Acknowledgment. This work is part of a project being supported by the Research Corporation.

References and Notes

(1) Work done as part of a project being supported by the Research Corporation.
(2) L. Pauling, *Proc. R. Soc. London, Ser. A*, **114**, 181 (1927).
(3) K. Fajans and G. Joos, *Z. Phys.*, **23**, 1 (1924).
(4) K. Fajans, *Z. Phys. Chem. B*, **24**, 103 (1934).
(5) K. Fajans and N. Bauer *J. Am. Chem. Soc.*, **64**, 3023 (1942).
(6) A. Heydweiller, *Phys. Z.*, **26**, 526 (1925).
(7) J. K. Tessman, A. H. Kahn, and W. Shockley, *Phys. Rev.*, **92**, 890 (1953).
(8) A. R. Ruffa, *Phys. Rev.* **130**, 1412 (1963).
(9) M. I. Petrashen', I. V. Abarenkov, and N. N. Kristofel', *Opt. Spectrosc.*, **9**, 276 (1960).
(10) E. M. Ledovskaya, *Phys. Status Solidi*, **31**, 507 (1969).
(11) E. Paschalis and A. Weis, *Theor. Chim. Acta*, **13**, 381 (1969).
(12) J. N. Wilson and R. M. Curtis, *J. Phys. Chem.*, **74**, 187 (1970).
(13) J. Pirenne and E. Kartheuser, *Physica*, **30**, 2005 (1964).
(14) J. Heinrichs, *Phys. Rev. B*, **2**, 518 (1970).
(15) G. Schoknecht, *Z. Naturforsch. A*, **12**, 983 (1957).
(16) M. V. Linkoaho, *Acta Crystallogr., Sect. A*, **25**, 450 (1969).
(17) J. Krug, H. Witte, and E. Wolfel, *Z. Phys. Chem. (Frankfurt am Main)*, **4**, 36 (1955).
(18) M. Merisalo and O. Inkinen, *Ann. Acad. Sci. Fenn. A*, VI, No. 207 (1966).
(19) V. W. Maslen, *Proc. Phys. Soc.*, **91**, 466 (1967)
(20) O. Inkinen and M. Jarvinen, *Phys. Kondens Mater.*, **7**, 372 (1968).
(21) L. K. Patomaki and M. V. Linkoaho, *Acta Crystallogr., Sect. A*, **25**, 304 (1969).
(22) M. Jarvinen and O. Inkinen, *Phys. Status Solidi*, **21**, 127 (1967).
(23) V. Meisalo and O. Inkinen, *Acta Crystallogr.*, **22**, 58 (1967).
(24) M. Linkoaho, private communication.
(25) O. Inkinen, *Acta Crystallogr., Sect. A*, **25**, 214 (1969).
(26) S. Miyake, *Acta Crystallogr., Sect. A*, **25**, 257 (1969).
(27) K. Kurki-Suonio, *Acta Crystallogr., Sect. A*, **24**, 379 (1968).
(28) O. Aikala and K. Mansikka, *Phys. Kondens. Mater.*, **14**, 105 (1972).
(29) J. Thorhallsson, C. Fisk, and S. Fraga, *Theor. Chim. Acta*, **10**, 388 (1968).
(30) K. Kurki-Suonio, V. Meisalo, and E. Peltola, *Ann. Acad. Sci. Fenn. A*, VI, No. 198 (1966).
(31) F. Weinhold, *Proc. R. Soc. London, Ser. A*, **327**, 209 (1972).
(32) H. D. Cohen, *J. Chem. Phys.*, **45**, 10 (1966).
(33) J. Lahiri and A. Mukherji, *Phys. Rev.*, **153**, 386 (1967); **155**, 24 (1967).
(34) D. Cubicciotti, *J. Chem. Phys.*, **31**, 1646 (1959); **33**, 1579 (1960); **34**, 2189 (1961).
(35) M. P. Tosi and F. G. Fumi, *J. Phys. Chem. Solids*, **25**, 45 (1964).
(36) J. E. Mayer, *J. Chem. Phys.*, **1**, 270 (1933).
(37) I. M. Boswarva, *Phys. Rev. B*, **1**, 1698 (1970).
(38) A. J. Michael, *J. Chem. Phys.*, **51**, 5730 (1969).
(39) A. V. Vinogradov, V. V. Pustovalov, and V. P. Shevelko, *Zh. Eksp. Theor. Fiz.*, **63**, 477 (1972).
(40) R. R. Teachout and R. T. Pack, *Atomic Data*, **3**, 195 (1971).
(41) L. Pauling, "The Nature of the Chemical Bond", 3rd ed, Cornell University Press, Ithaca, N.Y., 1960, p 538.
(42) A. J. Dekker, "Solid State Physics", Prentice-Hall, Englewood Cliffs, N.J., 1957, p 122.
(43) K. Fajans, *J. Phys. Chem.*, **74**, 3407 (1970).
(44) C. Litt, *Phys. Rev. A*, 7, 911 (1973).

Polarizability Changes on Ion Hydration

Howard Coker

Department of Chemistry, University of South Dakota, Vermillion, South Dakota 57069 *(Received October 7, 1975; Revised Manuscript Received June 25, 1976)*

A repartitioning of Fajans' molar solution polarizabilities allows the polarizability changes on cation hydration to be described by a model which attributes the changes solely to solvent perturbation. A single adjustable parameter correlates the changes for the alkali cations and the four heavier alkaline earth cations to within 0.01 Å^3. The polarizability changes on halide ion hydration arise primarily from a polarizability decrease attending anion compression by the solvent. A polarizability enhancement arising from hydrogen bond formation is about twice as important as the polarizability decrement arising from compression of the solvent. These two perturbations are quite important for the fluoride ion and are nearly negligible for the iodide ion. The structure around the iodide ion in solution appears to differ from that of the other three halide ions. The free-ion polarizabilities indicated for the fluoride, chloride, bromide, and iodide ions are, respectively, 1.48 ± 0.08, 4.11 ± 0.06, 5.43 ± 0.08, and 7.83 ± 0.08 Å^3.

Introduction

Fajans and his co-workers have reported their studies of the refractivities of aqueous electrolyte solutions in a long series of publications.[2-4] One of the results of that study has been a set of polarizabilities for individual ions in solution. The partitioning of the molar polarizabilities into cation and anion contributions was accomplished by taking the solution polarizability of the sodium ion to be 0.080 Å^3 at the wavelength of the sodium D line. A set of free-ion polarizabilities was generated by assuming that the free-ion polarizabilities of the three heavier alkali-metal cations and those of the three heavier halide ions are well approximated by the solution polarizabilities. An iterative procedure was then used to obtain

the partitioning of the solution polarizabilities that gave the free-ion polarizabilities with the smoothest periodic variation. The solution polarizabilities of the ions of higher charge density differ from the free-ion polarizabilities because of the perturbation of the ions by the solvent and because of the perturbation of the solvent molecules.

A set of free-ion polarizabilities based upon a study of the refractivities of ionic crystals was presented in the foregoing paper, a paper which will subsequently be denoted I. One of the results of that empirical study was a polarizability for the free fluoride ion which is in essential agreement with the coupled Hartree–Fock polarizability of 1.40 Å^3.[5] The polarizability of the free fluoride ion obtained by Fajans[6] is lower than the CHF polarizability by more than 40%. In this communication, two simple models will be presented to account for the polarizability changes attending hydration. These models will be seen to justify a new partitioning of the solution polarizabilities, a partitioning which leads to a polarizability for the free fluoride ion which is consistent with the CHF polarizability.

Cation Solution Polarizabilities

The static solution polarizabilities of Fajans[4] for the alkali metal, alkaline earth metal, and aluminum ions are listed in column 1 of Table I. The dispersion of the polarizabilities from their values at the frequency of the sodium D line was not given for the magnesium and calcium ions. The dispersion for the magnesium ion was taken to be the average of the dispersions for the sodium and aluminum ions. The dispersion for the calcium ion was then taken to be the average of those for the magnesium and strontium ions. Since the dispersions corrections are only 0.02–0.03 Å^3, their rather crude estimate is adequate.

Free-ion polarizabilities are listed in column 2. The lithium ion polarizability is the accurate ab initio value of Weinhold.[7] Those with indicated uncertainties were obtained in I via an empirical study of the polarizabilities of ions in crystals. The remaining polarizabilities are the CHF polarizabilities scaled by the ratio of the experimental to the CHF polarizability of the corresponding noble gas. This scaling procedure was shown in I to have an empirical justification for the alkali metal cations. While the approximation may be expected to have less validity as applied to the more highly charged ions, the absolute errors involved are unlikely to be large enough to affect materially the results of this study.

The differences between the solution polarizabilities and the free-ion polarizabilities are given in column 3. Fajans[2] interpreted the negative values of the polarizability changes on hydration in terms of a principle which is electrostatic in orgin: Polarizability is reduced in the field of positive charge and enhanced in the field of negative charge. In particular, he attributed the polarizability decreases to a decrease in the polarizability of the water in the region near the solvated cations. Of note, therefore, are the positive values obtained for the three heavier alkali metal cations.

These positive values might be attributed to errors in the free-ion polarizabilities. However, the empirical polarizabilities were seen in I to agree with Pauling's polarizabilities and with the scaled ab initio polarizabilities. A repartitioning of the polarizabilities which renders each of the polarizability changes on hydration negative at least merits consideration. Shown in the final column of Table I are polarizability changes which are related to those of the previous column by

$$\Delta\alpha_h = (\alpha_s - \alpha_g) - 0.19Z \qquad (1)$$

TABLE I: Polarizability Changes on Cation Hydration (Å^3)

	α_s	α_g	$\alpha_s - \alpha_g$	$\Delta\alpha_h$
Li^+	−0.112	0.0285	−0.14	−0.33
Na^+	0.086	0.158	−0.07	−0.26
K^+	0.887	0.85 ± 0.02	0.04	−0.15
Rb^+	1.487	1.41 ± 0.02	0.08	−0.11
Cs^+	2.564	2.42 ± 0.03	0.14	−0.05
Mg^{2+}	−0.686	0.078	−0.76	−1.14
Ca^{2+}	0.264	0.522	−0.26	−0.64
Sr^{2+}	0.76	0.84 ± 0.02	−0.08	−0.46
Ba^{2+}	1.73	1.73 ± 0.05	0.00	−0.38
Al^{3+}	−1.04	0.045	−1.08	−1.65

in which Z is the charge of the ion. The suggested repartitioning implies that *all* of the cations significantly reduce the polarizability of the hydrating water molecules. Fajans assumes the polarizability decrement for the barium ion to be negligible. The repartitioning yields a polarizability change on hydration of the barium ion that is larger than that for any of the alkali metal ions. Clearly, rather different perspectives are involved with respect to the degree to which cations perturb the solvent.

Two models will be presented for the polarizability changes attending cation hydration, a continuum model and one that treats the first hydration sphere discreetly. The equation

$$-\Delta\alpha = n\alpha_{H_2O}(1 - e^{-CF}) \qquad (2)$$

will be used in both models. The number of water molecules in the first hydration sphere is denoted n, C is an adjustable parameter, and F is the electrostatic force acting between the cation and one of the water molecules in the first hydration sphere. The equation presumes that the cation polarizability changes are negligible and that the relative decrease of the polarizability of a water molecule is proportional to F. A similar model was used in I to describe the polarizability changes experienced by the halide ions in the alkali halides. The continuum and molecular models differ in the expressions used for the force compressing the water molecules against the cations.

The continuum model is a rather crude one based upon the Born model for the enthalpy of ionic hydration. Ignoring the negligible numerical difference between energy and enthalpy, the total force acting between the cation and the solvent was taken to be the rate of change of the enthalpy of hydration with respect to an effective radius of the cation, the radius which reproduces the enthalpies of hydration.

$$nF_c = \frac{Z^2e^2}{2r_c^2}\left[1 - \epsilon^{-1} - \frac{T}{\epsilon}\left(\frac{\partial \ln \epsilon}{\partial T}\right)_p\right] = \frac{AZ^2}{r_c^2} \qquad (3)$$

The Born radius is denoted r_c and ϵ is the static dielectric constant of water. The numerical coefficient A is 1.158 if the force is in millidyne and r_c is in angstroms. A was obtained from the dielectric constant of water at 25 °C and its temperature coefficient given by Latimer.[8] The values of r_c listed in Table II were obtained using the tabulation of enthalpies of hydration given by Friedman and Krishnan.[9]

The use of eq 2 requires both the number of water molecules in the primary hydration sheath and the polarizability of the water molecule. The hydration number has been taken to be six in each case and the polarizability of the water molecule was taken to be 1.15 Å^3, that calculated from the molar refraction of liquid water.[4] The model is rather insensitive to these two parameters, however, since the right-hand side of

TABLE II: Polarizability Changes on Cation Hydration for the Continuum Model

	r_c, Å	nF, mdyn	$n\alpha_{H_2O}CF$, Å^3	$-\Delta\alpha_c$, Å^3	$-(\Delta\alpha_c - \Delta\alpha_h)$, Å^3
Li^+	1.25	0.742	0.38	0.37	0.04
Na^+	1.57	0.469	0.24	0.24	0.02
K^+	1.94	0.309	0.16	0.16	0.01
Rb^+	2.06	0.273	0.14	0.14	0.03
Cs^+	2.22	0.235	0.12	0.12	0.07
Mg^{2+}	1.40	2.37	1.23	1.12	−0.02
Ca^{2+}	1.67	1.65	0.85	0.80	0.16
Sr^{2+}	1.84	1.37	0.71	0.67	0.21
Ba^{2+}	2.02	1.13	0.58	0.56	0.18
Al^{3+}	1.32	6.02	3.12	2.51	0.86

eq 2 is rather well approximated by $-n\alpha_{H_2O}CF$. As may be seen by comparing columns 3 and 4 of Table II, the disagreement becomes significant only for the more highly charged ions of smaller size.

The value chosen for C, 0.45 mdyn^{-1}, reproduces the values of $\Delta\alpha_h$ fairly well for the four lighter alkali metal ions and reproduces that of the magnesium ion fortuitously well. There are significant differences for the cesium ion and the three heavier alkaline earth cations. A variation more rapid than an inverse square is required for a better fit of the data.

The polarizability changes can be described more adequately if a molecular model is used, one that takes into account the molecular structure of the first hydration sphere. The force acting between the cation and a water molecule in the first hydration sphere is taken to be the sum of ion–dipole, ion–quadrupole, and ion–induced dipole terms. For simplicity, point dipole and point quadrupoles have been assumed, and they are presumed to be located at the center of the oxygen atom. The solvent external to the first hydration sphere is treated as a continuum. The expression for the total force acting between the cation and a water molecule is

$$F = \frac{AZ^2}{nr_c^2} + \frac{2Ze\mu\cos\theta_z}{r^3} + \frac{3ZeG}{2r^4} + \frac{2Z^2e^2\alpha}{r^5} \qquad (4)$$

with[10]

$$G = P_{xx}(3\cos^2\theta_x - 1) + P_{yy}(3\cos^2\theta_y - 1) + P_{zz}(3\cos^2\theta_z - 1) \qquad (5)$$

The principal quadrupole moments, P_{xx}, P_{yy}, and P_{zz} are given by Glaeser and Coulson[11] as −6.554, −5.157, and −5.496 in units of 10^{-26} esu. These refer to the oxygen atom as the center of the coordinate system with the Z axis as the symmetry axis and the XZ plane perpendicular to the plane of the water molecule. The angles θ_x, θ_y, and θ_z are the angles the axes make with respect to the vector directed from the ion to the oxygen atom. The dipole moment for water was taken to be that for the free water molecule, 1.85 D.[12] There are differing conventions in the literature with respect to the definition of dipole moment. The convention used here, $\mu = \Sigma q_i r_{ij}$, implies that the dipole moment is antiparallel to symmetry axis. The water molecules are assumed to be oriented with the symmetry axis directed toward the solvated cation.

The ion–oxygen distances, the four contributions to the force acting between the ion and the oxygen atom, the calculated values of the polarizability changes, $\Delta\alpha_m$, and the differences from $\Delta\alpha_h$ are given in Table III. The distances for the lithium, sodium, and potassium ions are taken from the study of Kristenmacher, Popkie, and Clementi.[13] The KPC study is a Hartree–Fock and Monte Carlo study of small clusters of water surrounding a central ion. For the sodium ion cluster with six water molecules, the sodium–oxygen distance is only 0.01 Å less than the sum of the Pauling radius for the sodium ion and the van der Waals' radius of oxygen, 1.40 Å. The potassium–oxygen distance is greater than the sum of the radii by 0.06 Å. The rubidium- and cesium–oxygen distances were assumed to be 0.09 and 0.10 Å larger than the sum of the radii. The uncertainties in the ion–oxygen distances for the rubidium and cesium ions are unlikely to introduce serious error since uncertainties as large as 0.05 Å for the rubidium ion and 0.10 Å for the cesium ion only introduce uncertainties of approximately 0.01 Å^3 in $\Delta\alpha_m$. Pauling crystal radii were used for the multivalent ions.

The value of r_c, the effective radius of the first hydration sphere, might be approximated by the sum of the ion–oxygen distance and the diameter of a water molecule, 2.80 Å.[14] The smaller value of r + 1.9 Å has been used. The KPC study of the $F(H_2O)_{27}^-$ cluster at 298 K indicates that the average distance for the next 12 oxygen atoms outside the first hydration sphere of six is about r + 2.0 Å. If r_c is based upon the six water molecules closest to the primary hydration sphere, its value would be r + 1.8 Å. Fortunately, the continuum contribution is less than 10% in each case, and the polarizability changes are quite insensitive to the value of r_c. The numerical values that have been suggested for the parameters of eq 4 lead to the expression

$$F_+ = \frac{0.193Z^2}{(r + 1.9)^2} + \frac{1.777Z}{r^3} - \frac{0.518Z}{r^4} + \frac{5.30Z^2}{r^5} \qquad (6)$$

for the force in millidyne and r in angstroms.

In only three cases is the difference between $\Delta\alpha_m$ and $\Delta\alpha_h$ significant. The assumed proportionality between polarizability decreases of the water molecules and F_+ can only be an approximation and the model clearly fails for the aluminum ion.

In addition to the breakdown of the proportionality, the expression for F_+ may also be expected to be inadequate for the aluminum ion. For example, the induced dipole moment implied by the aluminum–oxygen distance of 1.90 Å and the water polarizability of 1.15 Å^3 is 4.6 D, two and one-half times as large as the permanent dipole moment. One would expect the hyperpolarizability of water to become significant before the induced dipole moment became so large. In fact, it is rather surprising that the simple model which is used reproduces the polarizability change for the magnesium ion so well. The calculated value for the dipole moment of water induced by the magnesium ion is 2.6 D, 40% larger than the permanent dipole moment.

The KPC study indicates a coordination number of four for the lithium ion. Table III gives $\Delta\alpha_m$ for coordination numbers of both four and six. Assumption of six-coordinate lithium ions leads to an overestimate of $\Delta\alpha_h$ by 16% whereas good agreement is obtained for four-coordinate lithium ions. In view of

TABLE III: Polarizability Changes on Cation Hydration for the Molecular Model

	r, Å	F_c	F_{id}	$-F_{iq}$	F_{iid}	nF, mdyn	$-\Delta\alpha_m$	$-(\Delta\alpha_m - \Delta\alpha_h)$, Å^3
Li^+	1.94	0.0196	0.2437	0.0366	0.1929	0.4196	0.336[a]	0.006
	2.08	0.0122	0.1975	0.0277	0.1361	0.3181	0.386	0.06
Na^+	2.35	0.0107	0.1369	0.0170	0.0739	0.2045	0.251	−0.01
K^+	2.79	0.0088	0.0818	0.0085	0.0314	0.1135	0.140	−0.01
Rb^+	2.96	0.0082	0.0685	0.0067	0.0233	0.0933	0.116	0.006
Cs^+	3.16	0.0075	0.0563	0.0052	0.0168	0.0754	0.094	0.05
Mg^{2+}	2.05	0.0495	0.4125	0.0587	0.5856	0.9889	1.131	−0.01
Ca^{2+}	2.39	0.0419	0.2603	0.0318	0.2719	0.5423	1.645	0.005
Sr^{2+}	2.53	0.0393	0.2195	0.0253	0.2045	0.4380	1.526	0.07
Ba^{2+}	2.75	0.0357	0.1709	0.0181	0.1348	0.3233	1.392	0.01
Al^{3+}	1.90	0.1203	0.7772	0.1192	1.926	2.704	2.64	0.99

[a] $n = 4$; all others, $n = 6$.

the excellent agreement for the sodium, potassium, and rubidium ions, significant additional evidence has been given for the smaller coordination number.

The values of $\Delta\alpha_m$ for the cesium and strontium ions are in significant disagreement with $\Delta\alpha_h$. Evidence will be given later in the paper that these disagreements reflect errors in the free-ion polarizabilities rather than shortcomings of the present model.

The best fit for the ions other than the aluminum, strontium, and cesium was obtained with C equal to 0.181 mdyn^{-1} and with the solution polarizabilities decreased by $0.19Z$. The standard deviation of $\Delta\alpha_m$ from $\Delta\alpha_h$ for these seven ions is not greatly enhanced with polarizability shifts of $0.18Z$ and $0.20Z$, and with the values of C, respectively, set at 0.180 and 0.175 mdyn^{-1}. However, it begins to climb rapidly for greater differences from $0.19Z$, and this suggests an uncertainty in the partitioning of the molar solution polarizabilities of about $0.02Z$ Å^3.

Anion Solution Polarizabilities

The repartitioning of the molar solution polarizabilities justified in the previous section requires an increase of 0.19 Å^3 in the solution polarizability of each of the halide ions. The revised solution polarizabilities are compared in Table IV with the free-ion polarizabilities obtained in I. The corresponding polarizability changes on hydration are *all significantly negative*. Fajans assumes these changes to be zero for the three heavier halide ions and his partitioning then requires a positive $\Delta\alpha_h$ for the fluoride ion.

As with the cations, the repartitioning implies qualitative differences with respect to polarizability changes on hydration. The forces acting upon anions in solution are smaller than those in crystals, but they are of the same order. Thus, smaller but significant decreases of anion polarizability on hydration may be expected. The results of the previous section indicate that a significant decrease in the polarizability of the water molecules in the first hydration sphere may also be expected.

One of the expressions used in I to describe the variation of halide ion polarizabilities was

$$\alpha = \alpha_g e^{-CF} \tag{7}$$

and it will be used again here. As in the treatment of $\Delta\alpha_h$ for the cations, continuum and molecular models will be used for the force acting between the ion and the solvent.

The two parameters required for the continuum model are C and r_c. The values of r_c were obtained from the enthalpies of hydration, and eq 3 was used to calculate the total force compressing each anion. One value of C was used for the fluoride ion, another value was used for the chloride ion, and a third value was used for the two heavier halide ions. These values were obtained from the variation of the halide ion polarizabilities in the alkali halides, so none of the parameters is adjustable.

TABLE IV: Halide Ion Polarizabilities (Å^3)

	Free		Solution
F^-	1.38 ± 0.1[a]	1.48[b]	1.20
Cl^-	3.95 ± 0.2	4.11	3.65
Br^-	5.22 ± 0.2	5.43	4.96
I^-	7.81 ± 0.3	7.83	7.30

[a] From I. [b] Revised values based on eq 7.

The application of eq 7 to the alkali halides was reinvestigated to define the values used for C. Cubicciotti's[15] data were used in I to define a single value for C, 0.334 mdyn^{-1}. When all of the alkali metal ion polarizabilities, excepting that of the cesium ion, were fixed using the values of α_g listed in Table I, C increased to 0.388 mdyn^{-1}. The polarizability for the cesium ion was left as a variable parameter because of the disagreement between $\Delta\alpha_h$ and $\Delta\alpha_m$ noted in the previous section.

Cubicciotti's data were used in I because he had included the alkali halides with the cesium chloride structure in his study, whereas the more recent study of Fumi and Tosi[16] omits the alkali halides with this structure. It was discovered, however, that there was essentially no change in the parameters whether or not the polarizabilities of CsCl, CsBr, and CsI were included in the least-squares fit to the crystal polarizabilities. Fumi and Tosi's data yielded a value of 0.445 mdyn^{-1} for C and also fit the crystal polarizabilities with a standard deviation of 0.81% vs. the standard deviation of 0.94% obtained using Cubicciotti's data. Thus, the more recent work of Fumi and Tosi is considered to give the more reliable values for C.

When the value of C for the fluoride ion was allowed to vary separately, σ was reduced to 0.76%. The corresponding value obtained for the cesium ion polarizability was 2.43 Å^3. Because the value of α_∞ for sodium iodide listed by Wilson and Curtis[17] was one of the more uncertain, and because the polarizability of sodium iodide was found to be consistently the polarizability least well fit, that polarizability was omitted to give a standard deviation of 0.56%. There was a slight further reduction of α to 0.55% when $C(Cl^-)$ was allowed to vary separately. The parameter allowing for the values of C to change with crystal structure was found to remain in the neighborhood of unity in several of the preliminary fittings of the po-

larizability data, and no provision for a change of C with crystal structure was made in the final fitting, a fitting for which polarizability of the cesium ion was also fixed at 2.43 Å^3. The further decrease in σ obtained when the values of C for each of the four anions were allowed to vary separately was insignificant.

The value of C for the fluoride ion, the value for the chloride ion, and common value for the two heavier halide ions were, respectively, 0.477, 0.442, and 0.421 mdyn^{-1}. The corresponding values obtained for the polarizabilities of the four halide ions are listed in Table IV, and are felt to be more reliable estimates of the true free-ion polarizabilities than those obtained in I.

Since the value obtained for C increased significantly when the polarizabilities of the potassium and rubidium ions were fixed at their free-ion values, the effect of a 0.02 Å^3 uncertainty in these values upon the values for C was determined. That this uncertainty is a reasonable estimate of the uncertainty for these ions was shown in the previous section. The corresponding uncertainty in the C values was found to be 4%.

The relative polarizability decreases calculated for the halide ions using the continuum model are shown in Table V. Also listed are the polarizability decreases for the water obtained using eq 2 with n equal to six. The simplicity of the model and the absence of any variable parameters argue strongly that the polarizability of a free halide ion is significantly greater than the polarizability of the halide ion in solution.

In order to treat the first hydration sphere discreetly, its structure must be defined. Two models have been proposed. The orientation of the water molecules which maximizes the ion–dipole, ion–induced dipole, and ion–quadrupole interactions is the inverse of the orientation assumed for cations. This orientation was assumed by Halliwell and Nyburg[18] in their description of enthalpies of ion hydration. The anion lies in the planes of each of the hydrating water molecules and the hydrogen atoms are equidistant from the anion.

The alternate model of Bernal and Fowler[19] assumes that hydrogen bonding interactions with the anion are maximized. Only one hydrogen atom lies between the oxygen atom and the anion, and the anion–hydrogen–oxygen angle is 180°. The angle between the symmetry axis of the water molecule and the radial axis passing from the anion through the oxygen atom is half of the water angle, 52.2°.

The KPC results demonstrate that the latter model is correct for the fluoride ion and provide very strong evidence that it is correct for the chloride ion. Hertz and Raedle[20] provide additional evidence for this less symmetrical model. Their NMR study of potassium fluoride solutions indicates that the dipole axis of water is oriented about 50° with respect to the radial axis.

The structure of the solvent around the bromide and iodide ions is not known. The weaker hydrogen bonds may not be sufficiently strong to stabilize the linear configuration. In addition, the coordination number of the bromide and iodide ions may exceed six.[13] In the absence of definitive information, there seems no better course than to assume the same model for each of the four halide ions. The hydration number has been taken to be six and the effect of hydrogen bonding upon the polarizability, beyond stabilizing the assumed structure, has been ignored. The value of r_c has again been taken to be r + 1.9 Å. With these parameters, eq 4 becomes

$$F_- = \frac{0.193}{(r + 1.9)^2} + \frac{1.089}{r^3} + \frac{0.975}{r^4} + \frac{5.30}{r^5} \qquad (8)$$

TABLE V: Polarizability Changes on Anion Hydration for the Continuum Model

	r_c, Å	nF, mdyn	$-\Delta\alpha_c$, %	$-\Delta\alpha(H_2O)$, Å^3
F^-	1.47	0.534	22.5	0.11
Cl^-	2.05	0.275	11.4	0.06
Br^-	2.14	0.253	10.1	0.05
I^-	2.60	0.171	6.9	0.04

The value of the fluoride ion–oxygen distance was taken from the KPC study of $F(H_2O)_{27}^-$ at 298 K. This value was observed to be midway between the ion–oxygen distances for the symmetrical clusters $F(H_2O)_6^-$ and $F(H_2O)_7^-$ at 0 K. Accordingly, the value of r for the chloride ion was taken to be the average of the ion–oxygen distances at 0 K for the six- and seven-coordinate species, 3.42 and 3.46 Å, respectively.

The values of r for the bromide and iodide ions were estimated by assuming the repulsive interaction between the anions and the hydrogen atom to be described by the Born exponential form. This leads to the relation

$$F_- e^{(r-r_-)/\rho} = S \qquad (9)$$

in which r_- is the radius for the halide ion and the radius for the hydrogen atom and the oxygen–hydrogen distance are absorbed in the constant S. The value of the hardness parameter ρ, 0.3394 Å, was taken from the paper by Fumi and Tosi.[16] When S was determined using the ion–oxygen distance for the chloride ion, the distances calculated for the bromide and iodide ions were, respectively, 3.62 and 3.89 Å. The value obtained for the fluoride ion distance was 2.78 Å in good agreement with the 2.75 Å of the KPC study.

Table VI lists the components of F_-, the total force on the anion presuming a coordination number of six, the relative polarizability changes of the halide ions on hydration, and the corresponding polarizability decrements of the solvent. The anion polarizability changes average less than 20% higher than the changes obtained using the continuum model. As may have been expected, this is much better agreement than the agreement between the continuum and molecular models for the cations for which the adjustable parameters C differ by more than a factor of 2.

The forces calculated using the continuum model are, respectively, 21, 11, and 2% lower than those calculated using the molecular model for the fluoride, chloride, and bromide ions. The periodic trend is broken by the case of the iodide ion for which the force is 18% lower than that calculated by the molecular model. The continuum model becomes exact in the limit of large r_c. If it is assumed that the effective dielectric constant has become equal to the bulk dielectric constant for distances larger than r_c for the bromide ion, the value of r_c for the iodide ion should be larger than that for the bromide ion by the difference in the ionic radii. The difference in the Fumi and Tosi radii[16] for these two ions leads to a value of r_c for the iodide ion of 2.33 rather than 2.60 Å, and to a force of 0.213 mdyn, a force only 2% larger than that obtained using the molecular model. If the difference between the Pauling radii is used, the two models agree to three significant figures. The convention used by Pauling to fix the absolute values of the ion radii makes his set of radii more nearly additive than the set used by Fumi and Tosi. Since additivity has been assumed in the above calculations, it might be argued that the use of Pauling radii is more appropriate.

The agreement obtained in the calculation of the force using the alternate method for the estimation of r_c is significant for two reasons. First, because of the known asymptotic behavior

TABLE VI: Polarizability Changes on Anion Hydration for the Molecular Model

	r, Å	F_c	F_{id}	F_{iq}	F_{iid}	nF, mdyn	$-\Delta\alpha_m$, %	$-\Delta\alpha(H_2O)$, Å^3
F^-	2.75	0.0089	0.0524	0.0170	0.0337	0.672	27.4	0.14
Cl^-	3.44	0.0068	0.0268	0.0070	0.0110	0.310	12.8	0.06
Br^-	3.63	0.0063	0.0228	0.0056	0.0084	0.259	10.3	0.05
I^-	3.89	0.0058	0.0185	0.0043	0.0060	0.208		0.04

of the continuum model, the uniform periodic trend of the numerical differences between the two calculations indicates that the molecular model is adequate without any need for an arbitrary scaling parameter. Secondly, there is the implication that the structure around the iodide ion in aqueous solution differs from that assumed in the molecular model, so the continuum model must be used for the estimation of the perturbation of the iodide ion polarizability.

The effect of hydrogen bonding upon the force acting between the halide ions and the first hydration sphere was ignored in eq 8. The perturbation of the polarizability is significant, however, and cannot be ignored. This becomes evident through the calculation of idealized solution polarizabilities, polarizabilities that would obtain in the absence of solvent polarizability changes and polarizability changes arising from hydrogen bond formation.

The idealized solution polarizabilities, α_s^i, may be calculated using eq 7 and the free-ion polarizabilities determined from the crystal polarizabilities. The value obtained for the fluoride ion is 1.07 Å^3. Perhaps slightly more accurate is the value calculated from the polarizability of the fluoride ion in sodium fluoride. The force compressing the fluoride ion in sodium fluoride most nearly approximates the force calculated for the fluoride ion using eq 8. The value so obtained is 1.06 Å^3. The forces calculated for the three heavier halide ions are all less than the forces these ions experience in the cesium halides, so the crystal polarizabilities of the halide ions in these salts were used to calculate the idealized solution polarizabilities. These polarizabilities, the differences from the solution polarizabilities of Table IV, and $\Delta\alpha_H$, the polarizability changes arising from hydrogen bond formation, are listed in Table VII. The latter were calculated assuming the difference between a solution polarizability and the corresponding idealized solution polarizability to be the sum of $\Delta\alpha(H_2O)$ and $\Delta\alpha_H$.

TABLE VII: Perturbations of Idealized Solution Polarizabilities (Å^3)

	F^-	Cl^-	Br^-	I^-
α_s^i	1.06	3.59	4.88	7.28
$\alpha_s - \alpha_s^i$	0.14	0.06	0.08	0.02
$\Delta\alpha(H_2O)$	−0.14	−0.06	−0.05	−0.04
$\Delta\alpha_H$	0.28	0.12	0.13	0.06

Discussion

The polarizabilities that have been obtained for the free cations and anions may be checked for internal consistency through the use of Fajans' ratios. Maintenance of a systematic variation of these ratios provides little guidance with respect to the fluoride ion, but it can provide significant guidance with respect to the relative values of the three heavier halide ions. Because the noble gas polarizabilities are well known, and because the ratios monotonely decrease with atomic number and have a lower bound of unity, maintenance of a systematic variation provides rather tight bounds upon the polarizabilities of the cations. A set of polarizabilities and the corresponding ratios are given in Table VIII. The noble gas polarizabilities are those of Teachout and Pack.[21]

Two significant changes of cation polarizabilities are indicated by the ratios, a change of the cesium ion polarizability to 2.48 Å^3 and a change of the strontium ion polarizability to 0.92 Å^3. Both of these values are only 0.01 Å^3 higher than the values predicted by the polarizability changes on hydration. The ratios also indicate a decrease of 0.01 Å^3 for the rubidium ion and an increase of 0.01 Å^3 for the barium ion. With these four changes in the estimates of the free-ion polarizabilities, the polarizability changes on hydration of the five alkali metal and the four alkaline earth metal ions are all reproduced to 0.01 Å^3. Since the free-ion polarizabilities have all been independently obtained, the agreement has been achieved using only two adjustable parameters, the constant $C(H_2O)$ and the correction to Fajans' partitioning of the molar solution polarizabilities. The simple model that has been proposed has proved more effective than was anticipated. The overall consistency that has been obtained suggests that the free cation polarizabilities of Table VIII are accurate to within about 1%.

The cesium ion polarizability indicated by the ratios is 0.05 Å^3 higher than the revised crystal value given in the previous section. The recent x-ray diffraction study of potassium bromide by Meisalo and Inkinen[22] indicates that *both* the potassium and bromide ions are compressed in the crystal relative to the free ions. Thus, the difference between the two cesium ion polarizabilities may be attributed to compression of the cesium ion in the cesium halides. The relative difference indicated by the ratios is much larger for the strontium ion. The difference probably has its primary source in the relatively poor fit in I of the polarizabilities of the alkaline earth chalcogenide crystals.

A test for the consistency of the anion polarizabilities in addition to Fajans' ratio test is obtained if the relative decreases on crystal and solution formation are required to decrease periodically. Table IX was constructed using the revised free-ion polarizabilities of Table IV. The perturbations decrease monotonely with atomic number.

Fajans' ratio test indicates a value of 7.90 Å^3 for the polarizability of the iodide ion. The difference between the predicted polarizability and the polarizability determined from the alkali iodides is 1%. This is the same as the uncertainty suggested for the cation polarizabilities used to define most of the ratios. The polarizability of 7.90 Å^3 for the iodide ion leads to a calculated decrease in iodide ion polarizability on formation of sodium iodide of 21.6%. This decrease breaks the periodic trend slightly, so it does not appear that the polarizability of the iodide ion can be larger than about 7.90 Å^3 without the polarizabilities of the chloride and bromide ions being coordinately larger.

The differences between the free anion polarizabilities and the solution polarizabilities have been attributed to three perturbations: a decrease of anion polarizability arising from anion compression, a decrease in solvent polarizability arising from solvent compression, and a polarizability change at-

TABLE VIII: Fajans' Ratios

	α_-	$Q'(-/0)$	α_0	$Q'(0/+)$	α_+	$Q'(+/++)$	α_{++}
Ne	1.48	3.75	0.395	2.50	0.158	2.03	0.078
Ar	4.11	2.505	1.641	1.942	0.845	1.625	0.52
Kr	5.43	2.190	2.480	1.771	1.40	1.522	0.92
Xe	7.90	1.936	4.044	1.631	2.48	1.425	1.74
	Q''				Q'''		
Ne	1.499	1.239					
				1.496	1.287	1.247	
Ar	1.290	1.195					
				1.144	1.096	1.068	
Kr	1.236	1.164					
				1.121	1.086	1.068	
Xe	1.198	1.144					

TABLE IX: Anion Polarizability Decreases on Crystal and Solution Formation (%)

	F^-	Cl^-	B^-	I^-
Li^+	40.1	30.1	26.5	25.0
Na^+	31.1	24.0	21.5	20.9
K^+	22.5	18.9	17.4	15.8
Rb^+	20.1	17.0	15.1	14.0
Cs^+[a]	19.3	15.3	14.2	12.5
Solution	18.9	11.2	8.7	6.8

[a] The cesium halide crystal polarizabilities are all those for the NaCl structure as determined in I.

tending hydrogen bond formation. Since delocalization of the halide ion electrons into the hydrogen bond may be expected to enhance polarizability, the values of $\Delta\alpha_H$ should be positive as they are seen to be. They should also decrease monotonely. In view of the fact that the fitting to the crystal polarizabilities was to within a standard deviation of about 0.02 Å^3 and the fact that Fajans' indicated the dispersions of the halide ion polarizabilities from their values for the sodium D line to be provisional, the slight break in the trend for the bromide ion is not significant.

The most important of the three perturbations is that arising from the compression of the halide ion. Polarizability enhancement arising from hydrogen bond formation is about twice as important as the polarizability decrement of the solvent. Both of these perturbations are small for the iodide ion. The trends in the perturbations make it unlikely that the absolute value of the iodide ion polarizability deviates greatly from 7.83 Å^3. The adequacy of the continuum model for the iodide ion was supported in the previous section. That it predicts an idealized solution polarizability for this ion only 0.02 Å^3 different from the experimental solution polarizability is striking. One might have expected nonelectrostatic factors to be more important. An uncertainty of 1% is assigned to the polarizability of the iodide ion.

Scaling of the coupled-Hartree–Fock and Thomas–Fermi polarizabilities of the alkali metal cations by the ratio of the experimental to the theoretical polarizabilities for the corresponding noble gases was justified empirically in I. Similar scaling of the CHF polarizability of the chloride ion yields a predicted polarizability of 4.13 Å^3 in excellent agreement with the empirical polarizability of 4.11 Å^3. Scaling of the CHF polarizability of the fluoride ion yields a polarizability of 1.58 Å^3, 0.10 Å^3 higher than the empirical polarizability.

The data in the literature on the pressure variation of the molar polarizabilities of the alkali halides are sparse and much of it is rather inaccurate. However, the application of eq 7 to the available data suggests that the effective values of C decrease as the force compressing the halide ion increases. Since average values were used in this study, the polarizabilities that have been obtained may be somewhat low. Perhaps the empirical estimate for the fluoride ion, the ion for which the polarizability perturbation is the greatest, is low by about 0.1 Å^3 as suggested by the above scaling. The CHF polarizability for the fluoride ion of 1.40 Å^3 may be taken as a lower limit.[23] Error limits of 0.08 Å^3 are suggested for the empirical polarizability of the fluoride ion. Uncertainties of 0.06 and 0.08 are suggested, respectively, for the chloride and bromide ions. For all four halide ions, the empirical polarizabilities of the halide ions are considered more likely to be low than high.

The suggestion of Wilson and Curtis[17] that the change of polarizability experienced by an atom or ion on compression be proportional to the compressive force implies eq 7, an equation which must be valid for small perturbations. The importance of second-order terms has not yet been ascertained, but the linear approximation has been quite adequate to show how solution and crystal polarizabilities may be consistently related. The polarizabilities obtained for the alkali metal, alkaline earth metal, and halide ions are also consistent with polarizabilities determined by ab inito calculations. Of special note is the resolution of the discrepancy between the CHF polarizability of the fluoride ion and the solution-based polarizability of Fajans.

The calculation of enthalpy changes attending ion hydration is an old and difficult one, one which continues to receive attention, and one for which there is a voluminous literature.[9,10,13,14,18,19] The calculation of the polarizability changes on ion hydration is a simpler problem because of the relative unimportance of the continuum term, and because the static approximation may be expected to be a good one for the first hydration sphere. An expression for the electrostatic contribution to the enthalpy of hydration may be obtained by integration of eq 4. In that expression, the continuum term is one of the more important terms (24% in the case of the potassium ion, 36% in the case of the chloride ion). The dynamic character of the solvent structure outside the first hydration sphere and the slow convergence of the continuum term make the calculation of enthalpies of hydration much more difficult even within the framework of the simplified models used here.

Acknowledgment. This work is part of a project being supported by the Research Corporation.

References and Notes

(1) Work done as part of a project being supported by the Research Corporation.
(2) K. Fajans and G. Joos, *Z. Phys.*, **23**, 1 (1924).
(3) K. Fajans, *Z. Phys. Chem. B*, **24**, 103 (1934).
(4) K. Fajans and N. Bauer, *J. Am. Chem. Soc.*, **64**, 3023 (1942).
(5) J. Lahiri and A. Mukherji, *Phys. Rev.*, **153**, 386 (1967); **155**, 24 (1967).
(6) K. Fajans, *J. Phys. Chem.*, **74**, 3407 (1970).
(7) F. Weinhold, *Proc. R. Soc. London, Ser. A*, **327**, 209 (1972).
(8) W. M. Latimer, K. S. Pitzer, and C. M. Slansky, *J. Chem. Phys.*, **7**, 108 (1939).
(9) H. L. Friedman and C. V. Krishnan, *Water, Compr. Treatise*, **3**, 55 (1973).
(10) B. E. Conway, "Physical Chemistry, an Advanced Treatise", Vol. IXA, H. Eyring, Ed., Academic Press, New York, N.Y., 1970, p 16.
(11) R. M. Glaeser and C. A. Coulson, *Trans. Faraday Soc.*, **61**, 389 (1965).
(12) A. L. McClellan, "Tables of Experimental Dipole Moments", W. H. Freeman, San Francisco, Calif., 1963, p 25.
(13) H. Kistenmacher, H. Popkie, and E. Clementi, *J. Chem. Phys.*, **61**, 799 (1974).
(14) S. Goldman and R. Bates, *J. Am. Chem. Soc.*, **94**, 1476 (1972).
(15) D. Cubicciotti, *J. Chem. Phys.*, **31**, 1646 (1959); **33**, 1579 (1960); **34**, 2189 (1961).
(16) M. P. Tosi and F. G. Fumi, *J. Phys. Chem. Solids*, **25**, 45 (1964).
(17) J. N. Wilson and R. M. Curtis, *J. Phys. Chem.*, **74**, 187 (1970).
(18) H. F. Halliwell and S. C. Nyburg, *Trans. Faraday Soc.*, **59**, 1126 (1963).
(19) J. D. Bernal and R. H. Fowler, *J. Chem. Phys.*, **1**, 515 (1933).
(20) H. G. Hertz and C. Raedle, *Ber. Bunsenges. Phys. Chem.*, **77**, 521 (1973).
(21) R. R. Teachout and R. T. Pack, *Atomic Data*, **3**, 195 (1971).
(22) V. Meisalo and O. Inkinen, *Acta Crystallogr.*, **22**, 58 (1967).
(23) H. D. Cohen, *J. Chem. Phys.*, **45**, 10 (1966).

Conductance–Concentration Function for Associated Symmetrical Electrolytes. Supplementary Comments

Raymond M. Fuoss

Sterling Chemistry Laboratory, Yale University, New Haven, Connecticut 06520

(Received April 29, 1976)

Publication costs assisted by Sterling Grant

Comparison of the Fuoss 1975 conductance equation with previous equations shows that is the only one which is based on a model which rigorously permits the use of macroscopic dielectric constant D and viscosity η in the theoretical calculation of relaxation field and electrophoresis. Earlier theories, based on the primitive model, set D and η at the surface of an ion (where the field is of the order of hundreds of megavolts per centimeter) equal to the macroscopic values. Practical use of the equation is then discussed (limitations regarding concentration range, problems of slow convergence, etc.). Finally, several misprints in the original paper are corrected.

The purposes of this communication are: (1) to present a critical comparison of the 1975 conductance equation[1,2] with earlier (now obsolete) equations; (2) to describe the practical application of the equation for analysis of data; and (3) to list several additional corrections to the 1975 paper.

Conductance as a function of concentration is given by the equation

$$\Lambda(c) = \gamma[\Lambda_0(1 - \Delta X/X) - \Delta\Lambda_e] \quad (1)$$

where $\Lambda(c)$ is equivalent conductance, $\Lambda_0 = \Lambda(0)$, ΔX is relaxation field, X is external field, and $\Delta\Lambda_e$ is the electrophoretic term. The fraction γ is the ratio, to the stoichiometric centration c, of the concentration $c\gamma$ of ions which are assumed to contribute to net transport of charge. The physical interpretation of γ clearly depends on the model chosen to represent the system: for the classical Debye–Hückel model, $\gamma = 1$, independent of concentration; for the primitive model, $(1 - \gamma)$ is that fraction of solute present as contact pairs; for the Bjerrum model, $(1 - \gamma)$ is that fraction of ions whose center-to-center distances lie in the range $a \leq r \leq \beta/2 = e^2/2DkT$; for the Fuoss model[3], $(1 - \gamma)$ is that fraction of ions for which $a \leq r \leq R$, where R is the diameter of the Gurney sphere around a given ion, outside of which the solvent by definition is described by its macroscopic dielectric constant D and viscosity η. For the last model, we assume

$$1 - \gamma = K_A c\gamma^2 f^2 \quad (2)$$

(Note the introduction of a new symbol here; K_A means the association constant determined from conductance data; $(1 - \gamma)$ includes both contact pairs and solvent-separated pairs. In general, $K_A \leq K$, where K is the association constant determined by spectroscopic methods which can only count contact pairs.)

For the primitive model (rigid charged spheres of diameter a in a continuum described by D and η), the relaxation field is given by

$$\Delta X = \text{grad}_x \psi'(a) \quad (3)$$

(where $\psi'(r)$ is the potential of the relaxation field) and the electrophoretic term by

$$\Delta\Lambda_e = [A/\eta(DT)^{1/2}] \int_a^\infty r^2 \rho(r)\, dr \quad (4)$$

where $\rho(r)$ is the average charge density of the ionic atmosphere. Note that a appears explicitly in the definitions of both ΔX and $\Delta\Lambda_e$. Equation 3 is the classical equation first derived by Debye and Hückel in 1923 and (4) is the 1928 Onsager equation; these equations have been used in all theoretical treatments of conductance prior to 1975. While they do correctly describe the behavior of the *model*, they cannot

describe any real physical system at nonzero concentrations because they set $D(a) = D$ and $\eta(a) = \eta$. For $r = 2.5 \times 10^{-8}$ cm, the field strength e/r^2 is about 0.8×10^6 esu/cm; at the surface of an ion, the field strength is therefore of the order of hundreds of megavolts per centimeter. At such field strengths, the dielectric constant certainly cannot equal the bulk value (if, indeed, the concept of dielectric constant has any meaning whatsoever at $r = a$!). The classical equations do predict the observed limiting slopes for $\Lambda - c^{1/2}$ curves; this is simply because the a parameter does not appear in the final expressions for $\Delta X(0)$ and $\Delta\Lambda(0)$. In fact, the limiting slope can be calculated for point ($a = 0$) charges, the ultimate in simplicity for models. However description of real systems for $c \neq 0$ requires the use of distance parameter in the mathematical development ("higher terms"), and as long as one uses the primitive model, the use of $D(a) = D$ and $\eta(a) = \eta$ is mandatory.

Both ΔX and $\Delta\Lambda$ are the consequences of long-range *volume* forces acting on the reference ion, averaged over *all* the ions surrounding that ion; as such, no ion-specific parameters (such as "ion size") should appear in their description. The 1975 model for the first time permits a calculation of ΔX and $\Delta\Lambda$ which meets this specification: ΔX is defined as the negative gradient of $\psi(r)$ at $r = R$, and $\Delta\Lambda$ as proportional to a definite integral taken between limits $r = R$ and $r = \infty$. (Equations 3 and 4 with a replaced by R.) Recalling the definition of R, it is clear that the macroscopic values of D and η may be used in calculating $\Delta X(R)$ and $\Delta\Lambda(R)$. For the 1975 model, ΔX and $\Delta\Lambda$ are the long-range electrostatic and hydrodynamic effects on the central ion averaged over all the *unpaired* ions of the ionic atmosphere; the paired ions in the sphere $R \leq r \leq \infty$ surrounding the central ion are seen as dipoles by the latter and the forces they exert are neglected as $1/r^4$ forces in contrast to the $1/r^2$ Coulomb forces due to the unpaired ions. What happens inside the spheres of diameter R which contain paired ions is irrelevant to the computation of volume forces acting on unpaired ions; these events are, of course, determinative for the association process and their description must necessarily include system-specific parameters such as size, shape, and charge distribution of both ions and solvent molecules. Briefly summarized, the 1975 model separates the effects of long-range and short-range forces and thereby permits a rigorous theoretical treatment of the former.

Symbolically, the 1975 equation may be written

$$\Lambda = \Lambda(c; \Lambda_0, K_\Lambda, R) \tag{5}$$

The explicit equation is long and complicated; for practical use, the leading terms in $c^{1/2}$ and $c \ln c$ were kept explicit, and interpolating polynomials (which match the explicit functions within 0.01%) were constructed for the higher terms. Based on these, several computer programs have been written[4] which derive numerical values for the three parameters, given a set of (c_j, Λ_j) data, $j = 1, 2, \ldots, N$.

The basic program starts with preliminary values of Λ_0 (from Walden's rule or by freehand extrapolation of a Λ–$c^{1/2}$ plot), K_Λ (estimated by the Ostwald–Arrhenius equation $K_\Lambda \approx (1 - \Lambda/\Lambda_0)/c(\Lambda/\Lambda_0)^2$ using the data for the point at highest concentration), and R (set equal to β for $D \geq 30$ and to $\beta/2$ for $D \leq 30$). Then by successive approximations, the computer seeks those values of Λ_0, K_Λ, and R which minimize

$$\sum = \{\sum[\Lambda(\text{calcd}) - \Lambda(\text{obsd})]^2\}^{1/2} \tag{6}$$

where successive values of Λ(calcd) are obtained by adding algebraically increments

$$\delta\Lambda = (\partial\Lambda/\partial\Lambda_0)\delta\Lambda_0 + (\partial\Lambda/\partial K)\delta K + (\partial\Lambda/\partial R)\delta R \tag{7}$$

to the preceding values. The standard deviation σ is defined as

$$\sigma = \sum/(N - 3)^{1/2}$$

Geometrically described, the minimum in the four-space $\sigma = F(\Lambda_0, K_\Lambda, R)$ is the target. For many sets of data which have been analyzed, the program converges within three or four cycles to $\Lambda_0 \pm 0.01\%$, $K_\Lambda \pm 2\%$, $R \pm 2\%$. We shall consider next cases for which convergence does not occur within 10 cycles.

Failure to converge may be the consequence of a poor choice of concentration range. Consider first the case of too narrow a concentration range. In principle, the conductance function can be written

$$\Lambda(\text{obsd}) = \Lambda_0 - Sc^{1/2} + Ec \ln \tau + a_1 c + a_2 c^{3/2} + \ldots \tag{8}$$

where S and E are given by theory. Define

$$Y(c) = \Lambda(\text{obsd}) + Sc^{1/2} - Ec \ln \tau \tag{9}$$

It is clear that Λ_0 is $Y(0)$ and that it can be determined by extrapolation on a Y–c plot. Now define

$$Z(c) = Y(c) - \Lambda_0 \tag{10'}$$

$$= a_1 c + a_2 c^{3/2} + \ldots \tag{10''}$$

The quantity $Z(c)$ is what is left of Λ(obsd) after one subtracts what is known; for systems whose conductance curves lie near the limiting tangent, $Z(c)$ is of course very much smaller than the total observed conductance. Data of 0.01% precision in Λ(obsd) can easily be uncertain to several percent in $Z(c)$. The above separation of Λ(obsd) into its components shows that K_Λ and R are derived by the computer from $Z(c)$; obviously, too narrow a concentration range cannot lead to reliable values of these two parameters. The data should therefore span at least a decade in concentration; $c(\text{max}) \geq 10c(\text{min})$. The lowest concentration should not be too high, else the distance from $c(\text{min})$ to $c = 0$ will be too great for reliable extrapolation to Λ_0. On the other hand, if $c(\text{max})$ is too low, a good value of Λ_0 may usually be obtained, but at low concentrations, the curve lies near the limiting tangent and since K_Λ and R are essentially determined by the difference between Λ(obsd) and the tangent, the values become uncertain. The highest concentration should not exceed

$$c(\text{max}) = 2 \times 10^{-7} D^3 \tag{11}$$

the concentration above which ion pairs become statistically undefinable.[5] At higher concentrations, the effects of three-ion interactions must be included in $\Lambda(c)$.

The program sometimes fails to converge when K_Λ is numerically small (≤ 0.5). The program starts with an initial estimate, and then calculates a sequence of δK_j's, in search of a final $K_\Lambda = K_\Lambda + \delta K_n$. If K_Λ is small, it may happen that one of the δK's is negative and greater than the current K_Λ value; then the computer delivers a negative number for $K_{j+1} = K_j + \delta K_j$, and the calculation is terminated by a "STOP IF ($K < 0$)" command. For such cases, a scanning program is used: the computer seeks values of Λ_0 and R which minimize σ for a sequence of values $K_\Lambda = 0.0, 0.1, \ldots, 1.0$. Then a plot of σ vs. K_Λ is used to locate the minimizing value for K_Λ and the corresponding values of Λ_0 and R are computed.

Another failure of the three-parameter program to converge may occur when the minimum in the four-space is shallow.[6] Since $\partial\Lambda/\partial K < 0$ and $\partial\Lambda/\partial R > 0$ [i.e., have opposite effects on

Λ(calcd)], successive increments $(\partial\Lambda/\partial K)\delta K$ and $(\partial\Lambda/\partial R)\delta R$ can be nearly equal and of opposite sign; the program then "see-saws" in an interminable loop. In such cases, a scanning program is again used: the computer seeks values of Λ_0 and K_Λ which minimize σ for a sequence of R values. The minimizing value of R is located on a σ–(β/R) plot, and then the corresponding values of Λ_0 and K_Λ are calculated. It sometimes happens that the σ–(β/R) plot has a very shallow minimum, or within experimental error, it may be practically a horizontal line with no discernable minimum. This situation has been observed for systems with both high and low dielectric constants. In the former case, the successive increments δR are numerically small, due to numerically compensating positive and negative terms in $\partial\Lambda/\partial R$, which depend on D, η, and the three parameters, and consequently by numerical coincidence, some elements in the determinants nearly vanish, with the result that a wide band of paired values of K_Λ and R can be found, *all* of which give a "good" fit to the data. In these cases, R is fixed at $R = \beta$, because we have found $R \approx \beta$ in many cases where the three-parameter equation did converge. For solvents of low dielectric constant, the change of Λ with concentration is primarily controlled by K_Λ $[(|\partial\Lambda/\partial K|) \gg (|\partial\Lambda/\partial R|)]$ and again a wide range of paired K_Λ–R values gives a good fit to the data. In these cases, R is set equal to $\beta/2$, because we have found $R \approx \beta/2$ for $D < 25$ in those cases where the three-parameter equation converged or the σ–(β/R) curve showed a distinct minimum.

It must be emphasized that arbitrarily setting $R = \beta$ at high D and $R = \beta/2$ at lower D in those cases where the σ–(β/R) curve is nearly flat is *not* a change in the model, because these values are acceptable solutions of the three-parameter equation in the corresponding ranges of dielectric constant. The fact that other values also satisfy the equation is beside the point. The situation of a flat σ–(β/R) curve is merely the consequence of numerical coincidence at high D and of relative insensitivity of Λ to R at low D. Selecting $R = \beta$ or R to $\beta/2$ is justified by the facts that values near these are found for systems for which the programs do converge, and that the values β at high D and $\beta/2$ at low D lie in the range of R values for which the respective σ–β/R plots are flat. To set $R = \beta$ or $\beta/2$ in general, however, would in effect reduce the equation to a two-parameter equation based on a model in which paired cations were those which find nearest unpaired partners at distances β or $\beta/2$. The three-parameter equation is based on a model in which paired ions satisfy the condition $a \leq r \leq R$, where R is a parameter *determined by the data* (i.e., not arbitrarily fixed a priori).

The physical interpretation of a flat σ–β/R plot (assuming that it is not the trivial consequence of too narrow or too low a concentration range) is found in the mass action eq 2, where the product γf appears. If R is made larger, more ions are counted as pairs and therefore γ decreases. However, more pairs means fewer unpaired ions; that is, a reduced ionic strength and therefore a numerically greater activity coefficient. The net result is that the product γf is not very sensitive to R, provided that the appropriate value of K_Λ is used to compute γ. A flat σ–β/R plot simply means that a continuous band of paired K_Λ–R values, rather than a unique solution, is found for those systems for which the last two terms of (7) mutually cancel.

One further idiosyncrasy of the equation must be mentioned. Occasionally we have found unrealistically small or large values for R. In all of these cases, a plot of σ against (β/R) shows two minima, one at a patently absurd value and one near β or $\beta/2$. In every case, the value of σ at the former R was much greater than the value at the latter and also much greater than the estimated experimental error. This is merely a case of multiple roots, and one must rely on physical interpretation to decide between them.

Corrections

Thanks to Dr. Alan D. Pethybridge (University of Reading) several more misprints in the equations of ref 1 have been located. Dr. Pethybridge wrote a computer program based on the (corrected[2]) explicit equations. The program produced results which obviously were incorrect. An intercomparison of his Fortran equations, the published equations, and my original work sheets revealed four more discrepancies between my final equations and the printed version. Dr. Pethybridge made the corresponding corrections to his program: the corrected program now gives results which agree exactly with the results obtained using the program based on the interpolating polynominals which were constructed to match numerically the long and complicated explicit function $\Lambda(c)$. For a typical set of data, the explicit program required 47.5 s to converge, compared to 8 s for the short program.

The additional corrections follow:

Page 535. Equation 3.28, line 2, replace | by) to give . . . + $t^3/3)$; line 5, delete minus sign in coefficient to give . . . − $(qe^{-qt}/2)$.

Page 536. Equation 3.45, insert /3 and change central sign to give . . . $(1 + 2t + 2t^2/3 + t^3/3) - (1 + t +$.

References and Notes

(1) R. M. Fuoss, *J. Phys. Chem.*, **79**, 525 (1975).
(2) R. M. Fuoss, *J. Phys. Chem.*, **79**, 1983 (1975).
(3) R. M. Fuoss, *Proc. Nat. Acad. Sci. U.S.A.*, **71**, 4491 (1974).
(4) R. M. Fuoss, "Computer Programs for Chemistry", Vol. 5, K. B. Wiberg, Ed., Academic Press, New York, N.Y., 1976.
(5) R. M. Fuoss, *J. Am. Chem. Soc.*, **57**, 2604 (1935).
(6) The sharpness of a minimum in the σ–β/R curve is of course a matter for arbitrary definition. For present purposes, we consider a minimum "sharp" if values of σ calculated at [R(min) ±5%] exceed σ(min) by at least 0.01 cm^2 Ω^{-1} mol^{-1}. See Figure 6, ref 1.

Studies of Nickel–Tungsten–Alumina Catalysts by X-Ray Photoelectron Spectroscopy

Kung T. Ng and David M. Hercules*

Department of Chemistry, University of Georgia, Athens, Georgia 30602 *(Received January 19, 1976; Revised Manuscript Received June 28, 1976)*

Publication costs assisted by the National Science Foundation

Nickel–tungsten catalysts supported on γ-alumina have been studied by ESCA. Various treatments such as reduction and sulfiding were carried out on the catalyst as a function of time and temperature. Chemical species present on the catalyst surface were identified and measured semiquantitatively. For the oxidic nickel–tungsten–alumina catalyst, nickel sesquioxide and nickel aluminate were detected on the catalyst surface. Tungsten was found to form a stable interaction complex with the γ-alumina support. When the catalyst was reduced at 500 °C in hydrogen, tungsten remained in the +6 oxidation state and was not reduced even after prolonged treatment. On the other hand, nickel was readily reduced to nickel metal. Sulfiding of the catalyst was carried out at different temperatures using different sulfiding mixtures. The sulfiding rate was found to increase with increasing temperature or hydrogen sulfide concentration. The oxidic catalyst was found to be very active in hydrodesulfurizing thiophene. When the catalyst was sulfided with a 9 vol % H_2S/H_2 mixture at 350 °C, nickel sulfide, nickel subsulfide, and tungsten disulfide were formed. Both carbon and oxygen signal intensities were reduced. Diffusion of nickel species to the surface and an increase in surface conductivity were also observed. Tungsten +3 species which are believed to be the active sites were not detected. The above results are explained in terms of structural models.

I. Introduction

Nickel–tungsten–alumina catalysts are important because of their catalytic action in hydrodesulfurization, hydrocracking, and hydrogenation processes.[1] Commercial nickel–tungsten–alumina catalysts are mostly prepared by impregnating nickel and tungsten onto γ-Al_2O_3 surfaces in the form of oxides. The catalysts are calcined at around 550 °C and sulfided before use.

During preparation, when the catalyst is still in the oxide state, interaction may occur among the supported species, or between the supported species and the support. Later when reduction and sulfiding occur, various sulfides will form on the catalyst surface, and their identification is important. Knowledge of the sulfiding mechanism and the promoter function is also of vital importance in the understanding of the catalyst. However, few studies of these aspects of nickel–tungsten–alumina catalysts have been reported.

Recently, there have been several attempts[2-7] to study the related cobalt–molybdena–alumina catalysts using x-ray photoelectron spectroscopy (ESCA). Several characteristics of ESCA make it particularly suitable for studying catalytic surfaces: (1) ESCA is capable of observing chemical changes in the first few monolayers; (2) Binding energy values identify the elements present on the surface; (3) Shifts in the binding energies are informative of the chemical environment of the atom; (4) ESCA has high surface sensitivity of detecting up to 10^{-4} monolayer; and (5) The technique can be quantitative.

The present work represents a study of nickel–tungsten–alumina catalysts using ESCA. Various treatments such as reduction and sulfiding were carried out as a function of time and temperature. Changes on the catalyst surface were monitored using ESCA. Different chemical species on the catalyst surface were identified and quantitated. The structure of the catalyst is discussed in light of our measurements.

II. Experimental Section

The catalysts used in the present study were obtained from Harsaw Chemical Co. They were Ni 4303, Ni 0301, and W 0801. All three catalysts had been prepared by impregnating nickel and/or tungsten onto a γ-Al_2O_3 support. Their weight percentages were as follows:

Catalyst	Wt % of Ni	Wt % of W
Ni 4303	6	19
Ni 0301	11	0
W 0801	0	8

NiS was prepared inside the reaction chamber by passing H_2S gas over a heated NiO pellet until reaction was complete. Ni_3S_2 was obtained by reducing the resultant NiS pellet in a hydrogen atmosphere. Ni_2O_3 was prepared by exposing an argon ion etched nickel foil to an oxygen atmosphere. Ni and W were cleaned by argon ion sputtering. Other compounds listed in Table I were used as received from ROC/RIC. They were all sampled in the pellet form in the same way as the catalysts.

H_2S gas was obtained from Matheson. The H_2S/H_2 mixture (9.2 vol % H_2S) was obtained from Linde. Hydrogen and helium were obtained from Linde (ultrahigh purity grade).

In order to remove both oxygen and water from H_2 and He, the carrier gas was passed successively through a 16 in. × 1 in. column of copper turnings heated to 550 °C; a 24 in. × 2 in. $CaSO_4$ column; and an 18 in. × 1.5 in. tube filled with Linde molecular sieves (50% 4A, 50% 5A) cooled to liquid nitrogen temperature. Thiophene was obtained from Eastman (99% pure) and was further purified by three freeze–thaw cycles under vacuum. The purified product was purged with clean helium for 12 h before use. Thiophene was introduced into the gas train by passing the carrier gas through a dispersion tube filled with thiophene. The dispersion tube was maintained at 20 °C which at saturation gives 7% thiophene (60 mm partial pressure) by volume.

TABLE I: Binding Energies and Relative Intensities of Various Species Possibly Found on the Catalyst Surface[a]

Sample	Al 2p	O 1s	C 1s	S 2p	Ni $2p_{3/2}$+ satellites			W $4f_{7/2}$
(1) W			284.2					30.7
			(4)					(62)
(2) WO_2		531.5	284.5					32.7
		(5)	(1)					(15)
(3) WO_3		531.0	284.8					35.0
		(10)	(3)					(20)
(4) WS_2			284.0	161.9				31.4
			(2)	(10)				(14)
(5) Ni			284.0		853.1			
			(4)		(24)			
(6) NiO		530.0	284.7		854.9	856.8	862.1	
		(8)	(3)			(10)		
(7) Ni_2O_3		531.8	284.8		857.1		863.0	
		(6)	(4)			(5)		
(8) Ni_3S_2			285.0	162.1	854.1			
			(2)	(7)		(13)		
(9) NiS			285.3	162.0	854.9			
			(3)	(9)		(11)		
(10) $NiWO_4$		531.5	286.0		857.5		863.7	35.2
		(14)	(4)			(3.3)		(11)
(11) $Al_2(WO_4)_3$	74.1	531.8	285.1					35.4
	(5)	(35)	(0.7)					(12.5)
(12) $NiAl_2O_4$	73.8	531.9	285.0		857.2		863.3	
	(7)	(18)	(1.4)			(2)		
(13) γ-Al_2O_3	74.1	532.0	284.8					
	(7)	(34)	(3)					

[a] Relative intensities are in parentheses. Binding energies are relative to Au $4f_{7/2}$ peak taken as 83.8 eV.

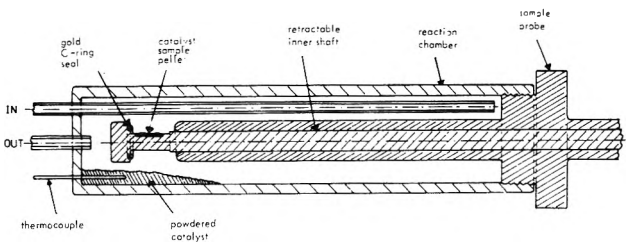

Figure 1. Diagram of reaction chamber and sample probe.

The sample probe and the reaction chamber are shown in Figure 1; both were made of stainless steel. The probe was specially designed for this work. The inner shaft of the probe was retractable and sealed at the end with a gold O-ring seal. This design enables transfer of the sample from the reaction chamber into the spectrometer without exposure to air. The probe when tightly retracted is able to hold a pressure differential of 10^{-8} Torr of helium. The reaction chamber is the outside cylindrical tube shown in Figure 1. It has an inlet and an outlet for the carrier gas. A thermocouple is used to measure the temperature in a pile of powdered catalyst. The temperature of the catalyst pellet is assumed to be the same as the powder. With the probe fully inserted into the reaction chamber, the dead space is roughly 70 cm^3. A tube furnace was used to bring the reaction chamber to the desired temperature.

Catalyst samples were first ground, sieved to 200 mesh, and pressed into pellets under a pressure of 15 000 psi. The size of the pellets was 15 × 6 × 0.5 mm. The weight of the pellets varied from 100 to 200 mg. The surface areas of the pellets, measured by the BET method, showed no change in surface area was introduced by the pelleting procedure. Other chemicals were pressed into pellets whenever possible.

As many as four pellets can be mounted onto the sample probe each time. The probe, with the samples attached, was inserted into the reaction chamber to receive various treatments. After the treatments, the probe tip was retracted and sealed. The whole probe was then unscrewed from the reaction chamber and was quickly inserted into the spectrometer. The probe was first opened in a prechamber and pumped downed to about 0.01 Torr before being introduced into the main chamber of the spectrometer.

ESCA spectra were recorded with an AEI ES 200 electron spectrometer using Al Kα radiation (1486.6 eV). The x-ray power supply was run at 12 kV and 25 mA. Pressure inside the sample chamber during the scans was ca. 5×10^{-9} Torr. The spectrometer was operated in the computer controlled scanning mode which permits several scans to be time averaged. Overlapping peaks were deconvoluted using a DuPont 310 curve resolver. Digital data were also punched out in paper tapes and were processed in a Hewlett-Packard 2114A computer to calculate peak areas.

The compounds listed in Table I were all run at least three times. Binding energy and relative intensity values were averaged before they were reported. The reported binding energy values were all referenced to gold $4f_{7/2}$ line taken as 83.8 eV.[8] The gold reference was introduced onto the sample surface by vacuum deposition. For catalyst samples, the Al 2p line from the alumina support was used as a secondary binding energy reference and was assigned a value of 74.1 eV, by referencing to gold.

Binding energies were measured with a precision of ±0.15 eV. Relative intensities are reported with a precision of ±4%. Absolute intensity values used in making the sulfiding curves are reported with a precision of ±8%.

Catalyst samples were scanned after they had received one or more of the following treatments: calcination, reduction, sulfidation, and reoxidation.

Calcination was performed on every catalyst sample to remove hydrocarbons from the catalyst surface. In order to obtain reproducible results, calcinations were all carried out

in helium at 400 °C for 2 h. The gas purification system and the reaction chamber must be adequately flushed with helium to remove any trace of residual hydrogen. Helium was admitted into the reaction chamber at a rate of 80 cm^3/min. At the end of 2 h, the tube furnace was switched off. The helium flow rate was increased to 200 cm^3/min and the probe was cooled from 400 to 100 °C in approximately 10 min. The sample was then ready to be loaded into the spectrometer or to receive another treatment.

Reduction was carried out after the sample had been calcined. The calcined sample was quickly brought up to the reduction temperature in a hydrogen stream of 80 cm^3/min. After the desired reduction time was achieved the tube furnace was switched off and opened. Hydrogen was immediately switched off and helium at a flow rate of 200 cm^3/min was admitted to cool the sample to room temperature.

Sulfiding was also carried out after the sample had been calcined. The sulfiding mixture was admitted at a rate of 100 cm^3/min. At the end of sulfiding, the sample was flushed and cooled as in the case of reduction. The sample after being scanned was not reused. A new pellet was employed to obtain the next point in the sulfiding curve. This is because the sulfided catalyst is very active and picks up contaminants from the spectrometer.

Reoxidation was done by exposing the catalyst sample to air or oxygen for a given period of time.

III. Results and Discussion

Chemical species, which could possibly be found on the catalyst surface after calcination, reduction, or sulfidation, are listed in Table I together with their binding energies and relative intensities. Relative intensities are in parentheses under the corresponding binding energy values.

The binding energy values for the tungsten $4f_{7/2}$ peaks are in general 1 eV lower than those given by Biloen and Pott.[9] However, their values were obtained by referencing to the C 1s line of the deposited carbon on the surface, taken as 285.0 eV. Binding energy values thus obtained can be erroneous,[10] especially when the surface is active. Even with the 1 eV correction, the binding energy of the W $4f_{7/2}$ line for WO_2 still differs by 0.7 eV. Reduction of both WO_3 and WO_2 has been carried out to various extents in the present study. The peak assignable to WO_2 was found to fall at ca. 32.7 eV.

Binding energies of the Ni $2p_{3/2}$ signals are found to be slightly higher than those given by Kim and Davis.[11] The slight discrepancy may be due to the different calibrations of the spectrometers or due to the use of a different reference material. Their values are referenced to the C 1s line of graphite taken as 284.0 eV.

It can be seen from Table I that Ni/W/γ-Al_2O_3 catalyst is ideal to be studied by ESCA. Large chemical shifts (3–4 eV) exist between the different forms of the catalyst, such as between the oxidic catalyst and the sulfided catalyst.

Intensity Measurements with ESCA. ESCA signal intensity values obtained from single measurements have an uncertainty in the range of 8–20%. In addition, ESCA signal intensities may be a function of the chemical environment of the measured atoms.[12,13] Therefore, great care must be taken when drawing conclusions from ESCA intensity results. Changes in signal intensities of a few percent may not mean anything; on the other hand, a consistent trend in ESCA signal intensities of a few percent should not be neglected.

ESCA signal intensities are depth dependent also. An ESCA signal will be attenuated by $(1 - \exp(-x/\lambda))$, where λ is the mean free path of the photoelectron in angstroms and x is the sampling depth. The electron mean free path is a function of both the substance and the kinetic energy of the photoelectron. The mean free path is ca. 20–50 Å, which corresponds to 10–20 atomic layers.

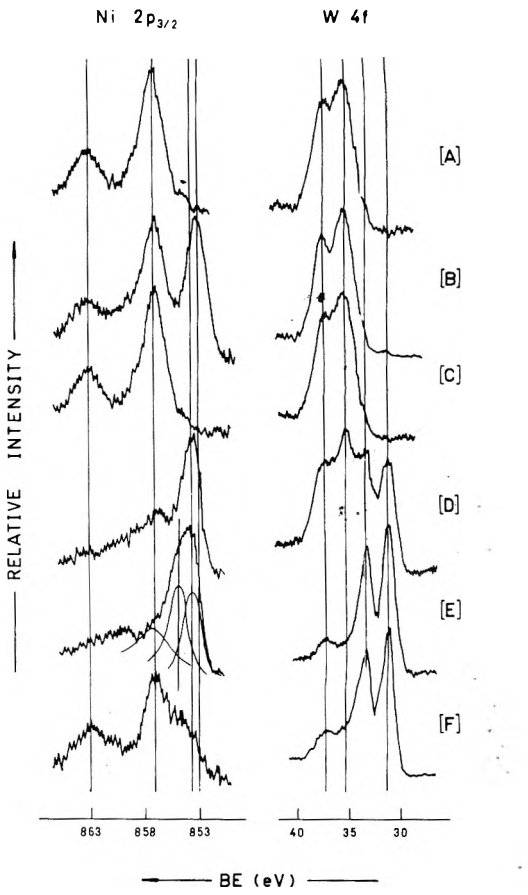

Figure 2. Ni $2p_{3/2}$ and W 4f ESCA spectra of the catalyst Ni 4303 with different treatments: (A) calcination in He at 350 °C for 2 h; (B) reduction in H_2 at 500 °C for 2 h; (C) reduction in H_2 at 500 °C for 2 h, then exposure to O_2 at 20 °C for 0.5 h; (D) sulfiding with 7% thiophene/H_2 mixture at 450 °C for 11 h; (E) sulfiding with H_2S at 450 °C for 1 h; (F) sulfiding with H_2S at 450 °C for 1 h, then exposure to air at 20 °C for 2 days.

Fortunately, in dealing with supported catalysts, only the first few atomic layers are of interest. If an electron mean free path of 30 Å and an interatomic layer distance of 2 Å are assumed for the catalyst, a photoelectron signal coming from the sixth atomic layer will be attenuated by only 0.28. Most of the sulfiding experiments in the present study were carried out to the stage where the first few atomic layers are only partially sulfided. Therefore, no corrections are really necessary to compensate for the layer structure of the catalysts. The precision of ESCA intensity measurements of the catalysts are generally fairly good, usually better than ±4%.

Preliminary Studies. Preliminary studies were carried out with the Ni/W/Al_2O_3 catalyst (Ni 4303) and the results are shown in Figure 2. The peaks at around 857 eV correspond to the Ni $2p_{3/2}$ electrons and their satellites. The peaks at around 35 eV are the W 4f doublets.

Figure 2A corresponds to the catalyst as received. Calcination in He at 350 °C for 2 h does not change the shape of these two spectra. The only difference is a decrease in C 1s signal intensity and a general increase in the intensities of other signals. This shows that the catalyst has probably been calcined by the manufacturer and that some hydrocarbon may have been picked up in the pelleting process. The W $4f_{7/2}$ line

at a 35.4 eV corresponds to that of aluminum tungstate. The Ni $2p_{3/2}$ line at 857.1 eV together with the large satellite peak at 863.0 eV, corresponds to either Ni_2O_3 or nickel aluminate, but not NiO.

Figure 2B corresponds to the catalyst that has been reduced at 500 °C for 2 h. Essentially there is no change in the W 4f electron spectrum. This agrees with the results of Biloen and Pott[9] that tungsten species supported on γ-Al_2O_3 are not reducible at 500 °C. Both WO_2 and WO_3 are reduced to tungsten metal under the same conditions. A new peak appears in the Ni $2p_{3/2}$ electron spectra at 853.1 eV, corresponding to the nickel $2p_{3/2}$ line of nickel metal.

Figure 2C corresponds to the same catalyst as Figure 2B except that it has been exposed to oxygen for 30 min. The W 4f signal shows no significant change while the nickel metal peak disappears completely. The Ni $2p_{3/2}$ electron spectrum is now identical with that of Figure 2A.

Figure 2D corresponds to the catalyst calcined in He at 450 °C for 2 h and then sulfided with a thiophene/H_2 mixture. Two doublets are evident in the W 4f spectrum. The new doublet has its $4f_{7/2}$ line at 31.8 eV and corresponds to WS_2. The spectrum shows that about 40% of the tungsten on the catalyst surface has been sulfided to give WS_2. A new peak also appears in the Ni $2p_{3/2}$ spectrum. This new peak has a BE of 857.9 eV which corresponds to Ni_3S_2. Only a small peak is left at the BE of 857.1 eV. After deconvolution of the peaks, the results show that about 80% of the nickel has been converted into Ni_3S_2.

Figure 2E corresponds to the catalyst that has been calcined in He at 400 °C for 2 h and then sulfided in H_2S for 1 h. The W 4f spectrum shows that almost all of the tungsten on the catalyst surface has been converted into WS_2. The Ni $2p_{3/2}$ electron spectrum shows a broad peak at about 854 eV. This broad peak can be deconvoluted into two peaks having BE values of 854.1 and 855.7 eV corresponding to Ni_3S_2 and NiS, respectively, in about a 40:60 ratio. The large satellite peak at 863.0 eV disappeared in both Figure 2D and 2E. This satellite has been attributed by Kim and Davis[11] to the monopole charge transfer transition that accompanies the primary photoemission. The absence of this satellite peak implies that there are no longer any oxygen ligands attached to nickel. The rate of sulfiding is observed to be much faster with H_2S than with a 7 vol % thiophene in H_2 mixture.

Figure 2F corresponds to the catalyst in Figure 2E exposed to air for 2 days at room temperature. The WS_2 signal shows no change while the nickel signal shows that nickel sulfides are mostly oxidized. The results are not surprising as WS_2 is stable in air but NiS and Ni_3S_2 are not.

Reduction Vs. Time and Temperature. The nickel/tungsten/alumina catalyst (Ni 4303) was reduced in H_2 at 450 °C. The percentage reduction for both nickel and tungsten is plotted as a function of time in Figure 3. The W 4f signal remains unchanged after 6 h of reduction showing that tungsten species on the catalyst surface are very stable. On the other hand, the nickel species are readily reduced to nickel metal. The spectra corresponding to the 2-h reduction have previously been shown in Figure 2B. Reduction of nickel levels off at about 75%, indicating that some 25% of the surface nickel will not be reduced even after prolonged hydrogen treatment.

The fact that tungsten is not reducible shows that supported tungsten catalysts and supported molybdenum catalysts may be basically different in their desulfurization mechanisms. Supported molybdenum trioxide on γ-Al_2O_3 has been shown by Seshadri and Petrakis[14] to be reduced to molybdenum +5 and +4 species. The anion vacancies produced are believed to be the active sites in hydrodesulfurization, according to Lipsch and Schuit.[15] However because of lack of reduction for tungsten oxide the anion vacancy theory will not explain the desulfurizing activity of this catalyst.

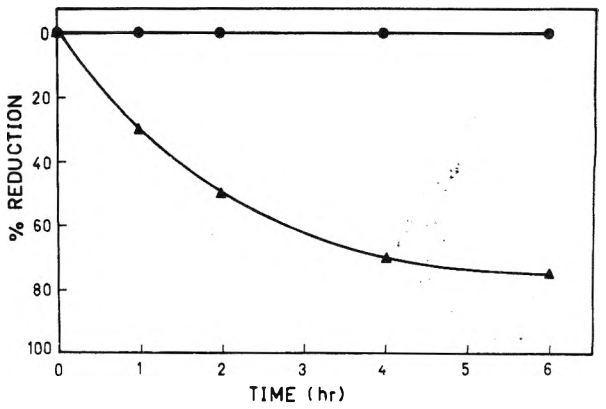

Figure 3. Percentage reduction of tungsten (●) and nickel (▲) as a function of reduction time for catalyst Ni 4303. Reduction at 450 °C with H_2 at a flow 80 cm^3/min.

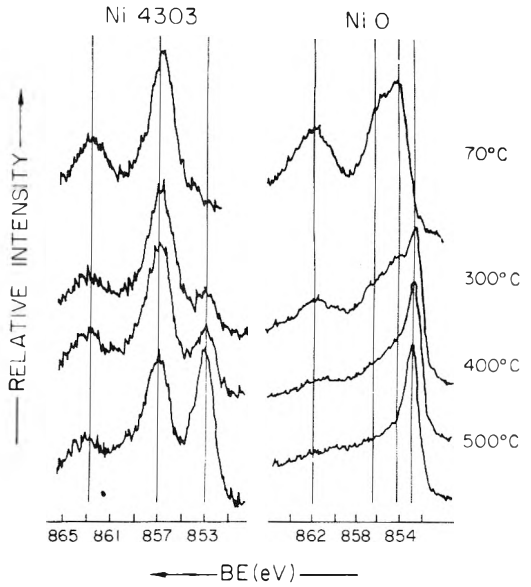

Figure 4. Ni $2p_{3/2}$ ESCA spectra for the catalyst Ni 4303 and nickel oxide after reduction with H_2 at different temperatures for 2 h.

We have compared the reduction behavior of the Ni/W/Al_2O_3 (Ni 4303) catalyst and various Ni and W compounds that might be present on the surface. In order to provide a valid comparison, two pellets of different materials were mounted on opposite sides of the sample probe and reduced simultaneously. This ensures identical reduction conditions for both samples. First, a Ni/W/Al_2O_3 catalyst pellet and a NiO pellet were compared as shown in Figure 4. Two things are apparent. First, the peak shapes and binding energies of the unreduced samples are quite different, indicating NiO is not present on the catalyst surface. Second, the behavior on reduction is quite different. An important observation is that even at 500 °C, there is still a substantial percentage of the surface nickel on the catalyst which is not reduced. Both NiO and Ni_2O_3 were completely reduced to the metal in 2 h at this temperature. Thus there must be some species present other than an oxide.

Two possible species are $NiWO_4$ or $NiAl_2O_4$ formed from

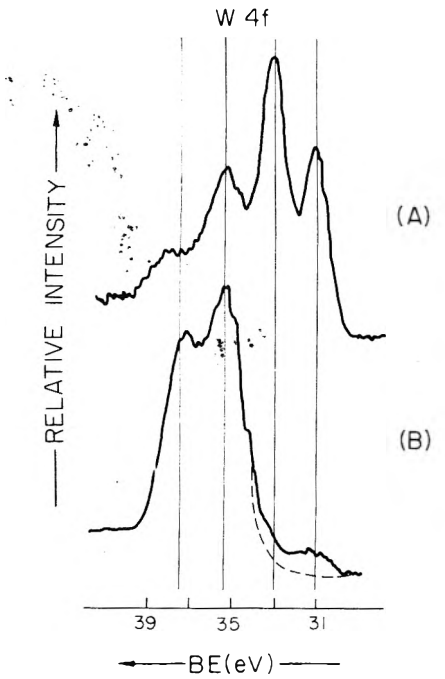

Figure 5. W 4f ESCA spectra of (A) $Al_2(WO_4)_3$ and (B) catalyst Ni 4304 after reduction with H_2 at 550 °C for 6 h.

interaction of the oxide with the support. However, $NiWO_4$ was found to be completely reduced to nickel metal when treated at 500 °C for 2 h eliminating it as a reaction product. $NiAl_2O_4$, on the other hand, was found to be fairly stable toward reduction. Treatment at 550 °C for 2 h in hydrogen caused only 50% reduction. This indicates that $NiAl_2O_4$ may actually be present on the catalyst surface. This finding agrees with the results of Lo Jacono et al.[16] who proposed that Ni^{2+} ions can occupy the tetrahedral sites in γ-Al_2O_3, forming a "surface spinel".

The portion of surface nickel species which is readily reduced and reoxidized at lower temperatures is believed to be Ni_2O_3 on the basis of binding energy measurements and the behavior of NiO shown in Figure 4. The exact percentage of the nickel that has interacted with the support is not directly obtainable from binding energy measurements, because Ni_2O_3 and $NiAl_2O_4$ give identical nickel electron spectra. However, the metal reduction curve in Figure 3 implies about 75% Ni_2O_3.

Biloen and Pott[9] proposed that tungsten has interacted with γ-Al_2O_3 forming $Al_2(WO_4)_3$ as a surface species. We carried out reduction studies on $Al_2(WO_4)_2$ and the catalyst Ni 4303 at 550 °C for 6 h. The results are shown in Figure 5. It can be seen that most of the tungsten in $Al_2(WO_4)_3$ has been reduced from tungstate to W(+4) and W(0), while only a small portion of the tungsten on the catalyst has been reduced.

Our reduction experiments indicate that the W(+6) species is more stable than aluminum tungstate toward reduction at high temperatures. A surface interaction complex is therefore proposed. This complex is probably formed during calcination as follows:

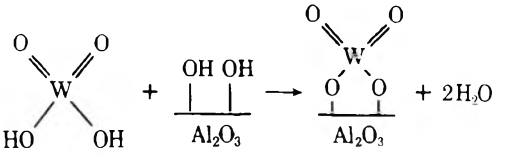

A similar interaction complex has previously been proposed by Dufaux et al.[17] for MoO_3/γ-Al_2O_3 catalysts.

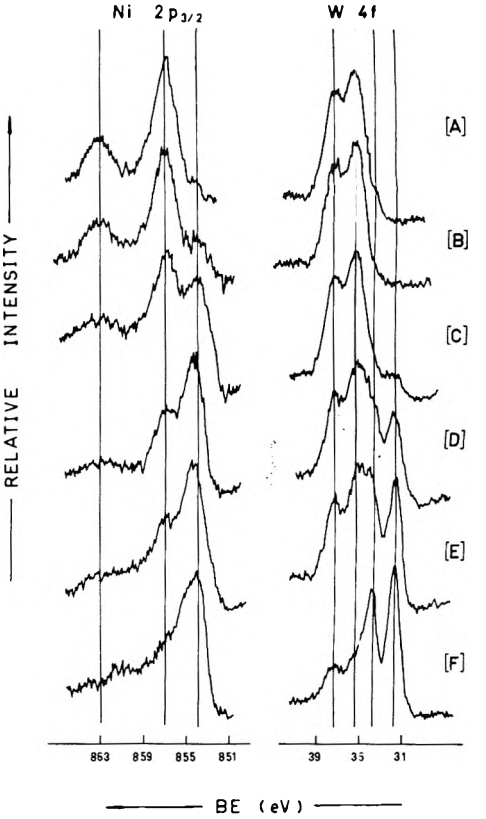

Figure 6. Ni $2p_{3/2}$ and W 4f ESCA spectra of the catalyst Ni 4303 after sulfiding at 310 °C with 9% H_2S/H_2 at different time intervals: (A) as received; (B) 1 min; (C) 12 min; (D) 95 min; (E) 240 min; (F) 600 min.

Sulfiding under Different Conditions. Sulfiding of the Ni/W catalyst (Ni 4303) was carried out at different temperatures using different sulfiding mixtures. Catalysts Ni 0301 and W 0801 were also sulfided for comparison purposes. It should be pointed out that the Ni concentration in catalyst Ni 0301 is somewhat higher than normal and the W concentration in W 0801 somewhat lower than normal. We feel, however, that these represent valid comparisons with Ni 4303 for ESCA measurements.

Figure 6 shows the changes in the W 4f and Ni $2p_{3/2}$ spectra for catalyst Ni 4303 produced by sulfiding at 310 °C. A broad Ni $2p_{3/2}$ peak appears upon sulfiding which can be deconvoluted into two narrow peaks at 854.7 and 854.1 eV corresponding to NiS and Ni_2S_2, respectively. The production of Ni_2S_2 is quite unexpected because the concentration of H_2S in the sulfiding mixture is quite high. W 4f electron spectra are shown on the right column in Figure 6. On sulfiding a new doublet is seen to emerge at 33.8 and 31.8 eV, corresponding to WS_2.

Figure 7 shows sulfiding curves for the catalyst Ni 4303. The intensity of the ESCA S 2p signal is used to indicate the extent of sulfiding. One S 2p doublet is observed in the S 2p spectra, which corresponds to S^{2-}.

The two middle curves correspond to sulfiding with an H_2S/H_2 mixture (9.2 vol % H_2S) at two different temperatures. They indicate that the higher the sulfiding temperature, the faster will be the rate of sulfiding. The top curve corresponds to sulfiding with pure H_2S at 450 °C. Compared to the curve in the middle, it is seen that the higher the H_2S concentration, the faster will be the rate of sulfiding. Sulfiding with pure H_2S is 93% complete after 1 h. Sulfiding with 9.2 vol % H_2S in H_2 is only 80% complete after a total of 4 h. Complete sulfidation with the 9.2 vol % H_2S/H_2 mixture takes at least 15 h.

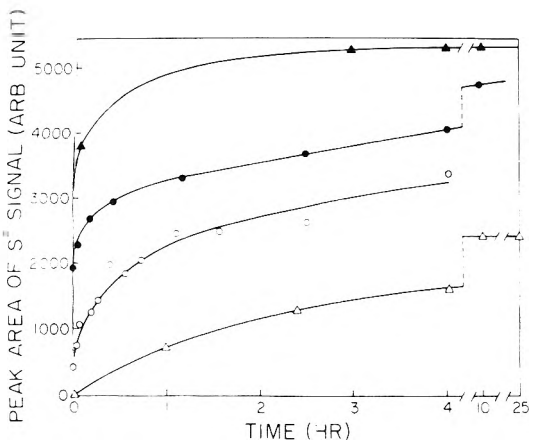

Figure 7. Sulfide signal intensity as a function of sulfiding time for the catalyst Ni 4303: (▲) with H_2S at 450 °C; (●) with 9% H_2S/H_2 mixture at 450 °C; (O) with 9% H_2S/H_2 mixture at 350 °C; (△) with 7% thiophene/H_2 mixture at 450 °C.

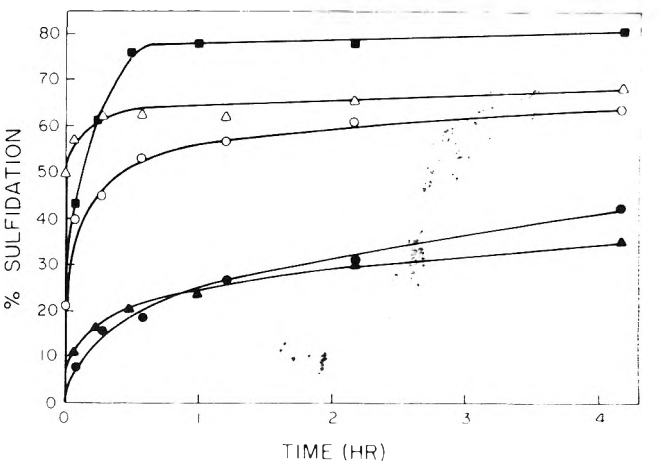

Figure 8. Percentage sulfidation as a function of sulfiding time. Sulfiding was carried out at 350 °C with 9.2% H_2S/H_2 mixture at a flow rate of 100 cm^3/min. Solid points represent tungsten. Open points represent nickel. (■) Aluminum tungstate; (●) Ni 4303; (▲) W 0801; (O) N 4303; (△) Ni 0301.

Sulfiding at 450 °C with a H_2S/H_2 mixture was faster than with a thiophene/H_2 mixture at the same temperature as seen from the lower curve of Figure 7. Sulfiding with thiophene/H_2 was 50% complete after 25 h and then leveled off. It is believed that thiophene is first hydrogenated and decomposed into H_2S and other hydrocarbons. It is the H_2S produced that sulfides the catalyst surface, accounting for the slower rate of sulfiding using H_2/thiophene.

Other observations were also made from the electron spectra. Sulfiding with the H_2S mixture produced both NiS and Ni_3S_2, while sulfiding with thiophene produced only Ni_3S_2. This is indicative of the lower H_2S concentration in the thiophene mixture during sulfiding. The intensity of the C 1s signal stays constant at about 100 counts/s when sulfiding is done with the H_2S mixture, but for thiophene the C 1s signal increases steadily from 100 to 400 counts/s in the 25-h sulfiding period. This indicates that a carbon layer is building up on the catalyst surface. This may be one of the reasons that sulfiding stops at 50% completion.

Sulfiding with an H_2S/H_2 Mixture. Three catalysts were sulfided using an H_2S/H_2 mixture: Ni 4303, Ni 0301, and W 0801. The supported nickel oxide catalyst (Ni 0301) was found to have the highest initial rate of sulfiding but leveled off after less than 1 h of sulfiding. The tungsten oxide catalyst (W 0801) showed similar behavior, showing only a slight increase in S 2p intensity after 1 h of sulfiding. The curve for W 0801 was virtually identical with that of Massoth et al.[24] who used a microbalance to obtain their curve. On the other hand, the Ni/W catalyst (Ni 4303) showed a low initial rate of sulfiding for ca. 30 min but maintained a fairly constant rate of H_2S uptake even after 4 h.

Figure 8 shows a plot of the percentage of sulfidation vs. sulfiding time for the three catalysts. For the nickel species, the catalyst Ni 4303 is found to have a lower rate of conversion at the beginning but slowly catches up with the catalyst Ni 0301. Both catalysts reach ca. 65% conversion after 4 h of sulfiding. Under the experimental conditions, both catalysts are found to produce NiS and Ni_3S_2.

The rate of conversion to WS_2 for both catalysts is slow. After a total of 4 h sulfiding time, only 40% of the tungsten has been converted into WS_2. However the slopes remain fairly steep at this point indicating that conversion is continuing. Aluminum tungstate was found to sulfide at a very rapid rate. It reaches a plateau at 80% conversion within the first 30 min. This observation supports the argument that tungsten in-

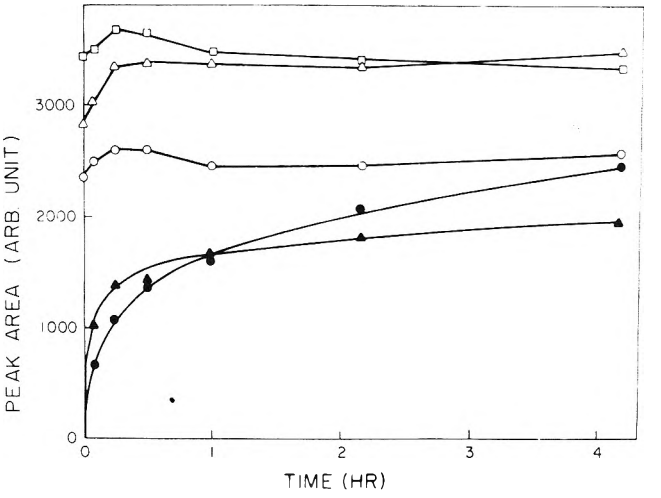

Figure 9. Signal intensities of various ESCA peaks for the catalyst W 0801 as a function of sulfiding time. Sulfiding was carried out at 350 °C with a 9.2% H_2S/H_2 mixture at a flow rate of 100 cm^3/min: (□) O 1s (×10); (△) W 4f (×2); (O) Al 2p (×3); (●) W^{4+}; (▲) S^{2-}.

teracts with the support to give a surface interaction complex, but not $Al_2(WO_4)_3$.

ESCA signal intensities vs. sulfiding time were obtained for catalyst Ni 0301. $Ni(S^{2-})$ and S^{2-} will be used to designate the sulfided nickel signal and the sulfide signals, respectively. The intensity ratio of $S^{2-}/Ni(S^{2-})$ stabilized at 0.75 after ca. 20 min. Compared with 0.54 for Ni_3S_2 and 0.85 for NiS, this result indicates that the sulfiding product contains more NiS than Ni_3S_2. The total ESCA signal intensities for Al 2p, C 1s, and Ni $2p_{3/2}$ were essentially constant over the same time period. A 14% decrease in the intensity of the O 1s was observed, probably due to the fact that some oxygen atoms are being replaced by sulfur atoms during sulfiding.

Aluminum tungstate was also sulfided. The purpose of this experiment was to establish the S^{2-} and W^{4+} intensities for comparison with catalysts. The W^{4+}/S^{2-} intensity ratio was constant at 2.3 after 30 min of treatment with H_2S/H_2. This agrees fairly well with the intensity ratio of 2.5 observed for WS_2. The O 1s signal was found to decrease to about ⅓ of its original value. The Al 2p binding energy was shifted to 74.1 eV indicating that Al_2O_3 was formed.

Figure 9 corresponds to sulfiding the tungsten oxide cata-

lyst, W 0801. After 4 h of sulfiding, the decrease in O 1s intensity was about 6%. An important correlation was observed between the rate of increase in the S^{2-} signal and the rate of increase in the W^{4+} signal. The behavior of the tungsten catalyst would be expected to parallel that of aluminum tungstate, i.e., the intensity of the W^{4+} signal should all the times be about 2.3 times that of the S^{2-} signal. However, it is seen in Figure 9 that the S^{2-} signal increases quickly in the first 15 min and then slows down. The W^{4+} signal, on the other hand, rises only slowly at the beginning, in the first hour of sulfiding, the W^{4+} signal intensity is actually smaller than the S^{2-} signal intensity. The W^{4+}/S^{2-} intensity ratio increases steadily. This ratio eventually reaches the value of 2.4 after 15 h of sulfiding, corresponding exactly to the value for WS_2. This behavior implies that the sulfiding must go through some intermediate step before WS_2 is finally formed.

Alumina is very resistant to sulfiding under the conditions of our experiment; extended sulfiding produced a S^{2-} signal only 5% that of the catalyst. Therefore, sulfiding of the alumina cannot account for the above behavior. The only stable product of the sulfiding is WS_2.

A reasonable explanation for this behavior is that an intermediate is involved. If one of the two terminal oxygens in the surface interaction complex is replaced by a sulfur, an intermediate complex (still W^{+6}) results:

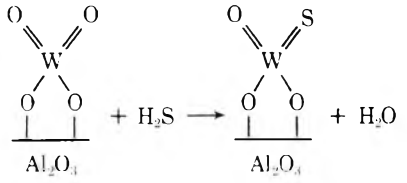

Although the W 4f binding energies of the complex and original catalyst should differ, the difference will be small since the tungsten is still in the +6 state. The new ESCA signal would be obscured under the broad envelope of the original W^{+6} peaks.

The intermediate complex is more resistant to sulfiding than the original surface network, requiring another 15 h of treatment for complete sulfiding. This high stability is probably due to the two strong W–O–Al bonds linking the complex to the surface. The slowness in formation of WS_2 may be responsible for the small size of the WS_2 crystallites, on the average a factor of 10 smaller than unsupported nickel tungsten sulfide.[3]

Figure 10 corresponds to sulfiding of the catalyst Ni 4303. Nickel sulfides are formed fairly quickly and level off after 2 h. The plateau corresponds to about 70% of the nickel being converted into NiS or Ni_3S_2. The W^{4+} and S^{2-} curves are similar to those in Figure 9 for the catalyst W 0801. The magnitude of the W^{4+} signal corresponds to about 40% of the total tungsten signal after 4 h of sulfiding. It can be conjectured that sulfiding will take 15–20 h to reach a plateau. Intermediate complexes must be present during sulfiding. The activity toward hydrodesulfurization of this intermediate complex is not known but will be a topic of further study.

Figure 11 is an extension of Figure 10 to include more lines at longer times. Intensities of the W 4f and Al 2p signals remain essentially constant. The C 1s signal decreases by 60% in the first 1.5 h; the O 1s signal decreases steadily by about 10% over the first 4 h. The intensity of the Ni $2p_{3/2}$ signal stays constant for the first 2 h, begins to increase for about 1 h and then levels off. The increase in intensity is ca. 50%. The same increase in intensity for the Ni $2p_{3/2}$ signal was observed in another sulfiding experiment of the catalyst Ni 4303 at 450 °C. The only difference between the two was that the increase in Ni $2p_{3/2}$ signal intensity occurs during the first hour of sulfiding at 450 °C.

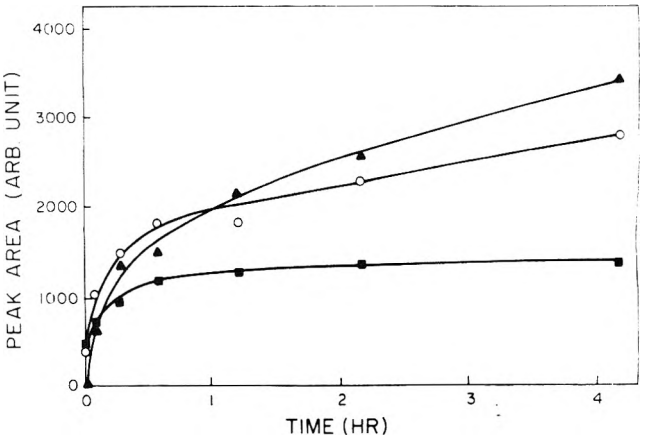

Figure 10. Signal intensities of new ESCA peaks for the catalyst Ni 4303 as a function of sulfiding time. Sulfiding was carried out at 350 °C with a 9.2% H_2S/H_2 mixture at a flow rate of 100 cm^3/min: (▲) W^{4+}; (O) S^{2-}; (■) Ni(S^{2-}).

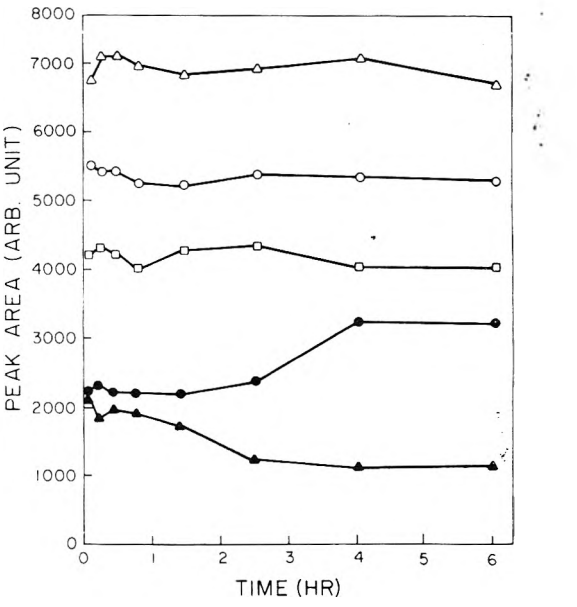

Figure 11. Signal intensities of various ESCA peaks for the catalyst Ni 4303 as a function of sulfiding time. Sulfiding was carried out at 350 °C with a 9.2% H_2S/H_2 mixture at a flow rate of ~00 cm^3/min: (△) Al 2p; (O) O 1s (×7); (□) W 4f (×2); (●) Ni $2p_{3/2}$; (▲) C 1s.

Since no corresponding increase in the intensity of the sulfided nickel signal (Ni(S^{2-})) was observed in Figure 10, the increase in Ni signal intensity in Figure 11 must be in the unsulfided portion of nickel. This sudden increase in the intensity of Ni occurs when the tungsten is about 50% converted into WS_2. The increase in Ni intensity must arise from diffusion of Ni^{2+} ions to the surface from the bulk.

The surface conductivity was also observed to increase during sulfiding. Oxidic Ni/W catalysts are electrical insulators. Therefore when they are scanned in the spectrometer, the sample surface was always found to be charged positively due to the ejection of the photoelectrons from the surface. The amount of surface charging is inversely proportional to the surface conductivity and can be easily obtained from the ESCA spectra. Surface charging is usually on the order of 3–4 eV for inuslators. A plot of the surface charging plus work

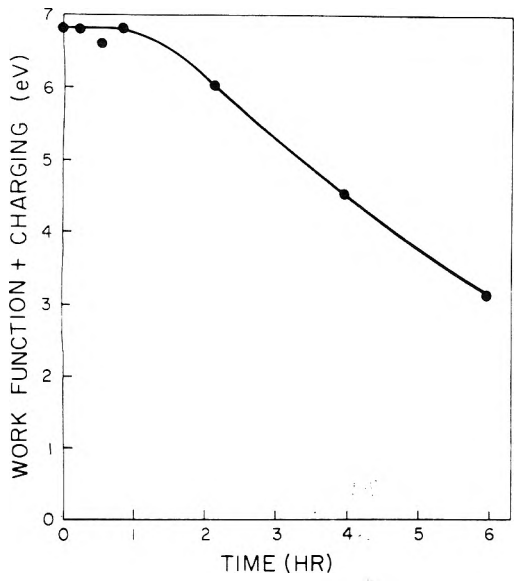

Figure 12. Work function and surface charging on the catalyst Ni 4303 as a function of sulfiding time. Sulfiding was carried out at 350 °C with a 9.2% H_2S/H_2 mixture at a flow rate of 100 cm^3/min.

function vs. the sulfiding time is shown in Figure 12. The increase in surface conductivity may be due to formation of WS_2 on the surface. WS_2, with a work function of 0.15 eV,[1] can be considered a conductor. Figure 12 shows that at the time when the conversion of tungsten complex into WS_2 reaches about 50%, the concentration of WS_2 crystallites is high enough to form a conductive network on the catalyst surface. The relation between the activity of a catalyst and its surface conductivity (or the position of the Fermi level) is still not clear at the present time.[1]

Structure of the Ni/W/γ-Al_2O_3 Catalyst. At the present time, three models have been proposed for hydrodesulfurization catalyst systems.

A monolayer model was discussed in detail by Schuit and Gates[19] for both oxidic and sulfided cobalt-molybdena-alumina. It seems reasonable to assume parallelism between the cobalt-molybdena-alumina and the nickel-tungsten-alumina systems. In a monolayer model, molybdenum forms a monolayer, chemically bonded to the surface of the alumina support. The charge of the Mo^{6+} monolayer is compensated by O^{2-} ions situated in a capping layer on top of the monolayer.

Incorporation of cobalt results in the locating of Co^{2+} ions in tetrahedral sites somewhere below the surface layer of the support with accompanying O^{2-} ions forced to remain in the capping layer. The primary effect of the penetration of the promoter cations is the expulsion of tetrahedrally coordinated Al^{3+} ions from the bulk into the surface monolayer. The stability of the monolayer is thus increased because the Al^{3+} ions help to bond the monolayer to the alumina surface.

Sulfiding of the catalyst is assumed to be restricted to removal or exchange of O^{2-} ions located in the capping layer. Since S^{2-} is much larger than O^{2-}, the maximum of S^{2-} ions in this layer is fixed at two instead of four per unit mesh.

Removal of S^{2-} ions in the capping layer, for instance, by hydrogen reduction results in the formation of Mo^{3+} ions which are supposed to be the active sites. Formation of the single Mo^{3+} sites is only possible in the presence of cobalt. Therefore the function of the promoter cations in the monolayer model is to increase the reduction of molybdenum and to stabilize the molybdenum monolayer.

An intercalation model has been proposed by Voorhoeve and Stuiver,[20,21] Voorhoeve,[22] and Farragher and Cossee.[23] It was postulated that, although intercalation of Ni in the ideal crystal of WS_2 is energetically unfavorable, it does occur at the crystal edges provided that the crystals are small. Voorhoeve's arguments are based on ESR data and the assignment of a resonance at 3250 Oe to W^{3+}. The resonance was observed in sulfur deficient $WS_{1.95}$ but not in stoichiometric WS_2; it increased with surface area and with the amount of Ni. The intercalated Ni^{2+} ions are octahedrally surrounded by S^{2-} anions and their special promoter function is to increase the number of exposed W^{3+} ions which are believed to be the active sites. Farragher and Cossee[23] estimated that because of the smallness of the WS_2 crystals in commerical catalysts, the intercalation could increase the Ni/W ratio from 0.3 to 1.0.

A synergetic model has been proposed by Hagenbach et al.[24] The function of promoters in this model is to explain in terms of electron transfer between adjacent sulfide phases. This model might be valid at high promoter content as pointed out by Farragher and Cossee in their discussion with Delmon.[25]

Recently DeBeer et al.[26] postulated that a change of monolayer structure to the intercalation structure was possible during presulfiding. This would involve migration of the promoter cations to the catalyst surface and a change from tetrahedral to octahedral sites.

On the whole, the results of our reduction experiments on the oxidic catalyst are consistent with the monolayer model. Tungsten is found to be dispersed on the support surface as a monolayer of the interaction complex. The maximum surface covered by the tungsten complex can be calculated as 89% using an oxide concentration of 9.1×10^{18} O^{2-} ions/m^2 for the (110) γ-Al_2O_3 surface.[27] Hence the majority of the alumina surface is covered by the tungsten complex monolayer.

Nickel was found to be present on the catalyst surface as either Ni_2O_3 or $NiAl_2O_4$ in a ratio of approximately 3 to 1. Since the majority of the catalyst surface is covered by the tungsten monolayer, and the nickel to tungsten atomic ratio for the catalyst Ni 4303 is about unity, most of the Ni_2O_3 probably sits on top of the tungsten monolayer. The W 4f/Ni $2p_{3/2}$ intensity ratio for $NiWO_4$ is 5.8. The same intensity ratio for the catalyst Ni 4303 is found to be 4.0. This substantial decrease in the W 4f/Ni $2p_{3/2}$ intensity ratio for the catalyst is consistent with Ni_2O_3 dispersed on top of the tungsten monolayer. The other portion of nickel, corresponding to nickel aluminate, is probably located below the tungsten monolayer. This is consistent with the monolayer model in that the promoter Ni^{2+} ions can penetrate into the surface layers of γ-Al_2O_3 and occupy the tetrahedral sites forming a "surface spinel", $NiAl_2O_4$.

The results of our sulfidation experiments show that the tungsten monolayer is broken up during sulfiding to form WS_2 crystallites. When sulfidation of the catalyst Ni 4303 is completed (see Figure 2E), tungsten is found to be completely converted into WS_2 and nickel is completely converted into NiS and Ni_3S_2. The satellite line at 836.0 eV BE which corresponds to Ni-O bonding is no longer observed. So it can be concluded that monolayer structure no longer exists due to the absence of any bonding between γ-Al_2O_3 and the supported species.

During sulfidation, a stable tungsten intermediate complex is formed which slowly converts into WS_2. The slowness in formation of WS_2 affects the size of WS_2 crystallites. γ-Al_2O_3 supported nickel-tungsten sulfide is reported[2] to have an average crystallite size ten times smaller than the unsupported nickel-tungsten sulfide. A smaller crystallite size implies a

larger surface area and possibly a larger number of active sites.

At the completion of sulfidation, the W 4f/Ni $2p_{3/2}$ intensity ratio has decreased to a value of 2.8 showing that nickel sulfides are well-dispersed on the catalyst surface and possibly on the WS_2 crystallite surface too. Diffusion of Ni^{2+} ions to the catalyst surface is also observed during sulfidation.

Although all of our observations are consistent with the intercalation model, the existence of an intercalation structure is not confirmed in the present study. Diffusion of Ni^{2+} ions to the surface of the catalyst is not conclusive evidence for the intercalation structure due to the high concentration of nickel originally present on the catalyst surface.

An ESCA signal which is attributable to W^{3+} could not be observed in our studies. However W^{3+} ions still could be present for the following reasons. There is only 0.7 eV difference in binding energies between W^{4+} species in WS_2 and W(0) in tungsten metal. Any W^{3+} ions in WS_2 will give a signal that overlaps significantly with the intense WS_2 signal. Under these circumstances, a W^{3+} ion concentration of less than 5% could not be detected.

The ESCA signal corresponding to intercalated Ni^{2+} ions is also difficult to observe. This is partly because the intercalated Ni^{2+} ions can have a concentration lower than 1%,[23] and partly because the binding energies of Ni^{2+} ions and intercalated Ni^{2+} ions in WS_2 may be very similar.

Summary

The salient findings of this study are as follows:

(1) NiO, WO_3, $NiWO_4$, and $Al_2(WO_4)_3$ species are shown to be absent on the catalyst surface.

(2) Nickel is present on the catalyst surface as Ni_2O_3 and $NiAl_2O_4$.

(3) Tungsten interacts with the γ-Al_2O_3 support to form a monolayer of an interaction complex.

(4) Ni_2O_3 species are dispersed on top of the tungsten monolayer.

(5) On reduction, Ni_2O_3 species are reduced to nickel metal, whereas tungsten species are not reducible.

(6) The rate of sulfiding is faster at higher temperatures.

(7) The rate of sulfiding is faster when a sulfiding mixture of higher concentration of H_2S is used.

(8) Sulfiding with a 7 vol % of thiophene in H_2 gives Ni_3S_2 and WS_2.

(9) Sulfiding with a 9 vol % of H_2S in H_2 gives NiS, Ni_3S_2, and WS_2.

(10) A tungsten surface complex intermediate was formed during sulfiding. The intermediate has both a terminal oxygen and a terminal sulfur.

(11) Ni^{2+} ions are found to diffuse to the surface during sulfiding.

(12) Surface conductivity increases steadily during sulfiding.

(13) ESCA signals corresponding to W^{3+} ions or other anion vacancies are not observed.

Acknowledgments. The authors wish to thank J. C. Carver for valuable discussions. This work was supported in part by funds provided by the National Science Foundation under Grant No. MPS 75-05961.

References and Notes

(1) O. Weisser and S. Landa, "Sulphide Catalysts, Their Properties and Applications", Pergamon Press, New York, N.Y., 1973.
(2) A. W. Miller, W. Atkinson, M. Barber, and P. Swift, *J. Catal.*, **22**, 140 (1971).
(3) Armour, P. C. H. Mitchel, B. Folkesson, and R. Larsson, *J. Less Common Metals*, **36**, 361 (1974).
(4) E. L. Apteker, M. G. Chadinor, A. M. Alekeev, and O. V. Krylov, *React. Klnet. Catal. Lett.*, **1**, 493 (1974).
(5) T. A. Patterson, J. C. Carver, D. E. Leyden, and D. M. Hercules, *Spectrosc. Lett.*, **9**, 65 (1976).
(6) A. Cimino and B. A. DeAnglis, *J. Catal.*, **36**, 11 (1975).
(7) R. M. Friedman, R. I. DeClerck-Grimee, and J. J. Fripiat, *J. Electron Spectrosc.*, **5**, 437 (1974).
(8) C. K. Jorgensen, *Theor. Chim. Acta*, **24**, 241 (1972).
(9) P. Biloen and G. T. Pott, *J. Catal.*, **30**, 169 (1973).
(10) W. P. Dianis and J. E. Lester, *Anal. Chem.*, **45**, 1416 (1973).
(11) K. S. Kim and R. E. Davis, *J. Electron Spectrosc.*, **1**, 25 (1972–1973).
(12) C. D. Wagner, *Anal. Chem.*, **44**, 1050 (1972).
(13) K. T. Ng and D. M. Hercules, *J. Electron Spectrosc.*, **7**, 257 (1975).
(14) K. S. Seshadri and L. Petrakis, *J. Catal.*, **30**, 195 (1973).
(15) J. M. J. G. Lipsch and G. C. A. Schuit, *J. Catal.*, **15**, 174 (1969).
(16) M. Lo Jacono, M. Schiavello, and A. Cimino, *J. Phys. Chem.*, **75**, 1044 (1971).
(17) M. Dufaux, M. Che, and C. Naccache, *C. R. Acad. Sci. Paris, Ser. C*, **268**, 2255 (1969).
(18) G. C. A. Schuit and B. C. Gates, *AIChE J.*, **19**, 417 (1973).
(19) F. E. Massoth and D. L. Bidlack, *J. Catal.*, **16**, 303 (1970).
(20) R. J. H. Voorhoeve and J. C. M. Stuiver, *J. Catal.*, **23**, 228 (1971).
(21) R. J. H. Voorhoeve and J. C. M. Dtuiver, *J. Catal.*, **23**, 243 (1971).
(22) R. J. H. Voorhoeve, *J. Catal.*, **23**, 236 (1971).
(23) A. L. Farragher and P. Cossee, "Proceedings of the 5th International Congress on Catalysis", J. W. Hightower, Ed., North-Holland, Amsterdam, 1973, p 1301.
(24) G. Hagenbach, P. Courty, and B. Delmon, *J. Catal.*, **31**, 264 (1973).
(25) A. L. Farragher and P. Cossee, "Proceedings of the 5th International Congress on Catalysis", J. W. Hightower, Ed., North-Holland, Amsterdam, 1973, p 1301.
(26) G. H. J. DeBeer, T. H. M. Van Sint Fiet, G. H. A. M. Van Der Steen, A. C. Zwaga, and G. C. A. Schuit, *J. Catal.*, **35**, 296 (1974).
(27) J. H. DeBoer, R. B. Fahim, B. G. Linsen, W. J. Visseren, and W. F. N. M. DeVleesschauwer, *J. Catal.*, **7**, 163 (1967).

Surface Structure and Catalytic Activity of a Reduced Molybdenum Oxide–Alumina Catalyst. 1. The Adsorption of Pyridine in Relation with the Molybdenum Valence

T. Fransen, O. van der Meer, and P. Mars*

Twente University of Technology, Department of Chemistry, Enschede, The Netherlands *(Received January 16, 1976)*

Publication costs assisted by the Twente University of Technology

The adsorption of pyridine on a complete monolayer molybdenum oxide–Al_2O_3 catalyst was studied. Both Lewis and Brönsted acid sites are present on a catalyst with a Mo valence of ~4.1. The orientation of adsorbed pyridine was studied by means of its interaction with surface OD groups, which leads to the formation of only 2-deuteriopyridine. The fraction of molybdenum ions active for hydrogenation reactions and that for pyridine adsorption is approximately equal to the Mo^{5+} content, i.e., ~0.2. It is concluded that ensembles of Mo ions of higher and lower valencies (possibly Mo^{5+} and Mo^{4+}) are the sites active for the chemisorption of organic molecules and hydrogen and for hydrogenation reactions.

Introduction

The nature and strength of the acid sites of surface oxides have been the subject of various investigations by means of infrared spectroscopy. To this extent the spectra of adsorbed pyridine appeared to be better interpretable than those of ammonia.[1-4]

In a previous paper we mentioned the existence of Lewis and Brönsted acid sites on a reduced molybdena–alumina catalyst as indicated by pyridine adsorption.[5] Kiviat and Petrakis[6] also found such adsorption sites on a similar catalyst but they could not verify whether the adsorption takes place on the alumina or on the molybdenum oxide. We shall discuss their conclusions in this paper. We report on the investigations of a catalyst, which consists of an alumina carrier almost completely covered with a monomolecular layer of molybdenum oxide.[7,8] The orientation of the adsorbed pyridine toward the surface was studied by observing its interaction with deuterium present on the surface. Measurements of the mean valence of Mo after reduction and of the maximum amount of pyridine adsorbed provided data for discussing the topography of the surface after reduction and the nature of sites active for hydrogenation reactions.

Experimental Section

a. *Preparation of the Catalyst.* From a stream of water vapor saturated with $MoO_2(OH)_2$ this compound was adsorbed on γ-Al_2O_3 at 600 °C. In most cases Degussa alumina (75 $m^2\ g^{-1}$) was used as a carrier. The catalyst, which contained 10.2% MoO_3 by weight, was reduced in a stream of purified hydrogen during 16–24 h at 450 °C.[8]

b. *Valence Measurements.* The average valence of molybdenum was determined by means of a method described by Bourret.[9] This method is based on the determination of the amount of $NaIO_4$ necessary to oxidize the molybdenum to Mo(VI). Oxygen was carefully excluded. The reduced samples were stirred in the oxidizing solution until the color due to reduced molybdenum ions had vanished. A blank run was always taken with pure alumina which took not more than a few percent of the periodate needed for the reduced Mo catalysts. The accuracy of the method was checked by means of pure bulk MoO_2 tabletted with pure γ-alumina. Mo valencies between 4.01 and 4.08 were found in the last case.

c. *Quantitative Adsorption Measurements.* The adsorption of pyridine was studied by using a quartz spring balance. The spring sensitivity was 1 mm/10 mg. A load of 0.5 g of catalyst was used.

d. *Infrared Measurements.* The same equipment and procedures were used as described elsewhere.[7] Because of the strong absorption due to the relatively high amount of reduced molybdenum oxide an attenuation comb in the reference beam together with electronic transmission scale expansion always had to be used.

e. *ESR Measurements.* A Varian X-band spectrometer was used with a 100-kHz modulation unit. The measurements were carried out after reduction in situ.

f. *Materials.* Reagent grade Merck pyridine was used after having been dried and outgassed by the freezing, pumping, and thawing technique. D_2 was supplied by Baker (purity >99%), MoO_3 by Schuchardt, and bulk MoO_2 by K & K Laboratories Inc.

Results

1. *Determination of the Mean Valence of Mo in the Reduced Catalyst.* Reduction of the complete monolayer catalyst by means of purified hydrogen at 450 °C during 16 h or longer yields a mean Mo valence of 4.14 (standard deviation 0.13 after 10 runs). Even reduction for some weeks does not change this value. Catalysts containing less molybdenum than that corresponding to a complete molybdenum(VI) oxide monolayer, prepared by adsorption of polymolybdate anions from solutions of various acidities,[8] however, are reduced less (Table I). They do not reach the mean valence of four under the chosen circumstances. This fact is in agreement with the results of Sondag[10] and Massoth,[11] among others, as well as with the change of the Mo^{5+} content with increasing Mo percentage found by other authors.[12] Variation of the temperature of course has a great influence on the final degree of reduction.

2. *The Infrared Absorption Spectrum of Pyridine on Steam-Treated Alumina.* The alumina was treated with steam at 600 °C (p = 500 Torr) for a few hours, i.e., under the

TABLE I: Mo Valences of $MoOx-Al_2O_3$ Catalysts with Different Percentages of Mo[a] after Reduction for 16 h at 450 °C in Hydrogen

% MoO_3	Mean Mo valence	% MoO_3	Mean Mo valence
2.8	5.7	17.8	4.6
4.9	5.2	22.0	4.4
11.7	4.6		

[a] The carrier was Ketjenfine alumina (S_g = 220 m^2/g). A full monolayer corresponds to about 27% MoO_3.

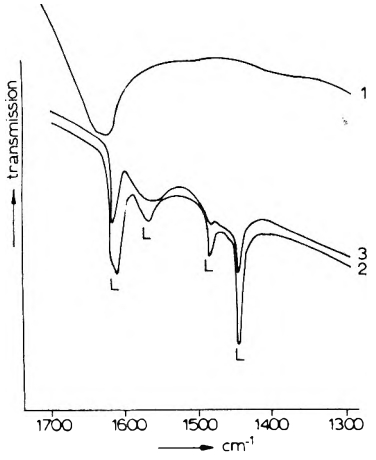

Figure 1. Spectra of pyridine adsorbed on Al_2O_3: (1) background without pumping off water; (2) after evacuation at 150 °C for 0.5 h; (3) same treatment at 250 °C; L = Lewis bound pyridine.

same conditions as the alumina used for the preparation of the catalyst. This is necessary because of some change of the OH group spectrum after this treatment, which is indicative of a change of the surface structure.[7]

The spectrum of pyridine adsorbed at room temperature at p = 10 Torr and pumped off at 150 °C (Figure 1) is almost identical with the spectrum measured by Parry.[3] The bands around 1450 and 1620 cm^{-1} show Lewis acidity. Even the presence of some water vapor (p = 10 Torr, t = 400 °C, see background spectrum) before the adsorption of pyridine does not create protons able to form a Brönsted adsorbed species.

3. *The Spectrum after Adsorption of Pyridine on Moly-Alumina with a Mean Mo Valence Near Four.* The absence of a 1630-cm^{-1} band before pyridine adsorption clearly shows that water has been carefully removed by evacuation at 450 °C and 10^{-5} Torr (Figure 2, spectrum 1).

The main changes in the spectrum of samples with pyridine adsorbed at room temperature (compare Figures 1 and 2) are due to the presence of additional bands in Figure 2 above 1600 cm^{-1} and of a weak band at 1540 cm^{-1}. These bands reflect the existence of a pyH^+ species on the molybdenum(IV) oxide-Al_2O_3 surface.[3,4,6] Obviously, some water has been taken up by the disk during pyridine adsorption. The presence of more water yields more Brönsted acidity (Figure 3) as shown by the intensity of the 1540- and 1640-cm^{-1} bands. This is in agreement with the observations made in case of silica-alumina.[3,4]

4. *The Interaction of Adsorbed Pyridine with OD Groups.* H-D exchange was brought about by means of D_2 at 450 °C until all OH hydrogens had vanished. The disk was then evacuated at the same temperature to obtain some resolution

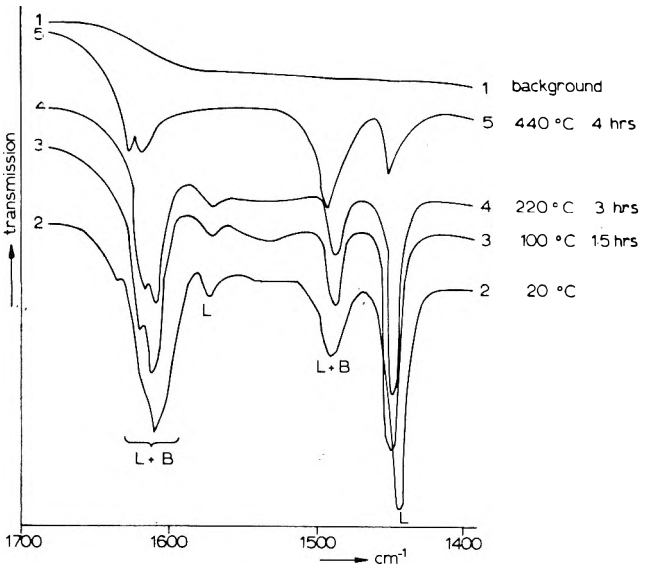

Figure 2. Spectra of pyridine adsorbed on a "dry" molybdenum oxide(IV)-Al_2O_3 catalyst: L = Lewis bound pyridine, B = Brönsted bound pyridine. (1) Background after evacuation at 450 °C for 8 h. The evacuation conditions after adsorption of pyridine are indicated.

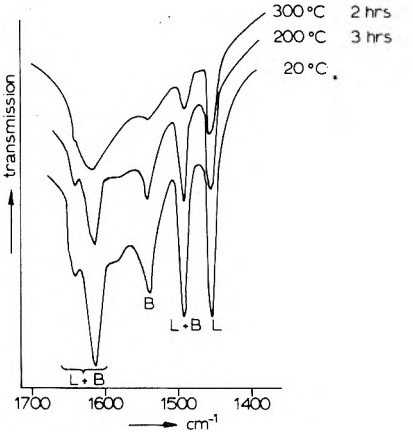

Figure 3. Spectra of pyridine adsorbed on a water containing molybdenum oxide(IV)-Al_2O_3 catalyst.

of the OD groups spectrum and to remove water and deuterium from the system. The evacuation took place for a short time to avoid elimination of too many chemisorbed deuterium atoms (Figure 4B, spectrum 1).

After adsorption of pyridine at room temperature all bands found around 1500 cm^{-1} (see Figure 4A) may be ascribed to coordinately bound species. Neither pyD^+ nor pyH^+ can be detected: the 1540-cm^{-1} pyH^+ band is substituted by the corresponding pyD^+ band which coincides with the 1490-cm^{-1} band[13] (Figures 1 and 2). The adorption disturbs all OD groups. Upon evacuation and raising the temperature a slight restoration of the original OD groups spectrum is observed due to some desorption of pyridine (Figure 4B). At temperatures above 300 °C the OD groups tend to vanish and at the same time a band at 1435 cm^{-1} appears. The relative increase in intensity of this band stops when the OD groups are no longer detectable. This shows that a surface reaction has taken place.

5. *Experiments Pertaining to the Adsorption Capacity of Alumina and of Molybdenum(IV) Oxide-Al_2O_3.* The quartz spring balance measurements at 350 °C reveal that on the

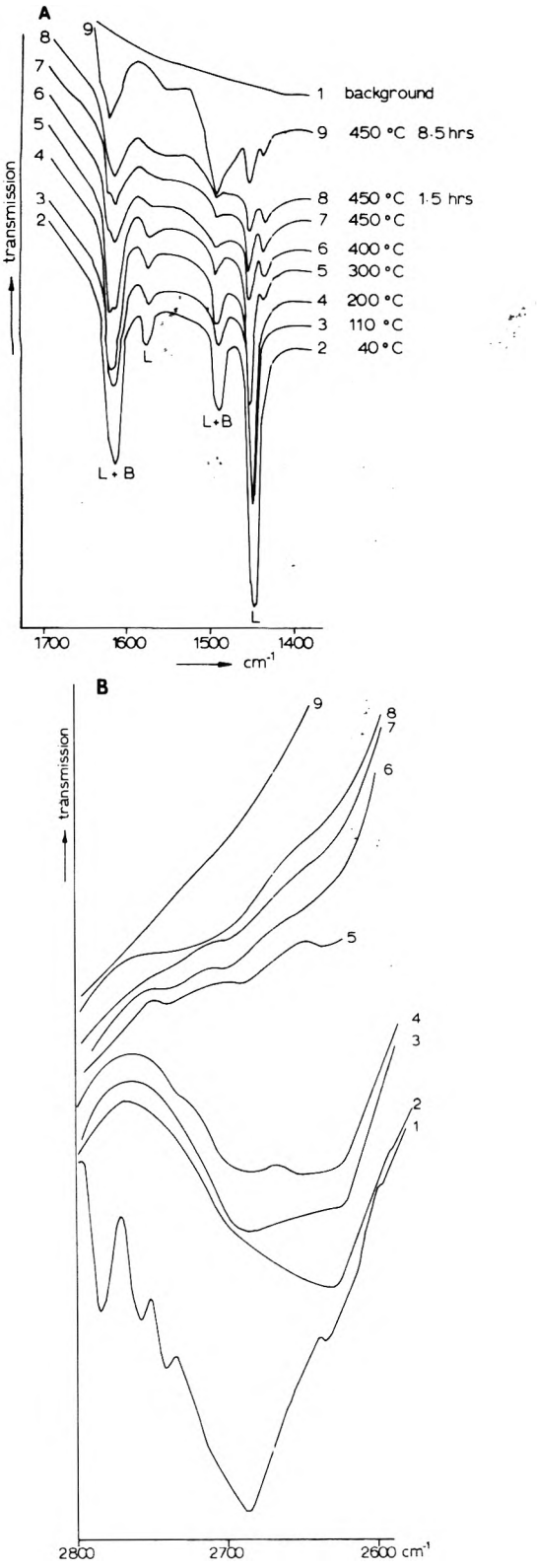

Figure 4. (A and B) Spectra during the reaction of adsorbed pyridine with OD groups after evacuation for 0.5 h unless otherwise indicated. The numbers in Figure 4A correspond with those in Figure 4B: (4A) spectra of pyridine; (4B) spectra of OD groups.

reduced moly–alumina the maximum concentration of pyridine (reached at p = 8 Torr) is about twice that on pure alumina, i.e., 2.5×10^{-3} and 1.3×10^{-3} mmol m^{-2}, respectively. Nearly the same ratio was found in our laboratory at 300 °C when using the dynamic adsorption method.[14]

Discussion

The Molybdenum Valence. As shown, the average valence of the Mo ions is 4.1 after reduction at 450 °C for 16 h. This value is hardly time dependent. Also, the presence of water (p = 15 Torr) during the reaction does not cause a remarkable change in the valence state,[15] which is in contrast with what was found by Sondag[10] and Massoth.[11] The fact, reported in the literature,[11] that a lower coverage of the alumina by molybdenum(VI) oxide yields a higher mean valence is established by our measurements (see Table I). This supports the conclusion that those parts of the alumina which strongly bind the molybdenum(VI) ions stabilize the higher valences.[11,12]

Many authors have reported the detection by ESR of Mo(V) ions having reduced the catalyst with hydrogen.[12,16] Qualitative ESR measurements in our laboratory revealed the presence of Mo(V) ions even after reduction at 450 °C for 1 week (providing a valence of four). Recently, Seshadri and Petrakis,[16] studying a catalyst with a Mo percentage comparable with that of a complete monomolecular molybdenum(VI) oxide layer, found that after reduction at 450 °C for some hours, at least 10% of the Mo ions had a valence of five, which is in accordance with the measurements performed by Masson and Nechtschein.[12] The inaccuracy in the determination of the valence (i.e., 4.1 ± 0.1) does not allow us to ascribe this fact to the stabilizing influence of the carrier. Also a disproportionation reaction may occur, viz.

$$2\mathrm{Mo(IV)} \rightleftarrows \mathrm{Mo(III)} + \mathrm{Mo(V)}$$

The Adsorption of Pyridine on Alumina. The absence of Brönsted acidity when pyridine is adsorbed (Figure 1) is in agreement with the conclusions of Parry,[3] among others.

The maximum amount of pyridine to be adsorbed, i.e., 1.3×10^{-3} mmol m^{-2}, corresponds to a surface occupation of the same order of magnitude found by Knözinger and Stolz on this oxide.[17]

Pyridine Adsorbed on Reduced Moly–Alumina. The spectra observed are in accordance with those of Kiviat and Petrakis.[6] Even after careful elimination of water the weak band at 1540 cm^{-1} reveals the existance of some Brönsted acidity.

Previously[7] we showed that reduction of a complete molybdenum(VI) oxide monolayer on alumina involves a shrinkage of this layer so that the reduced molybdenum oxides covers the alumina only partly (for about 80%). Part of the pyridine may therefore be adsorbed on the bare alumina. The intensities and the positions of the OH absorption bands of the free alumina in molybdenum(IV) oxide–alumina are almost identical with those of pure alumina. This gives evidence that the adsorption capacity of the alumina as such will not differ much from that of the pure carrier, i.e., 1.3×10^{-3} mmol m^{-2} of alumina. From this and the adsorption capacity of molybdenum(IV) oxide–alumina observed (twice as much as that of the carrier) the conclusion arises that pyridine is mostly adsorbed on the molybdenum oxide. The maximum pyridine–Mo ratio is about 0.20 mol $atom^{-1}$, assuming 80% coverage of the carrier by molybdenum(IV) oxide. Kiviat and Petrakis,[6] working with the KBr technique, did not obtain spectroscopic evidence for the adsorption of pyridine on *pure* molybdenum oxide. As it is difficult to make unsupported molybdenum oxides with a reasonable surface area, it seems likely that their experimental technique was not sensitive enough.

The rather strong adsorption of pyridine on supported molybdenum(IV) oxide is sustained by the observation that the hydrogenation of xylene and of olefins on this oxide is poisoned by pyridine and other amines.[14,19] The amine–Mo

ratio necessary for complete suppression of these reactions is about 0.20 mol atom^{-1}, and thus equals the pyridine adsorption capacity we found.

In contrast to the observations of pyridine adsorbed on a *dry* catalyst much Brönsted acidity was detected when water was present. The absence of this water effect when working with pure alumina shows that this proton acidity must be connected with the molybdenum. Upon increasing the temperature of evacuation the Brönsted bound pyridine disappears. We may therefore assume that this type of acidity cannot play a role in catalytic hydrogenation reactions at higher temperatures.

Above 400 °C even the spectrum of the "Lewis" pyridine changes (Figure 2, spectrum 5). Possibly under these circumstances some adsorbed pyridine is decomposed.

The Interaction of Adsorbed Pyridine with Adsorbed Hydrogen on Reduced Moly-Alumina. Similar to the literature[4,17,18] we found that the intensities of the bands due to CH (CD) vibrations of pyridines are very weak after adsorption, especially when evacuation has taken place at temperatures above 200 °C. Moreover, the interpretation of these bands is hindered as they show complicated shifts in comparison with the spectrum of unadsorbed pyridine.[18] These facts indicate that the CH and CD stretching region is not very suitable in this case for H–D exchange studies. The 2000–1000-cm^{-1} region, however, is as shown in Figure 4. On heating, pyridine reacts with the alumina OD groups: all OD groups vanish and at the same time a new band (1435 cm^{-1}) appears. This band must be attributed to adsorbed 2-deuteriopyridine: a shift of 11 cm^{-1} by Lewis adsorption (original ν19b vibration absorbs at 1424 cm^{-1} [20]) is in agreement with the shift we measured of the corresponding ν19b band of nondeuterated pyridine (at 1439 cm^{-1}),[21] 4-deuteriopyridine (at 1413 cm^{-1}),[20] and pyridine-d_5[20,21] (at 1301 cm^{-1}). These facts inspire us to assume that, whatever deuterated pyridine species is concerned the ν19b band will always show a similar shift by Lewis chemisorption.

The mere creation of 2-deuteriopyridine indicates that the adsorbed molecules are orientated toward the surface in such a way that they interact with it only through their nitrogen atoms and through the hydrogen atoms at the ortho positions.

The questions arises whether the *reacting* pyridine is adsorbed on the alumina and/or on the molybdenum oxide. A separate experiment on *pure* alumina also showed the generation of 2-deuteriopyridine. On the other hand, we know that molybdenum(IV) oxide on alumina is able to chemisorb hydrogen above 300 °C, possibly in the form of hydroxyl groups.[22,23] Perhaps the 2755-cm^{-1} band, due to an extra OD group next to those of Al_2O_3,[7] reflects this chemisorption (see also Figure 4). Because hydrogenation takes place only on molybdenum oxide and not on alumina, the interaction of adsorbed pyridine with chemisorbed hydrogen has to occur on the former species too. Because of these facts we may suppose that during the *hydrogenation of pyridine* the first and relatively rapid addition of hydrogens will occur at the ortho positions. Further hydrogenation will proceed more slowly because the chemisorbed dihydropyridine must bend toward the surface in order to pick up adsorbed hydrogen atoms.[24] Such a proposal for the reaction mechanism, viz.

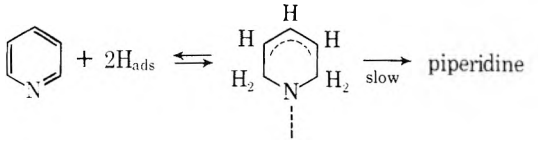

corresponds with the kinetics determined by Sonnemans, van den Berg, and Mars,[14] who found that between 300 and 375 °C the reaction rate is proportional to $p_{H_2}^{1.5}$. These kinetics suggest different chemisorption sites for pyridine and hydrogen, as is in agreement with our findings which will be reported in the future.[23]

A Model for the Surface of Reduced Moly-Alumina. Our observations that the Al–OH groups of the reduced, originally complete, monolayer molybdenum(IV) oxide–Al_2O_3 catalyst are not disturbed indicate that a rather large area of the carrier is bare. This implies that the molybdenum oxide units may form monomolecular platelets.[7]

We may wonder what are the sites on these "islands" active for (de)hydrogenation reactions. From our results and those from the literature it is striking that about 10–20% of the Mo ions behave differently.

First, pyridine adsorption preferentially takes place on the latter fraction. Secondly, the hydrogenation of pyridine occurs on the same part of the surface. Some investigators[12,16] also found via ESR measurements that at least 10% of the Mo ions have a valence of five after reduction with hydrogen. The amount of Mo^{5+} ions parallels the Mo content up to maximum monolayer coverage,[12] similar to catalytic activities for hydrogenation.[25] These facts induce us to state that Mo^{5+} ions are involved in the catalytic reactivity. These ions, being more or less bare (C_{4v} symmetry[16,26,27]), are exclusively able to react with gas-phase molecules and may be protected against further reduction due to stabilization by the carrier or may be formed by disproportionation of Mo^{4+}.

The relative amount of active sites, about 10–20%, points to the existence of ensembles of Mo with a higher valence (5 or even 6) with surrounding molybdenum with a lower valence (4 or even 3). This combination will be able to chemisorb organic molecules and hydrogen on neighboring atoms and to facilitate hydrogenation.

Conclusion

(1) Reduction of a completely covered molybdenum(VI) oxide–Al_2O_3 monolayer catalyst yields Mo ions with a mean valence of nearly four. Reduction of a moly-alumina catalyst with a lower Mo content proceeds more difficultly.

(2) Both Lewis and Brönsted acid sites are present on a reduced catalyst; perhaps only the former plays a role in catalytic reactions at higher temperatures.

(3) Adsorbed pyridine interacts via its ortho hydrogen with hydrogen chemisorbed on the molybdenum(IV) oxide–alumina surface. Pyridine adsorbed on this catalyst has the same orientation as when it is adsorbed on pure Al_2O_3. Most of the adsorbed pyridine is associated with the molybdenum part of the catalyst.

(4) Only 10–20% of the Mo ions are active for pyridine adsorption and play a role in catalytic reactions. These ions are characterized by a valence of five and are surrounded by oxygens in a C_{4v} symmetry.

(5) The sites active for (de)hydrogenation reactions consist of ensembles of molybdenum oxide units. Pyridine adsorption, poisoning, and valence measurements indicate that in these ensembles the higher (five) valent ions adsorb the compound to be (de)hydrogenated. The lower (four) valent Mo ions play a role in the adsorption of hydrogen.

References and Notes

(1) L. H. Little, "Infrared Spectra of Adsorbed Species", Academic Press, London, 1966.
(2) L. Kubelkova and P. Jiru, *Z. Phys. Chem. (Frankfurt am Main)*, **80**, 140

(1972).
(3) E. P. Parry, *J. Catal.*, **2**, 371 (1963).
(4) M. R. Basila, T. R. Kantner, and K. H. Rhee, *J. Phys. Chem.*, **68**, 3197 (1964).
(5) J. Sonnemans, F. Goudriaan, and P. Mars, *Proc. Int. Congr. Catal., 5th*, part II, 1085 (1972).
(6) F. E. Kiviat and L. Petrakis, *J. Phys. Chem.*, **77**, 10, 1232 (1973).
(7) T. Fransen, O. van der Meer, and P. Mars, *J. Catal.*, **42**, 79 (1976).
(8) J. Sonnemans and P. Mars, *J. Catal.*, **31**, 209 (1973).
(9) P. Bourret, J. Lecuire, and C. Weiss, *Chim. Anal.*, **52**, 48 (1970).
(10) P. Sondag, D. Q. Kim, and F. Marion, *C.R. Acad. Sci. Paris*, **259**, 8, 4704 (1964).
(11) F. E. Massoth, *J. Catal.*, **30**, 204 (1973).
(12) J. Masson and J. Nechtschein, *Bull. Soc. Chim. Fr.*, **10**, 3933 (1968).
(13) D. Cook, *Can. J. Chem.*, **39**, 2009 (1961).
(14) J. Sonnemans, G. H. van den Berg, and P. Mars, *J. Catal.*, **31**, 220 (1973).
(15) T. Fransen, P. C. van Berge, and P. Mars, manuscript in preparation.
(16) K. S. Seshadri and L. Petrakis, *J. Catal.*, **30**, 195 (1973).
(17) H. Knözinger and H. Stolz, *Fortschr. Kolloid. Polym.*, **55**, 16 (1971).
(18) F. Pratesi and R. Freymann, *C.R. Acad. Sci. Paris, Ser. B*, **266**, 327 (1968).
(19) F. Goudriaan, Thesis, Twente University of Technology, The Netherlands, 1974 (in English).
(20) F. A. Andersen, B. Bak, S. Brodersen, and J. Rastrup-Andersen, *J. Chem. Phys.*, **23**, 6, 1047 (1955).
(21) L. Corrsin, B. J. Fax, and R. C. Lord, *J. Chem. Phys.*, **21**, 7, 1170 (1953).
(22) W. K. Hall and F. E. Massoth, *J. Catal.*, **34**, 41 (1974).
(23) T. Fransen, J. Hofman, and P. Mars, unpublished results.
(24) J. Sonnemans, J. Janus, and P. Mars, *J. Phys. Chem.*, following paper in this issue.
(25) A. S. Russell and J. J. Stokes Jr., *Ind. Eng. Chem.*, **38**, 1071 (1946).
(26) M. Dufaux, M. Che, and C. Naccache, *J. Chim. Phys.*, **67**, 527 (1970).
(27) A. Ismayel-Milanovic, J. M. Basset, H. Praliaud, M. Dufaux, and L. de Mourgues, *J. Catal.*, **31**, 408 (1973).

Surface Structure and Catalytic Activity of a Reduced Molybdenum Oxide–Alumina Catalyst. 2. The Mechanism of Pyridine Hydrogenation and Piperidine Dehydrogenation

J. Sonnemans,† J. M. Janus, and P. Mars*

Twente University of Technology, Department of Chemistry, Enschede, The Netherlands *(Received January 16, 1976)*

Publication costs assisted by the Twente University of Technology

The dehydrogenation of piperidine has been studied and found to have an order of −1.5 with respect to the hydrogen partial pressure. By combining these results with those obtained for pyridine hydrogenation on the same catalyst a complete rate equation for piperidine dehydrogenation together with the stoichiometric number of the rate-determining step of these reactions could be derived. This number appeared to be one. A mechanism for pyridine hydrogenation is presented on the basis of these results and those from adsorption studies using the infrared spectroscopic technique. The rate-determining step is found to be the formation of adsorbed trihydropyridine.

Introduction

Hydrogenation of aromatic nitrogen containing compounds is the first step for their denitrogenation on metal oxide or sulfide catalysts, such as $CoO–MoO_3–Al_2O_3$.[1–4] The kinetics of this hydrogenation has been studied with the aid of model compounds such as quinoline[2] and pyridine.[3,5] Only little information is available regarding the mechanism of this hydrogenation, the active sites, and the rate-determining step.

The kinetics of the hydrogenation of pyridine has been studied by varying the temperature, the reaction time, the pyridine partial pressure, and the hydrogen pressure. The conversion as a function of the reaction time shows a first-order process.[3,6] However, the rate constant is found to be inversely proportional to the initial pyridine partial pressure.[3,5] An explanation for these results, also observed for other nitrogen containing compounds,[7] can be given by considering the rate equation[5]

$$-\frac{dP_{py}}{dt} = k_1\theta_{py}P_{H_2}{}^a = \frac{k_1 b_{py}P_{py}P_{H_2}{}^a}{1 + b_{py}P_{py} + \Sigma b_{prod}P_{prod}} \quad (1)$$

where θ_i is the degree of occupation, b_i the adsorption constant of compound i, P, the partial pressure, and k_1, the rate constant.

A Langmuir type of adsorption of the nitrogen bases has been assumed. The adsorption of hydrogen and nitrogen bases occur on different sites[5] and experiments with the volumetric technique confirmed that the presence of nitrogen bases does not influence the rate of hydrogen chemisorption.[8]

Because the adsorption constants of the nitrogen bases appear to be almost equal and $b_N P_{N_0} \gg 1$ (P_{N_0} = total pressure of the nitrogen base), this equation can be simplified as

$$-\frac{dP_{py}}{dt} = k_1 \frac{P_{py}}{P_{N_0}} P_{H_2}{}^a \quad (2)$$

The influence of hydrogen pressure has been studied by varying this pressure from 15 to 75 atm.[5] The results obtained at 300 and 375 °C show the order with respect to hydrogen to be 1.5–1.6 (Figure 1). A discussion on details of the mechanism

† Present address: AKZO Chemie Nederland B.V., Amsterdam-N, The Netherlands.

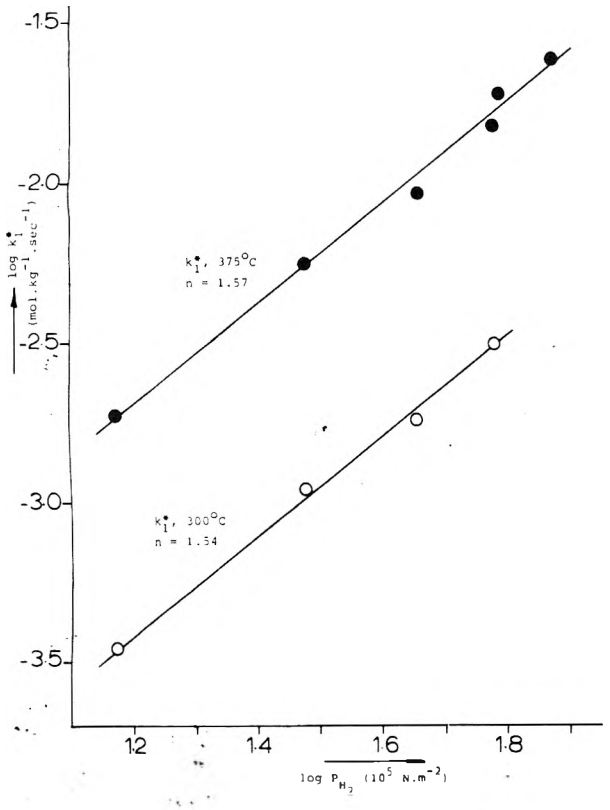

Figure 1. Effect of the hydrogen pressure on the pseudo rate constant of the pyridine hydrogenation at 300 and 375 °C (values from Table II in ref 5): (○) = k_1^* at 300 °C; (●) k_1^* at 375 °C.

could not be given due to lack of data on the piperidine dehydrogenation.

The conversion of *piperidine* has been studied at 300 and 325 °C. It was shown[7] that the (hydro)cracking of piperidine can be described by the following equation:

$$-\frac{dP_{pip}}{dt} = k_2 \frac{P_{pip}P_{H_2}}{P_{pip_0}} \quad (3)$$

At these temperatures the conversion into pyridine is less than 1% of the total amount of products formed (Figure 1 in ref 7), so that no conclusions about the dehydrogenation reaction could be drawn.

In this paper, experiments on the piperidine conversion at higher temperatures will be reported. The mechanism of the pyridine hydrogenation on the reduced (CoO)–MoO_3–Al_2O_3 catalyst is discussed on the basis of kinetic experiments on both the pyridine hydrogenation and the piperdine dehydrogenation and adsorption studies of pyridine and hydrogen.

Experimental Section

Procedures. The equipment used for the kinetic experiments has been described elsewhere.[4] More detailed information is given in ref 5 for the pyridine hydrogenation and in ref 7 for the piperidine dehydrogenation. For the piperidine conversion at higher temperatures a reactor was used with an internal diameter of 4 mm. Measurements with a thermocouple showed that the temperature drop over the catalyst bed was always within 2 °C. The height of the catalyst bed was about 2.5 cm. Separate experiments showed that the influence of the metal wall of the reactor and of the internal and external diffusion on the conversion could be neglected. The stability of the catalyst was good enough to ignore the decline in activity.

TABLE I: Conversion of Piperidine as a Function of Hydrogen Pressure[a]

P_{H_2}, 10^5 N m^{-2}	Product composition,[b] mol % (P_i/P_{pip_0})				
	C_5	pip	py	NPP	Loss
40	3.7	59.6	6.5	5.8	18.6
50	4.6	61.1	4.4	7.5	14.9
60	6.1	63.5	3.9	9.3	7.9
70	6.4	65.6	2.7	9.9	5.5
80	7.2	64.4	2.5	11.2	3.5
90	7.6	65.2	2.2	11.8	1.4

[a] T = 375 °C; $P_{pip_0} = 0.33 \times 10^5$ N m^{-2}; 0.27 g of CoO–MoO_3–Al_2O_3; $t = 0.14 \times 10^7$ kg N s m^{-2} mol^{-1}. [b] Products observed are pentane and pentene (C_5), ammonia (not well analyzed), pentylamine (very small amount), piperidine (pip), pyridine (py), and *n*-pentylpiperidine (NPP). The percentage loss is based on the balance of pentyl groups.

The reaction time is defined as $t = mP\phi_t^{-1}$ in which m is the mass of the catalyst (kg), P is the total pressure (N m^{-2}), and ϕ_t is total moles fed to the reactor (mol s^{-1}).

The product distributions have been determined by gas chromatographic analyses[9] of samples taken from the gas stream or samples obtained after total condensation of the reaction products with the aid of liquid nitrogen.

Materials. The catalyst was 4% CoO–12% MoO_3–γAl_2O_3 (Ketjenfine, 235 m^2 g^{-1}) with particle diameter of 0.21–0.30 mm. Before use, the catalyst was reduced with hydrogen at 450 °C for at least 16 h.

Piperidine was distilled under a nitrogen atmosphere on molecular sieves and brought into the saturator immediately after distillation. The pyridine content of the piperidine was found to be very low.

Results

The conversion of piperidine has been studied at 350 and 375 °C as a function of reaction time and hydrogen pressure. The influence of the hydrogen pressure on the piperidine conversion and the product distribution is shown in Table I. The decreasing amount of pyridine at higher hydrogen pressures points to a negative order with respect to hydrogen. Determination of the order with respect to piperidine for this reaction was not possible because in our measurements the reaction time has not been varied sufficiently. However, from a discussion of adsorption constants of the relevant bases it can be concluded that this order is unity.[5]

At longer reaction times the pyridine–piperidine equilibrium was established. At 375 °C we observed a constant ratio of about 7 between the pyridine and the piperidine partial pressures at $t > 0.3 \times 10^7$ kg N s m^{-2} mol^{-1} ($P_{H_2} = 60 \times 10^5$ N m^{-2}, $P_{pip_0} = 0.33 \times 10^5$ N m^{-2}). Calculation of the equilibrium constant $K = P_{pip}P_{py}^{-1}P_{H_2}^{-3}$ from these values showed a somewhat higher value (3.2×10^{-20}) than the one calculated from the data of Goudriaan[6] (1.6×10^{-20} N^{-3} m^6). This may point to the establishment of a pseudoequilibrium in our experiment.[6]

Discussion

Kinetics of Piperidine Dehydrogenation. As discussed in the Introduction the kinetics of pyridine hydrogenation can be described by eq 2 in which a = 1.5. The activation energy was found[6] to be 66 kJ mol^{-1}.

In order to formulate the kinetics of the piperidine dehy-

drogenation one has to take into account the facts that several reactions occur in the whole process and that the selectivity of the pyridine formation is rather low. From the results presented in Table I, the order with respect to hydrogen for the dehydrogenation of piperidine can be calculated by using the following reaction scheme:

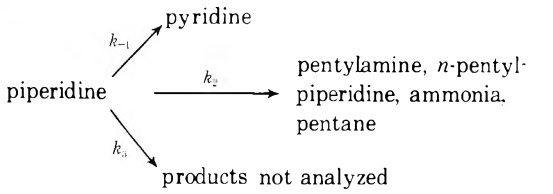

Here the complex cracking and hydrocracking reactions[7] have been aggregated in reaction 2. Reaction 3 is assumed to be a parallel reaction.

On the bases of the kinetics found for piperidine cracking and because the adsorption coefficients of the nitrogen bases are nearly equal,[5] we formulate the rate equation of piperidine conversion:

$$\frac{-dP_{pip}}{dt} = k_{-1}\frac{P_{pip}}{P_{pip_0}}P_{H_2}{}^{x} + k_2\frac{P_{pip}}{P_{pip_0}}P_{H_2}{}^{y} + k_3\frac{P_{pip}}{P_{pip_0}}P_{H_2}{}^{z} \quad (4)$$

Integration of this yields

$$\frac{P_{pip_0}}{t}\ln\frac{P_{pip_0}}{P_{pip}} = k_{-1}P_{H_2}{}^{x} + k_2P_{H_2}{}^{y} + k_3P_{H_2}{}^{z} = k_{-1}^{*} + k_2^{*} + k_3^{*} \quad (5)$$

From the piperidine conversion and eq 5, the sum of the rate constants can be calculated; the ratios of the amounts of pyridine to cracking products ($2P_{NPP} + P_{C_5}$), and to the unanalyzed products formed give the individual rate constants k_i^*.

The data obtained for $k_{-1}P_{H_2}{}^{x}$ ($= k_{-1}^*$) have been plotted in Figure 2 as a function of hydrogen pressures. An order of 1.44 ± 0.26 (90% confidence region) with respect to hydrogen is found. Similar plots for k_2^* and k_3^* show an order of 0.8 with respect to hydrogen for the (hydro)cracking of piperidine, which is in agreement with previous results,[7] and a rather high negative order with respect to hydrogen for the formation of heavy products not analyzed.

Two points may have an effect on the interpretation of the kinetics. They are the following:

(a) The establishment of the pyridine–piperidine equilibrium. The piperidine conversion into pyridine is found to be about 25% from equilibrium if the equilibrium constant is calculated from the data reported by Goudriaan.[6] Correction of the results for the reverse reaction (pyridine → piperidine) will increase the order with respect to hydrogen for the piperidine dehydrogenation.

(b) Another reaction involving the formation of heavy products. The curved line for k_3^* in Figure 2 points to another reaction scheme, for instance, a consecutive reaction instead of a parallel reaction for the formation of products not analyzed. The negative order in hydrogen for k_3^* as well as the results of the piperidine conversion at low hydrogen pressure[7] indicate the formation of heavy products from partly dehydrogenated piperidine. Incorporation of this possibility in the reaction scheme will result in a lower order in hydrogen for the piperidine dehydrogenation.

In conclusion, therefore, we may state that the order with

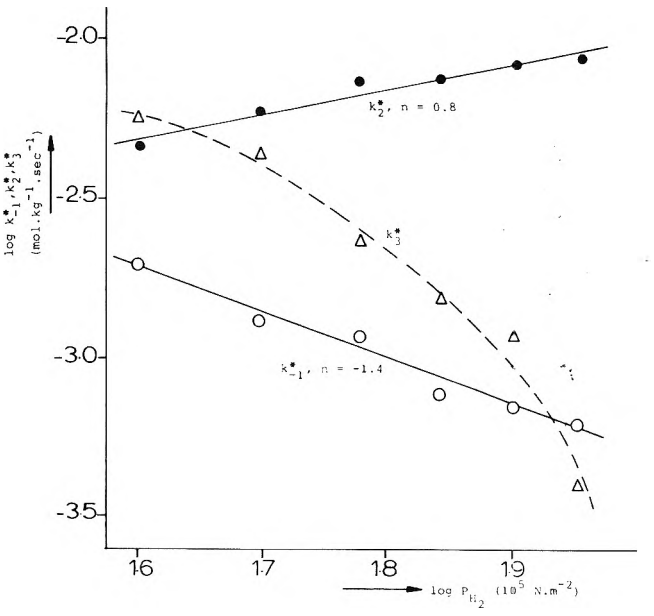

Figure 2. The three pseudo rate constants of the piperidine conversion reactions as a function of the hydrogen pressure (calculated from Table I): (○) k_{-1}^*; (●) k_2^*; (△) k_3^*.

respect to hydrogen for the piperidine dehydrogenation will lie between −1 and −2. The rate equation for this reaction can be formulated as

$$r_{dehydrogenation} = k_{-1}\frac{P_{pip}}{P_{pip_0}}P_{H_2}{}^{(-1\text{ to }2)} \quad (6)$$

The Stoichiometric Number. According to Manes, Hofer, and Weller[10] and Horiuti[11] the following relation applies:

$$k_1/k_{-1} = K^{1/\gamma} \quad (7)$$

where K is the equilibrium constant ($= P_{pip_{eq}} \cdot P_{pyr_{eq}}{}^{-1}P_{H_{2eq}}{}^{-3}$), and γ, the stoichiometric number of the rate-determining step of the reaction; i.e., the number of times the rate determining step of the reaction occurs, compared with the overall reaction. Values of γ can be derived from eq 7 by means of: (a) the kinetic expression of the forward and the backward reactions;[12] (b) the enthalpy of the reaction in comparison with the difference in energy of activation of the forward and the backward reactions; (c) the substitution of the values of k_1, k_{-1}, and K.

(a) At the equilibrium, the rate of dehydrogenation is equal to that of hydrogenation. Assuming the rate equations found also apply in the neighborhood of equilibrium, and combining eq 2 and 6 with $a = 1.5$ and $P_{N_0} = P_{pip_0}$, we obtain:

$$k_{-1}\frac{P_{pip_{eq}}}{P_{N_0}}P_{H_2}{}^{-(1\text{ to }2)} = k_1\frac{P_{pyr_{eq}}}{P_{N_0}}P_{H_2}{}^{1.5} \quad (8)$$

Combination of this result with eq 7 gives:

$$\frac{P_{pip_{eq}}P_{H_2}{}^{-(1\text{ to }2)}P_{N_0}}{P_{pyr_{eq}}P_{H_2}{}^{1.5}P_{N_0}} = \left(\frac{P_{pip_{eq}}}{P_{pyr_{eq}}P_{H_2}{}^{3}}\right)^{1/\gamma} \quad (9)$$

From eq 9 we conclude that γ must have the value of unity. The kinetic equation of piperidine dehydrogenation, therefore, takes the form

$$r_{dehydrogenation} = k_{-1}\frac{P_{pip}}{P_{N_0}}P_{H_2}{}^{-1.5} \quad (10)$$

(b) Substitution of the exponential temperature functions of k_1, k_{-1}, and K in eq 7 provides

$$E_1 - E_{-1} = \Delta H°/\gamma \qquad (11)$$

E_1 was found to be 66 kJ mol^{-1}. Previously[7] it was reported that E_{-1} exceeds the value of 160 kJ mol^{-1}. From a few measurements of the piperidine conversion as a function of temperature, the value of E_{-1} was estimated to be 230 kJ mol^{-1}. $\Delta H°$ has a reported[6] value of -160 kJ mol^{-1}. Substitution of these values in eq 11 also shows that γ has a value of unity.

Because the values of E and E_{-1} are practically not influenced by the form of the kinetic expression for the relevant reactions, this method may be regarded not to depend on that described in section a.

(c) From the values of k_1[5] and k_{-1}, we calculated an equilibrium constant with a value of 6×10^{-20} N^{-3} m^6, assuming $\gamma = 1$ in eq 7. This is quite in agreement with the value of 2×10^{-20} N^{-3} m^6 calculated from the data given by Goudriaan.[6] This also supports that $\gamma = 1$.

For two reasons this result must be regarded as practically independent of the others. The calculated values of k_1 and k_{-1} remain in about the same order of magnitude when using rate equations different from (2) with $a = 1.5$ and (10), respectively. Moreover, the value of K differs largely from unity, so that from eq 7 γ can be calculated accurately. From these results it is obvious that the stoichiometric number of the rate-determining step of the pyridine hydrogenation into piperidine is unity.

Mechanism of Pyridine Hydrogenation. The following elementary steps may occur in pyridine hydrogenation:

$$\text{pyridine (py)} \rightleftharpoons \text{py}_{\text{ads}} \qquad \text{(a)}$$

$$\text{hydrogen } (H_2) \rightleftharpoons H_{2_{\text{ads}}} \qquad \text{(b)}$$

$$H_{2_{\text{ads}}} \rightleftharpoons H_{\text{ads}} + H_{\text{ads}} \qquad \text{(c)}$$

$$\text{py } H_{x_{\text{ads}}} + H_2 \rightleftharpoons \text{py } H_{(x+2)_{\text{ads}}} \quad (0 \leq x \leq 4) \qquad \text{(d)}$$

$$\text{py } H_{y_{\text{ads}}} + H_{2_{\text{ads}}} \rightleftharpoons \text{py } H_{(y+2)_{\text{ads}}} \quad (0 \leq y \leq 4) \qquad \text{(e)}$$

$$\text{py } H_{z_{\text{ads}}} + H_{\text{ads}} \rightleftharpoons \text{py } H_{(z+1)_{\text{ads}}} \quad (0 \leq z \leq 5) \qquad \text{(f)}$$

$$\text{pip}_{\text{ads}} \rightleftharpoons \text{piperidine} \qquad \text{(g)}$$

The stoichiometric number of unity means that the rate-determining step occurs once with respect to the overall reaction. For the reaction steps b and c the value of γ amounts to 3. Hence, these steps cannot be rate determining under our reaction conditions.

Reaction steps a and g are not rate determining either. Deriving rate equations based on these suppositions and assuming a low coverage of the surface with hydrogen we get the rate equations $r_{\text{hydr}} = kP_{\text{py}}P_{\text{N}_0}{}^{-1}$ and $r_{\text{hydr}} = kP_{\text{py}}P_{\text{N}_0}{}^{-1}P_{\text{H}_2}{}^3$, respectively. These are, however, in contradiction with the experimental results. Steps d, e, and f of the reaction scheme given above remain as possible rate-determining steps. The order 1.5 with respect to hydrogen for the pyridine hydrogenation[5] indicates one of the following steps to be rate determining:

$$\text{py } H_{\text{ads}} + H_2 \rightarrow \text{py } H_{3_{\text{ads}}} \qquad \text{(h)}$$

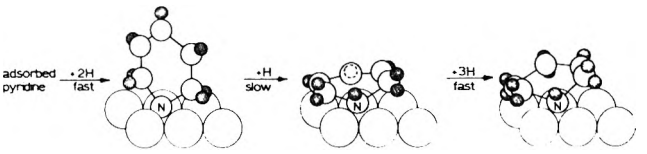

Figure 3. Scheme of the mechanism of pyridine hydrogenation.

$$\text{py } H_{\text{ads}} + H_{2_{\text{ads}}} \rightarrow \text{py } H_{3_{\text{ads}}} \qquad \text{(i)}$$

$$\text{py } H_{2_{\text{ads}}} + H_{\text{ads}} \rightarrow \text{py } H_{3_{\text{ads}}} \qquad \text{(j)}$$

This result, showing that after the rather slow formation of trihydropyridine a further hydrogenation taking place fast, may be surprising. However, it is understandable if the state of adsorption of the pyridine molecule is considered. In our laboratory Fransen showed by means of infrared spectroscopic measurements of adsorbed pyridine on a reduced molybdenum oxide–Al_2O_3 catalyst that a fast exchange particularly between the surface OD groups and the ortho H of pyridine occurs.[13] This points to a more or less perpendicular position of the pyridine molecule on the catalyst surface. This fact suggests that two hydrogen atoms may be added rapidly to the adsorbed pyridine, whereafter the slow uptake of the third hydrogen atom takes place and as a consequence the hybridization of the nitrogen atom is changed. The partly hydrogenated molecule may now move the unhydrogenated bonds to the surface, which in its turn may be rapidly hydrogenated. This supports the conclusion that reaction j is rate determining. This process is depicted in Figure 3. In this figure the hydrogen atoms are supposed to originate from the hydroxyl groups of molybdenum. The observation of the existence of separate adsorption sites for hydrogen and pyridine supports this mechanism.

Acknowledgment. We express our gratitude to Mr. T. Fransen for his valuable discussions.

References and Notes

(1) R. A. Flinn, O. A. Larson, and H. Beuther, *Hydrocarbon Process Petrol. Refiner*, **42**, 129 (1963).
(2) J. Doelman and J. C. Vlugter, Proceedings of the World Petroleum Congress, 6th, Frankfurt, Germany, 1963, Section 3, paper 12-PD 6.
(3) H. G. McIlvried, *Ind. Eng. Chem., Proc. Des. Devel.*, **10**, 125 (1971).
(4) J. Sonnemans, F. Goudriaan, and P. Mars, *Proc. Int. Congr. Catal., 5th*, 1085 (1972).
(5) J. Sonnemans, G. H. van den Berg, and P. Mars, *J. Catal.*, **31**, 220 (1973).
(6) F. Goudriaan, Thesis, Twente University of Technol., Enschede, The Netherlands, 1974 (in English).
(7) J. Sonnemans, W. J. Neijens, and P. Mars, *J. Catal.*, **34**, 215 (1974).
(8) T. Fransen, unpublished results.
(9) T. Beugeling, M. Boduszyński, F. Goudriaan, and J. Sonnemans, *J. Anal. Lett.*, **4**, 727 (1971).
(10) M. Manes, L. J. E. Hofer, and S. Weller, *J. Chem. Phys.*, **18**, 1355 (1950).
(11) J. Horiuti, *Adv. Catal.*, **9**, 339 (1957).
(12) J. Happel, H. Blanck, and T. D. Hamill, *Ind. Eng. Chem., Fundam.*, **5**, 289 (1966).
(13) T. Fransen, O. van der Meer, and P. Mars, *J. Phys. Chem.*, preceeding paper in this issue.

Effect of Temperature on the Charge Transfer Band of Methiodide of Some Nitrogen Heteroaromatics

Sanjib Bagchi and Mihir Chowdhury*

Department of Chemistry, Presidency College, Calcutta-700 073, India *(Received October 25, 1975; Revised Manuscript Received June 7, 1976)*

Spectra of methiodides of pyridine and diazines in solution have been studied in the temperature range 50 to −50 °C. The observed blue shift of the charge transfer (CT) band with a decrease in temperature is explained as being due to an increase of solvation of the intimate ion pair. No such shift, however, is observed in the emission studies. The intensity of the CT absorption decreases with a decrease in temperature and this has been attributed to a modification of equilibria between several types of ion pairs and dissociated ions in the solution. A spectrophotometric method (noniterative) has been suggested for the determination of the ion-pair dissociation constant (K_d) and ϵ_{max}. Other thermodynamic quantities ($\Delta H°$ and $\Delta S°$) have also been determined from such studies.

Introduction

It has long been known that the charge-transfer (CT) bands of N-heteroaromatic methiodides are very sensitive to a change of solvent and temperature.[1] Kosower[2] has introduced Z values (which are transition energies in kilocalories per mole of 1-ethyl-4-methoxycarbonylpyridinium iodide) to characterize the solvating ability of the medium. The lack of correlation of the Z value with any macroscopic solvent parameter shows that the nature of the solvent–solute interaction is not simple. In recent years the effect of temperature and pressure on the CT band of such compounds in solution has been studied.[3,4] These workers suggest a change of solvation with temperature and pressure change. In the present work the CT transition energies and dissociation constants of some N-heterocyclics in solution have been investigated as a function of temperature.

We have studied absorption and emission spectra of *N*-methylpyridinium iodide and the methiodides of three diazines (pyridazine, pyrimidine, and pyrazine) in various solvents over a wide range of temperatures (50 to −50 °C). The dissociation constant and other thermodynamic properties ($\Delta H°$ and $\Delta S°$) of these complexes have also been determined from spectral studies.

Experimental Section

Materials. Methyl iodide was prepared by the action of iodine and red phosphorus on methyl alcohol.[5] Pyridine (BDH, LR grade) was refluxed with sodium hydroxide and distilled. Pyridazine, pyrimidine, and pyrazine (Fluka AG) were used without further purification. Methiodides were prepared by mixing the components in a well desiccated vessel in the dark. Temperature was controlled during mixing. After the reaction the excess reactants were removed by washing with ether (sodium dried). The components were then dried under vacuum. These were then recrystallized from dry ethanol. The process of recrystallization was continued until the crystals gave identical spectra before and after the recrystallization process. As the compounds are highly hydroscopic, all the operations were carried out in a desiccated chamber.

* Present address: Department of Physical Chemistry, I.A.C.S., Calcutta 32, India

For the pyridine derivative λ_{max}^{CT} and ϵ_{max} were determined in $CHCl_3$ and compared with standard data.[6] For the preparation of films, the substance and polystyrene were dissolved in dry $CHCl_3$ and the solvent was then allowed to evaporate inside a desiccator.

Solvents were purified and dried by standard procedures[7] and distilled immediately before the experiment.

Spectrophotometric Measurements. Spectrophotometric measurements for the determination of thermodynamic quantities were carried out in a Zeiss VSU2P spectrophotometer using stoppered cells (1 cm) placed in a thermostatted cell holder. To ensure that temperature equilibrium had been established, data were taken only when the optical density at a particular wavelength did not change with time.

Measurements of the absorption spectra of the transparent solid samples and that of solutions at various temperatures were done in a double-beam recording instrument made from a monochromator (the monochromator of VSU2P was utilized), two RCA 1P28 photomultipliers, and a G1B1 potentiometric recorder.[8] The cell compartment in the low temperature experiments consisted of an unsilvered dewar vessel into which vapor of either nitrogen or oxygen was passed. The temperature was controlled to within ±1 °C by regulating the rate of flow of cold vapor. Experiments at high temperature were done in the usual thermostatted cell holder. For temperature measurements a copper–constantan thermocouple was used; one junction of the thermocouple was inserted into the solution. A cold finger type of dewar was used for recording the absorption spectra of solids and polymer films.[9] Emissions were studied in alcohol glass cooled to liquid N_2 temperature. The excitation source used a 400-W Phillips Hg lamp, and the emitted light was analyzed by an SPM2 monochromator.[9] To study the emission at various temperatures, liquid N_2 was allowed to evaporate in the unsilvered dewar and the temperature of the sample varied with changes in the height of the liquid nitrogen level.

Dissociation Constant. (a) *Spectrophotometric Method.* Most of the earlier spectrophotometric methods for the determination of the dissociation constant of electron donor–acceptor complexes involved approximate linear treatments (Benesi–Hildebrand, Scott, or Foster–Hammick–Wardley plots). Dissociation constants calculated by these methods are only approximate, especially for moderately strong complexes.

To obtain accurate values of K_d one has to adopt iterative procedures.[10] Recently accurate values of K_d have been obtained by direct computations using essentially curve fitting or arbitrary guess techniques.[11] We, therefore, looked for a simplified procedure which has been outlined below.

There are three distinctly different species, viz. contact or intimate ion pairs (D^+,A^-), solvent separated ion pairs ($D^+\|A^-$), and free ions (D^+ and A^-). The following equilibria describe the state of a solute in a solution:

$$\begin{aligned} D,A &\rightleftharpoons D^+\|A^- & K_s &= [D^+\|A^-]/[D^+,A^-] \\ D^+,A^- &= D^+ + A^- & K_d &= [D^+][A^-]f_\pm^2/[D^+,A^-] \quad (1) \\ D^+\|A^- &= D^+ + A^- & K_1 &= K_d/K_s \end{aligned}$$

For equilibria involving ions, the activity coefficients are taken into consideration. Activity coefficients of other neutral species are taken as unity.

First, let us consider that only one form of ion pair (intimate) is present (i.e., $K_s = 0$). The total concentration is

$$C_0 = [D^+,A^-] + [D^+] \quad (2)$$

For the case in which only the intimate ion pair absorbs (i.e., at λ_{max}^{CT}) at the wavelength of measurement, if A is the molar absorbance for a 1-cm path length of solution and ϵ is the molar absorption coefficient of (D^+,A^-), eq 2 can be written (using eq 1):

$$\frac{f_\pm C_0}{\sqrt{A}} = \frac{1}{\epsilon} f_\pm \sqrt{A} + \sqrt{\frac{K_d}{\epsilon}} \quad (3)$$

Thus, a plot of $f_\pm C_0/\sqrt{A}$ vs. $f_\pm\sqrt{A}$ gives a straight line and we can calculate the values of K_d and ϵ from a single plot without recourse to any approximation. Figure 1 gives some representative plots.

If the solvent separated ion pair is also taken into consideration, eq 3 is modified to

$$\frac{f_\pm C_0}{\sqrt{A}} = \frac{1 + K_s}{\epsilon} f_\pm \sqrt{A} + \sqrt{\frac{K_d}{\epsilon}} \quad (3a)$$

Comparing (3) and (3a) we conclude that we can determine from the $f_\pm C_0/\sqrt{A}$ vs. $f_\pm\sqrt{A}$ plot the constants $K = K_d/(1 + K_s)$ and $\epsilon/(1 + K_s)$ instead of K_d and ϵ, respectively.

Values of $f_\pm$ were calculated by employing the Debye–Hückel equation using the distance parameter $a = 5$ Å as used by Ewald and Scudder.[4]

(b) *Conductometric Method.* For the determination of the dissociation constant of the ion pair by conductometric method we adopted the procedure used by Fuoss and Kraus.[12] According to this method the equivalent conductance (Λ) of an intermediate electrolyte at a concentration C is related to the dissociation constant K_d and the equivalent conductance at infinite dilution (Λ_0) by the relation

$$\frac{F(x)}{\Lambda} = \frac{1}{K_d\Lambda_0^2}\frac{\Lambda C f_\pm^2}{F(x)} + \frac{1}{\Lambda_0} \quad (4)$$

$F(x)$ is a function of x represented by the continued fraction:

$$\begin{aligned} F(x) &= 1 - x(1 - x(1 - x(1 - \ldots)^{-1/2})^{-1/2})^{-1/2} \\ &= \frac{4}{3}\cos^2\frac{1}{3}\cos^{-1}\left(-\frac{3}{2}x\sqrt{3}\right) \end{aligned}$$

and $x = [(A + B\Lambda_0)\sqrt{\Lambda C}]/\Lambda_0^{3/2}$ where A and B are Onsager constants. The method is iterative. A preliminary value of $F(x)$ was obtained using a value of Λ_0 (obtained by extrapolating the experimental plot of Λ vs. $\sqrt{C}$). Values of $f_\pm$ were calculated by employing the Debye–Hückel equation. The results were then plotted as required by eq 4 and the value for Λ_0 so obtained was employed to recalculate $F(x)$. The whole operation was then repeated until the output value of Λ_0 was within 2% of the input value. The results of the conductometric study are given in Table IV.

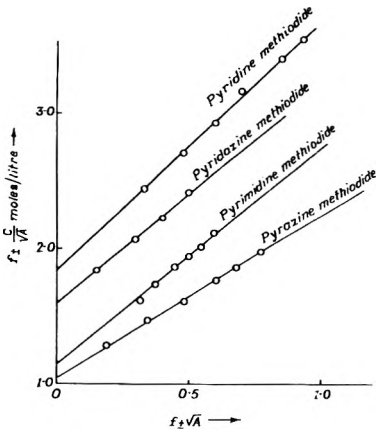

Figure 1. Representative plot of eq 3.

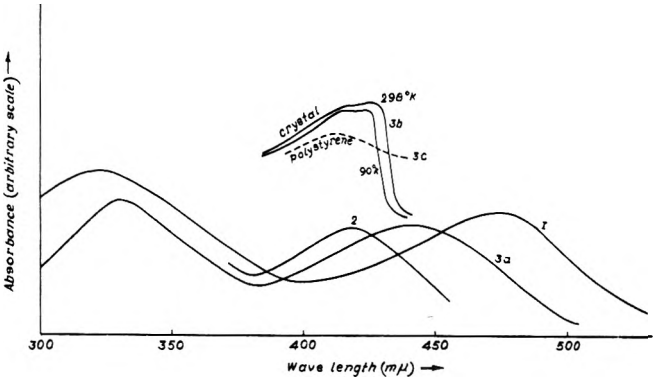

Figure 2. Charge transfer band of various complexes: (1) pyrazine methiodide in CH_2Cl_2; (2) pyrimidine methiodide in CH_2Cl_2; (3) pyrimidine methiodide in CH_2Cl_2 (a), crystal (b), in polystyrene film (c).

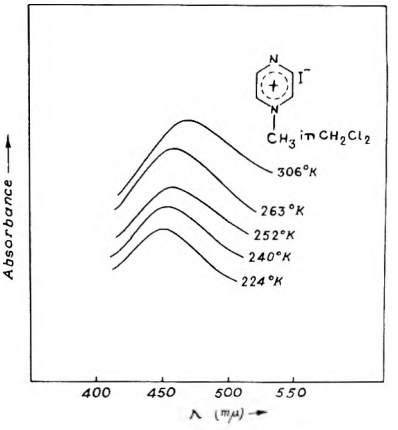

Figure 3. CT absorption spectra of pyrazine methiodide in CH_2Cl_2 at various temperature. Different temperature curves have been displaced for display purpose.

Results

(A) *Effect of Temperature on Absorption Bands.* (a) *Spectra of Solution.* The CT absorption in solution (Figure 2) appears as broad bands rendering the accurate determination of λ_{max} (or $\bar{\nu}_{max}$) difficult and somewhat uncertain. (The

TABLE I: Values of the Band Maxima (at 25 °C) and the Temperature Coefficients of Band Maxima of Various Methiodides in Different Solvents

Solvent	z values,[a] kcal/mol	Pyridine methiodide		Pyridazine methiodide		Pyrimidine methiodide		Pyrazine methiodide	
		$\bar{\nu}_{max}^{298\,K}$, cm^{-1}	$\Delta\bar{\nu}_{max}/\Delta T$, cm^{-1}/K	$\bar{\nu}_{max}^{298\,K}$, cm^{-1}	$\Delta\bar{\nu}_{max}/\Delta T$, cm^{-1}/K	$\bar{\nu}_{max}^{298\,K}$, cm^{-1}	$\Delta\bar{\nu}_{max}/\Delta T$, cm^{-1}/K	$\bar{\nu}_{max}^{298\,K}$, cm^{-1}	$\Delta\bar{\nu}_{max}/\Delta T$, cm^{-1}/K
Crystal				23 250	2			22 720	2
Polystyrene				24 390	0				
1,2-Dichloroethane	62.5	26 320	12 ± 2	22 730	15 ± 2	23 920	14 ± 2	20 830	15 ± 2
Chloroform	53.2	26 500	12 ± 2	22 880	16 ± 2			21 050	16 ± 2
Methylene chloride	64.2	26 600	16 ± 2	22 990	16 ± 2	24 100	14 ± 2	21 050	16 ± 2
Acetone	65.7	27 170	16 ± 2	23 420	20 ± 2			22 220	18 ± 2
Dioxane		26 180	5 ± 1						
Acetonitrile	71.3	27 400	30 ± 3	25 000	20 ± 2	25 970	20 ± 2	23 920	28 ± 3
Dimethylformamide	68.5	27 250	22 ± 3	25 000	20 ± 2	25 640	18 ± 2	23 640	25 ± 3
1,2-Dichlorobenzene		25 970	5 ± 1						
Ethyl alcohol	79.6							27 700	28 ± 3
n-prOH	78.3							26 340	24 ± 2
i-prOH	76.3							26 200	24 ± 2
t-BuOH	71.3							25 320	22 ± 2
t-AmOH				25 640	23 ± 3			24 390	20 ± 2

[a] Reference 2.

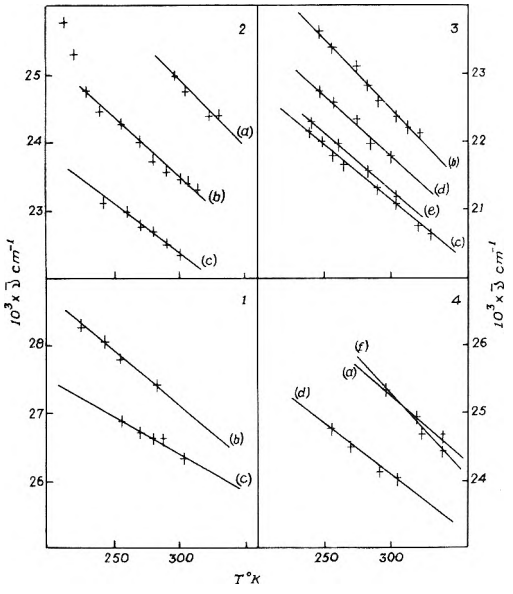

Figure 4. Effect of temperature on the energy of CT transition of different complexes: (1) pyridine methiodide; (2) pyridazine methiodide; (3) pyrazine methiodide; (4) pyrimidine methiodide.

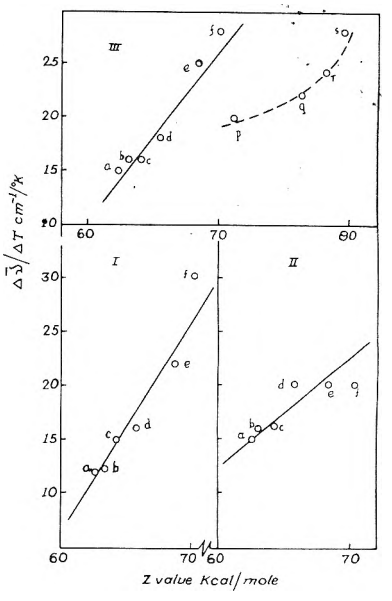

Figure 5. The temperature shift as a function of Z value of solvent: (I) pyridine methiodide; (II) pyridazine methiodide; (III) pyrazine methiodide: (a) CH_2ClCH_2Cl; (b) $CHCl_3$; (c) CH_2Cl_2; (d) acetone; (e) DMF; (f) CH_3CN; (p) *t*-AmOH; (q) *t*-BuOH; (r) *i*-PrOH; (s) EtOH.

CT absorption spectrum of these compounds will be discussed from a spectroscopic and theoretical point of view in a separate communication.) The temperature shift, however, is far greater than these uncertainties. Figure 3 shows a set of absorption curves at various temperatures in one particular solvent. Band maxima ($\bar{\nu}_{max}$) at 298 K and temperature coefficients ($d\bar{\nu}_{max}/dT$ cm^{-1}/K) in various solvents are listed in Table I.

Band width and shape remain unaffected by temperature changes. In solution the shifts are reversible and continuous, $\bar{\nu}_{max}$ increasing with decreasing temperature. A plot of $\bar{\nu}_{max}$ vs. T is linear (within experimental error) as can be seen from Figure 4. The value of $d\bar{\nu}_{max}/dT$ depends on the nature of the solvent. Although no correlation is obtained with any macroscopic solvent parameter, it appears that temperature coefficients show a correlation with Z values (Figure 5). It is seen that the alcoholic solvents form a separate group. Among nonalcoholic solvents dimethylformamide (DMF) and acetonitrile are not in line with other solvents, but this is not surprising in view of the strong complexing ability of these solvents. In fact, in DMF the compound decomposes when the temperature is raised above 60 °C.

(b) *Crystals and Polymer Films.* Absorption bands in rigid environments were studied up to 90 K and they show no significant temperature sensitivity. A slight shift in band maxima

TABLE II: Values of the Equilibrium Constant and Other Thermodynamic Quantities of Different Ion Pairs

	Acetone				Acetone and cyclohexane (10:1)			
Ion pair	K at 293 K $\times 10^3$	ϵ at 293 K	$\Delta H°$, kcal/mol	$\Delta S°$, eu/mol	K at 293 K $\times 10^3$	ϵ at 293 K	$\Delta H°$, kcal/mol	$\Delta S°$, eu/mol
Pyridine methiodide	1.90	555	-0.37 ± 0.02	-13.68 ± 5.0	1.08	610	-0.78 ± 0.04	-16.19 ± 5.0
Pyridazine methiodide	1.42	550	-0.82 ± 0.04	-17.37 ± 5.0	1.13	750	-1.2 ± 0.04	-19.00 ± 5.0
Pyrimidine methiodide	0.803	660	-0.59 ± 0.05	-16.10 ± 5.0	0.65	760		
Pyrazine methiodide	0.96	860	-0.96 ± 0.06	-17.00 ± 5.0	0.78	960	-1.6 ± 0.1	-19.60 ± 5.0

TABLE III: Values of the Equilibrium Constant, $\Delta H°$, and $\Delta S°$ of an Ion Pair as a Function of Solvent

Compd	Solvent	Z value	$K^{20\,°C} \times 10^3$	ϵ at 20 °C	$\Delta H°$, kcal/mol	$\Delta S°$, eu/mol
Pyrazine methiodide	MeOH	83.6	2.85	250		
	EtOH	79.6	1.76	535	-1.32 ± 0.10	-16.98 ± 4.0
	n-prOH	78.3	1.00	630	-1.73 ± 0.10	-21.16 ± 6.0
	i-prOH	76.3	0.40	900	-2.8 ± 0.20	-21.65 ± 6.0
	t-BuOH	71.3	0	920		

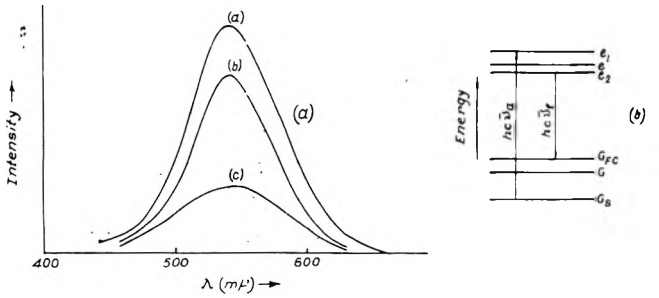

Figure 6. (a) CT luminescence spectrum of pyridine methiodide in alcohol glass (without the phosphoroscope): (a) 77 K; (b) melt; (c) intermediate temperature. (b) Schematic energy levels of methiodides in various environments: (G) ground state; (G_s) solvated ground state; (G_{FC}) FC ground state; (e) excited state (CT); (e_1) FC excited state (solvated); (e_2) equilibrium excited state (solvated).

(Figure 2) with temperature may be attributed either to the expandability of solids or to the population of higher vibrational levels in the ground state of the complex at higher temperatures.

(c) The relative ordering of the solvents (in terms of $d\bar{\nu}_{max}/dT$) seems to be independent of the solutes; but complications may often arise due to specific solute–solvent interaction.

(B) *Effect of Temperature on Emission.* The compounds were found to luminesce when cooled to liquid N_2 temperature. There is a gap between the onset of emission and absorption. For methylpyridinium iodide the observed luminescence was interpreted as charge transfer fluorescence.[3] We have studied the luminescence using a phosphoroscope and verified that the lifetime of the emission is less than 10^{-3} s. While the position of the emission band for the compound remained unchanged with change in temperature, the intensity of the band gradually diminished as temperature was lowered (Figure 6a). (In the case of methiodides of the diazines more than one emission band was detected. The band positions were found to remain unchanged, but the relative intensities of the bands changed as the temperature changed. This might be due to the existence of either more than one configuration in the complex or more than one excited level of different lifetime. Further work is in progress.)

TABLE IV: Dissociation Constant and Λ_0 for Methyl Pyridinium Iodide in Acetone (Conductometric Study)

Temp, K	$K_d \times 10^3$	Λ_0, Ω^{-1} cm^2
293	1.75	215 ± 5

(C) *Thermodynamic Quantities and Intensity.* Dissociation constants (K) and other thermodynamic quantities were determined in acetone and acetone–cyclohexane (10:1) for all compounds. Because of the overlap of the CT band with other higher energy bands for other compounds, data in alcoholic solvents could be obtained only with pyrazine methiodide. K and ϵ were determined in the temperature range 293–323 K. From these data $\Delta H°$ and $\Delta S°$ were determined. They are listed in the Tables II–IV. The dissociation constant was determined at various wavelengths (near λ_{max}^{CT}) and the same value was obtained showing that only the 1:1 complex was present in solution.

Intensity of the CT band increases with increasing temperature. In $CHCl_3$ and CH_2Cl_2 when the solute is present completely as ion pairs ($K_d = 0$) there is a 2% decrease in intensity for a ~10° decrease in temperature. In dissociating solvents, the increase of optical density at λ_{max}^{CT} with increase in temperature can be attributed to a change of association equilibria ($\Delta H°$ is negative). However ϵ_{max} determined for these solvents from plots of eq 3 shows again a 2% increase with a ~10° increase in temperature.

Discussion

Temperature Shifts. It appears from the results that the observed temperature shift is a characteristic of the liquid state and as such it should be related with the thermal motion of the molecules in the liquid state. The continuous shift (absence of any isobestic point) excludes the possibility of any specific interaction between solute and solvent. The study of absorption spectra in mixed solvents[2] also supports this view.

To understand the cause and the nature of such thermochromism, we first consider the theory of solvent effects on spectra. Of the different species present in solution, only intimate ion pairs contribute to the CT band and the envi-

ronmental effect is determined by the solvation characteristic of these species.

Ground states of methiodides have high dipole moments[2] and the dipolar interaction between the solute and the solvent is the main perturbative role on the ground state energy. Kosower[2] has shown that the stabilization of the ground state and the simultaneous destabilization of the Franck–Condon (FC) excited state lead to the characteristic solvent sensitivity. The effect of pressure and/or temperature on the energies of the ground and the FC excited state of the ion pair might be attributed to the modification of solvent perturbation through either: (i) the change of Onsager cavity (a), or (ii) the change in reaction field of solvent molecules at the location of the solute molecule due to change of solvation.

If (i) were the important factor, there would be a correlation of the shift with change of density. Thus the ratio of the temperature shift to pressure shift $(R) = (\Delta\bar{\nu}/\Delta T)_p/(\Delta\bar{\nu}/\Delta p)_T$ should have been equal to α/β, where α is the thermal expansion coefficient and β the compressibility. The results of Ewald and Scudder[4] show that $R \simeq 10^8$ dyn/cm^2/K in acetone. α/β for the same solvent is $\sim 10^7$, in the same units,[13] which is about a factor of 10 less than the experimental value. Thus the effect of temperature and pressure cannot be rationalized in terms of density change.

On the other hand, if solvation were the important factor, R should have been roughly equal to $\Delta E/T\Delta V$ where ΔE and ΔV are changes in energy and volume, respectively, for complete desolvation of the ion pair. The value of ΔE might be taken as half of the difference of the Z value of the solvent and that of a nonpolar solvent (such as benzene); for acetone, this is about 4 kcal/mol.[6] Taking the value of $\Delta V \approx 16$ cm^3/mol, we calculate at 300 K, $\Delta E/T\Delta V \approx 10^8$ dyn/cm^2/K. Thus we conclude that solvation is the important factor. Indeed for one component liquids compressed to 5 kbars, Weigang and Robertson[14] concluded that the coordination number increases with pressure. The change of solvation was also assumed by Mason[15] and Ewald et al.[4] to account for the change of λ_{max}^{CT} with temperature and pressure.

To consider the process of solvation in detail, we assume that there are different solvated species, DAS_i (S = solvent molecule and $i = 0, 1, 2, \ldots$ up to a maximum limiting value), in equilibrium:

$$DAS_{i-1} + S \rightleftharpoons DAS_i \qquad k_i = \frac{[DAS_i]}{[DAS_{i-1}][S]} \tag{5}$$

Let C_i be the concentration of the ith species, DAS_i, for which the ground state energy is E_i. E_0 is the ground state energy of the desolvated complex ($E_0 > E_1 > E_2 > E_3 > E_4 > \ldots > E_{i-1} > E_i$). From (5) we write for dilute solutions

$$C_i = k_i C_{i-1} = (k_1 k_2 \ldots k_i) C_0 = K_i C_0$$

The total concentration of the ion pair is

$$\sum_i C_i = \left(1 + \sum_i K_i\right) C_0 = C_0 \Sigma' \tag{6}$$

and the total concentration of the solute in the absence of any common ion is

$$C = \sum_i C_i + C_D + = \sum_i C_i + \sqrt{K_d \sum_i C_i} \tag{7}$$

The molar absorbance for a 1-cm path length of solution at a particular wave number is

$$A_{\bar{\nu}} = \sum \epsilon_i^{\bar{\nu}} C_i = (\epsilon_0^{\bar{\nu}} + \sum K_i \epsilon_i^{\bar{\nu}}) C_0 = C_0 \Sigma^{(\bar{\nu})} \tag{8}$$

where $\epsilon_i^{\bar{\nu}}$'s are the molar absorption coefficients of the species at the wave number $\bar{\nu}$.

Considering (4), (5), and (6), we write

$$\frac{C}{\sqrt{A_{\bar{\nu}}}} = \frac{\Sigma'}{\Sigma^{(\bar{\nu})}} \sqrt{A_{\bar{\nu}}} + \sqrt{\frac{K_d \Sigma'}{\Sigma^{(\bar{\nu})}}} \tag{9}$$

This equation is identical with eq 3 with $f_\pm = 1$; the only difference is that $\Sigma^{(\bar{\nu})}/\Sigma'$ appears in place of ϵ. Now

$$\frac{\Sigma^{(\bar{\nu})}}{\Sigma'} = \frac{\epsilon_0 + K_1\epsilon_1 + K_2\epsilon_2 + \ldots}{1 + K_1 + K_2 + \ldots} = \frac{\sum_i C_i \epsilon_i}{\sum_i C_i}$$

and this can be interpreted as the number averaged extinction coefficient according to this model.

Thus we may equivalently speak of an average solvated species at a particular temperature. The average solvation number is given by

$$\bar{n} = \frac{\sum_i i C_i}{\sum C_i} = \frac{\sum_i i K_i}{\left(1 + \sum_i K_i\right)} \tag{10}$$

The average ground state energy ($\bar{E}$) according to this model is

$$\bar{E} - E_0 = \frac{\sum_i (E_i - E_0) K_i}{\left(1 + \sum_i K_i\right)} \tag{10a}$$

and from (10), we obtain

$$\frac{d\bar{n}}{dT} = \frac{1}{RT^2}\left[\frac{\sum_i (E_i - E_0)K_i + \sum_{i,j} (i-j)(E_i - E_j)K_iK_j}{\left(1 + \sum_i K_i\right)^2}\right] \tag{11}$$

and from (10a)

$$\frac{d\bar{E}}{dT} = \frac{1}{RT^2}\left[\frac{\sum_i (E_i - E_0)^2 K_i + \sum_{i,j} (E_i - E_j)^2 K_iK_j}{\left(1 + \sum_i K_i\right)^2}\right] \tag{12}$$

$$\frac{d\bar{E}}{dT} = \frac{1}{RT^2}\left[\frac{\sum_i (E_i - E_0)^2 K_i}{1 + \sum_i K_i} - \left(\frac{\sum_i (E_i - E_0)K_i}{1 + \sum K_i}\right)^2\right] \tag{12a}$$

From the expression for $d\bar{n}/dT$ we conclude that $d\bar{n}/dT$ is negative. Thus, average solvation increases as the temperature is lowered, which, in effect, stabilizes the ground state to a greater extent, causing the blue shift. This conclusion also follows from the fact that $d\bar{E}/dT$ is positive, as seen from (12). At sufficiently low temperature, however, it is expected that the value of $\bar{n}$ reaches a saturation limit and no such blue shift with further lowering of temperature is expected. Moreover, the magnitude of the shift should be small at very high temperatures.

From (12a) we may write

$$RT^2\frac{d\bar{E}}{dT} = \frac{\sum_i (E_i - E_0)\sum_i (E_i - E_0)K_i}{\left(1 + \sum_i K_i\right)} - \frac{\sum_{i,j} E_iE_j(K_i + K_j)}{\left(1 + \sum_i K_i\right)} - \left[\frac{\sum_i (E_i - E_0)K_i}{1 + \sum_i K_i}\right]^2$$

$$= \text{constant} \times (\bar{E} - E_0) - (\bar{E} - E_0)^2 - \frac{\sum_{i,j} E_iE_j(K_i + K_j)}{1 + \sum_i K_i}$$

$$= f(\bar{E} - E_0)$$

The magnitude of the shift is thus dependent on $(\bar{E} - E_0)$, which is characteristic of the solvent. Hence, change of solvent polarity should parallel the change caused by thermal perturbation but complications might occur due to specific solute–solvent interaction. No functional relation between $\bar{E}$ and T can be obtained at the present state of development, however.

From the above discussion it follows that the temperature shift depends on the strength of the solute–solvent interaction. The more ionic the ground state is, the more will be the extent of stabilization and the greater the extent of the shift. An interesting conclusion from this model is a red shift with decrease in temperature of the CT band of the molecular complexes with nonpolar ground states (benzene–iodine and other related complexes); because the relevant interaction in such a case is the dispersion interaction which destabilizes the ground state. However, the magnitude of such a shift would be relatively small, because the strength of interaction is small.

Effect of Temperature on Emission. The configuration of the solvent molecules around a solute molecule does not change during the excitation process in accordance with the Franck–Condon principle. However, the Franck–Condon (FC) state is not the stable equilibrium state for the excited solute molecule, since the dipole moment of the excited state is in a different direction from that in the ground state. The equilibrium excited configuration is realized by reorientation of the solvent molecules. When an excited molecule returns to the ground state by radiative transition, the two electronic states of the solute involved in the process are the equilibrium excited state and the FC ground state. In considering the effect of solvation on these states we conclude that $\bar{\nu}_f \ll \bar{\nu}_a$ (Figure 6b). In this case also, the change of temperature will modify solvation and a blue shift is expected with an increase in temperature. However as the extent of the shift depends on the solute–solvent interaction in the excited state, and as the magnitude of the dipole moment in the excited state is expected to be much smaller compared to that in the ground state, the extent of the shift of the band maxima of the emission band should be small.

Thermodynamic Quantities and Intensity. The dissociation constant as determined from (3a) is given by

$$K = \frac{K_d}{1 + K_s} = \frac{[D^+][A^-]}{[D^+,A^-][D^+][A^-]}$$

Thus, spectrophotometric determination of the dissociation constant for these types of complexes cannot distinguish between two forms of ion pairs (e.g., intimate and solvent separated). This is also true of conductance studies. Hence, spectrophotometric and conductometric studies should give the same dissociation constant. We have verified this for pyridine methiodide at room temperature (Table IV). From Table III we find that dissociation increases as Z increases, this is in accord with the general behavior that the solvent with greater polarity favors free ions.[16]

The values of $\Delta H°$ (Table II) show that ion-pair dissociation is exothermic. It will be noted that cyclohexane, when added to acetone, further decreases the value of $\Delta H°$. It is probable that cyclohexane molecules replace some of the acetone molecules in the cybotactic region of the ion pair, increasing its energy, while separated ions, being much more solvated, are only slightly affected by such a change.

The negative value of ΔS^c for dissociation indicates a desolvation during ion association, an observation also noted by other workers.[4] The extent of desolvation increases as we add a nonpolar solvent (Table II).

In the diazine series, the magnitudes of $\Delta H°$ and $\Delta S°$ are less for the 1,3-diazine derivative, indicating that in this complex the ion pair is relatively less desolvated than in the other two compounds. Thus it appears that the ion of the 1,3 derivative is relatively less solvated than those of the other two isomers. This may be due to the difference in the distribution of π-electron densities in these ions. No correlation could be observed with the molecular properties of the ions.

By fixing the complex while varying the solvents we obtain an interesting result. It appears from the Table III that as the solvent polarity (Z value) decreases, the ion pair dissociation becomes more exothermic and there is more and more desolvation. Now we have seen that the spectrophotometric method cannot distinguish between intimate and solvent-separated ion pairs. Hence, the larger the amount of solvent-separated ion pairs at equilibrium, the smaller will be the apparent extent of desolvation on total ion pair formation. The extent of solvent-separated ion pairs decreases in the order ethanol, 1-propanol, and 2-propanol as is evident from the ϵ data (see discussion below). Thus, on going from ethyl to propyl alcohols, the magnitude of $\Delta S°$ apparently increases.

Intensity

The widely differing values of the experimentally determined ϵ in different solvents (Tables II–IV) at a particular temperature are suggested to be due to the presence of solvent-separated ion pairs.[10] This is evident from eq 3a, because what we determine is $\epsilon_{app} = \epsilon/(1 + K_s)$ and the true value of ϵ can be obtained only when one has an idea of K_s. Solvent polarity coupled with specific solute-solvent interaction may lead to higher values of K_s, thus lowering the value of ϵ_{app}. In the alcohol series (where specific interaction is constant) the value of K_s seems to decrease with decrease in dielectric constant of the solvent. By a similar argument we account for the observed variation of ϵ_{app} with temperature (in a particular solvent) through change of the K_s due to a change of the solvent dielectric constant with temperature. The most convincing example is the change of ϵ with temperature in nondissociating solvents ($K_d = 0$), e.g., $CHCl_3$ and CH_2Cl_2. The increase of ϵ values on addition of cyclohexane to an acetone solution supports this idea.

References and Notes

(1) A. Hantzsch, *Berichte*, **52**, 1535, 1544 (1919).
(2) E. M. Kosower, *J. Am. Chem. Soc.*, **80**, 3253, 3261, 3267 (1958).
(3) J. S. Brinen, J. G. Koren, H. D. Olmstead, and R. C. Hirt, *J. Phys. Chem.*,

69, 3791 (1965).
(4) A. H. Ewald and J. A. Scudder, *J. Phys. Chem.*, **76**, 249 (1972).
(5) A. I. Vogel, "A Text Book of Practical Organic Chemistry", Longmans, Green and Co., New York, N.Y., 1955.
(6) E. M. Kosower, "An Introduction to Physical Organic Chemistry", Wiley, London, 1968.
(7) A. Weissberger, "Technique of Organic Chemistry", Vol. 7, Interscience, New York, N.Y., 1955.
(8) Description of a similar apparatus is given in R. Mukherjee, S. C. Bera, and M. Chowdhury, *Indian J. Phys.*, **43**, 621 (1968).
(9) S. C. Bera, R. Mukherjee, and M. Chowdhury, *J. Chem. Phys.*, **51**, 754 (1969).
(10) R. A. Mackay and E. J. Poziomek, *J. Am. Chem. Soc.*, **92**, 2432 (1970).
(11) R. Foster in "Molecular Complexes", Vol. 2, P. Elek, Ed., London, 1973.
(12) R. M. Fuoss and C. A. Kraus, *J. Am. Chem. Soc.*, **55**, 476 (1933).
(13) N. A. Lange, Ed., "Hand Book of Chemistry", 9th ed, Handbook Publishers, Cleveland, Ohio, 1956.
(14) O. E. Weigang, Jr., and W. W. Robertson in "High Pressure Physics and Chemistry", R. S. Bradley, Ed., Vol. 1, Academic Press, New York, N.Y., 1963.
(15) S. F. Mason, *J. Chem. Soc.*, 2437 (1960).
(16) J. F. Grast in "Solute-Solvent Interaction", J. F. Coetzee and C. D. Ritcher, Ed., Marcel Dekker, New York, N.Y., 1969.

On the Optical, Electrical, and Magnetic Properties of Alkali Metal Amine Solutions

S. Nehari and K. Bar-Eli*

Department of Chemistry, Tel-Aviv University, Ramat-Aviv, Israel *(Received May 27, 1975; Revised Manuscript Received April 9, 1976)*

The extinction coefficients of the M and S bands of solutions of alkali metals in diamines were measured by two independent methods and found to be 42 500 and 2100 M^{-1} cm^{-1}, respectively. The electrical conductivity of the species associated with the bands, namely, the metal anion and the solvated electron, was measured as a function of temperature and concentration where the latter was determined by the bands' absorbances. The results were extrapolated to infinite dilution by Shedlovsky's method and the values of Λ_0's, Walden products, and dissociation constants of the ion pairs were found. The results were confirmed by measuring the conductivity together with the paramagnetic species concentration. The results of this work and the data of others show conclusively that the main conduction mechanism is through Stokes' law, however, a small effect of other factors is observed.

Introduction

Solutions of alkali metals in ammonia, amines, and ethers[1-7] have been of considerable experimental and theoretical interest for more than a century.[1,2] Their electrical, optical, and magnetic properties have been studied extensively[2] and many theories have been advanced to explain them.[3]

Due to thermodynamic instability, all solutions decompose, and sooner or later only the metal cation and an unknown product anion (or ion pair) will remain (in the case of ammonia the anion is of course the amide ion NH_2^-). This instability, which is never overcome completely, adds to the difficulty of establishing reliable relationships between concentration and other properties such as absorbance and electrical conductivity. This inherent instability has resulted in many inconsistencies in the literature.

We have exploited this instability in order to conveniently measure the relationships between concentrations, absorbances, conductivities, and magnetic properties. In the first stage we have established the extinction coefficients of the M and the S bands by two different methods described below. In the second stage the decay of the solutions was followed by measuring simultaneously the absorbance and conductivity. In this way a relationship between concentrations and conductances was obtained without the necessity of preparing a new solution for each measurement. Each new solution preparation gave many concentration–conductivity data, where previously only one such datum was obtained. Proper corrections were introduced for the presence of the decay products. Finally the decay of the paramagnetic species was followed in the ESR cavity together with conductivity decay, thus confirming relationships between the conducting and paramagnetic species.

According to Golden, Guttman, and Tuttle,[3a] the following species are assumed to exist (in amounts depending on the total concentration of metal dissolved, and on the equilibrium constants) in dilute solutions: (1) A metal cation (M^+). (2) A metal anion (M^-) which absorb in the visible or the near-ir, depending on the metal. Its absorption band is designated the M band.[4c] The similarity between the M-band properties and the CTTS spectra of halide ions[8,9] was shown by Golden, Guttman, and Tuttle,[3a] and later confirmed by others[4b,7,10-12] by various methods. (3) The solvated electron (e^-) which absorbs at 1400 nm regardless of the metal dissolved S band.[4c] (4) The ion pairs of the cation and the negative species, namely, $M^+ \cdot M^-$ and $M^+ \cdot e^-$. Both ion pairs are assumed to have the same extinction coefficients as their parent anions. The monomer[13] (M) and dimer (M_2) suggested by Arnold and Patterson[3d] are assumed not to be present in any significant concentrations in the solvents we used, namely, ethylenediamine (EDA) and 1,2-propylenediamine (PDA).

These species are interrelated by the following equilibria:

$$M^+ \cdot M^- \rightleftharpoons M^+ + M^- \quad (1)$$

$$M^+ \cdot e^- \rightleftharpoons M^+ + e^- \quad (2)$$

$$M^- \rightleftharpoons M^+ + 2e^- \quad (3)$$

The equilibrium constants depend mainly on the temperature,

the metal dissolved, and the solvent. Thus, for example, in ammonia the S band dominates, while in propylenediamine the M band dominates.[4b]

Experimental Section

As was shown by Hurley, Tuttle, and Golden[4c] it is of utmost importance to work with quartz vessels with solutions of metals other than sodium. A careful cleaning procedure of the vessels described earlier[11] was used throughout to minimize the decomposition rates.

Metals used were Koch light 99.95% purity, and were distilled several times before using. Amines from Fluka AG were dried over sodium (reflux for few hours) and distilled twice from the blue solution to a sodium containing reservoir, from which the final distillation to the reaction vessel took place. Details about the vessels can be found elsewhere.[14]

Optical densities were measured in Cary-14 spectrophotometer; the optical cells were kept in a quartz dewar with flat windows, through which cold nitrogen was passed in order to keep it at a constant desired temperature.[14,15] The temperature was measured by a chromel–alumel thermocouple the voltage of which controlled, through a feed-back device, the rate of cold nitrogen flow. The temperature could be thus kept to within ±1 °C. Different optical paths were used for different concentrations, the results of the optical densities reported were reduced however to 1 cm path length in all cases.

Two bright platinum 1 × 3 × 5 mm electrodes with separation of 5 mm were sealed in the optical cell in the joint conductivity–absorbance experiments. The ESR measurements were done in the usual quartz capillaries in Varian 4502 x-band spectrometer. Again platinum electrodes were sealed as near as possible to the capillary. In the earlier experiments[14] it was found that the solution started to decompose from the sealed bottom of the capillary; sealing the capillary with a hydrogen torch (instead the usual propane torch) stopped this phenomenon.

Conductivity measurements were done by a Universal Bridge B221 by Wayne-Kerr, working at an alternating current of 1592 Hz to avoid any polarization and electrolysis effects. The cell constant was measured with standard solutions of analytical KCl, and compared to the same solutions in a standard cell whose constant is known.

The solvent used for the conductivity measurements was distilled a few times until its conductivity was below 0.05 $\mu\Omega^{-1}$ and remained constant.

Extinction Coefficients Measurements

These measurements were described earlier,[16] and we shall give here only an outline.

Immediately after the preparation, when the decomposition is negligible, one obtains from electroneutrality $[M^+] = [M^-] + [e^-]$ and from conservation of matter $C = [M^+] + [M^-] + [M^+ \cdot e^-] + 2[M^+ \cdot M^-]$ where C is the total metal concentration. Combining these equations, and assuming that the ion pair has the same extinction coefficient as the parent anion, one obtains

$$C = 2\frac{OD_v}{\epsilon_v} + \frac{OD_{ir}}{\epsilon_{ir}} \tag{4}$$

where OD and ϵ are the optical density and extinction coefficients, respectively, and the indexes v and ir refer to the visible M band and to the ir S band, respectively. The total metal concentration is measured in two ways: (a) immediately after the optical measurements are finished, the solution is transferred to a side arm, the solvent is distilled out, and the side arm is disconnected from the main vessel. The residue in the side arm is then dissolved in 0.1 N HCl and the amount of metal estimated by atomic absorption. Four such side arms connected to each vessel enabled us to conduct several experiments in each vessel. (b) After the optical data were taken, the solution was frozen and pumped in order to eliminate any hydrogen formed. After thawing, ammonium bromide was introduced from a side arm through a break seal, the hydrogen evolved was pumped by a Töppler pump, and its pressure measured under constant volume. The solvent was frozen during this pumping in order to avoid transferring its vapors. The differences between the two methods did not amount to more than 5%.

Method a gives the total concentration of metal, while method b gives only the amount of the metal which has not yet decomposed. An agreement between the two methods indicates therefore that the solution is still fresh and that there are very little decomposition products.

A second method to find the extinction coefficients is to regenerate the "blue" solution electrolytically from a deteriorated one.[17]

If the decomposition rate is small, the rate of establishing equilibrium and mixing is fast, as was shown earlier[4b,7a] one obtains

$$\frac{1000I}{FV} = \frac{2}{\epsilon_v}\frac{dOD_v}{dt} + \frac{1}{\epsilon_{ir}}\frac{dOD_{ir}}{dt} \tag{5}$$

where I is the current in amperes, F, the Faraday, and V, the volume of solution in milliliters. Measuring the rate of increase of absorbances vs. the current creating them can give us the desired extinction coefficients. In eq 5 the derivatives are those at the beginning of the current transfer, since later on deterioration of the created species is appreciable.

In Na/PDA solutions there is no S band, and the M band best fits a Gaussian curve. In dilute ($\approx 10^{-4}$ M) K/EDA solutions the M band is negligible, and the S band fits a Lorentzian curve. The parameters of the curves were used to separate the spectra wherever appreciable overlap between the bands occurred. After the separation, the coefficients of eq 4 and 5 were determined by multiple regression.[18] This method gives the two coefficients directly without recourse to any further simplifying assumptions.

Whenever only one band is predominant, we can ignore one term in eq 4 and 5, and a simple linear relationship should hold between the metal concentration and absorbance or between the current and the rate of increase of absorbance. This is shown in Figures 1 and 2 for the case of M band in Na/PDA.

Within experimental error, all measured solutions give the same values for ϵ_v and ϵ_{ir} by both methods, namely $\epsilon_v = 42\,500 \pm 1500\ M^{-1}\ cm^{-1}$ and $\epsilon_{ir} = 2100 \pm 1000\ M^{-1}\ cm^{-1}$.

Although the calculations by the multiple regression method are more accurate and reliable, it is illustrative to plot the data on the plane. Few variations of eq 4 and 5 are possible, e.g.

$$OD_{ir}/OD_v = (C/OD_v)\epsilon_{ir} - 2\epsilon_{ir}/\epsilon_v \tag{6}$$

where the slope gives ϵ_{ir}, and the intercept is twice the ratio between the extinction coefficients. An example of such plot is shown in Figure 3. The figure shows very clearly the smallness of ϵ_{ir} compared to ϵ_v.

The numbers cited are for maximum absorbance, namely, 670, 660, 870, and 860 nm for the M bands of Na/PDA, Na/EDA, K/PDA, and K/EDA solutions, respectively, and 1280 nm for the S band of K/EDA, all at room temperature.[11] No

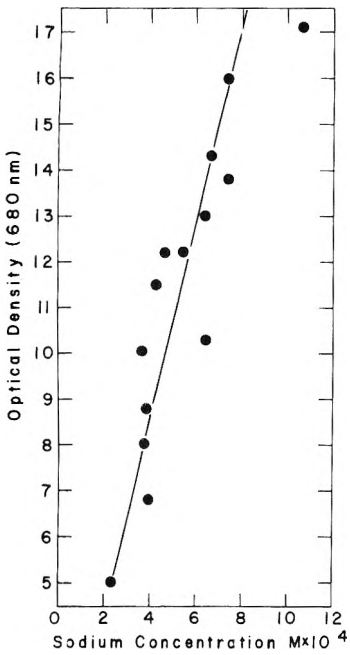

Figure 1. Optical density of M band of sodium PDA solution vs. concentration.

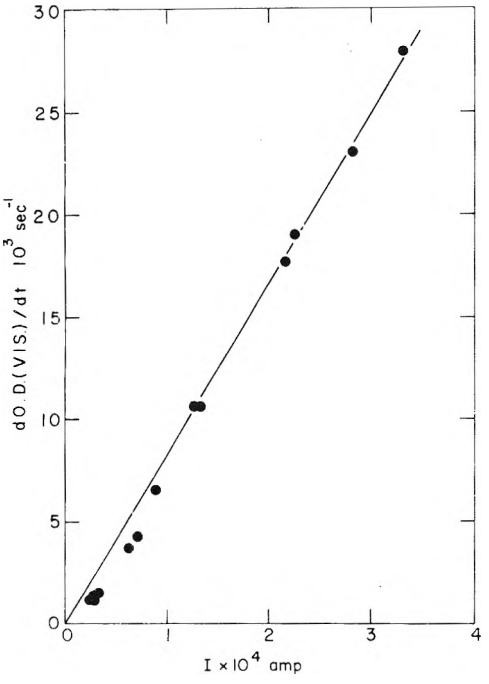

Figure 2. Rate of increase of M band vs. current in decayed sodium–PDA solution.

temperature dependence of the extinction coefficients was detected.

The value of ϵ_v should be compared with that of DeBacker and Dye[19] who obtained 82 500 M^{-1} cm^{-1} and with that of Windwer and Surdheim[20] who obtained 23 500 M^{-1} cm^{-1} for concentrated (0.016 M) K/EDA solutions where the S band is negligible. Since the latter authors worked in pyrex vessels, their result is probably the extinction of Na^- rather than that of K^-. The comparison is still valid, however, because no difference was found between the different anions.

The latter result is in good agreement with ours if we note that it was computed directly from OD_v/C, while in our case,

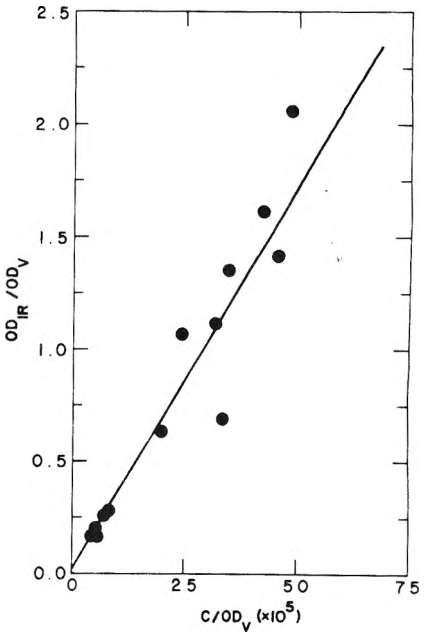

Figure 3. Plot of eq 6 for potassium–EDA solutions.

by neglecting the second term in eq 4, one would have obtained $\Theta D_v/C = \epsilon_v/2$. The value obtained for ϵ_{ir} seems low for the extinction coefficient of a solvated electron,[21,22] and is in discrepancy with the ratio $\epsilon_v/\epsilon_{ir} \approx 4$–3 obtained by Dye, DeBacker, Eyre, and Dorfman[21] and Huppert and Bar-Eli.[4b]

The discrepancy between the present results and those reported in ref 4b can be reconciled by assuming two kinds of solvated electron both of which absorb in the ir. One species is photoejected from the anion and has a lifetime of a few milliseconds, with high extinction coefficient, while the other exists permanently in equilibrium 3 with the anion, and has a small extinction coefficient. The existence of the first species is revealed only in pulse experiments.

Gaathon and Ottolenghi[23] point out that the ir band of Li/PDA solutions is blue shifted by 80 nm relative to the ir band formed by photolysis of Na/PDA solutions; this may indicate that the electron may be trapped in a different way when it is photoejected and when it is in a dark equilibrated solution. Thus this observation supports our conclusion, namely, that our measurement has given the extinction coefficient of the dark equilibrated electron, rather than the one of the photolyzed or radiolyzed electron.

Another possibility accounting for the low value of ϵ_{ir} is to assume that the ion pair $M^+ \cdot e^-$ has a different extinction coefficient than that of the solvated electron. If the dissociation constant of the ion pair is small and the kinetics of its formation is slow (in the time scale of the flash experiments), then it is possible that the photolysis and radiolysis experiments measure the extinction of the solvated electron, while steady state experiments measure the extinction of the ion pair.

In very dilute solutions, when the relative concentration of the solvated electron increases and that of the ion pair decreases, one would expect deviations from the Beer–Lambert law. These deviations were not observed. We believe therefore that the former explanation is more plausible. The relationships between the observed values (C, OD_v, and OD_{ir}) will become nonlinear with seven (four extinctions and three equilibrium constants) unknown parameters. The difficulties in deriving these parameters are obvious, and it seems that

our "simplified" assumption is more appropriate under the circumstances.

The value of the equilibrium constant for reaction 3, namely, K_3, can be computed from the absorbances of fresh solutions, the ion pairing constants found below and the known extinction coefficients. The values of pK_3 thus obtained are ≥ 10 (this value was computed from the lower limit of absorbance measurement in our system), 7.5, 6.4, and 4.9, for Na/PDA, Na/EDA, K/PDA, and K/EDA solutions, respectively, at room temperature.

Conductivity Measurements

The conductivity of metal–amine solutions is assumed to obey Kolrausch's law of independent mobilities.[35] The conductivity of the solutions is, therefore, the sum total of the conductivities of its components, namely, the metal anion, the solvated electron, and the decay products, each with an equivalent amount of the positive metal cation.

Let us first assume that there is only one band (e.g., Na/PDA or dilute K/EDA solutions), then by Kolrausch's law

$$1000\kappa_T = C_p\Lambda_p + C_x\Lambda_x \qquad (7)$$

where κ_T is the measured total specific conductivity, Λ is the equivalent conductivity, C, the concentration, and the subscripts p and x refer to the decay product and the species associated with the absorption band (either visible or ir), respectively.

C_x is known at any moment during the decay process from the measured absorbance and the extinction coefficient, $C_x = OD_x/\epsilon_x$; the total concentration, $C_0 = C_x + C_p$, which is constant during the decay, is found from the initial absorbance, $C_0 = OD_{0x}/\epsilon_x$ when no appreciable deterioration has occurred. A metal assay, after the experiment is over, can serve as a check for this value, as described above. The concentration of the decay products, C_p, is obtained by substraction $C_p = C_0 - C_x$.

The equivalent conductance of the decay products, Λ_p, is measured separately. Typical data of Λ_p vs. concentration is shown in Figure 4 together with the results of Dewald and Dye[26] in order to show the agreement between the two sets of data. From such data, Λ_p is taken once C_p is known. The desired value of Λ_x is now calculated from eq 8 at any point during the decay process:

$$\Lambda_x = [1000\kappa_T - (OD_{0x}/\epsilon_x - OD_x/\epsilon_x)\Lambda_p]\epsilon_x/OD_x \qquad (8)$$

Different initial absorbances were used (with different optical paths) in order to cover as wide a range of concentrations as possible.

When two bands appear, e.g., K/EDA solutions in medium concentrations one first calculates κ_{ir} from OD_{ir}, ϵ_{ir}, and Λ_{ir}, from the data of dilute solutions and then from $\kappa_v = \kappa_T - \kappa_p - \kappa_{ir}$, ϵ_v, and OD_v, Λ_v is derived.

It is obvious that the results of the equivalent conductances depend on the previously obtained extinction coefficients.

Typical results for Na/PDA solutions are shown in Figure 5 in which the equivalent conductance is plotted vs. the square root of concentration. It is seen that the behavior is typical of weak electrolytes in a low dielectric constant medium: the degree of dissociation increases with dilution which causes an extra increase of conductivity above the square-root law of strong electrolytes.

Various methods of extrapolation to zero concentration are used in the literature[27] in order to find the equivalent conductance at infinite dilution and the dissociation constant of

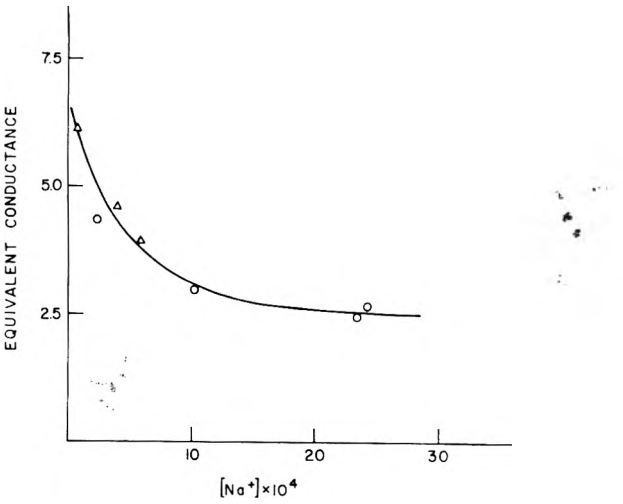

Figure 4. Equivalent conductivity vs. concentration of decay products of sodium–EDA solution: (△) this work; (○) ref 26.

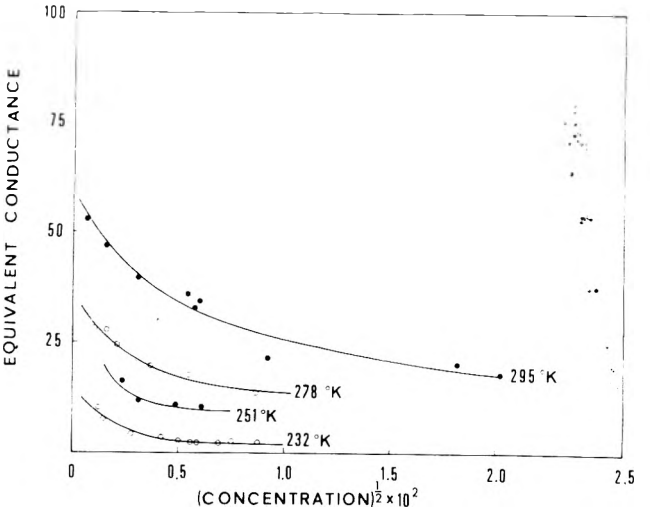

Figure 5. Equivalent conductivity vs. square root of concentration of M band of sodium–PDA solution.

the anion–cation pair. Using Shedlovsky's method, one uses the equation

$$\frac{1}{\Lambda S(z)} = \frac{1}{\Lambda_0} + \frac{S(z)\, f^2 C\Lambda}{K\Lambda_0^2} \qquad (9)$$

where $z = [(\alpha\Lambda_0 + \beta)/\Lambda_0^{3/2}]\sqrt{C\Lambda}$, α and β are known from Onsager's equation,[28] $S(z) = [(z/2) + \sqrt{1 + z^2/2}]^2$, f is the activity coefficient calculated by Debye–Hückel's formula, Λ_0, the equivalent conductance at infinite dilution, and K, the dissociation constant of the anion–cation pair.

A crude estimate of Λ_0 is obtained from a Λ–$\sqrt{C}$ plot, from which z, $S(z)$, and f are calculated. Values of $1/\Lambda_0$ and $1/K\Lambda_0^2$ are computed from the intercept and slope respectively of eq 9. The procedure is repeated with the new Λ_0 until the difference between two subsequent Λ_0 is smaller than 0.1 kohlrausch units. The results of Λ_0 are accurate within 5–20% depending on the number of points taken and their scatter. In the calculation of the activity coefficient, f, by the Debye–Hückel method a distance of 6 Å was used as the nearest approach between the ions of the ion pair.[26,29] Distances of 5.5[3a] and 4.5 Å (see below) were also tried with essentially the same results, since the concentrations are fairly low.

Other variants of eq 9 and other methods of extrapolation,

TABLE I

Metal	Solvent	Temp, C°	η, P	Λ_0, kohlrausch	$\Lambda_0\eta$	10^5K, M	Ref
Li	NH_3	−71	0.005	558.7	2.8	128	31e
Li	$MeNH_2$	−78.3	0.009 12	228.3	2.1	5.79	4a
Na	NH_3	−34	0.002 54	1022	2.60	723	31a
Na	NH_3	−33.9	0.002 56	1127	2.88	341	31b
Na	NH_3	−45	0.002 99	927	2.77	248	31b
Na	NH_3	−65	0.004 32	645	2.79	188	31b
Na	$MeNH_2$	−50	0.005 2	79	0.41		31d
Na	$MeNH_2$	−60	0.006 38	66	0.42		31d
Na	$MeNH_2$	−70	0.007 6	54	0.41		31d
Na	EDA	23–25	0.015 4	27	0.42		26
Na	EDA	22	0.015 8	67.1	1.06	4.9	*a*
Na	EDA	18	0.016 9	62.8	1.06	12.9	*a*
Na	EDA	14	0.018 1	64.5	1.17	2.57	*a*
Na	EDA	9	0.021 2	55.4	1.12	10.8	*a*
Na	EDA	5	0.023 6	57.14	1.35	2.52	*a*
Na	PDA	22	0.015	47	0.705	7.32	*a*
Na	PDA	18	0.018 6	47	0.87	7.15	*a*
Na	PDA	12	0.026	39.4	1.02	5.87	*a*
Na	PDA	3	0.044	27.5	1.21	2.12	*a*
Na	PDA	−5	0.062	28.4	1.76	2.53	*a*
Na	PDA	−10	0.076	17.3	1.32	4.3	*a*
Na	PDA	−22	0.148	15.2	2.25	2.06	*a*
Na	PDA	−41	0.7	7.1	4.96	0.41	*a*
K	EDA	23–25	0.015 4	139	2.14	15.4	26
K	EDA (M band)	22	0.015 8	115.3	1.84	19.9	*a*
K	EDA (M band)	9	0.021	69.0	1.45	22.2	*a*
K	EDA (M band)	5	0.023 6	60.3	1.42	15.9	*a*
K	EDA (S band)	22	0.015 8	32.3	0.52	10.6	*a*
K	EDA (S band)	13	0.018 8	36.7	0.69	10.4	*a*
K	EDA (S band)	9	0.021 2	33.4	0.7	8.29	*a*
Rb	EDA	23–25	0.015 4	117	1.80	16.9	26
Cs	NH_3	−33.9	0.002 56	1142	2.92	487	31c
Cs	NH_3	−45	0.002 99	954	2.85	330	31c
Cs	NH_3	−65	0.004 32	672	2.90	219	31c
Cs	$MeNH_2$	−50	0.005 21	249	1.30	14.4	31d
Cs	$MeNH_2$	−60	0.006 31	209	1.30	14.3	31d
Cs	$MeNH_2$	−70	0.007 63	167	1.30	13.8	31d
Cs	EDA	23–25	0.015 4	204	3.14	14.4	26

[a] This work.

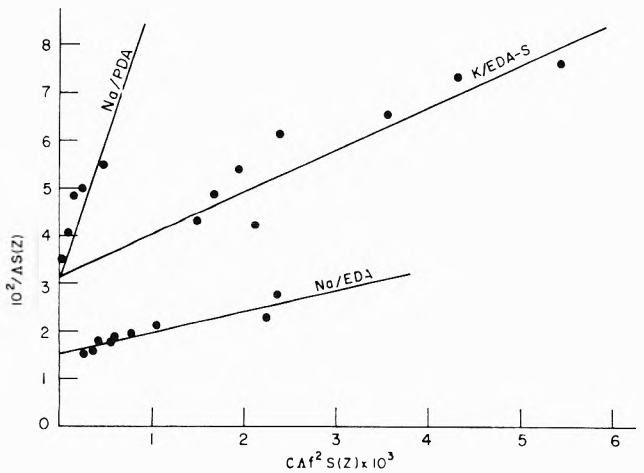

Figure 6. Typical Shedlovsky's plots of eq 9: Na/EDA and K/EDA (S band) 22 °C; Na/PDA 3 °C.

e.g., Kraus–Fuoss,[27b,c,30] were tried with essentially the same results.

In Figure 6, typical plots of eq (9) are shown. Table I summarizes the results of our experiments together with previous results.[26,31] From the results of Table I, a semilog plot of K_1 vs. reciprocal temperature of Na/PDA solutions is drawn in Figure 7. The slope of this curve, according to Fuoss[33] and Denison–Ramsey[34] theory of ion pairing is equal to e^2/akD where e is the electron charge, a is the distance of nearest approach between the cation and the anion of the ion pair, and k is Boltzmann's constant. A value of 4.68 ± 1 Å (70% confidence limit) for the distance between the ions is obtained, in agreement with our previous assumption. This value is quite reasonable in view of the fact that the size of the anion itself is approximately 3 Å.[3a,11]

Larger values of ion-pairing dissociation constants, but similar values (5 Å) for closest approach, were obtained by Dewald and Roberts[31b,c] for Na and Cs solutions in ammonia. In these cases the main negative species is the solvated elec-

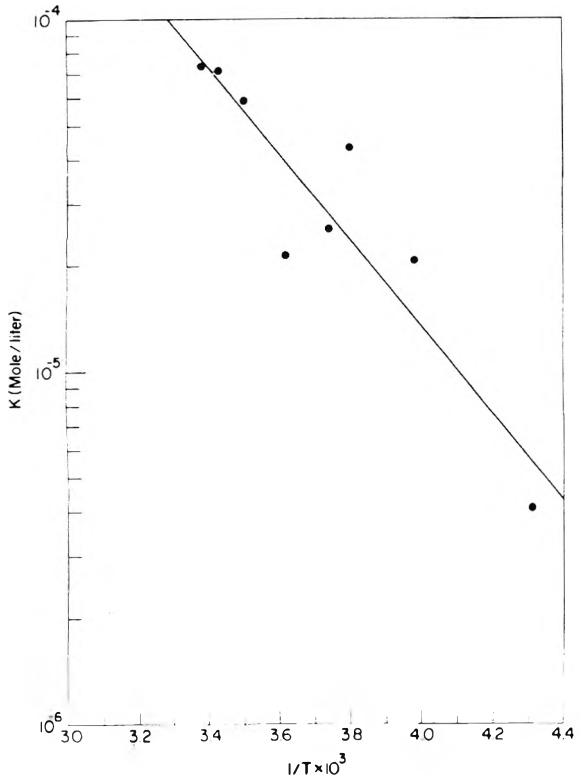

Figure 7. Logarithm of ion-pair dissociation constant (Shedlovsky) vs. reciprocal temperature of sodium–PDA solution.

tron, while in the case of Na/PDA the main negative species is the metal anion. Both species are, however, roughly of the same size. Table I shows also the Walden product $\Lambda_0\eta$. Viscosity data used were obtained partly in this laboratory[14] and partly from the literature.[26,31,32]

Most of the results of Walden's products may be averaged as follows: 2.84 for ammonia solutions, 1.53 for the M band in EDA and PDA solutions, 0.64 for the S band in EDA.

The values obtained by Dewald and Dye[26] for K/EDA solutions compare very well with ours if we notice that in their measurements they did not differentiate between the anion and the solvated electron, thus one should compare the sum of the Walden products of both the M band and the S band (1.53 + 0.64 = 2.17) to their value of 2.14. The dissociation constant is the average of our values for the two species.

The results for methylamine solutions depend upon the metal: 2.1, 0.41, and 1.3 for Li, Na, and Cs solutions, respectively.

Here, again, the different results may be due to the conductivity being the sum of the M and the S bands which are present in different amounts in solutions of the different metals.

Within each region the changes in the Walden product are much smaller than the changes in equivalent conductivity or the viscosity separately. One can safely conclude therefore that at least part of the conductivity is governed by Stokes' law mechanism.

The radius thus obtained for the solvated electron in EDA is 2.54 Å. Twice this radius matches quite well the distance of closest approach used earlier. A much smaller radius is formally obtained however for M^- in diamines, and for the solvated electron in ammonia, or in other words the conductance is too high to be determined only by Stokes' law. Other possible mechanisms such as tunnelling and successive exchanges of electrons between ions may be operative.

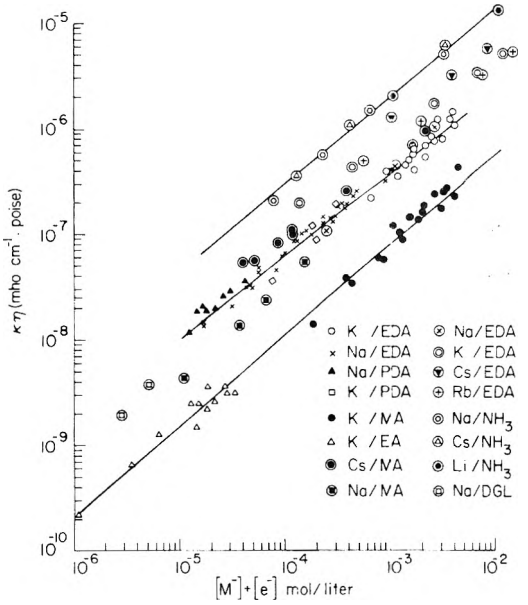

Figure 8. Log–log plot of $\kappa\eta$ vs. concentration. (Circled points) Literature data: Na/DGL (diglyme) ref 7; Cs/MA, Na/MA ref 31d; Cs/NH_3 ref 31c; Na/NH_3 ref 31b; Li/NH_3 ref 31e; Na/EDA, K/EDA, Rb/EDA, Cs/EDA ref 26. (Regular points) This laboratory; K/EDA, K/PDA, K/MA; K/EA; Na/PDA; Na/EDA.

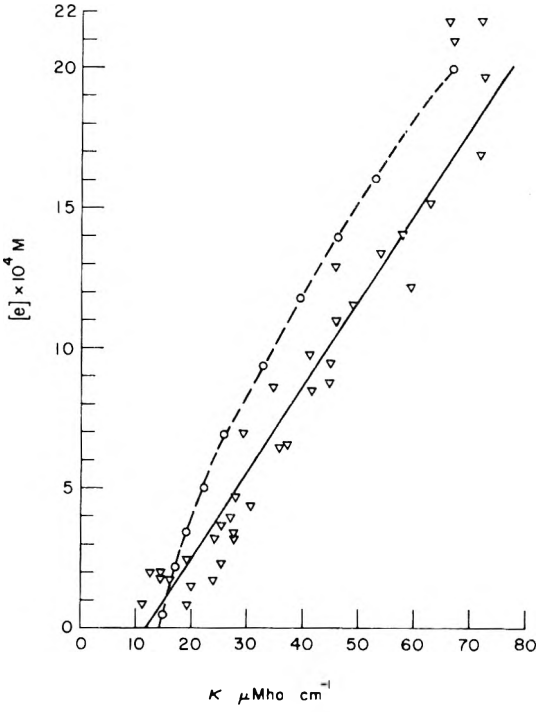

Figure 9. Solvated electron concentration (from ESR signal) vs. conductivity of potassium–EDA solution: (▽) measured; (○) computed by eq 12.

A different way to look at the data is a log–log plot of $\kappa\eta$ vs. concentration. This kind of plot has two advantages: (a) only raw data are used without recurrence to any kind of extrapolation; (b) changes in the mobilities which are caused by changes in viscosity are taken care of. Such a plot is shown in Figure 8 together with literature data in order to give a more complete picture.

We have also assumed that the extinction coefficients of M and S bands in methylamine and ethylamine are similar to

those of EDA and PDA. If this assumption is incorrect and the coefficients are higher, the line of these amines will move to the left and will coincide with the EDA–PDA line.

In spite of the differences, the similarity of conductance behavior among the various solvents, metals, and methods of measurements is striking.

In all cases straight lines were obtained with slope of 0.8, although the lines are positioned differently. The order of the lines is such that ammonia solutions conduct better than EDA and PDA and these better than methylamine and ethylamine. In ammonia all metals conduct the same way, but in EDA the Cs conducts slightly better than other alkali metals. This linearity shows beyond doubt that the conductivity is governed mainly but not solely by Stokes' law. Since the slope is smaller than one it means formally that the average radius of the conducting species increases slightly with concentration, in fact as $C^{1/5}$. Alternatively another mechanism, apart from Stokes, may contribute to conduction; slight changes in dielectric constant, electrophoretic effect, may all contribute to this phenomena.

ESR–Conductivity Measurements

Further confirmation of the above results was obtained by measuring the conductivity and paramagnetic resonance simultaneously. This could be done only in solutions which contain an appreciable amount of S band. In sodium solutions the concentration of paramagnetic species was estimated, by comparing to standard pitch, to be $1\text{–}2 \times 10^{-6}$ M. The specific conductances should therefore be 0.1 $\mu\Omega^{-1}$ cm^{-1} which is in order of magnitude of that of the pure solvent, and thus no correlation is found between the ESR signal and conductance.

In potassium–EDA solutions the amount of solvated electron is large and linear correlation between the ESR signal and conductivity is obtained (Figure 9).

This linear correlation is obtained as follows: given the total specific conductance:

$$1000\kappa_T = \lambda_{M^+}[M^+] + \lambda_{M^-}[M^-] + \lambda_{e^-}[e^-] + \lambda_{p^-}[p^-] \quad (10)$$

and using equilibrium 3 and conservation of matter and charge, one obtains

$$1000\kappa_T = (\lambda_{M^+} + \lambda_p)C + (\lambda_{M^-} - \lambda_{M^+} - 2\lambda_p)\frac{C[e^2]}{K_3 + [e^2]} + (\lambda_e - \lambda_p)[e] \quad (11)$$

or in terms of Λ's:

$$1000\kappa_T = \Lambda_p C + (\Lambda_{M^-} - 2\Lambda_p)\frac{C[e^2]}{K_3 + [e^2]} + (\Lambda_e - \Lambda_p)[e] \quad (12)$$

It was noted before that by the symbol Λ_x we mean the equivalent conductance of the species x as a whole, namely, the positive and the negative ion together, and C, the total metal concentration.

The deviations of eq 12 from linearity, at the range of concentrations concerned, will be small, and will be masked by the scatter of the points. Taking $C = 4.7 \times 10^{-3}$ M and $\Lambda_{M^-} = 30$, $\Lambda_e = 11$, and $\Lambda_p = 3$ kohlrausch (the measured values of the conductivities at this concentration) one obtains the calculated points of eq 12 which do not deviate from linearity except at the lowest solvated electron concentrations, as expected. Also the line obtained is fairly close to the measured one, thus confirming our assumptions and the values of conductivity found earlier. The reverse procedure, namely, finding the Λ's from the measured points, is obviously unreliable.

References and Notes

(1) W. Weyl, *Ann. Phys.*, **197**, 601 (1863).
(2) (a) "Metal-Ammonia Solutions: Proceedings of an International Conference on the Nature of Metal–Ammonia Solutions", Colloque Weyl II, J. J. Lagowski and M. J. Sienko, Ed., Butterworths, London, 1969; (b) "Electrons in Fluids: The Nature of Metal–Ammonia Solutions", Colloque Weyl III, J. Jortner and N. R. Kestner, Ed., Springer-Verlag, West Berlin, 1973; (c) R. F. Gould, Ed., *Adv. Chem. Ser.*, **No. 50** (1965); (d) "Metal–Ammonia Solutions", W. L. Jolly, Ed., Dowden, Hutchinson, and Ross 1972.
(3) (a) S. Golden, C. Guttman, and T. R. Tuttle, Jr., *J. Chem. Phys.*, **44**, 3791 (1966); (b) E. Becker, R. H. Lindquist, and B. J. Alder, *ibid.*, **25**, 97 (1956); (c) J. Jortner, *ibid.*, **27**, 823 (1957); (d) E. Arnold and A. Patterson, Jr., *ibid.*, **41**, 3089 (1964); (e) J. L. Dye, M. G. DeBacker, and L. M. Dorfman, *ibid.*, **52**, 6251 (1970); (f) J. L. Dye, *Pure Appl. Chem.*, 1 (1970).
(4) (a) D. S. Berns, E. C. Evers, and P. W. Franck, Jr., *J. Am. Chem. Soc.*, **82**, 310 (1960); (b) D. Huppert and K. Bar-Eli, *J. Chem. Phys.*, **74**, 3285 (1970); (c) I. Hurley, T. R. Tuttle, Jr., and S. Golden, ref 2a, p 449.
(5) S. H. Glarum and J. H. Marshall, *J. Chem. Phys.*, **52**, 5555 (1970).
(6) E. Saito, ref 2a, p 485.
(7) (a) J. G. Kloosterboer, Ph.D. Thesis, University of Amsterdam, 1970; (b) J. G. Kloosterboer, L. S. Giling, R. P. H. Rettschnick, and J. D. W. Van Voorst, *Chem. Phys. Lett.*, **8**, 462 (1971).
(8) T. R. Griffiths and M. C. R. Symons, *Trans. Faraday Soc.*, **56**, 1125 (1960).
(9) G. Stein and A. Treinin, *Trans. Faraday Soc.*, **56**, 1393 (1960).
(10) M. T. Lok, F. J. Tehan, and J. L. Dye, *J. Phys. Chem.*, **76**, 2975 (1972).
(11) K. Bar-Eli and G. Gabor, *J. Phys. Chem.*, **77**, 323 (1973).
(12) S. Matalon, S. Golden, and M. Ottolenghi, *J. Phys. Chem.*, 73, 3098 (1969).
(13) (a) K. Bar-Eli and T. R. Tuttle, Jr., *J. Chem. Phys.*, **40**, 2538 (1964); (b) K. D. Vos and J. L. Dye, *ibid.*, **38**, 2033 (1963); (c) R. Catterall, M. C. R. Symons, and J. W. Tippling, *J. Chem. Soc. A*, 1234 (1967).
(14) S. Nehari, Ph.D. Thesis, Tel-Aviv University, 1973.
(15) M. Ottolenghi, K. Bar-Eli, and H. Linschitz, *J. Chem. Phys.*, **43**, 206 (1965).
(16) S. Nehari and K. Bar-Eli, ref 2b, p 97.
(17) (a) R. K. Quinn and J. J. Lagowski, *J. Phys. Chem.*, **73**, 2326 (1969); (b) *ibid.*, **72**, 1374 (1968).
(18) C. A. Bennet and N. L. Franklin, "Statistical Analysis in Chemistry and Engineering", Wiley, New York, N.Y., 1967, p 250.
(19) M. G. DeBacker and J. L. Dye, *J. Phys. Chem.*, **75**, 3092 (1971).
(20) S. Windwer and B. R. Sundheim, *J. Phys. Chem.*, **66**, 1254 (1962).
(21) J. L. Dye, M. G. DeBacker, J. A. Eyre, and L. M. Dorfman, *J. Phys. Chem.*, **76**, 839 (1972).
(22) L. M. Dorfman, F. Y. Jou, and R. Wageman, *Ber. Bunsenges. Phys. Chem.*, **75**, 681 (1971).
(23) A. Gaathon and M. Ottolenghi, *Isr. J. Chem.*, **8**, 165 (1970).
(24) L. Onsager and R. M. Fuoss, *J. Phys. Chem.*, **36**, 2689 (1932).
(25) H. S. Harned and B. B. Owen, "The Physical Chemistry of Electrolytic Solutions", 3d ed., Reinhold, New York, N.Y., 1958, p 200 *ff*, eq 6.2.3.
(26) R. R. Dewald and J. L. Dye, *J. Phys. Chem.*, **68**, 128 (1964).
(27) (a) T. Shedlovsky, *J. Franklin Inst.*, **225**, 738 (1938); (b) C. A. Kraus and R. M. Fuoss, *J. Am. Chem. Soc.*, **55**, 476 (1933); (c) *ibid.*, **55**, 1019 (1933).
(28) L. Onsager, *Phys. Z.*, **28**, 271 (1927).
(29) J. L. Dye, R. F. Sankuer, and G. E. Smith, *J. Am. Chem. Soc.*, **82**, 4797 (1960).
(30) (a) R. M. Fuoss, *J. Am. Chem. Soc.*, **57**, 488 (1935); (b) H. M. Dagget, Jr., *ibid.*, **73**, 4977 (1951); (c) R. M. Fuoss and T. Shedlovsky, *ibid.*, **71**, 1496 (1949).
(31) (a) E. C. Evers and P. W. Frank, *J. Chem. Phys.*, **30**, 61 (1959); (b) R. R. Dewald and J. H. Roberts, *J. Phys. Chem.*, **72**, 4224 (1968); (c) R. R. Dewald, *ibid.*, **73**, 2615 (1969); (d) R. R. Dewald and R. W. Bowall, *ibid.*, **74**, 129 (1970); (e) E. C. Evers and F. R. Longo, *ibid.*, **70**, 426 (1966).
(32) "International Critical Tables", Vol. 7, p 211.
(33) R. M. Fuoss, *J. Am. Chem. Soc.*, **80**, 5059 (1958).
(34) J. T. Denison and J. B. Ramsey, *J. Am. Chem. Soc.*, **77**, 2615 (1955).
(35) Deviations from Kolrausch's law can be calculated according to Onsager and Fuoss.[24,25] The deviations, assuming complete dissociation, are smaller than 10%. Since the dissociation is not complete, the actual deviations are much smaller and the experimental accuracy involved does not warrant any other assumptions but that of independent mobilities.

Amphiphile Aggregation Number and Conformation from Carbon-13 Nuclear Magnetic Resonance Chemical Shifts

Bert-Ove Persson, Torbjörn Drakenberg,* and Björn Lindman

Department of Physical Chemistry 2, Chemical Center, P.O.B. 740, S-220 07 Lund 7, Sweden *(Received March 15 1976)*

The dependence of the ^{13}C NMR chemical shifts from the *n*-nonylammonium bromide carbons on the amphiphile concentration have been used to estimate the aggregation number in the NAB micelles, resulting in 37 ± 5 monomers/micelle. Furthermore, the observed downfield shift on micelle formation has been interpreted as caused by an increased proportion of the trans conformation of the alkyl chains in the micelles compared to the monomers.

It could be expected that ^{13}C NMR with its high resolution and large chemical shift range should be well suited for the study of the association of amphiphilic compounds, for example, ionic surface-active agents. Indeed it has been demonstrated in recent years that on micelle formation there are considerable changes in both shielding and relaxation and that it is possible to characterize the effects for a large number of carbons in an alkyl chain.[1-5] In the present communication we wish to demonstrate that two types of significant information on the amphiphile association process may be obtained from ^{13}C chemical shift investigations. First, it is possible by detailed studies of the concentration dependence of the chemical shift to deduce quantitative information on the amphiphile aggregation number and, secondly, the shift change on passage from the intermicellar solution to a micelle gives qualitative information on any accompanying conformational change of the alkyl chain.

Assuming an idealized situation where the amphiphile may occur either as a monomer or in a single type of micelle with an aggregation number n the chemical shift can be written

$$\delta_{obsd} = \frac{C_m}{C_t}\delta_m$$

Here C_m and C_t denote the concentration of micellized amphiphile and the total amphiphile concentration, respectively. δ_{obsd} is the observed chemical shift and δ_m the shift of micellized amphiphile, both taken relative to the chemical shift of the monomer. The monomer shift is obtained by extrapolation to zero amphiphile concentration. The concentrations of monomer and micelle in the equilibrium

$$nX \rightleftarrows X_n \text{ with } K = [X_n]/[X]^n$$

may be expressed as

$$[X] = C_t\frac{\delta_m - \delta_{obsd}}{\delta_m}$$

and

$$n[X_n] = C_t\frac{\delta_{obsd}}{\delta_m}$$

The expression for K may then be rewritten as

$$\ln (C_t\delta_{obsd}) = n \ln [C_t(\delta_m - \delta_{obsd})] + \ln K + \ln n - (n-1)\ln \delta_m \quad (1)$$

Consequently, a plot of $\ln (C_t\delta_{obsd})$ vs. $\ln [C_t(\delta_m - \delta_{obsd})]$ yields the aggregation number and the equilibrium constant if the simple model holds. δ_m may be estimated from plots of δ_{obsd} vs. the inverse amphiphile concentration.[1] Analogous procedures have been used previously for ^1H and ^{19}F chemical shifts.[6,7]

To illustrate these principles we present variable concentration ^{13}C chemical shift data for aqueous solutions of a cationic surfactant, *n*-nonylammonium bromide (NAB). Chemical shifts of the three methylenes in the center of the alkyl chain are presented in Figure 1. The critical micelle concentration obtained from the plots of Figure 1 (cf. ref 1) is 0.11 mol kg^{-1} and thus in close agreement with results obtained by other methods.[8,9] A previously found[8] change in the NAB micellar structure at high concentrations is verified by the ^{13}C NMR chemical shifts. In plots using eq 1 in order to obtain the aggregation number, the results for the highest concentrations were not included. As can be inferred from Figure 2 the chemical shift data follow closely the behavior predicted by the model used. Up to quite high concentrations our results can thus be explained by aggregation of NAB into a single type of micelle, which, according to least-squares treatments, has an aggregation number of 37 ± 5. Although direct comparisons are not possible this result is found to be in good agreement with studies by other methods.[10]

The information on the association process may be derived without knowledge of the cause of the shift changes but such a knowledge is of interest since it may shed light on the micelle structure. Regarding the origin of the chemical shift changes on micelle formation we can visualize two principal mechanisms. We may either have "medium effects", i.e., direct effects of the environment, or we may have "conformation effects", i.e., the chemical shift may change as a result of a change in conformation of the alkyl chain. Several different observations seem to rule out a sizeable contribution from medium effects to the δ_m values of the methylene and methyl groups. Thus the shift changes are quite different on micelle formation and on transfer to an organic solvent (Table I). Also, the variation of δ_m along the alkyl chain does not correspond at all to the variation in environment.[11] Furthermore, it has been observed that, while, for example, ^{13}C shifts of carbonyl groups may vary strongly with the solvent, solvent effects are small for alkyl groups.[12] Good direct support for the predominance of conformational effects is found in a study by Batchelor et al.[13]

Since a downfield shift can be related to an increasing importance of the trans conformation[13,14] it can be inferred from Table I that micelle formation is accompanied by a partial changeover from gauche to trans conformations in the alkyl chains. It is significant that the effects are largest in the middle

TABLE I: ^{13}C Chemical Shifts for *n*-Octanoic Acid in Various Solvents and for Sodium *n*-Octanoate and *n*-Nonylammonium Bromide in Aqueous Solution Together with the Shift Changes (δ_m) on Micelle Formation[a]

	1-CH_2	2-CH_2	3-CH_2	4-CH_2	5-CH_2	6-CH_2	7-CH_2	8-CH_2	-CH_3
$C_7H_{15}COOH$ in cyclohexane	34.9	25.7	30.2	30.1	32.8	23.7			14.7
$C_7H_{15}COOH$ in dioxane	34.5	26.0	30.2	30.1	32.8	23.7			14.8
$C_7H_{15}COOH$ in CH_3COOH	34.6	25.5	29.8	29.8	32.5	23.4			14.3
$C_7H_{15}COOH$ in neat	35.1	25.8	30.3	30.2	32.9	23.8			14.9
$C_7H_{15}COONa$, dilute in H_2O	39.2	27.5	30.3	29.8	32.9	23.6			15.1
$C_7H_{15}COONa$, δ_m	+0.33	+0.48	+1.02	+1.01	+0.95	+0.67			+0.46
$C_9H_{19}NH_3Br$, dilute in H_2O	41.4	28.4	27.1	30.0	29.9	29.8	32.7	23.6	15.1
$C_9H_{19}NH_3Br$, δ_m	+0.20	+0.58	+1.08	+1.22	+1.08	+1.09	+0.89	+0.64	+0.45

[a] The chemical shifts (in ppm) are given relative to external TMS without any susceptibility corrections with a positive shift being downfield. (Susceptibility corrections are calculated to be at most 0.2 ppm and would have the effect of slightly increasing the shifts of the aqueous solutions as compared to the organic solutions.) Numbering of the methylenes starts from the polar head. For $C_9H_{19}NH_3Br$ the assignment of the 4-CH_2, 5-CH_2, and 6-CH_2 signals is only tentative.

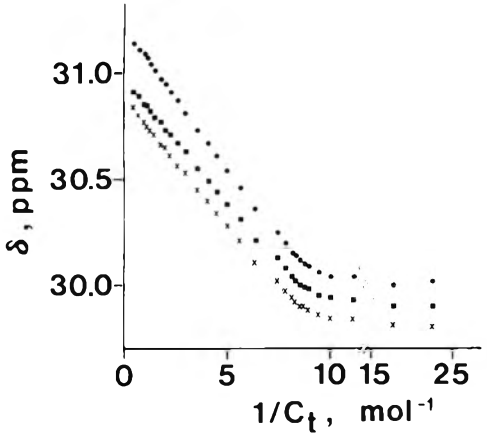

Figure 1. Variation of the ^{13}C chemical shifts of the three central methylene groups of *n*-nonylammonium bromide with the inverse concentration. Shifts are referred to tetramethylsilane with a downfield shift being positive. Temperature 30 °C.

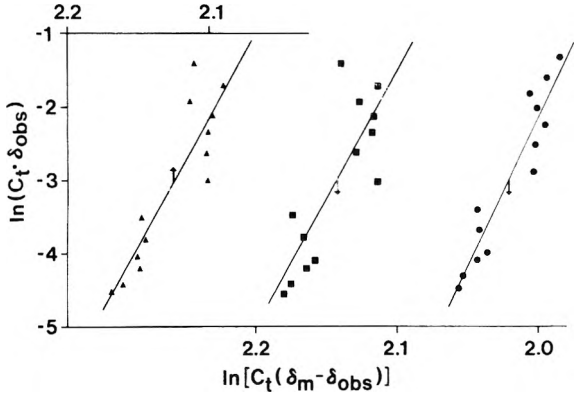

Figure 2. Plots for obtaining the micelle aggregation number of nonylammonium bromide using the data of Figure 1. The principles used are described in the text.

of the chain while relatively small at either end. It is difficult presently to put these results on a quantitative basis but it should be mentioned that Cheney and Grant[14] have estimated the shift change between the gauche and anti forms of an alkane chain to be 4.8 ppm.

It seems reasonable to believe that ^{13}C chemical shifts should be useful for the study of conformation changes in surfactant systems. It is interesting to note that we observe, at the transition from globular to cylindrical NAB micelles, a downfield shift for the α-CH_2 group but an upfield one for the ω-CH_3 group.

Experimental Section

All ^{13}C NMR spectra were recorded on a Varian XL-100 spectrometer at 25.16 MHz and in the Fourier transform mode. Proton noise decoupling and deuterium lock were used.

Typical settings for the FT parameters were: spectral width 1000 Hz, acquisition time 2–4 s, flip angle 80°, number of transients 1000 to 10000, resulting in an optimal accuracy in the shift determination of ±0.2 to ±0.4 Hz.

The lock signal was obtained from benzene-d_6 in a 5-mm tube inside the 12-mm tube with the sample. The chemical shifts have been related to TMS by assuming that the shift of cyclohexane in the sample with cyclohexane as solvent is 27.8 ppm downfield from TMS.

No susceptibility correction has been applied, but this should not be more than 0.2 ppm when the solvent is changed from cyclohexane to water.

The surfactants were obtained from Eastman Kodak Co. (Rochester, N.Y.). No impurities could be detected from ^{13}C NMR spectra of concentrated solutions. Homologues, however, might be difficult to detect.

References and Notes

(1) T. Drakenberg and B. Lindman, *J. Colloid Interface Sci.*, **44**, 184 (1973).
(2) M. Alexandre, C. Fouche:, and P. Rigny, *J. Chim. Phys.*, **70**, 1073 (1973).
(3) D. Leibfritz and J. D. Roberts, *J. Am. Chem. Soc.*, **95**, 4996 (1973).
(4) G. C. Levy, R. A. Komoroski, and J. A. Halstead, *J. Am. Chem. Soc.*, **96**, 5456 (1974).
(5) U. Henriksson and L. Ödberg, *Colloid Polym. Sci.*, **254**, 35 (1976).
(6) N. Muller and F. E. Platko, *J. Phys. Chem.*, **75**, 547 (1971).
(7) J. H. Fendler, E. J. Fendler, R. T. Medary, and O. A. El Seoud, *J. Chem. Soc., Faraday Trans. 1*, **69**, 280 (1973).
(8) G. Lindblom and B. Lindman, *J. Phys. Chem.*, **77**, 2531 (1973).
(9) P. Mukerjee and K. J. Mysels, *Natl. Stand. Ref. Data Ser., Natl. Bur. Stand.*, **No. 36** (1971).
(10) K. Shinoda, "Colloidal Surfactants", Academic Press, New York, N.Y., 1963.
(11) P. Mukerjee and K. J. Mysels, *ACS Symp. Ser.*, **9**, 239 (1975).
(12) J. B. Stothers, "Carbon-13 NMR Spectroscopy" in "Organic Chemistry, A Series of Monographs", Vol. 24, Academic Press, New York, N.Y., 1972.
(13) J. G. Batchelor, J. H. Prestegard, R. J. Cushley, and S. R. Lipsky, *Biochem. Biophys. Res. Commun.*, **48**, 70 (1972).
(14) V. B. Cheney and D. M. Grant, *J. Am. Chem. Soc.*, **89**, 5319 (1967).

Ligand Field Spin–Orbit Coupling Calculations for d^7, d^8, d^9 (d^3, d^2, d^1) Five Coordinated Complexes of C_{3v} Symmetry

A. Bencini and D. Gatteschi*

Laboratorio CNR and Istituto di Chimica Generale, Università di Firenze, 50132 Florence, Italy *(Received February 9, 1976)*

The complete matrices for ligand field spin–orbit coupling perturbations are provided for d^1, d^2, and d^3 ions in C_{3v} symmetry. The importance of using such matrices for the interpretation of the electronic properties of trigonal bipyramidal five-coordinated complexes is stressed, in contrast with previous uses in the literature of D_{3h} matrices.

Introduction

The electronic properties of coordination compounds of transition elements have been extensively investigated in the last years and an increasing amount of experimental information has been obtained by the use of single crystal electronic spectroscopy in linearly polarized light at very low temperature and under high resolution conditions[1,2] of magnetic circular dichroism spectroscopy,[3] electron spin resonance spectroscopy,[4–7] *etc.* For the interpretation of these experimental data it is necessary to use a method of calculation which can keep pace with the more sophisticated experimental techniques, allowing for small perturbations such as the low symmetry components of ligand field and spin–orbit coupling. These, in fact, determine the nature of the ground electronic level and are responsible for the large number of electronic transitions observed experimentally.

Ligand field calculations have been generally used, because they provide a simple way of parameterization of energy levels, although, in some instances, also more sophisticated models were employed. Complete ligand field spin–orbit coupling matrices, however, are easily available only for cubic symmetries,[8–10] as a consequence of the intial impetus in the study of octahedral or tetrahedral complexes, while there is not much in the literature for low symmetry chromophores. To have complete matrices in low symmetries, however, is particularly important for five-coordinated trigonal bipyramidal complexes, for which the cubic matrices cannot provide even a first approximation to the energy levels.

In that class of complexes, molecules having the full idealized D_{3h} symmetry are very rare, the main distortions being toward either C_{3v} or C_{2v} configurations of donor atoms.[11–13] It has been often assumed, however, that the electronic levels of a complex of C_{3v} symmetry must be close to those calculated in D_{3h} symmetry, and all the theoretical treatments have been restrained to this latter symmetry.[14–16] In the following sections we will show that the effect of a full C_{3v} perturbation can determine a dramatic deviation of the levels from those of D_{3h} symmetry and that it can also cause, in some instances, a change in the spin–orbit split ground level. Since the interpretation of the fine structures of the electronic spectra depends strongly on the nature of the ground level, this result is of paramount interest in correctly assigning the experimentally observed electronic transitions and we intend to report here the complete matrices for d^1, d^2, and d^3 ions in C_{3v} symmetry.

The Model of Calculation

Our ligand field calculations were performed in the well-known "weak-field coupling scheme".[8] The choice of the coupling scheme, however, is unimportant in the ligand field formalism, when we perform "complete" calculations, i.e., when we consider all the interactions among the levels originating from different states of the d^n manifold. Eigenvalues and eigenvectors of the spin–orbit coupling operator were obtained by direct diagonalization of its perturbation matrices in the C_{3v} symmetry adapted $|LSM_LM_S\rangle$ basis functions.

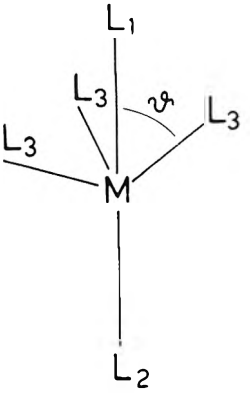

Figure 1. The most general configuration of donor atoms for a five coordinate complex of C_{3v} symmetry.

The $|LSM_LM_S\rangle$ basis functions for d^1, d^2, and d^3 configurations correspond to those reported by Slater,[17] with some corrections in order to have them correctly connected by phase through the vector coupling coefficients.[18] C_{3v} symmetry adapted linear combinations of these functions were written by considering their transformation properties under symmetry operations through the rotation matrices $D^j(\alpha, \beta, \gamma)$.[15,16] Actually, in order to classify the LS functions according to the irreducible representations of the C_{3v} symmetry group it is sufficient to know their behavior under the group generators $C_3(z)$ and, say, σ_{xz}.[19] In Table I[20] we report the symmetry classification of the LS functions with L varying from 5 to 0.

The symmetry functions for the double group C_{3v}* were obtained by taking the direct product of the orbital and spin functions[21] through the coupling coefficients reported by Koster et al.[22] They are reported in Tables II–IV,[20] together with the appropriate symmetry labels. The perturbation matrices were constructed with a computer program which expressed the matrix elements as a function of the one electron spin–orbit coupling constant ζ and of monoelectronic ligand field parameters. In order to achieve the maximum of generality of our treatment, we have used the ligand field parameters: $V22 = \langle \pm 2|V| \pm 2\rangle$, $V11 = \langle \pm 1|V| \pm 1\rangle$, $V00 = \langle 0|V|0\rangle$,

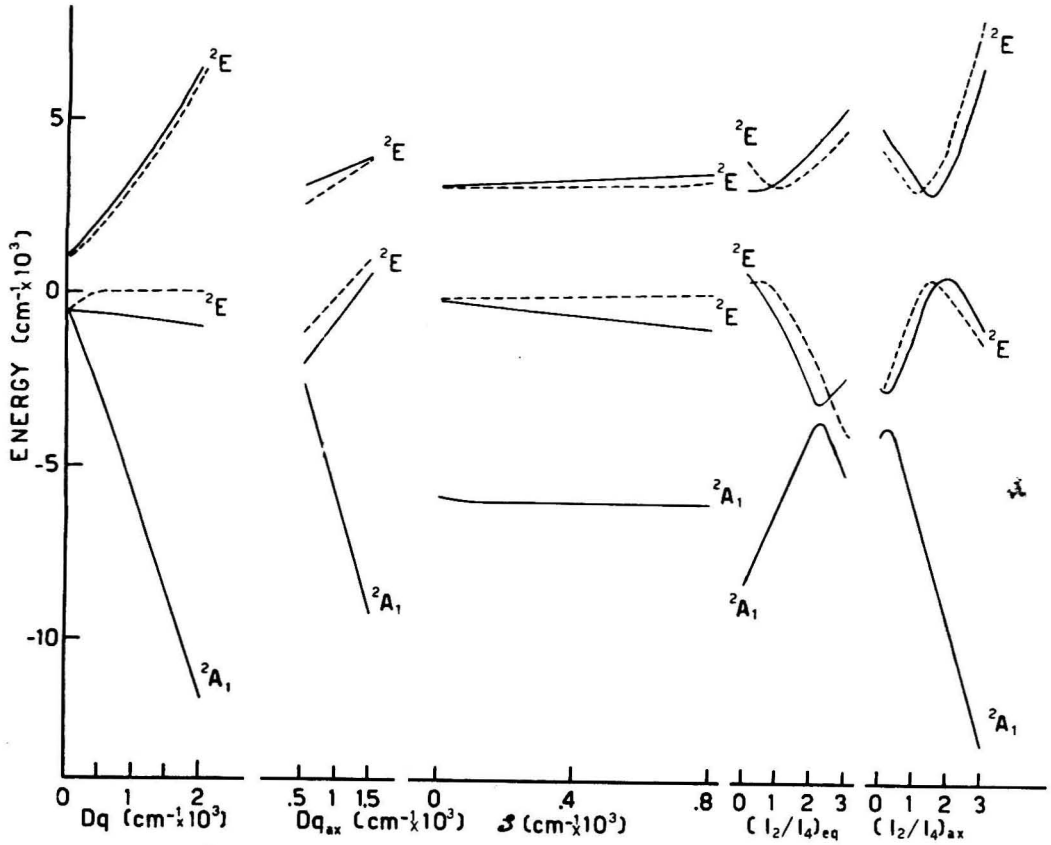

Figure 2. Energy level diagram for a d^9 ion in a five coordinate chromophore of C_{3v} symmetry: (—) Γ_4 levels; (- - - -) Γ_5 levels. Left diagram: $Dq_{ax} = Dq_{eq}$; $(I_2/I_4)_{ax} = (I_2/I_4)_{eq} = 1$; $\zeta = 660$ cm^{-1}. From the left to the right the effect of changing Dq_{ax}, ζ, $(I_2/I_4)_{eq}$, and $(I_2/I_4)_{ax}$ with $Dq_{eq} = 1000$ cm^{-1}

and $V2M1 = \langle 2|V|-1\rangle = -\langle -2|V|1\rangle$ where V is the appropriate Hamiltonian operator referring to the perturbation due to the ligands and $|\pm 2\rangle$, $|\pm 1\rangle$, $|0\rangle$ represent the one electron d orbitals. In fact, in the last years, it has become clear[23–27] that all the most common ligand field parameterizations, including the angular overlap model, can be considered to be equivalent, and that, therefore, it is desirable to be able to pass from one to another in order to make the best use of the method according to the problem which is being studied. In Table V[20] are reported the relations between our parameters and the most common ligand field parameters for five coordinate complexes, in the nonadditive scheme[25] (which in C_{3v} symmetry requires three parameters Dq, Ds, and Dt), in the additive scheme[25] (which requires up to six parameters, Dq and I_2 for each set of independent donor atoms), and the angular overlap model[25] (which, for linearly ligating donors and neglecting δ bonds, requires up to six parameters, e_σ' and e_π' for each set of independent donor atoms). The angle θ is the angle L_1–M–L_3 (Figure 1). The spin–orbit coupling energy has been evaluated through the hamiltonian operator

$$\mathcal{H}_{so} = \zeta \sum_i l_i \cdot s_i$$

where the sum is over all the electrons of the configuration, l_i and s_i are the orbital and spin angular momentum operators and ζ is the spin–orbit coupling constant for a d electron.

TABLE V: Relations between the Most Common Parameterizations of the Ligand Field for Five Coordinate Complexes (For every V_{ij} the first equation refers to the crystal field model in the additive scheme, the second to the angular overlap model, and the third to the crystal field model in the nonadditive scheme. The parameters are defined as in ref 27.)

$$V00 = (2/7)\, I_2^{L1} + (2/7)\, I_2^{L2} + ((9\cos^2\theta - 3)/7)\, I_2^{L3} + (12/7)\, Dq^{L1} + (12/7)\, Dq^{L2} + (9/14)(35\cos^4\theta - 30\cos^2\theta + 3)\, Dq^{L3} = (4/5)\, e_\sigma^{L1} + (4/5)\, e_\sigma^{L2} + ((15(3\cos^2\theta - 1)^2 - 12)/20)\, e_\sigma^{L3} - (2/5)\, e_\pi^{L1} - (2/5)\, e_\pi^{L2} + ((45\sin^2 2\theta + 24)/20)\, e_\pi^{L3} = -4\,Dq - 2\,Ds - 6\,Dt$$

$$V11 = (1/7)\, I_2^{L1} + (1/7)\, I_2^{L2} + ((9\cos^2\theta - 3)/14)\, I_2^{L3} - (8/7)\, Dq^{L1} - (8/7)\, Dq^{L2} - (3/7)(35\cos^4\theta - 30\cos^2\theta + 3)\, Dq^{L3} = (-1/5)\, e_\sigma^{L1} - (1/5)\, e_\sigma^{L2} + ((45\sin^2 2\theta - 24)/40)\, e_\sigma^{L3} + (3/5)\, e_\pi^{L1} + (3/5)\, e_\pi^{L2} + ((15(3\cos^2\theta - 1)^2 - 12)/10)\, e_\pi^{L3} = (8/3)\,Dq - Ds + Dt$$

$$V22 = (-2/7)\, I_2^{L1} - (2/7)\, I_2^{L2} - ((9\cos^2\theta - 3)/7)\, I_2^{L3} + (2/7)\, Dq^{L1} + (2/7)\, Dq^{L2} + (3(35\cos^4\theta - 30\cos^2\theta + 3)/28)\, Dq^{L3} = (-1/5)\, e_\sigma^{L1} - (1/5)\, e_\sigma^{L2} + ((45(\cos^2\theta - 1)^2 - 24)/40)\, e_\sigma^{L3} - (2/5)\, e_\pi^{L1} - (2/5)\, e_\pi^{L2} + ((15(3 - \cos^4\theta) - 12)/10)\, e_\pi^{L3} = (-2/3)\,Dq + 2\,Ds - Dt$$

$$V2M1 = (15/2)\sin^3\theta\cos\theta\, Dq^{L3} = (15/2)\sin^3\theta\cos\theta\,((3/10)\, e_\sigma^{L3} - (4/10)\, e_\pi^{L3}) = (10\sqrt{2}/3)\, pq$$

Table VI – The matrix elements different from zero of the perturbation hamiltonian for a d^1 ion.[a]

[a] The column number corresponds to the j and the row number to the i index of the H_{ij} matrix element.

Γ_4

	1	2	3
1	V00	2 V11 − 0.5 ℑ	V22 + ℑ
2	1.2247 ℑ		

Γ_5

	1	2
1	V11 + 0.5 ℑ	2 V22 − ℑ
2	V2M1 − i ℑ	

TABLE VII: Matrix Elements Different from Zero of the Perturbation Hamiltonian for a d^2 Ion (The column number corresponds to the *i* and the row number to the *j* index of the H_{ij} matrix element.)

Γ_1

	1	2	3
1	12α +0.4 V22 +1.6 V11	12α + V22 + V11	12α +0.6 V22 + V11 +0.4 V00 − −0.5 i
2	1.8972 V2M1	−0.8660 i	−0.6324 V2M1
3	1.7317 i	0.6325 V2M1	0.4899 V22 −0.4899 V00
5	0.8 V22 −0.8 V11	−0.5 i	0.6545 i
7	0.7557 i		−1.1710 i
9	1.0140 i		

	4	5	6
4	12α + V22 + V00 + i	15 B +2α +1.6 V22 + +0.4 V11	15 B +2α +0.4 V22 + V11 + +0.6 V00 −0.5 i
6	0.7745 V2M1	0.7070 i	0.8364 i
8	0.8660 i	1.1831 i	−1.9997 i
		1.4140 i	

	7	8	9
7	12 B +2 C +20α +0.0571 V22 + +0.9143 V11 +1.0286 V00	12 B +2 C +20α + V22 + V11	5 B +2 C +6α +1.1428 V22 + +0.2856 V11 +0.5714 V00
8	0.7170 V2M1	−0.5346 V2M1	0.9561 V22 −0.4780 V11 − −0.4780 V00
9	0.2556 V22 +0.5110 V11 − −0.7667 V00	−1.7889 V2M1	
10	0.2138 V22 −0.8551 V11 + +0.6414 V00		

	10
10	22B +7 C +4α +0.8 V22 +0.8 V11 +0.4 V00

Γ_2

	1	2	3
1	12α + V22 + V11	12α +0.6 V22 + V11 + 0.4 V00 − −0.5 i	12α + V22 + V00 + i
3	0.8660 i	−0.6324 V2M1	0.7745 V2M1
5	0.5 i	0.4899 V22 −0.4899 V00	−0.8660 i

	4	5
4	15 B +2α +0.4 V22 + V11 + +0.6 V00 −0.5 i	12 B +2 C +20α + V22 + V11

Γ_3

	1	2	3
1	12α + V22 + V11	12α +0.4 V22 +1.6 V11	12α + V22 + V11
3	4.5 i	1.8973 V2M1	−0.6123 i
6	0.6123 i	1.2247 i	0.6324 V2M1
12	0.1336 i	0.8 V22 −0.8 V11	0.1336 i
13	0.7071 i	−0.5976 i	−0.7071 i
15	−0.9257 i	0.5854 i	−0.9257 i

	4	5	6
4	12 α +0.6 V22 + V11 + +0.4 V00	12 α +0.6 V22 + V11 + +0.4 V00 +0.5 i	12α +V22 + V00
6	−0.6324 V2M1	1.1179 i	0.7746 V2M1
7	1.1180 i	−0.6324 V2M1	−0.6546 i
9	0.4899 V22 −0.4899 V00	0.4899 V22 −0.4899 V00	−0.7559 i
11	−0.7318 i	0.7318 i	
14	−0.9561 i	−0.3380 i	

	7	8	9
7	12α + V22 + V00 − i	15 B +2α +1.6 V22 +0.4 V11	15 B +2 α +0.4V22 + V11 + +0.6 V00
10	0.7745 V2M1	0.5 i	−1.0246 i
11	−0.3273 i	−1.0246 i	
14	1.0689 i		

	10	11	12
10	15 B +2 α +0.4 V22 + V11 + +0.6 V00 +0.5 i	12 B +2 C +20 α +0.1428 V22 + + V11 +0.8571 V00	12 B +2 C +20 α +0.4286 V22 + +1.1428 V11 + 0.4286 V00
15	1.4489 i	0.2021 V2M1	−1.2370 V2M1
		−0.5344 V2M1	0.4948 V22 −0.9896 V11 + +0.4948 V00
		0.3498 V22 −0.3498 V00	
		1.0496 V2M1	

	13	14	15
13	12 B +2 C +20 α +2 V22	5 B +2 C +6 α +0.8571 V22 + + V11 +0.1428 V00	5 B +2 C +6 α +0.5714 V22 + +0.8571 V11 +0.5714 V00
14	−1.3092 V2M1	0.5714 V2M1	

TABLE VIII: Matrix Elements Different from Zero of the Perturbation Hamiltonian for a d^3 Ion (The column number corresponds to the *i* and the row number to the *j* index of the H_{ij} matrix element.)

Γ_4

	1	2	3
1	12 α + V22 + V11 + V00	12 α +1.6 V22 +0.4 V11 + V00	12 α + V22 + V11 + V00
3	0.5 i	−1.8974 V2M1	−0.5774 i
7	−0.5774 i	1.1546 i	−0.6325 V2M1
20	0.6455 i	−0.8 V22 +0.8 V11	0.6455 i
22	0.1220 i	−0.9760 i	0.1220 i
23	0.6456 i	−0.5455 i	−0.6456 i
26	0.5 i	−0.2887 i	0.5 i
28	0.1443 i	0.3219 i	0.1443 i
31	0.2077 i	−0.1314 i	0.2077 i
34	0.7104 i	1.1004 i	0.7104 i
38	−0.5 i	−0.4492 i	0.5 i
		− i	

	4	5	6
4	12 α +1.4 V22 + V11 +0.6 V00 + +0.5 i	12 α +1.4 V22 + V11 +0.6 V00 − −0.1666 i	12 α + V22 +2 V11 − i
6	0.6325 V2M1	0.9128 i	−0.7746 V2M1
7	−0.9130 i	0.6325 V2M1	−0.5175 i
9	−0.4899 V22 +0.4899 V00	−0.4899 V22 +0.4899 V00	0.4564 i
22	1.1573 i	−0.4255 i	−0.4155 i
28	−0.4565 i	−0.9448 i	−1.4206 i
31	0.1313 i	0.2886 i	
34	0.4492 i	0.1667 i	
		−0.1867 i	
		0.3033 i	
		−0.6353 i	
		1.0374 i	

	7	8	9
7	12 α + V22 +2 V11 +0.3334 i	15 B +2α +0.4 V22 +1.6 V11 + V00	15 B +2 α +1.6 V22 + V11 + +0.4 V00 +0.5 i
10	−0.7746 V2M1	0.4714 i	1.39 i
19	−.955590 i	−0.9266 i	0.6842 i
20	−0.5590 i	−0.5674 i	
22	−0.8453 i	−0.4561 i	
24	0.1443 i	−0.2793 i	
26	0.1443 i	0.8818 i	
28	−0.3334 i	−0.4083 i	
31	0.2399 i		
34	0.8203 i		

	10	11	12
10	15 B +2α +1.6 V22 + V11 + +0.4 V00 −0.1666 i	9 B +3 C +30α +1.2 V22 + V11 + +0.8 V00	9 B +3 C +30 α +0.5714 V22 + +1.7143 V11 +0.7143 V00
29	−0.3276 i	−0.3 i	−0.4779 V2M1
30	−0.8024 i	0.3463 i	−0.5477 i
32	−0.1612 i	0.3 i	−0.8166 i
33	−0.3950 i	−0.2925 V2M1	1.6096 V2M1
35	−0.8817 i	0.2449 V22 −0.2449 V00	−0.7302 i
36	−1.2469 i	0.6531 i	−0.7171 V22 +0.4781 V11 + +0.2390 V00
		0.8640 i	0.1886 V2M1
		0.1633 i	−0.1278 V22 +0.5110 V11 − −0.3832 V00
		−0.3162 V22 +0.3162 V00	
		−1.2412 V2M1	
		0.9872 V2M1	

	13	14	15
13	9 B +3 C +30α +1.2 V22 + + V11 +0.8 V00	9 B +3 C +30α +0.6476 V22 + +1.6095 V11 +0.7429 V00 − i	9 B +3 C +30α +0.8667 V22 + +1.3333 V11 +0.8 V00 +0.2 i
15	−0.3463 i	−0.4260 V2M1	−0.3651 V2M1
16	0.3 i	0.4363 V2M1	−0.2828 i
19	−0.6531 i	−0.8945 i	−0.2828 i
20	0.2449 V22 −0.2449 V00	0.0143 V22 −0.4571 V11 + +0.4429 V00 −0.8 i	0.5667 V2M1
22	−0.8640 i	1.0601 V2M1	0.0534 V22 +0.5345 V11 − −0.5880 V00 −0.7483 i
23	0.1633 i	0.8015 V2M1	−0.2332 V2M1
25	−0.1998 V2M1		
26	−0.3162 V22 +0.3162 V00		
35	0.8547 V2M1	−0.6677 V22 +0.4032 V11 + +0.2646 V00	−0.5270 V22 +0.2108 V11 + +0.3162 V00
		0.2191 V2M1	−0.7310 V2M1
		0.1105 V22 −0.4421 V11 + +0.3316 V00	−0.1460 V22 +0.5848 V11 − −0.4385 V00
		−0.3867 V2M1	−0.5817 V2M1
		0.0879 V22 −0.3518 V11 + +0.2638 V00	−0.1164 V22 +0.4653 V11 − −0.3491 V00
		−0.3078 V2M1	0.2618 V2M1
		−0.0990 V22 +0.3958 V11 − −0.2969	

	16	17	18
16	9 B +3 C +30α + 1.6 V22 + +0.8 V11 +0.6 V00 −0.4 i	9 B +3 C +30 α +2 V22 + V11 + +0.5 i	4 B +3 C +20α + V22 + +1.4286 V11 +0.5714 V00
19	0.9798 i	−1.3171 V2M1	−0.3584 V2M1
20	−0.9798 i	0.2886 V2M1	0.6708 i
21	−0.9817 V2M1	0.8008 V2M1	0.4627 V2M1
23	−0.4899 V22 +0.9798 V11 − −0.4899 V00 −0.4899 i	0.6374 V2M1	−0.4879 i
27	+0.0577 V2M1		−0.4226 i
30	−0.5063 V2M1		−0.6773 V22 +0.4615 V11 + +0.2185 V00
33	−0.4031 V2M1		−0.3338 V22 +0.7778 V11 − −0.4440 V00
36	−0.9068 V2M1		0.7319 i

19
19 4 B +3 C +20α +1.3 V22 + + V11 +0.7 V00
20 −0.45 i
22 0.3969
23 −0.3
24 −0.3873 V22 +0.3873 V00
26 −0.3227 i
28 −0.5590
29 −0.1016 V2M1
32 −0.5110 V2M1
38 0.9682 i

20
20 4 B +3 C +20α +1.3 V22 + + V11 +0.7 V00
22 −0.3969 i
23 −0.3 i
24 0.3227 i
25 −0.2447 V2M1
26 −0.3872 V22 +0.3872 V00
28 0.5590 i
35 −0.3887 V2M1
38 0.9682 i

21
21 4 B +3 C +20α +1.0429 V22 + +1.3429 V11 +0.6143 V00 −0.15
22 −0.1009 V2M1
23 0.2672 V2M1
25 0.5455 i
27 0.2646 V22 −0.3024 V11 + +0.0378 V00 +0.4724
28 0.3585 V2M1
30 −0.5970 V22 +0.3315 V11 + +0.2655 V00
31 0.1981 V2M1
33 −0.1931 V22 +0.2638 V11 − −0.0707 V00
34 1.0037 V2M1
36 0.0742 V22 −0.2968 V11 + +0.2227 V00

22
22 4 B +3 C +20α +1.1571 V22 + +1.1429 V11 +0.7 V00 +0.3001
24 0.1220
26 0.1220 i
27 0.1603 V2M1
28 −0.4226 V22 +0.3381 V11 + +0.0845 V00 +0.4227
30 −0.2333 V2M1
31 −0.3755 V22 +0.0476 V11 + +0.3279 V00
33 −1.1827 V2M1
34 0.0999 V22 −0.7597 V11 + +0.6597 V2M1
36 −0.3672 V2M1

23
23 4 B +3 C +20α +1.4 V22 + +1.2 V11 +0.4 V00 −0.6
24 0.6455
26 −0.6455 i
27 −0.4241 V2M1
30 −0.2470 V2M1
33 −1.2519 V2M1
36 0.2777 V2M1

24
24 24 B +3 C +12 α + +1.5 V22 + + V11 +0.5 V00
26 0.25 i
28 −0.9044
29 −1.3327 V2M1
31 0.9936
32 −0.0610 V2M1
34 0.2458
38 −0.25

25
25 24 B +3 C +12 α + +1.2 V11 +0.8 V00
26 0.3160 V2M1
27 0.3886 i
29 −0.7690 i
30 −0.6283 i
33 −0.1904 i
33 −0.1534 i
35 0.5344 V22 −0.8551 V11 + +0.3207 V00
37 −0.5 i

26
26 24 B +3 C +12 α + +1.5 V22 + + V11 +0.5 V00
28 0.1444 i
31 −0.9936 i
34 −0.3458 i
35 −0.9291 V2M1
38 −0.25

27
27 24 B +3 C +12 α +1.0333 V22 + +1.2667 V11 +0.7 V00 +0.0832
28 0.1053 V2M1
29 −0.8887
30 −0.4101 V22 −0.2924 V11 + +0.7025 V00 −0.7255
31 0.9948 V2M1
32 −0.3198
33 0.4198 V22 −0.2327 V11 − −0.1871 V00 −0.1795
34 0.0456 V2M1
35 0.1962 V22 +0.2618 V11 − −0.4582 V00

28
28 24 B +3 C +12 α + +1.1667 V22 + +1.3333 V11 +0.5 V00 −0.1667
30 0.3145 V2M1
31 0.9628 V22 −0.7961 V11 − −0.1669 V00 −0.5737
33 0.0144 V2M1
34 −0.6492 V22 +0.3102 V11 + +0.3390 V00− 0.1419
36 1.1382 V2M1

29
29 20 B + 5 C +(193 B^2 +8 BC + +4 C^2)$^{1/2}$ +6 α +0.4803 V22 + +1.6279 V11 +0.8885 V00
32 0.4004 V22 −0.6238 V11 + +0.2264 V00
30 −0.2869
33 0.8944
35 0.0156 i
36 0.0110
37 0.3334
39 0.5675

30
30 20 B +5 C +(193 B^2+8 BC + +4 C^2)$^{1/2}$+6 α +0.8642 V22 + +1.3207 V11 +0.8151 V00 + +0.1174
31 −0.1180 V2M1
32 0.8941
33 0.0576 V22 +0.2552 V11 − −0.3128 V00 −0.3651
34 0.7100 V2M1
35 −0.0178 i
36 0.5742 V22 −0.2871 V11 − −0.2871 V00 −0.0126

31
31 20 B +5 C +(193 B^2+8 BC + +4 C^3)$^{1/2}$+6 α +1.8951 V22 + +0.8642 V11 +0.2406 V00 − −0.2352
33 0.7100 V2M1
34 −0.2573 V22 +0.0576 V11 + +0.1996 V00 +0.7301

32
32 20 B +5 C −(193 B^2+8 BC + +4 C^2)$^{1/2}$+6 α +1.5186 V22 + +0.9408 V11 +0.54 V00
33 0.6964
35 1.0644 i
36 0.7526
37 1.1004
39 0.2793

33
33 20 B +5 C −(193 B^2+8 BC + +4 C^2)$^{1/2}$+6 α +1.3262 V22 + +1.2031 V11 +0.4706 V00 − −0.2843
34 0.1656 V2M1
35 −1.3026 i
36 0.4569 V22 −0.2285 V11 − −0.2285 V00 −0.9218

34
34 20 B +5 C −(193 B^2+8 BC + +4 C^2)$^{1/2}$+6 α +0.9146 V22 + +1.3262 V11 +0.7593 V00 + +0.5686

35
35 9 B +3 C +2α +1.4279 V22 + +1.0853 V11 +0.4857 V00
36 −0.4713 i
39 1.5274 i

36
36 9 B −3 C +2 α +1.0854 V22 + +1.2567 V11 +0.6569 V00 − −0.3332

37
37 12 α +1.4 V22 + V11 + +0.6 V00 −0.5
38 0.6324 V2M1
39 −0.4899 V22 +0.4899 V00

38
38 12 α +V22 +2 V11 +
39 −0.7746 V2M1

39
39 15 B +2 α +1.6 V22 + V11 + +0.4 V00 −0.5

Γ_3

1
1 12 α + V22 + V11 + V00
3 1.5 i
5 0.5
13 0.2112
14 1.1181
16 0.25
18 0.3597
20 1.2303

2
2 12 α +1.6 V22 +0.4 V11 + V00
3 −1.8974 V2M1
4 −0.1 i
6 −0.8 V22 +0.8 V11
12 −0.9448 i
15 −0.5 i
17 −0.2274 i
19 −0.7781 i

3
3 12 α + V22 + V11 + V00
5 0.5 i
6 −0.6325 V2M1
13 0.2112 i
14 −1.1181 i
16 0.25 i
18 0.3597 i
20 1.2303 i

4
4 12 α +1.4 V22 + V11 + +0.6 V00 +0.1666
5 0.6325 V2M1 +1.0541 i
7 −0.4899 V22 +0.4899 V00
12 0.9448
13 −0.6680 i
15 −0.1667
16 0.2635 i
17 −0.3033
18 −0.0758 i
19 −1.0374
20 −0.2594 i

5
5 12 α + V22 +2 V11 −0.3334
7 −0.7746 V2M1
12 0.2988 i
13 0.8453
15 −0.2635 i
16 0.3334
17 0.2398 i
18 −0.2398
19 0.8202 i
20 −0.8203

6
6 15 B + 2 α +0.4 V22 + 1.6 V11 + + V00
7 −0.4082 i
17 −0.9828 i
19 −0.4837 i
21 1.5272 i

7
7 15 B +12 α +1.6 V22 + V11 + +0.4 V00 +0.1666
17 0.8024
18 −0.8024 i
19 0.3950
20 −0.3949 i
21 1.2469

8
8 9 B +3 C +30 α +0.6476 V22 + +1.6095 V11 +0.7429 V00 + 0.4
9 −0.1260 V2M1 +0.5291 i
10 0.4363 V2M1
12 0.0143 V22 −0.4571 V11 + +0.4429 V00 +0.8
13 1.0801 V2M1 −0.3657 i
14 0.8015 V2M1
15 −0.6677 V22 +0.4032 V11 + +0.2646 V00
16 0.2191 V2M1
17 0.1105 V22 +0.4421 V11 + +0.3316 V00
18 −0.3867 V2M1
19 0.0879 V22 −0.3518 V11 + +0.2638 V00
20 −0.3078 V2M1
21 −0.0990 V22 +0.3958 V11 − −0.2969 V00

9
9 9 B +3 C +30 α +0.8667 V22 + +1.3333 V11 +0.8 V00 −0.2
11 −0.3651 V2M1
12 0.5667 V2M1 +1.0582 i
13 0.0534 V22 +0.5345 V11 − −0.5880 V00 +0.7483
15 −0.2332 V2M1
16 −0.5270 V22 +0.2108 V11 + +0.3162 V00
17 −0.7310 V2M1
18 −0.1460 V22 +0.5848 V11 − −0.4385 V00
19 −0.5817 V2M1
20 −0.1164 V22 +0.4653 V11 − −0.3491 V00
21 0.2618 V2M1

10
10 9 B +3 C +30 α +1.6 V22 + +0.8 V11 +0.6 V00 +0.4
11 −0.3162 i
12 −0.9817 V2M1
14 −0.4899 V22 +0.9798 V11 − −0.4899 V00 +0.4899
15 −0.0577 V2M1
17 −0.5063 V2M1
19 −0.4031 V2M1
21 −0.9068 V2M1

11
11 9 B +3 C +30 α +2 V22 + + V11 −0.5
13 −1.3171 V2M1
14 −1.5498 i
16 0.2886 V2M1
18 0.8008 V2M1
20 0.6374 V2M1

12
12 4 B +3 C +20 α +1.0429 V22 + +1.3429 V11 +0.6143 V00 +0.15
13 −0.1009 V2M1 −0.6363 i
14 0.2672 V2M1
15 0.2646 V22 −0.3024 V11 + +0.0378 V00 −0.4724
16 0.3585 V2M1 −0.2988 i
17 −0.5970 V22 +0.3315 V11 + +0.2655 V00
18 0.1981 V2M1
19 −0.1931 V22 +0.2638 V11 − −0.0707 V00
20 1.0037 V2M1
21 0.0742 V22 −0.2968 V11 + +0.2227 V00

13
13 4 B +3 C +20 α +1.1571 V22 + +1.1429 V11 +0.7 V00 −0.3
15 0.1603 V2M1 +0.6681 i
16 −0.4236 V22 +0.3381 V11 + +0.0845 V00 −0.4227
17 −0.2333 V2M1
18 −0.3755 V22 +0.0476 V11 + +0.3279 V00
19 −1.1827 V2M1
20 0.0999 V22 −0.7597 V11 + +0.6597 V00
21 −0.3672 V2M1

14
14 4 B +3 C +20 α +1.4 V22 + +1.2 V11 +0.4 V00 +0.6
15 −0.4241 V2M1
17 −0.2470 V2M1
19 −1.2519 V2M1
21 0.2777 V2M1

15
15 24 B +3 C +12 α +1.0333 V22 + +1.2667 V11 +0.7 V00 −0.0832
16 0.1053 V2M1 −0.2636 i
17 −0.4101 V22 −0.2924 V11 + +0.7025 V00 +0.7255
18 0.9948 V2M1 −0.3628 i
19 0.4198 V22 −0.2327 V11 − −0.1871 V00 +0.1795
20 0.0456 V2M1 −0.0898 i
21 0.1962 V22 +0.2618 V11 − −0.4582 V00

16
16 24 B +3C +12 α +1.1667 V22 + +1.3333 V11 +0.5 V00 +0.1667
17 0.3145 V2M1 +1.1472 i
18 0.9628 V22 −0.7961 V11 − −0.1669 V00 +0.5736
19 0.0144 V2M1 +0.3838 i
20 −0.6492 V22 +0.3102 V11 + +0.3390 V00 +0.1419
21 1.1382 V2M1

17
17 20 B +5 C +(193 B^2+8 BC + +4 C^2)$^{1/2}$+6 α +0.8642 V22 + 1.3207 V11 +0.8151 V00 − −0.1175
18 −0.1180 V2M1 +0.2351 i
19 0.0576 V22 +0.2552 V11 − −0.3128 V00 +0.3650
20 0.7100 V2M1 −0.7300 i
21 0.5742 V22 −0.2871 V11 − −0.2871 V00 +0.0125

18
18 20 B +5 C +(193 B^2+8 BC + +4 C^2)$^{1/2}$+6 α +1.8951 V22 + +0.8642 V11 +C.2406 V00 + +0.2352
19 0.7100 V2M1 +0.7300 i
20 −0.2573 V22 +0.0576 V11 + +0.1996 V00 −C.7300
21 −0.0230 i

19
19 20 B +5 C −(193 B^2+8 BC + +4 C^2)$^{1/2}$+6 α +1.3262 V22 + +1.2031 V11 +0.4706 V00 + +0.2843
20 0.1656 V2M1 −0.5686 i
21 0.4569 V22 −0.2285 V11 − −0.2285 V00 +0.9218

20
20 20 B +5 C −(193 B^2+8 BC + +4 C^2)$^{1/2}$+6 α +0.9144 V22 + +1.3262 V11 +0.7593 V00 − −0.5686
21 −1.8435 i

21
21 9 B +3 C +2 α +1.0854 V22 + +1.2567 V11 +C.6569 V00 + +0.3332

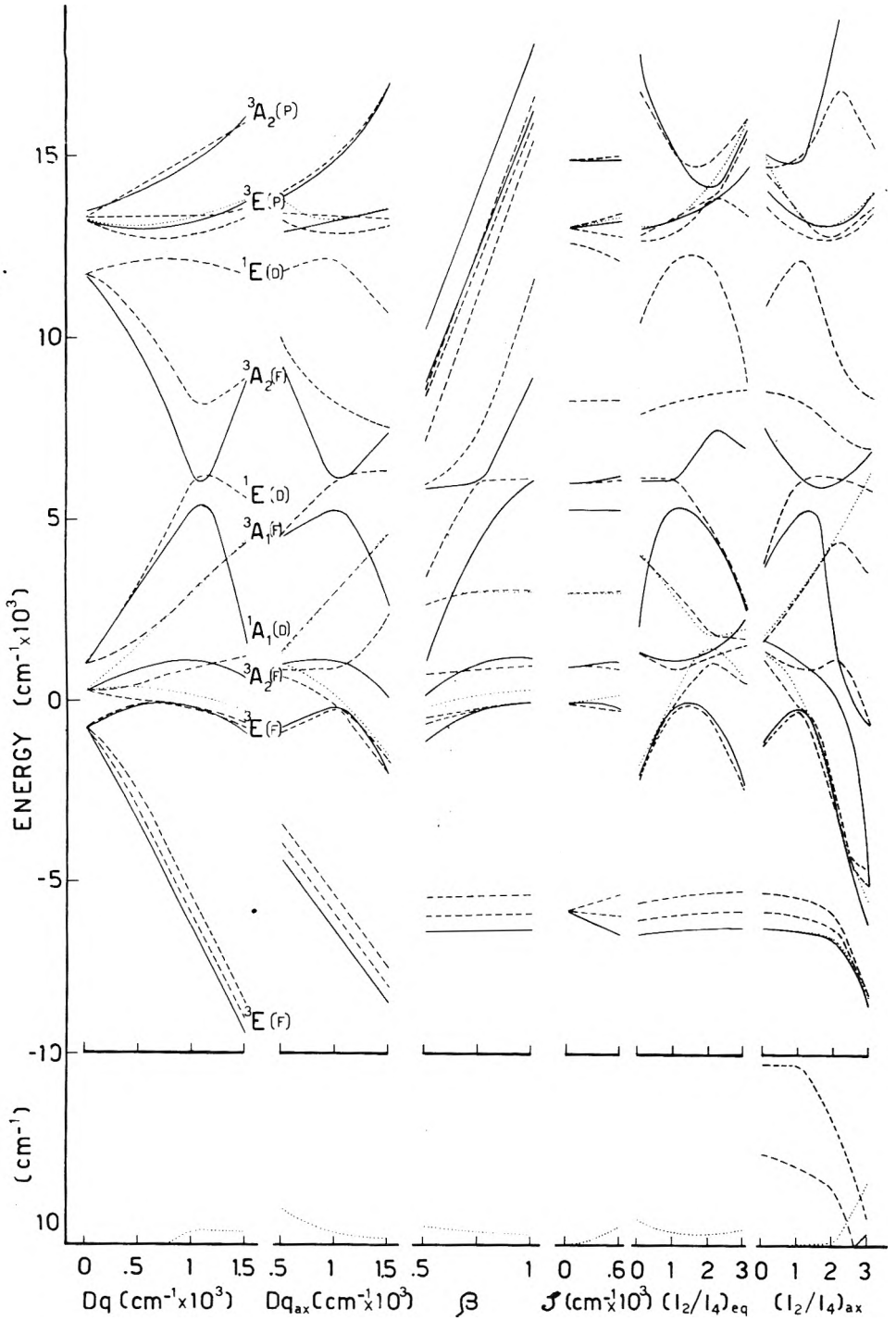

Figure 3. Energy level diagrams for a d^8 ion in a five coordinate chromophore of C_{3v} symmetry: (—) Γ_1 levels; (. . . .) Γ_2 levels; (- - - -) Γ_3 levels. Lower: Tanabe–Sugano type diagrams for the lowest energy levels. Upper left diagram: $Dq_{ax} = Dq_{eq}$; $\beta = B/B_0 = C/C_0 = 0.8$; $(I_2/I_4)_{ax} = (I_2/I_4)_{eq} = 1$; $\zeta = 500$ cm^{-1}; $\alpha = 70$ cm^{-1}. From the left to the right the effect of changing Dq_{ax}, β, ζ, $(I_2/I_4)_{eq}$, and $(I_2/I_4)_{ax}$ with $Dq_{eq} = 1000$ cm^{-1}. B and C as in ref 8, p 437.

The nonzero matrix elements of the perturbation matrices, calculated according to the illustrated procedure, are reported in Tables VI–VIII.[20] The electronic repulsion parameters appear only on the diagonal elements, according to the chosen formalism. The Trees correction has been considered in the form $\alpha L(L + 1)$.[1]

Energy Levels and Parameters

The C_{3v} matrices were checked by performing calculations with ligand configurations corresponding to T_d, O_h, and D_{3h} symmetries. In all cases a perfect agreement was found with the values previously reported.

Many five coordinate complexes are known for d^7, d^8, and d^9 ions, having actual or approximate C_{3v} symmetry,[11,12] and therefore we have performed our calculations for such ions. Many of these complexes show large deviations of the angle ϑ from 90°. We have chosen a value of 80° in order to show the effect of a large C_{3v} perturbation on the levels of D_{3h} symmetry.

In Figure 2 are reported the energy level diagrams for a d^9

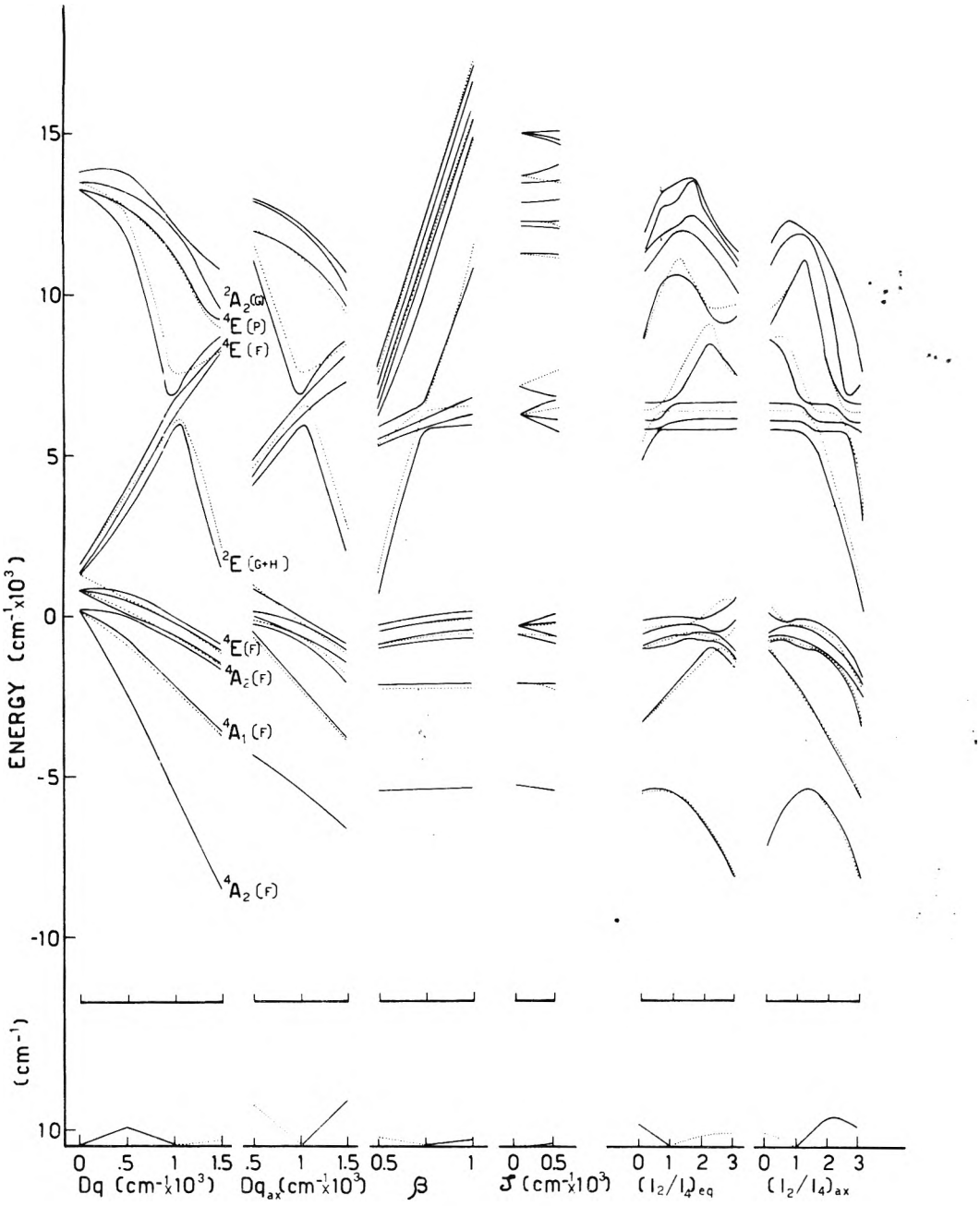

Figure 4. Energy level diagrams for a d^7 ion in a five coordinate chromophore of C_{3v} symmetry: (—) Γ_4 levels; (. . . .) Γ_5 levels. Lower: Tanabe-Sugano type diagrams for the lowest energy levels. Upper left diagram: $Dq_{ax} = Dq_{eq}$; $(I_2/I_4)_{ax} = (I_2/I_4)_{eq} = 1$; $\beta = B/B_0 = C/C_0 = 0.8$; $\zeta = 420$ cm^{-1}; $\alpha = 70$ cm^{-1}. From the left to the right the effect of changing Dq_{ax}, β, ζ, $(I_2/I_4)_{eq}$, and $(I_2/I_4)_{ax}$ with $Dq_{eq} = 1000$ cm^{-1}. B and C as in ref 8, p 437.

ion. The first diagram is calculated for five equivalent ligands, and the other ones correspond to a change of one parameter at a time, as indicated. The parameters reported are those of the crystal field formalism. The most dramatic effects are determined by the variation of the ratio between the quadratic and quartic radial integrals, (I_2/I_4),[26] which can also cause a change in the ground level. Further, the effect of varying such a parameter for the axial ligands is largely counterbalanced by the effect of varying the same parameter for the equatorial ligands. As a result the effect of changing both of them at the same time and of the same amount is very small. These results point out the necessity to design experiments which can allow the determination of the radial integral ratios (or conversely the e_σ'/e_π' ratios of the angular overlap model) and cast many doubts on the values of the parameters obtained by making guesses of the I_2/I_4 ratios.

In Figure 3 are reported the energy level diagrams for a d^8 ion. Again we observe a strong dependence of many levels on the I_2/I_4 ratios. The ground orbital level is in the present case ^3E, and it is split by spin–orbit coupling in such a way that in general Γ_1 state is the lowest in energy, Γ_2 being quite close to it. The variations of the $(I_2/I_4)_{ax}$ ratio can alter dramatically this pattern, allowing also a Γ_3 ground level.

In Figure 4 are reported the energy level diagrams for a d^7 ion. Also in this case the same considerations hold as for the previous diagrams. In the present case the spin–orbit split

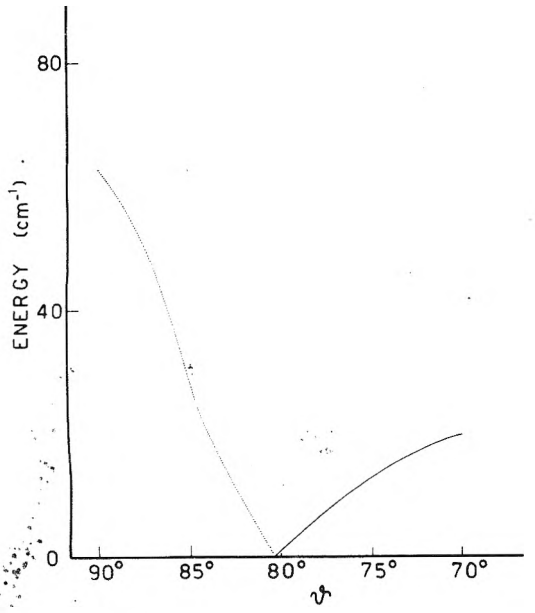

Figure 5. The dependence on the angle ϑ of the ground state for a d^7 ion in a five coordinate chromophore.

levels of the ground $^4A_2$ term are Γ_4 and $\Gamma_5 + \Gamma_6$. Which of them has lower energy depends fundamentally on the energy difference between the excited $^4A_2$ and $^4A_1$ ($^4A_2''$ and $^4A_1''$ of D_{3h} symmetry) and the ground term. In fact in C_{3v} symmetry the ground $^4A_2$ term is represented by a linear combination of functions having M_L equal to 0 and ± 3.

The latter component has matrix elements of $\mathcal{H}_{so}$ different from zero with $^4A_1$, a fact which is not operative in D_{3h} symmetry, and had not been previously appreciated for C_{3v} symmetry, where only simplified second-order spin–orbit coupling arguments had been used.[28-31] Further the coupling with the $^4A_1$ term is greater for the Γ_5 level than for the Γ_4 one ($(3i/2)\zeta$ and $(i/2)\zeta$ in absolute value, respectively), then the stabilization of the Γ_5 ($^4A_2$) level with respect to the Γ_4 ($^4A_2$) one increases as the mixing of the excited $^4A_2$ term with the ground $^4A_2$ term increases. The admixture of the two $^4A_2$ terms into the ground level is determined by the value of ϑ and, as it is shown in Figure 5, as ϑ is lowered from the value of 90° the energy separation between Γ_4 and $\Gamma_5 + \Gamma_6$ states decreases, until finally a cross over occurs.

The present results show, therefore, how it is necessary to make use of complete matrices in order to evaluate the properties, such as magnetic moments, **g** tensors, *etc.*, which depend largely on the nature of the ground level. In fact for low symmetry complexes the parameters required are many and to fix arbitrarily some of them is dangerous. Diagrams of the type of Figures 2–5 are therefore the best means of investigating the effect of the parameters, and sample calculations based on an insufficient number of experimental data are to be considered meaningless.

Acknowledgment. Thanks are due to Professor L. Sacconi, for his encouragement in the present work and to Professor I. Bertini for helpful discussions.

Supplementary and Miniprint Material Available: Table I, reporting the symmetry classification of the LM_L functions, Tables II–IV, reporting the basis functions for d^1, d^2, and d^3 ions in C_{3v} symmetry (3 pages), and full-size copies of Tables V–VIII (6 pages). Ordering information is available on any current masthead page.

References and Notes

(1) J. Ferguson, *Prog. Inorg. Chem.*, **12**, 159 (1970).
(2) N. S. Hush and R. J. M. Hobbs, *Prog. Inorg. Chem.*, **10**, 259 (1968).
(3) See, for instance, D. J. Hamm and A. F. Schreiner, *Inorg. Chem.*, **14**, 519 (1975); M. J. Harding and B. Briat, *Mol. Phys.*, **27**, 1153 (1974); J. C. Collingwood, P. Day, R. G. Denning, P. N. Quested, and T. R. Snellgrove, *J. Phys.* **E7**, 991 (1974); J. Ferguson, H. J. Guggenheim, and E. R. Krausz, *Mol. Phys.*, **27**, 577 (1974).
(4) B. McGarvey, *Transition Metal Chem.*, **3**, 90 (1966).
(5) T. F. Yen, Ed., "Electron Spin Resonance of Metal Complexes", Hilger, London, 1969.
(6) K. D. J. Root and M. T. Rogers, *Spectrosc. Inorg. Chem.*, **2**, 116 (1971).
(7) B. A. Goodman and J. B. Raynor, *Adv. Inorg. Chem. Radiochem.*, **13**, 242 (1971).
(8) J. S. Griffith, "The Theory of Transition-Metal Ions", University Press, Cambridge, 1961.
(9) J. Ferguson, *Aust. J. Chem.*, **23**, 635 (1970).
(10) A. D. Liehr and C. J. Ballhausen, *Ann. Phys.*, **6**, 174 (1959).
(11) P. L. Orioli, *Coord. Chem. Rev.*, **6**, 285 (1971).
(12) R. Morassi, I. Bertini, and L. Sacconi, *Coord. Chem. Rev.*, **13**, 343 (1973); L. Sacconi, *ibid.*, **8**, 351 (1972).
(13) J. S. Wood, *Prog. Inorg. Chem.*, **16**, 227 (1972).
(14) M. J. Norgett, J. H. M. Thornley, and L. M. Venanzi, *J. Chem. Soc. A*, 540 (1967).
(15) C. A. L. Becker, D. W. Meek, and T. M. Dunn, *J. Phys. Chem.*, **72**, 3588 (1968).
(16) C. A. L. Becker, D. W. Meek, and T. M. Dunn, *J. Phys. Chem.*, **74**, 1568 (1970).
(17) J. C. Slater, "Quantum Theory of Atomic Structure", Vol. II, McGraw-Hill, New York, N.Y., 1960.
(18) For d^3 ions the fractional parentage coefficients of Racah (G. Racah, *Phys. Rev.*, **63**, 367 (1943)) were used.
(19) Owing to the intrinsic parity of the LS basis functions this operation is equivalent to a rotation by π around y axis, $C_2(y)$.
(20) See paragraph at end of text regarding supplementary material.
(21) The spin function bases for the irreducible representations of C_{3v}* are reported in ref 22. In this reference the basis function for Γ_6 must be read $-(\phi(3/2, 3/2) - i\phi(3/2, -3/2))$. As it is easy to verify by inspection, the $+1/2$ and $-1/2$ components of Γ_4 originating from $S = 3/2$ spin states are respectively $-|3/2, 1/2\rangle$ and $|3/2, -1/2\rangle$.
(22) G. F. Koster, J. O. Dimmock, R. G. Wheeler, and H. Statz, "Properties of the Thirty-Two Point Groups", MIT Press, Cambridge, Mass., 1963.
(23) C. E. Schäffer, *Pure Appl. Chem.*, **24**, 361 (1970).
(24) S. E. Harnung and C. E. Schäffer, *Structure Bonding*, **12**, 257 (1972).
(25) C. E. Schäffer, *Structure Bonding*, **14**, 69 (1973).
(26) I. Bertini, D. Gatteschi, and A. Scozzafava, *Inorg. Chem.*, **14**, 812 (1975).
(27) I. Bertini, P. Dapporto, D. Gatteschi, and A. Scozzafava, *Inorg. Chem.*, **14**, 1639 (1975).
(28) J. S. Wood, *Inorg. Chem.*, **7**, 852 (1968).
(29) J. S. Wood and P. T. Greene, *Inorg. Chem.*, **8**, 491 (1969).
(30) J. S. Wood, *J. Chem. Soc. A*, 1582 (1969).
(31) D. M. Duggan and D. N. Hendrickson, *Inorg. Chem.*, **14**, 1944 (1975).

The Crystal Structure of Zinc-Exchanged Potassium Zeolite A, Zn_5K_2-A, Evacuated at 400 °C

N. V. Raghavan and Karl Seff*

Department of Chemistry, University of Hawaii, Honolulu, Hawaii 96822 *(Received January 15, 1976; Revised Manuscript Received June 28, 1976)*

Publication costs assisted by the Petroleum Research Fund
Publication costs assisted by

Fully K^+-exchanged zeolite A was five-sixths exchanged with Zn^{2+} and evacuated at 400 °C. The structure of a single crystal of this material, $Zn_{0.83}K_{0.17}[AlSiO_4]$-A·$0.29H_2O$, stoichiometry $Zn_5K_2Al_{12}Si_{12}O_{48}$·$3.5H_2O$ per unit cell, was determined using three-dimensional x-ray diffraction data gathered by counter methods, and was solved and refined in the cubic space group $Pm3m$; a = 12.075(2) Å. The five Zn^{2+} ions per unit cell occupy three nonequivalent positions, all on the unit cell threefold axes, near the centers of 6-rings. Of these ions, 1.5 lie very close to their 6-ring planes and have trigonal-planar three coordination. The remaining 3.5 ions are either recessed into the sodalite unit (1.0 Zn^{2+} ion, the maximum number by packing considerations involving coordinated H_2O or OH^-), or into the large cavity (2.5 Zn^{2+} ions). Each of these 3.5 ions is associated with one water molecule or hydroxide ion, which is recessed further into the corresponding cavity, to complete an approximately tetrahedral coordination sphere. The reaction $Zn^{2+} + H_2O \rightarrow ZnOH^+ + H^+$ is indicated by the tenacity with which (former) water molecules are held. This is in contrast to the results of similar experiments involving Mn^{2+} and Co^{2+}, where all water molecules were removed at 350 °C. The K^+ ions show a distinct preference for 8-ring sites (one in the 8-ring plane, and the other near that plane), despite the presence and ready availability of vacant 6-ring sites. Approximately one K^+ ion lies off the 8-ring plane because of the asymmetric distribution of nearest Zn^{2+} ions. Residual water molecules, or H^+ and $ZnOH^+$ ions, and the three-coordinate Zn^{2+} ions, may provide chemical mechanisms for selective sorption by reacting with components of the mixture. H-containing species are a source of Brönsted acidity, and the three-coordinate Zn^{2+} ions are coordinatively unsaturated.

Introduction

A plateau in the exchange isotherm of Zn^{2+} for K^+ in zeolite A was noted by Takaishi et al.[1] It is further reported[2] that $K_{12-2x}Zn_x$-A ($2 \leq x \leq 4$) activated at 400 °C effectively sorbs trace amounts of the principal impurity, PH_3, from SiH_4. The silane thus obtained can be used in the preparation of silicon of semiconductor purity. It is proposed that this is due to the partial blocking of the large pores of the zeolite by K^+ ions. The crystal structure of potassium- and zinc-exchanged zeolite A was investigated to observe the geometry of the "partial blockage" of the large pores by K^+ ions, and to provide a model from which intracrystalline diffusion rates could be estimated. Unfortunately, the composition of the structure reported here differs from that most effective for sorbing trace amounts of PH_3.

General discussions of the structure of zeolite A and of the terms used in its description are available.[3-5] The two former references are too the first reports of the synthesis[3] and structure[4] of this zeolite.

Experimental Section

Crystals of K-A were obtained from zeolite 4A, Na-A, by complete ion-exchange with 0.2 N aqueous KOH solution.[6] Approximately 0.1 g of K-A was allowed to exchange at 80 ± 5 °C with 100 ml of an aqueous solution 0.05 N in $ZnCl_2$ and 0.15 N in KCl. The ion exchange was carried out for a period of 6 days with daily agitation and renewal of solution. This procedure yielded clear colorless crystals.

A crystal 0.08 mm on an edge was dehydrated by a procedure[5] similar to that used for dehydrating zeolite 4A. The Pyrex capillary containing the crystal was sealed off by torch under vacuum after 44 h of dehydration at 400 °C and 10^{-6} Torr, and was mounted on a goniometer head. The zeolite has the formal name[7] $Zn_{0.83}K_{0.17}[AlSiO_4]$-A·$0.29H_2O$, with a unit cell composition of $Zn_5K_2Al_{12}Si_{12}O_{48}$·$3.5H_2O$, and will subsequently be referred to as Zn_5K_2-A.

The cubic space group $Pm3m$ (no systematic absences) appeared to be appropriate.[5,8-10] A Syntex four-circle computer-controlled diffractometer with a graphite monochromator and a pulse-height analyzer was used throughout for preliminary experiments and for the collection of diffraction intensities. Molybdenum radiation ($K\alpha_1$, λ = 0.709 30 Å; $K\alpha_2$, λ = 0.713 59 Å) was used. The cell constant, a = 12.075(2) Å, was determined by a least-squares treatment of 15 intense reflections for which $2\theta < 24°$ using $K\bar{\alpha}$, λ = 0.710 73 Å.

Reflections from two intensity equivalent regions of reciprocal space (hkl, $h \leq k \leq l$ and lhk, $l \leq h \leq k$) were examined analogously using the θ-2θ scan technique. Each reflection was scanned at a constant rate of 1.0° min^{-1} over a symmetric range from 1° (in 2θ) below the calculated $K\alpha_1$ peak to 1° above $K\alpha_2$ maximum. Background intensity was counted at each end of a scan range for a time equal to half the time required to measure the reflection. The intensities of three reflections in diverse regions of reciprocal space were recorded after every 100 reflections to monitor crystal and instrumental stability. Only small, random fluctuations of these check reflections were noted during the course of data collection. For each region of reciprocal space the intensities of all lattice points for which $2\theta < 70°$ were recorded.

The raw data from each region were corrected for Lorentz and polarization effects; the reduced intensities were merged; and the resultant estimated standard deviations were assigned for each averaged reflection by the computer program COM-

PARE.[11] The mean intensity for a reflection was calculated as

$$I = (I_{hkl} + I_{lhk})/2$$

where

$$I_{hkl} = [\mathrm{CT} - 0.5(t_c/t_b)(B_1 + B_2)](\omega)$$

CT is the total integrated count obtained in a scan time t_c, B_1 and B_2 are the background counts each measured in time t_b, and ω is the scan rate. The standard deviation of I is

$$\sigma(I) = (\sigma^2(I_{hkl}) + \sigma^2(I_{lhk}))^{1/2}/2$$

and the standard deviation of each unmerged reflection is

$$\sigma(I_{hkl}) = [(\mathrm{CT} + B_1 + B_2)\omega^2 + (pI_{hkl})^2]^{1/2}$$

The value of p was taken as 0.02,[12] a value found to be appropriate for the instrumentation used. No absorption correction was applied to the data.

A reflection was used in structural analysis only when all of the following conditions were fulfilled

$$(|I_{hkl} - I_{lhk}|/\sigma(I)) < 10.0 \quad (1)$$

$$(|I_{hkl} - I_{lhk}|/|I_{hkl} + I_{lhk}|) < 0.25 \quad (2)$$

$$(|B_1 - B_2|/|B_1 + B_2|) < 0.3 \quad (3)$$

for each reflection before merging, and

$$I_0 > 3.0\sigma(I_0) \quad (4)$$

for merged intensities.[13] If one of a pair of equivalent reflections was not measured, then the reflection was omitted from the data set. Of the 846 pairs of reflections examined, only those 244 which satisfied all of these conditions were used in further calculations. (All 244 diffraction intensities are available as supplementary material. See paragraph at end of text regarding supplementary material.)

Structure Determination

Full-matrix least-squares refinement was commenced using the zeolite framework ((Si,Al), O(1), O(2), and O(3); see Figures 1 and 2) atomic parameters of dehydrated K-A.[6] (Because of the indistinguishability of SiO_4 and AlO_4 tetrahedra, only the average species, (Si,Al), is considered in this work.) From a subsequent difference Fourier function, 4.5 Zn^{2+} ions were located, 2.0 at $x = y = z = 0.14$ and 2.5 at $x = y = z = 0.22$. Inclusion of these positions in isotropic least-squares refinement led to convergence with error indices

$$R_1 = \Sigma||F_o| - |F_c||/\Sigma|F_o| = 0.16$$

and

$$R_2 = (\Sigma w(|F_o| - |F_c|)^2/\Sigma w F_o^2)^{1/2} = 0.16$$

In the least-squares treatment, the quantity minimized is $(\Sigma w(|F_o| - |F_c|)^2)$ and the weights (w) are the reciprocal squares of $\sigma(F_o)$, the estimated standard deviation of each observation. Atomic scattering factors for O^- and $(Si,Al)^{1.75+}$ for the zeolite framework,[14] Zn^{2+} and K^+ for the exchangeable cations, and O^0 for H_2O or OH^- oxygen atoms were used.[15] (The function describing $(Si,Al)^{1.75+}$ is the mean of the Si^0, Si^{4+}, Al^0, and Al^{3+} scattering functions.) The scattering factors for $(Si,Al)^{1.75+}$ and Zn^{2+} were modified to account for the real parts ($\Delta f'$) of the anomalous dispersion correction.[16]

The thermal parameter on Zn(1) remained high (8.0 $Å^2$). An inspection of the electron density function indicated another peak at $x = y = z = 0.18$. Inclusion of this position and alternate refinement of occupancy and thermal parameters for the three different Zn^{2+} positions led to the values shown in Table I.

A difference Fourier synthesis using framework atomic and Zn^{2+} positions indicated a variety of positions which could be attributed to K^+ ions and H_2O or OH^-. The most significant of these had densities between 1.0 and 4.0 e $Å^{-3}$.

Several criteria were to be fulfilled before the conclusions suggested by the subsequent least-squares were accepted. First, the peaks were to refine close to their initially estimated positions. Also the occupancies of these sites should be chemically meaningful, and the corresponding thermal parameters should be realistic. Finally, the resultant positions should make suitable approaches to well-established parts of the structure (e.g., framework atoms, exchangeable ions, or water molecules).

Application of these criteria resulted in the acceptance of a few positions. Two and one-half oxygen atoms ($H_2O(3)$'s, see Table I), each of which completes a nearly regular tetrahedron about a Zn(3) ion, were located in the large cage (see Figures 1 (right) and 2). One oxygen ($H_2O(1)$) which completes a similar tetrahedron about the Zn(1) ion was located in the small cage (Figures 1 (left) and 2). The K^+ ions (K(1) and K(2)) were located at 8-ring sites.

In the least-squares refinement, the framework atoms were treated anisotropically and all remaining species in Table I were treated isotropically. Convergence was attained with $R_1 = 0.075$, $R_2 = 0.060$, and a goodness-of-fit, $(\Sigma w(F_o - |F_c|)^2/(m - s))^{1/2}$ of 3.06 where $m(244)$ is the number of observations and $s(36)$ is the number of variables in least-squares refinement. In this final cycle of refinement, shifts in positional and thermal parameters were all less than 0.5% of their corresponding estimated standard deviations.

A final difference Fourier function, with an estimated standard deviation of 0.1 e $Å^{-3}$, showed a few small, shallow peaks of density ca. 1.0 e $Å^{-3}$, either too close or too far from established portions of the structure; these are thus not regarded as meaningful structural features. In addition, a peak of height 2.2 e $Å^{-3}$ appeared at the unit cell origin. This peak has been noted in other zeolite structures.[10,17,18] Final positional, thermal, and occupancy parameters are presented in Table I. Bond lengths and bond angles are given in Table II.

Discussion

The five Zn^{2+} ions occupy three kinds of sites in this partially hydrated structure. All three equipoints are on the threefold axes, two on opposite sides of the 6-oxygen windows and one close to the O(3) plane of such a window.

The one Zn^{2+} ion in the sodalite unit, at Zn(1), is coordinated to an oxygen atom of a water molecule or OH^- ion, $H_2O(1)$ (see Figures 1 and 2), with a Zn^{2+}-to-oxygen distance of 2.2(1) Å. The Zn(1) ion is recessed 0.59 Å (Table III) into the sodalite unit from the (111) plane at O(3) with Zn(1)–O(3) distances of 2.19(1) Å. The O(3)–Zn(1)–O(3) angles are 113.0° (7), not far from tetrahedral.

One and one-half Zn^{2+} ions, at Zn(2) (see Figures 1 and 2), are located only 0.20 Å from the (111) plane at O(3), and are coordinated to three O(3)'s with Zn(2)–O(3) distances of 2.12(1) Å. The O(3)–Zn(2)–O(3) angle of 119.1° (9) indicates that Zn(2) has achieved approximate trigonal-planar coordination.

Two and one-half Zn^{2+} ions, at Zn(3) (see Figures 1 and 2), are located 0.91 Å into the large cage from the (111) plane at O(3), with Zn(3)–O(3) distances of 2.30(1) Å and O(3)–

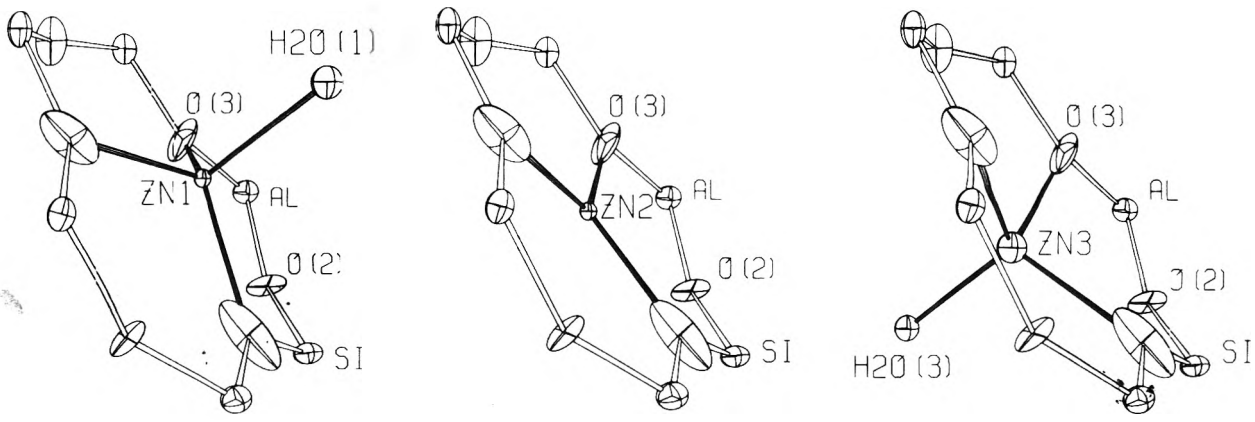

Figure 1. The sitings of the three nonequivalent Zn^{2+} ions, each in its respective 6-ring, are shown.[11] Zn(1) and $H_2O(1)$ in the left-hand view extend into the sodalite unit, and Zn(3) and $H_2O(3)$ in the right-hand view extend into the large cavity. (The positions $H_2O(1)$ and $H_2O(3)$ indicate where oxygen atoms have been located. The number of associated hydrogens is inferred by chemical reasoning. As discussed in the text, the coordinated species is likely to be OH^-; that is, the coordinated H_2O is likely to have dissociated.) The center view shows the three-coordinate triconal-planar Zn^{2+} ion at Zn(2). Ellipsoids of 50% probability are used.

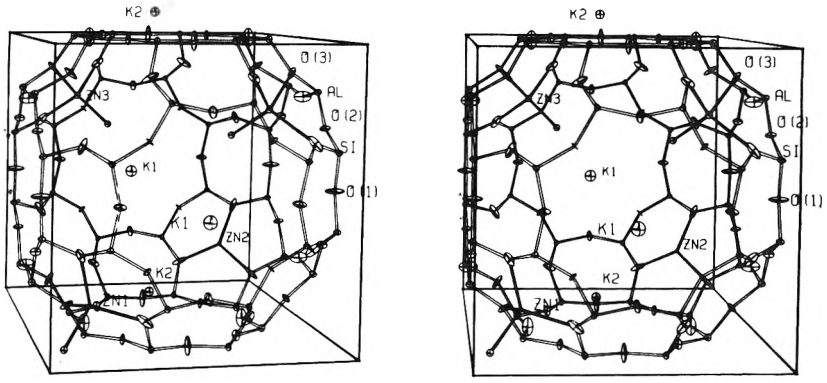

Figure 2. A stereoview of the unit cell is shown[11] with cations placed statistically within their equipoints so as to avoid unrealistically close intercationic approaches. The K^+ ions occupy four of the six 8-rings shown. Ellipsoids of 20% probability are used.

TABLE I: Positional, Thermal ($\times 10^4$), and Occupancy Parameters for Zn_5K_2-A[a]

	Wyckoff position	x	y	z	β_{11} or B_{iso}	β_{22}	β_{33}	β_{12}	β_{13}	β_{23}	Occupancy factor
(Si,Al)	24(*k*)	0	0.1833(3)	0.3684(3)	30(3)	21(3)	15(3)	0	0	5(4)	1[b]
O(1)	12(*h*)	0	0.2111(11)	½	214(23)	70(16)	13(10)	0	0	0	1
O(2)	12(*i*)	0	0.3012(6)	0.3012(6)	68(13)	20(6)	20(6)	0	0	39(16)	1
O(3)	24(*m*)	0.1140(5)	0.1140(5)	0.3279(7)	63(6)	63(6)	114(12)	103(16)	−112(13)	−112(13)	1
Zn(1)	8(*g*)	0.1571(10)	0.1571(10)	0.1571(10)	0.5(3)[c]						1/8
Zn(2)	8(*g*)	0.1948(8)	0.1948(8)	0.1948(8)	0.5(3)						3/16
Zn(3)	8(*g*)	0.2286(5)	0.2286(5)	0.2286(5)	1.6(2)						5/16
K(1)	12(*h*)	0	0.4484(51)	½	5(2)						1/12
K(2)	24(*m*)	0.0925(59)	0.4580(37)	0.4580(37)	3(1)						1/24
$H_2O(1)$	8(*g*)	0.0532(60)	0.0532(60)	0.0532(60)	7(7)						1/8
$H_2O(3)$	8(*g*)	0.3247(22)	0.3247(22)	0.3247(22)	1(1)						5/16

[a] Standard deviations are in the units of the least significant digit given for the corresponding parameter. The anisotropic temperature factor is $\exp[-(\beta_{11}h^2 + \beta_{22}k^2 + \beta_{33}l^2 + \beta_{12}hk + \beta_{13}hl + \beta_{23}kl)]$. [b] Occupancy for (Si) = ½; Occupancy for Al = ½. [c] Isotropic thermal parameter in units of Å^2.

Zn(3)–O(3) angles of 105.4° (6). The approximate tetrahedral coordination about each Zn(3) is completed by an oxygen atom of a water molecule or of a hydroxide ion, $H_2O(3)$, which is located farther into the large cage along a threefold axis, with a Zn(3)–$H_2O(3)$ distance of 2.01(5) Å and $H_2O(3)$–Zn(3)–O(3) angles of 113° (1).

The geometries about the Zn^{2+} ions reported herein are comparable to those observed in Zn_5Na_2-A·4H_2O,[19] which had been evacuated at 350 °C.

It is now clear that Zn^{2+} ions exchanged into zeolite A tend to hold coordinated water oxygen atoms (presumably as H_2O or OH^-) much more tenaciously than Mn^{2+} [10,18] or Co^{2+},[17]

TABLE II: Interatomic Distances (Å) and Angles (deg)[a]

Distances	
(Si,Al)-O(1)	1.624(4)
(Si,Al)-O(2)	1.639(5)
(Si,Al)-O(3)	1.684(4)
Zn(1)-O(3)	2.190(11)
Zn(2)-O(3)	2.118(9)
Zn(3)-O(3)	2.295(10)
Zn(1)-H_2O(1)	2.2(1)
Zn(3)-H_2O(3)	2.01(5)
K(1)-O(1)	2.87(6)
K(1)-O(2)	2.99(4)
K(1)···O(1)	3.54(2)
K(2)-O(1)	3.22(4)
K(2)-O(2)	2.90(6)
K(2)···O(2)	3.64(3)
Angles	
O(1)-(Si,Al)-O(2)	107.8(4)
O(1)-(Si,Al)-O(3)	112.8(3)
O(2)-(Si,Al)-O(3)	106.7(4)
O(3)-(Si,Al)-O(3)	109.7(6)
(Si,Al)-O(1)-(Si,Al)	156.1(10)
(Si,Al)-O(2)-(Si,Al)	149.4(7)
(Si,Al)-O(3)-(Si,Al)	136.7(6)
O(3)-Zn(1)-O(3)	113.0(7)
O(3)-Zn(1)-H_2O(1)	105.6(31)
O(3)-Zn(2)-O(3)	119.1(9)
O(3)-Zn(3)-O(3)	105.4(6)
O(3)-Zn(3)-H_2O(3)	113.3(14)
O(1)-K(1)-O(1)	100.1(12)
O(2)-K(1)-O(2)	107.0(10)
O(1)-K(1)-O(2)	53.5(8)
O(1)-K(2)-O(1)	99.8(13)
O(2)-K(2)-O(2)	93.6(15)
O(1)-K(2)-O(2)	50.6(8)

[a] The identities of the atoms can be seen in Figures 1 and 2. Numbers in parentheses are the estimated standard deviations in the units of the least significant digit given for the corresponding parameter.

TABLE III: Deviations (Å) of Atoms from the (111) Plane at O(3)[a]

Zn(1)	−0.59(2)	Zn(3)	0.91(2)
Zn(2)	0.20(2)	O(2)	0.32(2)

[a] A negative deviation indicates that the atom lies on the same side of the plane as the origin. Numbers in parentheses are the estimated standard deviations in the units of the least significant digit given for the corresponding parameter. See Figure 1 for the identities of the atoms.

after evacuation at elevated temperatures. The Zn_5Na_2-A structure was dehydrated under vacuum at 350 and 430 °C,[19] and nonframework oxygen atoms were found coordinated to Zn^{2+} in these structures also. Zeolite A partially exchanged with Mn^{2+} or Co^{2+} has been found by similar methods to be fully dehydrated after evacuation at 350 °C—somewhat lower temperatures would have sufficed. The latter results have been verified in subsequent experiments in which small molecules other than water have been added to the dehydrated zeolites; the structures of the resulting complexes[10] reaffirmed the absence of water. This effect is not consistent with the ionic radii[20] of these cations: Co^{2+}, 0.72 Å; Zn^{2+}, 0.74 Å; Mn^{2+}, 0.80 Å. It is consistent, however, with a cation hydrolysis process[21] by which H_2O dissociates to give OH^- coordinated to Zn^{2+} and zeolitic H^+. It appears that near-tetrahedral $ZnOH^+$ is more stable than similarly coordinated $MnOH^+$ or $CoOH^+$. This follows, in fact, as a consequence of the amphoteric properties of Zn^{2+}; water coordinated to Zn^{2+} is much more acidic than H_2O coordinated to Mn^{2+} or Co^{2+}.

It is reasonable that an exchange plateau[1] should be encountered at an exchangeable cation stoichiometry of Zn_5K_2. The structure of hydrated Zn_5Na_2-A[19] (approximate composition) revealed the presence of one tetrahydrated Zn^{2+} ion at the center of the sodalite unit. These four water molecules extend toward four tetrahedrally placed sodalite-unit 6-rings, making them less suitable as Zn^{2+} sites. The remaining four Zn^{2+} ions were located at the remaining four 6-ring sites in hydrated Zn_5Na_2-A, and would be expected to be at such sites, arranged tetrahedrally, in hydrated Zn_5K_2-A. A sixth Zn^{2+} ion which might enter the unit cell would be required to occupy a less suitable site than the previous 5, and some reluctance for it to do so, as indicated by the observed exchange plateau, is reasonable.

The preferred position for a monohydrated (or monohydroxylated) tetrahedrally coordinated 6-ring Zn^{2+} ion appears to be at Zn(1) in the sodalite unit. That position can be considered filled in a chemical sense, because adding another such ion would require an oxygen–oxygen approach distance through the center of the sodalite unit of 2.2 Å, or less if not through the center. The remaining monohydrated (or monohydroxylated) ions can occupy large cavity 6-ring sites without close oxygen–oxygen contacts. Apparently, the dehydration procedures employed were able to remove the water molecules from 1.5 of the 4.0 (at an intermediate stage) monohydrated (or monohydroxylated) Zn^{2+} ions at Zn(3), to give 1.5 three-coordinate Zn^{2+} ions per unit cell at Zn(2).

The two K^+ ions are associated with 8-rings of the zeolite framework. One ion, at K(1), lies in the plane of the 8-ring (see Figure 2), and the other, at K(2), is approximately 1.0 Å from the plane of another 8-ring. The K^+ ion at K(1) is in contact with one O(1) and two adjacent O(2)'s with distances of 2.87(6) and 2.99(4) Å, respectively. The other K^+ ion, at K(2), is in contact with O(2) at 2.90(6) Å, but is a greater distance, 3.23(4) Å, from two O(1) ions.

Two of the three large pores (8-rings) in this exchanged form of zeolite A are thus at least partially blocked by the K^+ ions. It is also indicated by this structure determination that the Zn^{2+} ions are responsible for the modified K^+ positions. Four 6-rings can be seen, in Figure 2, to share an edge with any 8-ring. Because the plane of the 8-ring is a mirror plane of the framework structure (assuming Si = Al), four additional 6-rings share edges with each 8-ring. Altogether, eight 6-rings, coincidently the number of 6-rings per unit cell, are associated with each 8-ring, and are arranged with full tetragonal symmetry about it. When five Zn^{2+} ions are distributed among these eight 6-rings, the most likely arrangements of divalent cations about each 8-ring are entirely asymmetric. (This assumes that distributions which locate six Zn^{2+} ions in some unit cells, and four in others, are disfavored.) A K^+ ion associated with an 8-ring must, then, be in an asymmetric electric field, and is likely to be displaced from the plane of the 8-ring, as the ion at K(2) is.

The standard deviations of the thermal and associated occupancy parameters of the K^+ positions are large, and consistent with the discussion of the previous paragraph. Other positions close to those reported may also be present at lower

occupancy, at the expense of the K^+ occupancies given, to preserve the total of approximately two per unit cell.

Only a single O(3) position is located, even though four chemically different 6-rings have been found: five 6-rings contain Zn^{2+} ions of three different kinds, and three are empty. The O(3) thermal ellipsoid is unusually elongated, as can be seen in the figures, principally along a Zn–O(3) direction, as though to average over a different O(3) positions. Accordingly, it is likely that all distances and angles involving O(3) are somewhat inaccurate. The probable averaging of O(3) positions does not obscure the result (see Table II) that the (Si,Al)–O(3) bond length is longer than the (Si,Al)–O(1) or (Si,Al)–O(2) distances, a result of O(3) coordination to Zn^{2+}. This effect has been reported and discussed in other zeolite systems.[22,23]

A molecule of PH_3 entering this zeolite is likely either to react with a coordinated H_2O to give coordinated OH^- and a PH_4^+ cation; or, if the water has already dissociated, to react with a zeolitic H^+ to give a PH_4^+ cation; or to react with $ZnOH^+$ to give ZnO and PH_4^+. A suitable 6-ring lattice site for PH_4^+ is available. PH_3 might also coordinate to a three-coordinate Zn^{2+} ion, which is also available in the structure, to relieve its severe coordinative unsaturation. These chemical processes are likely to be important in accounting for the selectivity of this zeolite for PH_3 over SiH_4, although higher selectivities, explicable by percolation theory and a sieving process,[1,2] can be found using $K_{12-2x}Zn_{2x}$-A, where $2 \leq x \leq 4$.

Acknowledgments. Acknowledgment is made to the Donors of The Petroleum Research Fund, administered by the American Chemical Society, for the support of this research. We are also indebted to the University of Hawaii Computing Center.

Supplementary Material Available: Listing of the observed and calculated structure factors (supplementary Table I, 2 pages). Ordering information is available on any current masthead page.

References and Notes

(1) T. Takaishi, Y. Yatsurugi, A. Yusa, and T. Kuratomi, *J. Chem. Soc., Faraday Trans. 1*, **71**, 97 (1975).
(2) (a) T. Takaishi, A. Yusa, and Y. Yatsurugi, "Proceedings of the 3rd International Conference on Molecular Sieves", Leuven University Press, Belgium, 1975; p 246; (b) A. Yusa, Y. Yatsurugi, and T. Takaishi, *J. Electrochem. Soc.*, **122**, 1700 (1975); (c) T. Takaishi and Y. Gomi, *Rev. Sci. Instrum.*, **47**, 303 (1976).
(3) D. W. Breck, W. G. Eversole, R. M. Milton, T. B. Reed, and T. L. Thomas, *J. Am. Chem. Soc.*, **78**, 5963 (1956).
(4) T. B. Reed and D. W. Breck, *J. Am. Chem. Soc.*, **78**, 5972 (1956).
(5) (a) R. Y. Yanagida, A. A. Amaro, and K. Seff, *J. Phys. Chem.*, **77**, 805 (1973); (b) K. Seff, *Acc. Chem Res.*, **9**, 121 (1976).
(6) P. C. W. Leung, K. B. Kunz, K. Seff, and I. E. Maxwell, *J. Phys. Chem.*, **79**, 2157 (1975).
(7) Nomenclature informally presented by R. M. Barrer, Third International Conference on Molecular Sieves, Zurich, 1973.
(8) K. Seff, *J. Phys. Chem.*, **76**, 2601 (1972).
(9) P. E. Riley, K. Seff, and D. P. Shoemaker, *J. Phys. Chem.*, **76**, 2593 (1972).
(10) R. E. Riley and K. Seff, *Inorg. Chem.*, **14**, 714 (1975).
(11) Principal computer programs used in this study: T. Ottersen, COMPARE data reduction program, University of Hawaii, 1973; full-matrix least-squares, P. K. Gantzel, R. A. Sparks, and K. N. Trueblood, UCLALS4, American Crystallographic Association Program Library (old) No. 317 (modified); Fourier Program, C. R. Hubbard, C. O. Quicksall, and R. A. Jacobson, Ames Laboratory Fast Fourier, Iowa State University, 1971; C. K. Johnson, ORTEP, Report ORNL-3794, Oak Ridge National Laboratory; Oak Ridge, Tenn., 1965.
(12) S. W. Peterson and H. A. Levy, *Acta Crystallogr.*, **10**, 70 (1975).
(13) A. J. C. Wilson, *Acta Crystallogr., Sect. B*, **29**, 1488 (1973).
(14) "International Tables for X-ray Crystallography", Vol. III, Kynoch Press, Birmingham, England, 1962, p 202.
(15) P. A. Doyle and P. S. Turner, *Acta Crystallogr., Sect. A*, **24**, 329 (1968).
(16) "International Tables for X-ray Crystallography", Vol. III, Kynoch Press, Birmingham, England, 1962, p 215.
(17) P. E. Riley and K. Seff, *Inorg. Chem.*, **13**, 1355 (1974).
(18) R. Y. Yanagida, T. B. Vance, Jr., and K. Seff, *Inorg. Chem.*, **13**, 723 (1974).
(19) A. A. Amaro, C. L. Kovaciny, K. B. Kunz, P. E. Riley, T. B. Vance, Jr., R. Y. Yanagida, and K. Seff, "Proceedings of the 3rd International Conference on Molecular Sieves", Leuven University Press, Belgium, 1975, p 113.
(20) "Handbook of Chemistry and Physics", 49th ed, The Chemical Rubber Company, Cleveland, Ohio, 1968.
(21) D. W. Breck, "Zeolite Molecular Sieves", Wiley, New York, N.Y., 1974, pp 462–463, and references therein.
(22) D. H. Olson and E. Dempsey, *J. Catal.*, **13**, 221 (1969).
(23) I. E. Maxwell and J. J. de Boer, *J. Phys. Chem.*, **79**, 1874 (1975).

Kinetics of Light Emission from Excited States of Molecular Iodine Produced in the Pulse Radiolysis of Gaseous Argon–Iodine Mixtures[1]

R. Cooper, F. Grieser,

Department of Physical Chemistry, University of Melbourne, Parkville, Australia

and M. C. Sauer, Jr.*

Chemistry Division, Argonne National Laboratory, Argonne, Illinois 60439 *(Received April 8, 1976)*

Publication costs assisted by Argonne National Laboratory

Light emission from molecular iodine has been studied in the time regime of ca. 20–1000 ns following the radiolysis of argon–iodine systems with 10^{-8}-s pulses. Several emission maxima were observed in the 280–530-nm region, corresponding to emission from known excited states of molecular iodine. The temporal characteristics of the emission are independent of wavelength; the intensity of the emission at 342 nm is the greatest by a factor of about 300. Detailed kinetic studies of the emission at 342 nm show that the emitting state is produced as a result of a sequence of ionic reactions, as well as by a nonionic sequence. The fact that the emission spectrum is the same for both sequences indicates a common precursor of the emitting state. Furthermore, the independence of the kinetics on wavelength indicates that the precursor must be common to all of the emitting states of I_2. A mechanism is suggested which involves the production of excited iodine atoms and subsequent energy transfer to I_2. These results are relevant to the current interest in the 342-nm emission band as a laser.

Introduction

Both the emission and absorption spectra of I_2 have been studied and continually analyzed since Mecke's[2] paper in 1923. The various detailed assignments of the transitions involved obtained by a number of investigators have been reviewed by Mulliken.[3]

The possibility of a tunable laser based on emission from excited I_2 was suggested by Tellinghuisen,[4] and work of McCusker et al.[5] indicates that energy absorbed by argon from an electron beam is efficiently transferred to iodine and emitted as light. Laser action on the 342-nm I_2 band has been recently reported for electron beam excited mixtures of argon with iodine containing compounds.[6–8] Consequently an understanding of the processes leading to excited vibronic levels of I_2 in such systems is of considerable importance.

This study deals with the kinetics of production and decay of excited I_2, produced by a short pulse (4 to 40 ns) of electrons, in an argon atmosphere.

Materials

Argon (Airco, "ultrapure", 99.999%) was used directly without further purification. Iodine (AR grade resublimed I_2, J. T. Baker) was vacuum sublimed, with brief pumping several times in the quartz irradiation vessel to remove traces of any volatile impurities that might be present. SF_6 (Matheson, research grade) was degassed by a number of freeze–pump cycles.

Experimental Section

The optical system used in this study was essentially the same as that described previously[9] and only minor changes were made.

An electron pulse from a linear accelerator (the pulse width was varied between 4 and 40 ns) was used as the perturbation source. The samples were contained in 16-cm long cylindrical quartz cells (with Suprasil windows) and the electron beam traversed the cell along the vessel's axis. Part of the light (that which was emitted in the direction of electron beam) was then reflected through a Bausch and Lomb monochromator, a radiation shielding wall, and onto a 1P28 photomultiplier tube. The amplified output from the tube was then displayed on a Tektronix 7904 oscilloscope and the trace photographed with a Polaroid camera, using 10 000 ASA film. The risetime of the setup was limited to about 3 ns by the photomultiplier circuitry.

Results and Discussion

The emission spectrum observed with 700 Torr of argon and ~0.3 Torr of I_2 using a 40-ns electron pulse is shown in Figure 1. The emissions bands observed correspond with excited I_2 emissions obtained using other techniques.[10–12] Similar emission bands were also obtained in neon and krypton atmospheres.[13]

The growth and decay behavior of these emissions was identical over the entire spectrum range. The effect of dose variation, additives (SF_6), and temperature change (25–80 °C) also resulted in identical kinetic behavior at each wavelength maximum. The emission maximum at 342 nm was of the order of ~300 times more intense than the other band heads and so most of the analyses were performed on this band.

The emission intensities, as a function of time, obtained with 4- and 40-ns pulses are shown in Figures 2 and 3, curves A. (In these, and succeeding figures, time zero is the pulse midpoint.) Using intermediate pulse lengths (10 and 20 ns) the pronounced shoulder seen in Figure 2 was observed to become less distinct, and eventually to become imperceptible as Figure 3 shows. The initial ~50 ns have not been shown because of the interference from Cerenkov light, produced by the electrons passing through the cell window, and from the fast decay of an emission from I_2 which occurs at 342 nm and which has been discussed in a separate report.[14]

The log plots of the decays using 4- and 40-ns pulses are

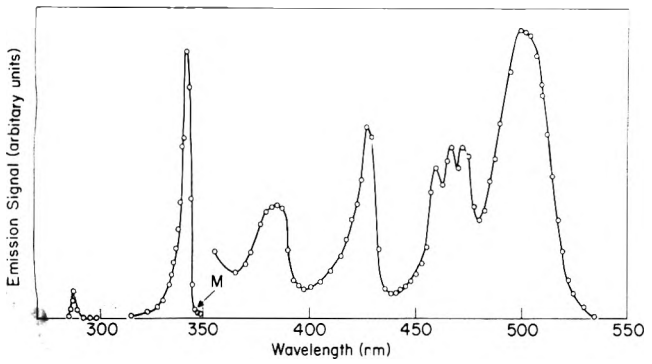

Figure 1. Emission spectrum of sample of 700 Torr of argon and ~0.3 Torr of I_2 obtained using a 40-ns pulse of 12-MeV electrons. Band pass: 280–345 nm, 1 nm; 350–540 nm, 2 nm. Scale factor M (X40). The data are *not* corrected for change in photomultiplier sensitivity over wavelength range.

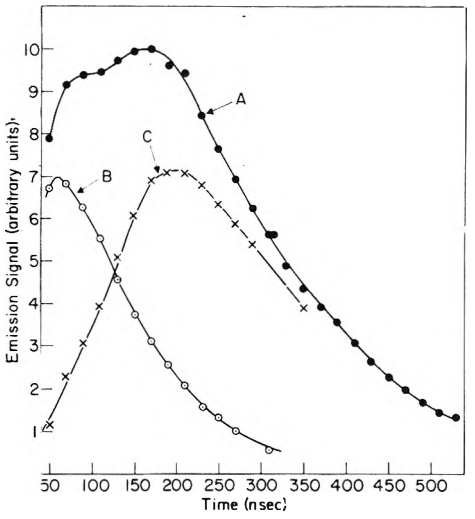

Figure 2. Emission–time signal at 342 nm for 700 Torr of argon + ~0.3 Torr of I_2 (curve A) and 700 Torr of argon + ~0.3 Torr of I_2 + 0.05 Torr of SF_6 (curve B). Curve C is the subtraction of curve B from curve A, and represents the "ionic" contribution to the total emission. These emission signals were obtained using a 4-ns pulse of ~12-MeV electrons.

displayed in Figure 4, which shows that the decays are first order over at least four half-lives.

To determine whether ionic processes were responsible for any part of the emission, 0.05 Torr of SF_6 was added. The results are shown in Figures 2 and 3, curves B, and show that ionic processes are important. Experiments using higher pressures of SF_6 produced no significant change in emission signals indicating that 0.05 Torr of SF_6 was sufficient to remove this ionic contribution to the overall emission yield. The emission–time signals over the spectrum range were again identical. The decays were first order at $1.10 \pm 0.05 \times 10^7$ s^{-1} and independent of dose or argon pressure in the range of 50–700 Torr. Increase in the I_2 concentration (by increase in temperature) gave a linear increase in the decay constant. The second-order rate constant so obtained was $\sim 1 \times 10^{11}$ M^{-1} s^{-1}.

The finding that at about 0.05 Torr of SF_6 a plateau is reached in the decrease in the integrated emission suggests that under these conditions electron capture by SF_6 is considerably more rapid than the alternative fates of the electron. The rate constant[15] for capture of thermal electrons by SF_6 is 1.65×10^{14} M^{-1} s^{-1}, which means that the half-time for

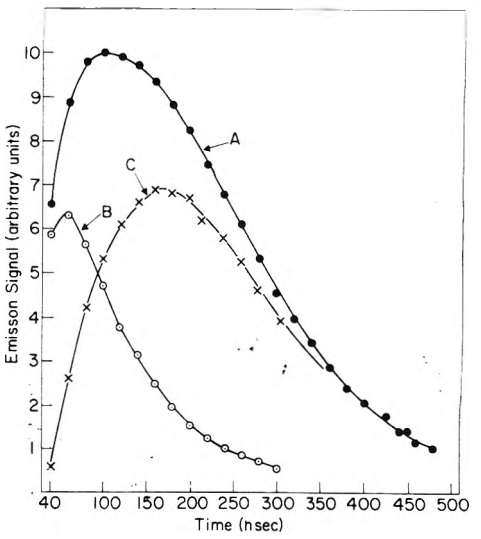

Figure 3. Emission–time signal at 342 nm for 700 Torr of argon + ~0.3 Torr of I_2 (curve A) and 700 Torr of argon + ~0.3 Torr of I_2 + 0.05 Torr of SF_6 (curve B). Curve C is the subtraction of curve B from curve A, and represents the "ionic" contribution to the total emission. These emission signals were obtained using a 40-ns pulse of ~12-MeV electrons.

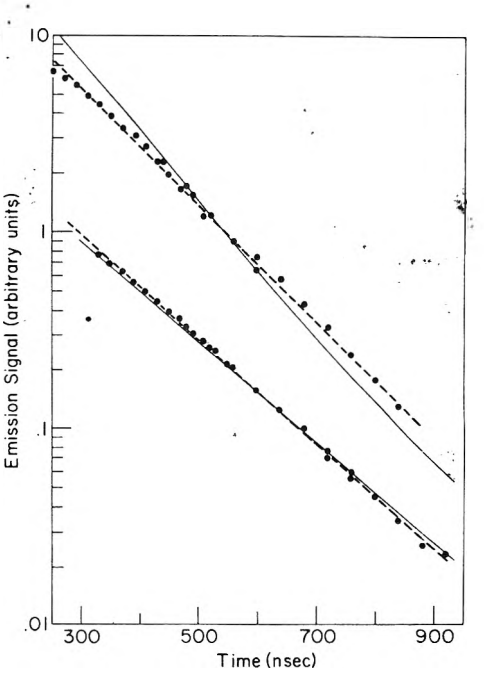

Figure 4. The log plot of decay of iodine emission signal at 342 nm using a 4-ns pulse (lower set) and a 40-ns pulse (upper set). The pseudo-first-order decays obtained from the slopes (dashed lines) are 6.1×10^6 and 6.9×10^6 s^{-1}, respectively. The solid curves are discussed the results of computer simulations using the mechanism in Table I.

electron capture by SF_6 is about 2 ns. The ion concentrations produced by the electron pulse are low enough that $e + Ar_2^+$ would have an initial half-time of at least 100 ns. Electron capture by I_2 would have a half-time of about 400 ns based on the rate constant of 1.1×10^{11} M^{-1} s^{-1} of Truby.[16] The latter value allows a qualitative rationalization of our findings, while previous determinations of this rate constant, giving values up to 200 times larger, do not.

Further evidence that such a low value for the rate constant of electron capture by I_2 is reasonable can be derived from the results shown in Figure 5. The effect of 0.05 Torr of SF_6 on

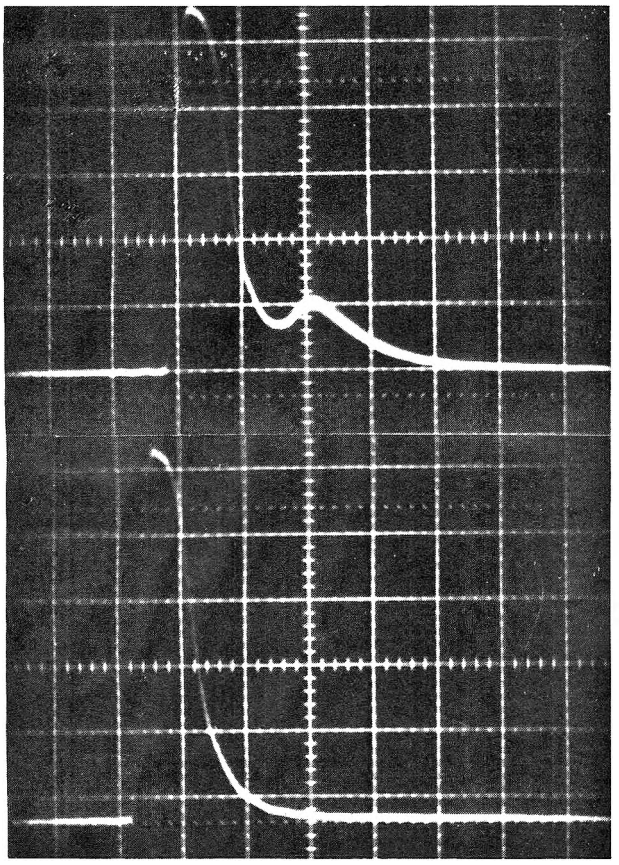

Figure 5. The emission signal of the 2p–1s transition in argon at 770 nm: (a) 350 Torr of argon + ~0.3 Torr of I_2; (b) 350 Torr of Ar + ~0.3 Torr of I_2 + 0.05 Torr of SF_6. Time scale: 50 ns/division. Pulse length: 20 ns. An RCA 4832 photomultiplier tube was used, and the rise time of the system was about 7 ns.

emission from argon 2p–1s[17] transitions in the 700–850-nm range was studied at 350 Torr of Ar, 0.3 Torr of I_2. The results for the transition at 770 nm are shown in Figure 5. The second peak in Figure 5a is almost certainly due to production of the 2p excited state by e + Ar_2^+. (The first peak represents the 2p state which is formed by direct excitation.) The fact that the presence of 0.3 Torr of I_2 does not prevent the formation of the second peak, while 0.05 Torr of SF_6 does (Figure 5b), can only mean that I_2 is not nearly as efficient as SF_6 in capturing electrons. With respect to the above argument, we should point out that it is energetically impossible, by about 1.5 eV, for the reaction of Ar^+ (or Ar_2^+) with I^- to form the 2p states of Ar.

The effect of SF_6 thus indicates that the total emission observed in samples of argon and I_2 is due to contributions from both nonionic and ionic processes, which result in the production of various excited states of I_2. Also, since the kinetics are similar for all the observed emission bands, the different electronic states produced must come from the same common intermediate precursor.

Processes possibly responsible for the production of excited levels of I_2 are considered below.

1. *"Nonionic" Formation of I_2*.* The time scale on which the nonionic formation and decay occurs suggests that excitation of I_2 is by a collisional energy transfer process.

The argon metastable states ($^3P_0$, $^3P_2$) and resonance states ($^1P_1$, $^3P_1$), produced either directly by fast electrons or by deactivation from higher excited states, are capable of energy transfer to I_2. Because the ionization potential of I_2 is ~9.3 eV and the electronic energy of the argon excited states is of the order of 11.5 eV, the direct transfer would lead primarily to ionization. However, evidence from absorption and photoionization studies[18] suggests that 25% or more of the interactions would result in excited state formation.

The argon excimer Ar_2*, which is formed by both two-body and three-body processes,[19] is also energetic enough to lead to the same processes as Ar*,[20] although it is conceivable that the excess energy of the Ar_2*/I_2 coupling is not used to ionize or dissociate I_2, but is shared between two translationally energetic Ar atoms and the various electronic levels of I_2. If excited molecular I_2 is produced directly by collision of Ar_2* with I_2, then there should be an argon pressure dependence of the growth and decay behavior due to the pressure dependence of the formation of Ar_2*. This is *not* observed over the pressure range (50 → 700 Torr) studied. Further, if Ar* and Ar_2* produce I_2* directly by collision with I_2 then the following kinetic consequence would result. The maximum in the emission–time curve for the nonionic processes should occur at ~25 ns, due to the short lifetime of I_2*[14] ($t_{1/2}$ = 6.7 ns). The observed data (curves B in Figures 2 and 3) show a maximum at ~60 ns and hence do not support such a mechanism.

A mechanism which does appear to be consistent with the observations involves excited iodine atoms. Excited iodine atoms could result from dissociative collisional excitation transfer from either excited argon atoms or dimers. These excited atoms could then transfer energy to molecular iodine by collisional processes, i.e.

$$Ar^* \text{ (or } Ar_2^*) + I_2 \rightarrow I^*$$

and

$$I^* + I_2 \rightarrow I_2^{**}$$

To agree with the experimentally observed emission behavior, a radiative lifetime of I* greater than ca. 100 ns is required.

The similarity of the kinetics observed at the various wavelength maxima indicates that the emitting states (I_2*[E, D, B, etc.]) have a common precursor. The relaxation time of this precursor to the emitting states must be fast compared with the collisional processes forming it, i.e.

$$I_2^{**} \rightarrow I_2^* \text{ (E, D, B, etc.)} \qquad \text{where } k > 10^8\ s^{-1}$$

Also, the lifetimes of I_2* must be short in comparison with the time scale of the collisional processes forming I_2** to fit with the observed similarity of the kinetics at various wavelengths.[21]

In the above processes I* represents all possible energetic iodine atomic states which are capable of producing the higher electronic levels in I_2. Such states may be those that emit between 1783 and 1876 Å. The $6s^4P_{5/2}$ iodine atomic state has a lifetime of 125 ns[22] and would be a suitable species in this reaction mechanism.[23] I_2* are all the various states of I_2 which can either emit light, be deactivated by argon, or dissociate as in the case of the $B(^3\pi_o{}^+{}_u)$ state.[24] The above reaction mechanism can account for the effects of dose, temperature, the lack of an argon pressure effect, and the common kinetics observed at various wavelengths.

In the above mechanism, the rate of energy transfer from Ar* and Ar_2* to I_2 will control the growth of emission whereas the decay will be controlled by the subsequent removal of I* by collisional transfer to I_2.

2. *"Ionic" Formation of I_2*.* The subtraction of the nonionic part of the I_2 emission from the total emission leaves curves C in Figures 2 and 3, i.e., the contribution to the emitting states from ionic precursors. There is a slight (~30 ns) shift

TABLE I: Reaction Mechanism

Reaction no.	Reaction[a]	Rate constant,[b] M^{-1} s^{-1} or s^{-1}
1	$e^- \rightarrow e_t^-$	2.2×10^7
2	$e_t^- + I_2 \rightarrow I^-$	3.0×10^{11}
3	$e_t^- + Ar_2^+ \rightarrow Ar^*$	5.1×10^{14}
4	$Ar_2^+ + I_2 \rightarrow I_2^+$	5.0×10^{11}
5	$e_t^- + I_2^+ \rightarrow I^*$	1.0×10^{15}
6	$Ar^* + I_2 \rightarrow I_2^+ + e^-$	6.6×10^{11}
7	$Ar_2^+ + I^- \rightarrow I^*$	1.0×10^{15}
8	$I_2^+ + I^- \rightarrow I^*$	1.0×10^{15}
9	$I^- + I_2 \rightarrow I_3^-$	2.3×10^{11}
10	$I_3^- + I_2^+ \rightarrow$ products[c]	1.0×10^{15}
11	$Ar^* + I_2 \rightarrow I^*$	6.6×10^{11}
12	$I^* + I_2 \rightarrow I_2^{**}$	7.0×10^{11}
13	$I_2^{**} \rightarrow I_2^*$ (E, D, B, etc.)	$>10^8$
14	$I_2^* \rightarrow h\nu$	1.0×10^8
15	$I_2^* \xrightarrow{M}$ quenching[d]	

[a] For simplification, irrelevant products are not included. [b] k_3 is from ref 27; the results of the simulation are not very sensitive to the ion recombination rate constant, so the other recombination rate constants are all taken to be 1×10^{15} M^{-1} s^{-1}. The simulated curves are sensitive to k_2, k_6, k_9, k_{11}, and k_{12}; hence, these were varied to obtain a reasonable fit with experiment. [c] Products other than I*, I_2^{**}, or I_2^*. [d] For the state emitting at 342 nm, k_{15} (for M = Ar) is negligible.[14]

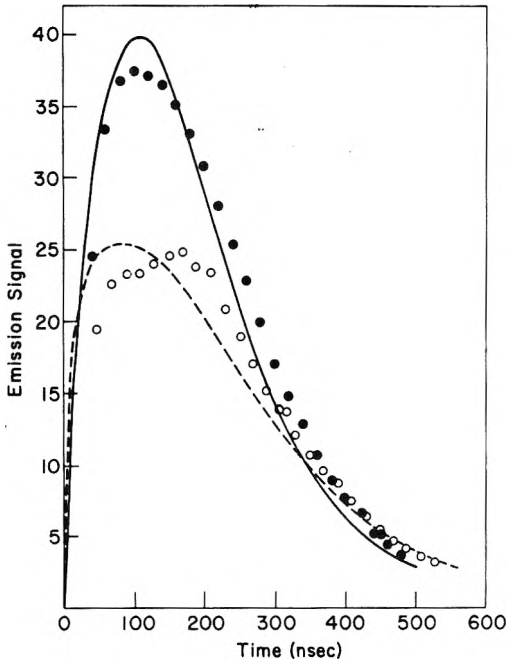

Figure 6. Total emission. The curves represent the simulated emission. The ordinate of the dashed curve is multiplied by 10: (●) normalized experimental data from Figure 3, curve A (40-ns pulse); (○) normalized experimental data from Figure 2, curve A (4-ns pulse).

in the maximum of curve C, with the 40-ns pulse compared to the 4-ns pulse. This is due to the fact that the ion recombination is slower with the 4-ns pulse, and in fact the emission from the nonionic and ionic processes is partially resolved (Figure 2, curve A). It was also found that the ratio of integrated emission vs. time signals of the "ionic" emission to the "nonionic" emission was constant with dose at 1.6 ± 0.3.

Ion recombination processes resulting in the formation of excited iodine atoms would satisfy the requirement of ionic precursors of I_2^*, and would result in the identical series of resultant emitting states from the ionic and nonionic sequences. Processes which are likely to be important in the ionic sequence include electron thermalization, which can be estimated to take times of about 100 ns in this system.[25] Electron capture by I_2 would be inefficient until the electrons approached thermal energy.[26] However, reaction of the electron with Ar_2^+ would not be as sensitive to electron energy.[27] A critical requirement of an ionic sequence capable of explaining the experimental observations is that one of the ions involved in the recombination reaction producing I* must also disappear by an additional process, which is pseudo-first order and which does not lead to I*. Otherwise, a "tail" would be observed at long times in the emission decay curves.

3. *Overall Mechanism.* Table I presents a reasonable sequence of processes qualitatively consistent with the observed phenomena and incorporates processes which can be expected to occur on the basis of fundamental studies pertinent to radiation chemistry.

The primary reactants of significance to this mechanism are Ar^+, Ar*, I*, and e^- (nonthermal); Ar^+ is assumed to be converted rapidly to Ar_2^+. Ar* and Ar_2^* are assumed to undergo the same reactions because no argon pressure effect was observed and hence the conversion of Ar* to Ar_2^* is not considered. Reaction 1 is only a qualitative approximation to the electron thermalization process which delays formation of electrons capable of participating in capture or ion combination reactions. An initial concentration of I* is expected to be produced from direct dissociative excitation of I_2 by subexcitation electrons.[28] Reactions 9 and 10 provide one means whereby a pseudo-first-order sink for one of the ionic species can explain the approximate first-order nature of the emission decays and the slight change in slope with initial concentrations.

A computer simulation[30] of the observed results using this mechanism was carried out. The calculations were performed for initial concentrations varying by a factor of 10 (corresponding approximately to the experimental situation). The higher initial concentrations used were; $[Ar_2^+] = [e^-] = [Ar^*] = 4.5 \times 10^{-8}$ M and $[I^*] = 1.8 \times 10^{-9}$ M. The results (full lines) are shown and compared with experimental points in Figure 6. The logrithmic plots resulting from these calculations are shown as solid curves in Figure 4.

The emission curves calculated show a fair fit with experiment. Three qualitative conclusions may be drawn from these results.

(1) The partial separation between the nonionic and ionic emission peaks is connected with electron thermalization processes.

(2) The effect of varying initial ion concentration on the overall decay rate is small and there is no second-order "tail" if either of the positive or negative ions reacts partially by a pseudo-first-order process which does not eventually produce I*.

(3) The calculated ratios of "ionic" to "nonionic" emission decreases only about 30% for an order of magnitude decrease in initial concentration, which is within the spread of the experimental values of this ratio.

Acknowledgment. R. C. and F. G. wish to acknowledge receipt of a travel grant from the Australian Research Grants Committee. F. G. acknowledges receipt of a CPRA research studentship.

References and Notes

(1) Work performed in part under the auspices of the U.S. Energy Research and Development Administration, and in part under the auspices of the Australian Research Grants Committee.
(2) R. Mecke, *Ann. Phys.*, **71**, 104 (1923).
(3) R. S. Mulliken, *J. Chem. Phys.*, **55**, 288 (1971).
(4) J. Tellinghuisen, *Chem. Phys. Lett.*, **29**, 359 (1974).
(5) M. V. McCusker, R. M. Hill, D. L. Huestis, D. C. Lorents, R. A. Gutcheck, and H. H. Nakano, *Appl. Phys. Lett.*, **27**, 363 (1975).
(6) R. S. Bradford, Jr., E. R. Ault, and M. L. Bhaumik, *Appl. Phys. Lett.*, **27**, 546 (1975).
(7) J. J. Ewing and C. A. Brau, *Appl. Phys. Lett.*, **27**, 557 (1975).
(8) A. K. Hays, J. M. Hoffman, and G. C. Tisone, *Chem. Phys. Lett.*, **39**, 353 (1976).
(9) M. C. Sauer, Jr., and W. A. Mulac, *J. Chem. Phys.*, **56**, 4996 (1972).
(10) R. D. Verma, *Proc. Indian Acad. Sci. A*, **48**, 197 (1958).
(11) P. Venkateswarlu, *Phys. Rev.*, **81**, 821 (1951).
(12) K. Wieland and J. Waser, *Nature (London)*, **160**, 643 (1947).
(13) With a xenon atmosphere the spectrum was markedly different. Details of the xenon results will be published in another paper.
(14) M. C. Sauer, Jr., W. A. Mulac, R. Cooper, and F. Grieser, *J. Chem. Phys.*, **64**, 4587 (1976).
(15) L. G. Christophorou, "Atomic and Molecular Radiation Physics," Wiley-Interscience, New York, N.Y., 1971, p 501.
(16) F. K. Truby, *Phys. Rev.*, **172**, 24 (1968).
(17) S. Arai and R. F. Firestone, *J. Chem. Phys.*, **50**, 4575 (1969).
(18) M. Yoshino, A. Ida, K. Wakiya, and H. Suzuki, *J. Phys. Soc. Jpn.*, **27**, 976 (1969).
(19) R. F. Firestone, USAEC Document No. C00-1116-20, Part 1, 24 July 1972.
(20) G. Hurst, T. Bortner, and T. Strickler, *Phys. Rev.*, **178**, 4 (1969).
(21) Although the radiative lifetime of the B state of iodine is long (between 1 and 4 μs (J. I. Steinfeld and A. N. Schweid, *J. Chem. Phys.*, **53**, 3304 (1970)), collision with argon efficiently deactivates the state (G. Capelle and H. P. Broida, *J. Chem. Phys.*, **58**, 4212 (1973)) and therefore, even at the lower pressure limit of our experiments I_2 ($B^3\pi_{o+u}$) is short-lived. The band system around 342 nm has a radiative lifetime of 6.7 ns (ref 14). Also, since emissions from other vibronic levels have the same kinetics as both the B state and the 342-nm band state, the lifetime of these iodine states must be short compared to the precursor reactions.
(22) J. B. Tellinghuisen, Ph.D. Thesis, University of California, Berkeley, Nov 1969.
(23) Excited iodine atoms with much shorter radiative lifetimes could participate in this mechanism if their lifetimes were artificially lengthened by resonance radiation trapping. However, this would require an appreciable concentration of ground state iodine atoms to be present in the system which we do not expect at times as short as hundreds of nanoseconds.
(24) G. Capelle and H. P. Broida, *J. Chem. Phys.*, **58**, 4212 (1973), and numerous other papers by J. I. Steinfeld and co-workers.
(25) J. M. Warman and M. C. Sauer, Jr., *J. Chem. Phys.*, **62**, 1971 (1975).
(26) See ref 15, pp 465 and 468.
(27) F. J. Mehr and M. A. Biondi, *Phys. Rev.*, **176**, 322 (1968).
(28) In order to have a correct ratio of ionic to nonionic emission *without* including an initial I^* concentration, the fraction of the ionization caused by Ar^* would have to be much larger than is reasonable on the basis of known effects of impurities on the *W* value of argon.[29] Further, direct excitation of molecular I_2 to high electronic levels has been observed by us[14] in subcollisional times: we presume that excited iodine atoms will be produced also.
(29) See ref 15, p 52.
(30) K. H. Schmidt, "A Computer Program for the Kinetic Treatment of Radiation-induced Simultaneous Chemical Reactions", Argonne National Laboratory Report No. ANL-7693, 1970.

PHYSICAL PHENOMENA

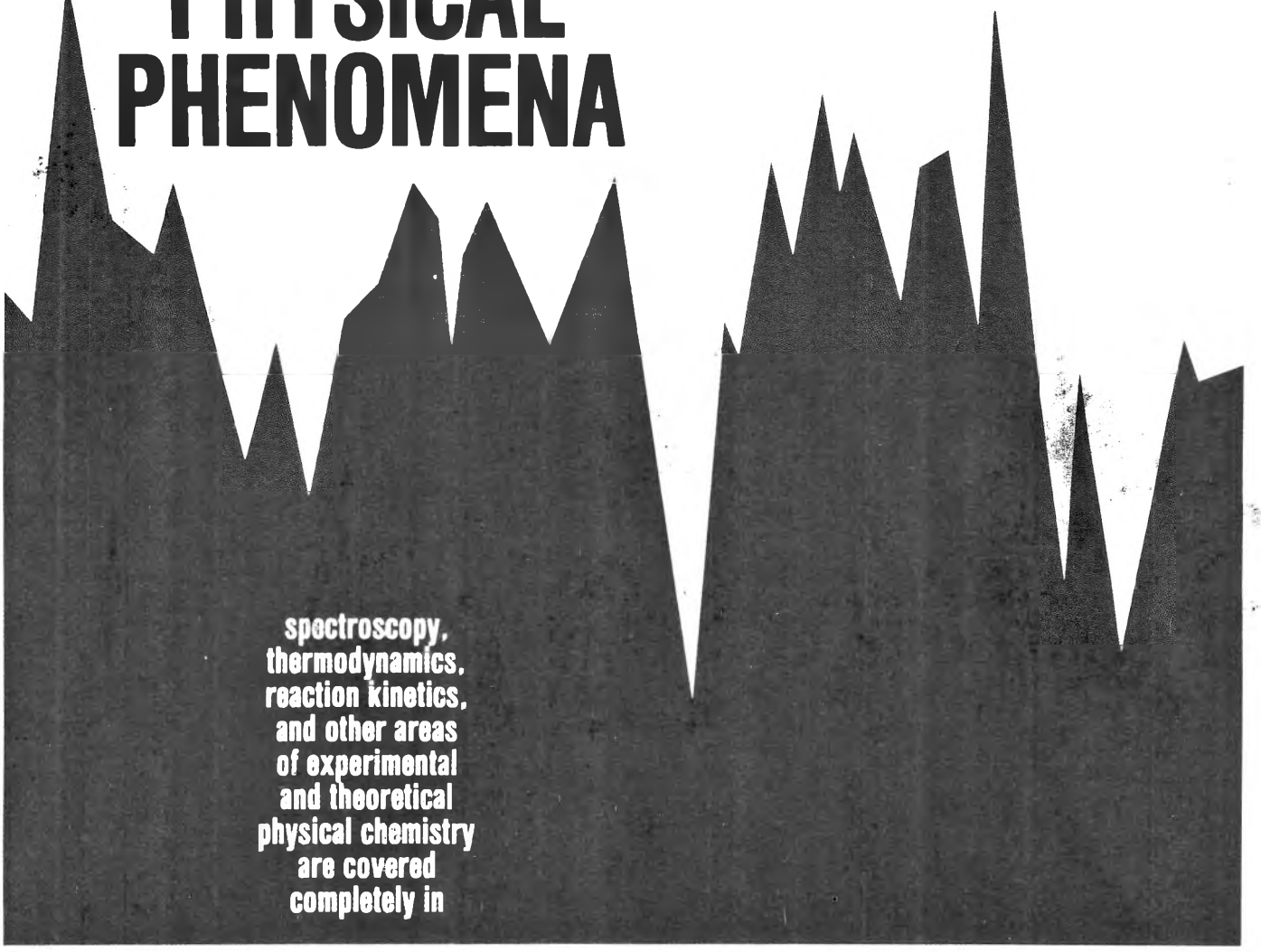

THE JOURNAL OF PHYSICAL CHEMISTRY

The biweekly JOURNAL OF PHYSICAL CHEMISTRY includes over 25 papers an issue of original research by many of the world's leading physical chemists. Articles, communications, and symposia cover new concepts, techniques, and interpretations. A "must" for those working in the field or interested in it, the JOURNAL OF PHYSICAL CHEMISTRY is essential for keeping current on this fast moving discipline. Complete and mail the coupon now to start your subscription to this important publication.

The Journal of Physical Chemistry
American Chemical Society **1976**
1155 Sixteenth Street, N.W.
Washington, D.C. 20036

Yes, I would like to receive the JOURNAL OF PHYSICAL CHEMISTRY at the one-year rate checked below:

	U.S.	*Canada***	*Latin America***	*Other Nations***
ACS Member One-Year Rate*	☐ $24.00	☐ $30.25	☐ $29.75	☐ $30.25
Nonmember	☐ $96.00	☐ $102.25	☐ $101.75	☐ $102.25

Bill me ☐ Bill company ☐ Payment enclosed ☐

Air freight rates available on request.

Name _____

Street _____ Home ☐ Business ☐

City _____ State _____ Zip _____

Journal subscriptions start January '76

*NOTE: Subscriptions at ACS member rates are for personal use only. **Payment must be made in U.S. currency, by international money order, UNESCO coupons, U.S. bank draft, or order through your book dealer.

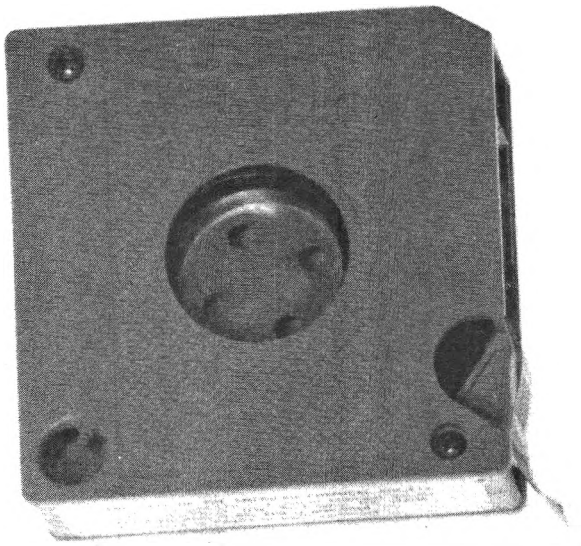

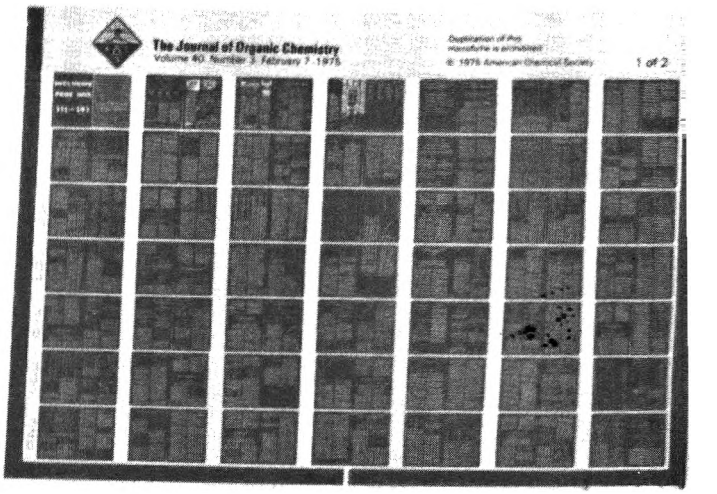

MICROFORMS

American Chemical Society publications in microform

MICROFILM OR MICROFICHE?

With the ACS microform program you can receive either, or both

Microfilm

All periodical publications back to volume one

Copying privileges included with current subscriptions

All non-print supplementary materials provided free on microfiche

Archival quality silver halide film supplied as you request; positive or negative; 16 or 35mm; cartridge, reel, or cassette.

Microfiche

Current issues of primary journals, beginning with January 1975

Individual issues or full volumes available

Supplementary materials also available on microfiche

Fiche supplied are archival quality silver halide, negative, 105 x 148mm (4" x 6"); 24x, with eye legible headers, start and end targets, and page numbers

For information about our microfilm/microfiche write:

Microform Program
Special Issues Sales
American Chemical Society
1155 16th Street, N.W.
Washington, D.C. 20036
(202) 872-4363